Dissertation
submitted to the
Combined Faculties of the Natural Sciences and Mathematics
of the Ruperto-Carola-University of Heidelberg, Germany
for the degree of
Doctor of Natural Sciences

Put forward by
Vladislav Gavryusev
Born in: Moscow, Russia
Oral examination: December 19th, 2016

Imaging of Rydberg Impurities in an Ultracold Atomic Gas

Referees: **Prof. Dr. Matthias Weidemüller**
                                     Prof. Dr. Selim Jochim

Abstract: This thesis investigates how a single highly excited atom, called Rydberg atom, can be optically imaged. Direct detection methods based on the scattering of light are hardly applicable due to the small scattering rate of the ground to Rydberg state transition. Instead, a cloud of ground state atoms, normally absorptive, is rendered transparent using electromagnetically induced transparency (EIT), involving an auxiliary probe Rydberg state. The cloud acts as a contrast medium, whose optical response is locally perturbed by the strong Rydberg-Rydberg interaction between the probe and the Rydberg impurity which we want to detect. This perturbation restores absorption within a small volume around the impurity, readily detected and spatially resolved on a camera. We call this technique Interaction Enhanced Imaging (IEI). To implement IEI we characterize the optical response of the EIT contrast medium in absence of interactions. By combining measurements of the spatially resolved optical spectrum and of the total Rydberg atom number, we can reconstruct the full one-body density matrix of the three-level system. Next, we excite $|nS\rangle$ or $|nP\rangle$ states and, using IEI, we demonstrate spatially resolved imaging, enabling us to study dipolar energy transport. To reach single impurity sensitivity we investigate our current detection fidelity and characterize the signal and noise contributions in IEI. We model our interacting system, finding good agreement with experimental data. Based on this model, we predict combinations of Rydberg states for which single-shot single impurity sensitivity should be possible in future experiments.

Zusammenfassung:

Diese Arbeit untersucht wie ein einzelnes, hoch angeregtes Atom, genannt Rydbergatom, optisch abgebildet werden kann. Direkte Abbildungsmethoden, die auf Streuung von Licht basieren, sind wegen der kleinen Streurate des Übergangs vom Grund- zum Rydbergzustand schwer anwendbar. Stattdessen wird eine Wolke von Grundzustandsatomen, die normalerweise absorptiv wäre, mit Hilfe von elektromagnetisch induzierter Transparenz (EIT) unter Einfluss eines zusätzlichen probe-Rybergzustands, transparent gemacht. Die Wolke dient als Kontrastmedium, dessen optisches Antwortverhalten lokal durch starke Rydberg-Rydberg-Wechselwirkung zwischen den probe- und impurity-Rydbergatomen, die wir detektieren möchten, modifiziert wird. Diese Störung stellt in einem kleinen Volumen um die impurity-Atome herum die Absorption wieder her die sogleich mit einer Kamera detektiert und räumlich aufgelöst wird. Wir nennen diese Technik Interaction-Enhanced-Imaging (IEI). Um IEI zu implementieren charakterisieren wir das optische Antwortverhalten von dem EIT-Kontrastmedium unter Abwesenheit der Wechselwirkung. Durch Kombination von Messungen von sowohl des räumlich aufgelösten optischen Spektrums als auch der Gesamtanzahl der Rydbergatome können wir die gesamte Einteilchen-Dichtematrix des Drei-Niveau-Systems rekonstruieren. Als nächstes regen wir ns oder np Zustände an und demonstrieren mit Hilfe von IEI räumlich aufgelöste Abbildung was uns erlaubt dipolaren Energietransport zu studieren. Um Einzel-impurity-Sensitivität zu erzielen untersuchen wir unsere aktuelle Detektionszuverlässigkeit und charakterisieren die Signal- und Rauschbeträge von IEI. Wir modellieren unser wechselwirkendes System und finden gute Übereinstimmung mit den experimentellen Daten. Basierend auf diesem Model sagen wir Kombinationen von Rydbergzuständen voraus für die Einzelrealisierungs- und Einzel-impurity-Sensitivität in zukünftigen Experimenten möglich sein sollte.

This thesis is based on the following manuscripts and publications:

- **Controlled coherent and incoherent motion of dipolar interacting Rydberg excitations**
  H. Schempp, G. Günter, V. Gavryusev, M. Ferreira-Cao, S. Whitlock, M. Weidemüller
  in preparation

- **Interaction-Enhanced Imaging of Rydberg P states**
  V. Gavryusev, M. Ferreira-Cao, A. Kekić, G. Zürn and A. Signoles
  arXiv:1602.04143 (2016), accepted for publication in Eur. Phys. J. ST

- **Density matrix reconstruction of three-level atoms via Rydberg electromagnetically induced transparency**
  V. Gavryusev, A. Signoles, M. Ferreira-Cao, G. Zürn, C. S. Hofmann, G. Günter, H. Schempp, M. Robert-de-Saint-Vincent, S. Whitlock and M. Weidemüller
  J. Phys. B **49**, 16 (2016)

- **Observing the dynamics of dipole-mediated energy transport by interaction enhanced imaging**
  G. Günter, H. Schempp, M. Robert-de-Saint-Vincent, V. Gavryusev, S. Helmrich, C. S. Hofmann, S. Whitlock, M. Weidemüller
  Science **342** 953-956 (2013)

The author furthermore contributed to the following publications:

- **Density-density correlations across the superfluid-to-Mott-insulator transition**
  D. Naik, V. Gavryusev, S. Conclave, S. Rosi, F. Minardi
  in preparation

Contents

Chapter 1

Introduction

Imaging single particles allows to study in detail the microscopic properties of the system they constitute and reaching such sensitivity level is one of the driving forces of scientific progress. New or improved detection techniques push the boundaries of what we can observe further, ranging from investigations at the smallest length scales in particle accelerators, up to the observation of stars and galaxies. Between those two extremes lies the research in atomic physics that in the past 30 years has greatly benefited from the achievement of ultracold temperatures [Nob, 1997; Nob, 2001] and the development of techniques to precisely control coupled atom-light systems, down to the single particle level [Nob, 2012]. The ability to tune interactions in ultracold gases has allowed to explore rich many-body physics [Bloch *et al.*, 2008], ranging from the superfluid to Mott-insulator quantum phase transition [Greiner *et al.*, 2002] to the reversible formation of a Bose-Einstein condensate of molecules from a degenerate Fermi gas [Regal and Jin, 2007]. The use of these highly controllable atomic systems together with optical lattices and high resolution fluorescence imaging has enabled to observe single atoms [Bakr *et al.*, 2009; Sherson *et al.*, 2010; Cheuk *et al.*, 2015; Ott, 2016] and to investigate many-body dynamics at the single-atom level [Bakr *et al.*, 2010; Greif *et al.*, 2016], paving the way towards quantum simulators [Lewenstein *et al.*, 2007; Bloch *et al.*, 2012; Cirac and Zoller, 2012].

When atoms in an ultracold atomic gas are excited to highly-lying electronic states, called Rydberg states, they change the nature of their interactions from short to long range, acquiring remarkable properties [Gallagher, 1994] such as huge polarizabilies, large dipole moments and strong electric dipole-dipole interactions [Saffman *et al.*, 2010]. The strength and the character of these interactions can be vastly tuned by the choice of states and by external electric fields. The interaction effects can be so strong to compete with the laser excitation to Rydberg states, leading to new

many-body phenomena such as the Rydberg blockade [Comparat and Pillet, 2010; Löw *et al.*, 2012], in which only a single Rydberg atom can be excited within a certain volume.

The properties of Rydberg atoms provide new avenues to investigate strongly correlated many-body physics [Weimer *et al.*, 2008; Pohl *et al.*, 2010; van Bijnen *et al.*, 2011; Viteau *et al.*, 2012; Hofmann *et al.*, 2013; Schempp *et al.*, 2014; Malossi *et al.*, 2014; Schauß *et al.*, 2015], to implement quantum information protocols [Jaksch *et al.*, 2000; Isenhower *et al.*, 2010; Saffman *et al.*, 2010; Saffman, 2016] and to create atom-light interfaces operating at the single photon level [Dudin and Kuzmich, 2012; Peyronel *et al.*, 2012; Maxwell *et al.*, 2013; Firstenberg *et al.*, 2013; Tiarks *et al.*, 2014; Gorniaczyk *et al.*, 2014]. To probe with high spatial and temporal resolution the dynamics and correlations at play in these complex systems an imaging method for Rydberg atoms is desirable.

In this thesis I investigate the question of how a single Rydberg atom can be optically imaged. Direct optical detection methods that are based on the scattering of light, like absorption or fluorescence imaging, are hardly applicable due to the small scattering rate of the ground to Rydberg state transition. Only recently a few alternative approaches have been demonstrated, either using field ionization [Schwarzkopf *et al.*, 2011; Lochead *et al.*, 2013] or through indirect fluorescence imaging [Schauß *et al.*, 2012; McQuillen *et al.*, 2013; Labuhn *et al.*, 2016]. Here we demonstrate a different fully optical method called Interaction Enhanced Imaging (IEI) [Günter *et al.*, 2012; Olmos *et al.*, 2011], which is state-selective, provides both high spatial and temporal resolution, making it ideally suited to study Rydberg dynamics.

At the root of the IEI technique lies the use of a narrow optical transition that can be perturbed by the presence of a Rydberg atom. For this purpose, we use the steep optical response induced by a quantum interference effect called electromagnetically induced transparency (EIT) [Fleischhauer *et al.*, 2005], which renders transparent an otherwise absorptive medium. EIT occurs in three-level atomic systems where two stable states are resonantly coupled by a weak and a strong light fields. In our imaging scheme one of these two is an auxiliary "probe" Rydberg state. If a different "impurity" Rydberg state that we aim to detect is also present, then strong Rydberg-Rydberg interactions between the two arise, locally perturbing the EIT optical response, such that absorption is restored within a blockade volume around the impurity. This allows to map the Rydberg state properties, e.g. interactions or energy shifts, onto a strong optical transition [Mohapatra *et al.*, 2007; Pritchard *et al.*, 2010; Tauschinsky *et al.*, 2010]. The transmitted light field can then be readily spatially resolved using a charge-coupled-device (CCD) camera, thereby exposing

the impurity position.

In this context, the atomic cloud coupled under EIT conditions is used as a contrast medium to optically reveal the presence of one or more Rydberg "impurities". Consequently, IEI is similar in spirit to techniques like super-resolution microscopy [Nob, 2014], magnetic resonance imaging [Nob, 2003], contrast-enhanced ultrasound [Claudon *et al.*, 2013] and X-ray based imaging methods [Attwood, 2007], which find application in many fields, including biology and medicine [Kherlopian *et al.*, 2008].

A study of EIT in absence of interactions is necessary to disentangle the effects of the impurity presence from the response of the unperturbed medium. Complete knowledge of the coupled atom-light system is encoded in its single atom density matrix. We probe the light part by measuring the transmission through the cloud and access the matter part by recording the Rydberg state population. By combining these two complementary measurements in a single Rydberg experiment for the first time, we extract the parameters that allow to perform a non-tomographic spatially resolved reconstruction of the full density matrix using prior knowledge on its form. The presented method constitutes a tool for modeling light propagation in interacting Rydberg ensembles under EIT coupling [Pritchard *et al.*, 2013; Firstenberg *et al.*, 2016; Han *et al.*, 2016] and for describing IEI.

After characterizing the contrast medium, we perform first IEI experiments with Rydberg $|n'S\rangle$ impurities, demonstrating their spatially resolved optical detection. Furthermore, we observe that for certain Rydberg states the impurities undergo a state-exchange process with the probe states [Mourachko *et al.*, 1998; Anderson *et al.*, 1998; Anderson *et al.*, 2002; Westermann, S. *et al.*, 2006; van Ditzhuijzen *et al.*, 2008], leading to a diffusive energy transport that we follow with high spatial and temporal resolution. The sensitivity in these first measurements is limited by the blockade volume per impurity and by the transport that spreads the signal over many camera pixels. Our goal is to image single Rydberg atoms and this leads us to investigate $|nP\rangle$ impurities that exhibit strong resonant dipole-dipole interactions with the auxiliary probe $|nS\rangle$ state, allowing for bigger blockade volumes than $|n'S\rangle$-$|nS\rangle$ state combinations. We inhibit transport by constraining the cloud volume and we demonstrate for the first time optical detection of Rydberg P-states with high spatial resolution and improved sensitivity, close to the best competing methods.

To understand the main aspects of our imaging technique and reach single Rydberg atom sensitivity, we investigate the detection fidelity and perform a detailed analysis of the signal and noise contributions in IEI, devising methods to reduce the impact of the latter. Finally, we develop a model to predict the signal to noise ratio (SNR)

to be expected in an IEI experiment, by extending a hard-sphere model that was first introduced to describe a strongly interacting Rydberg EIT medium [Petrosyan *et al.*, 2011; Ates *et al.*, 2011; Gärttner *et al.*, 2014b; DeSalvo *et al.*, 2016; Han *et al.*, 2016]. We compare its predictions with experimental data, finding good agreement, and we use it to calculate the achievable SNR for a broad range of impurity-probe state pairs and laser coupling parameters, allowing us to identify which Rydberg state combinations are the most promising for future experiments with single-shot single Rydberg atom sensitivity.

This thesis is structured as follows: Ch. 2 starts with a brief introduction to the key properties of Rydberg atoms and their interactions, which play a major role in this work. Then the experimental apparatus is described in Ch. 2.4 and the Rydberg state preparation methods are presented in Ch. 2.5, with a detailed study of the three-photon off-resonant excitation scheme developed to prepare $|nP\rangle$ Rydberg states. Ch. 3 focuses on the properties of the contrast medium under EIT coupling, introducing first the basic description of EIT, while in the second part we present the combined measurements which are used to reconstruct the density matrix of the non-interacting three-level atoms, obtaining complete information on the system. Then, in Ch. 4 we turn our attention to the IEI method, reviewing the state-of-the art of Rydberg imaging and discussing the first IEI measurements with $|n'S\rangle$ states. In Ch. 4.2 we examine the diffusive energy transport observed between $|n'S\rangle$-$|nS\rangle$ states. Next, in Ch. 4.3 we develop a model for IEI and in Ch. 4.5 we present the first state resolved optical detection of Rydberg P-states. In the last part of this thesis (Ch. 5), we address the question of single Rydberg impurity imaging. First, we estimate our current sensitivity by measuring the detection fidelity, then we investigate the signal and noise contributions to IEI and, at last, we explore how our goal can be reached. These predictions constitute the basis for future single-particle sensitive energy transport experiments, that would clarify at a microscopic level open questions like the role of disorder and decoherence on the dynamics.

Chapter 2

Ultracold interacting Rydberg gases: properties and experimental approach

This chapter is partially based on the following publication, from which parts of the text are reproduced verbatim in Sec. 2.5:

Interaction-Enhanced Imaging of Rydberg P states
V. Gavryusev, M. Ferreira-Cao, A. Kekić, G. Zürn and A. Signoles
arXiv:1602.04143 (2016), accepted for publication in Eur. Phys. J. ST

Atoms in highly excited states, called also Rydberg atoms, have been studied for more than a century (for reviews see [Gallagher, 1994; Stebbings and Dunning, 1983; Pillet and Gallagher, 2016]) and the development of laser-cooling has greatly expanded the field of investigation, with topics ranging from few- and many-body physics [Choi *et al.*, 2006; Comparat and Pillet, 2010; Löw *et al.*, 2012; Hofmann *et al.*, 2014], quantum non-linear optics [Pritchard *et al.*, 2013; Firstenberg *et al.*, 2016; Murray and Pohl, 2016], quantum simulation [Weimer *et al.*, 2008; Weimer *et al.*, 2010; Müller *et al.*, 2012] and quantum computing [Saffman *et al.*, 2010; Saffman, 2016], over to strongly correlated plasmas [Killian *et al.*, 2007; Pohl *et al.*, 2011] and ultracold chemistry [Bendkowsky *et al.*, 2009; Gaj *et al.*, 2014; Schlagmüller *et al.*, 2016]. Such a broad range of application is enabled by the "exaggerated" properties of Rydberg atoms. The large separation between the highly excited valence electron and the atomic core and the consequent loose binding lead to huge electric polarizabilities and strong long-range interactions with the surrounding atoms.

In this introductory chapter we first review some of the basic properties of Rydberg atoms. In particular in Ch. 2.2 we discuss the origin and type of Rydberg-Rydberg interactions. Then the experimental apparatus is presented in Ch. 2.4, which was enhanced during the course of this thesis, and the Rydberg state preparation is discussed in Ch. 2.5.

2.1 Alkali Rydberg atoms

Atoms with at least one electron excited to a high-lying atomic state with large principal quantum number n are called Rydberg atoms. In such a state the electron is weakly bound and is on average a factor of 100 to 1000 farther from the atom core compared to an electron in the ground state, consequently it experiences approximately a $1/r$ potential, making the Rydberg atoms very similar to hydrogen atoms.

In this thesis we work with highly excited states of rubidium which is an alkali atom and consequently has one valence electron. The other electrons fill the inner shells and shield the core charge, reducing it to a net core charge of $Z = 1$. Thanks to this shielding effect, the valence electron, once excited to a Rydberg state, experiences a hydrogen-like potential with a single positive charge. For this reason the wave functions of alkali Rydberg atoms closely resemble those of the hydrogen atom. However, in contrast to hydrogen, the valence electron in states with low angular momentum $\ell \leq 3$ can penetrate the finite size core and becomes exposed to core charges of $Z > 1$. This leads to a deviation of the core potential from being purely Coulombic at short range and lifts the ℓ-degeneracy known for the hydrogen atom. The effects of these deviations are accounted for using quantum defect theory [Seaton, 1983] and result mainly in a phase shift of the wave functions together with an increase of the eigenvalues energy relative to the hydrogen atom. The resulting increased binding energy E_n is

$$E_n = -hc\frac{R_{Rb}}{(n - \delta_{n,\ell,j})^2} = -hc\frac{R_{Rb}}{\mathsf{n}^{\star 2}} \,, \tag{2.1}$$

where $R_{Rb} = R_\infty/(1 + m_e/m_{Rb}) = 109736.62\,\mathrm{cm}^{-1}$ is the mass dependent effective Rydberg constant for ^{87}Rb with R_∞ the Rydberg constant [Mohr *et al.*, 2016]. The principal quantum number is reduced by a parameter called quantum defect $\delta_{n,\ell,j}$, leading to an effective principal quantum number $\mathsf{n}^\star = n - \delta_{n,\ell,j}$, for which the hydrogenic scalings hold. Since the quantum defect reflects the penetration of the core, it depends on the quantum numbers n, ℓ, j of the considered Rydberg state and

Quantity	$n^\star$ dependence
Electron binding energy E_n	$n^{\star -2}$
Level spacing $E_{n+1} - E_n$	$n^{\star -3}$
Ionizing field $\mathcal{E}^{(\infty)}$	$n^{\star -4}$
Orbital radius r	$n^{\star 2}$
Geometrical cross-section σ_{geo}	$n^{\star 4}$
Radiative lifetime τ	$n^{\star 3}$
Polarizability α	$n^{\star 7}$
Dipole moment $\mu = \langle nS | e r | nP \rangle$	$n^{\star 2}$
resonant dipolar interaction strength	$n^{\star 4}$
vdW interaction strength	$n^{\star 11}$

Table 2.1: Selected properties of Rydberg atoms and their scalings with the effective principal quantum number $n^\star = n - \delta_{n,l,j}$.

it is significant for $\ell \leq 3$, allowing to spectroscopically distinguish $|nS\rangle$, $|nP\rangle$ and $|nD\rangle$ states. For $\ell > 3$ the centrifugal barrier prevents the electron from being close to the core and the quantum defect becomes negligible, restoring a "hydrogen-like" degeneracy. The quantum defect can be approximated by the empirical Rydberg-Ritz formula [Jastrow, 1948] or found through spectroscopic measurements [Li *et al.*, 2003; Han *et al.*, 2006], which give $\delta_{n,\ell,j} = \delta_0 + \delta_2/(n - \delta_0)^2$ with $\delta_0 = 3.1311804$ and $\delta_2 = 0.1784$ for Rydberg S states ($\ell = 0$).

The scaling of some important Rydberg atom properties with the effective principal quantum number $n^\star$ is shown in Table 2.1. These scalings illustrate the "exaggerated" properties of the Rydberg atoms. Particularly striking is the scaling with $n^{\star 11}$ of the van der Waals interaction strength, which is typically more than 10 orders of magnitude stronger than for ground state atoms. Another important property is the huge polarizability $\propto n^{\star 7}$ and consequent small ionizing field $\mathcal{E}^{(\infty)}$. On one hand it allows to ionize the Rydberg atoms by moderate electric fields in order to probe them by ion detection. On the other hand even weak electric fields can strongly affect the charge distribution of the Rydberg electron and induce an electric dipole moment. Thus experiments with Rydberg atoms require good experimental control of electric stray fields.

2.2 Rydberg-Rydberg atom interactions

Interactions between Rydberg atoms are described in the framework of the multipole expansion of electromagnetic interactions. Rydberg atoms, being neutral atoms, do not have a net charge and the most important contribution is from electrical dipole interactions, therefore, thanks to their huge dipole moments μ, these excited states show exceptionally strong interactions compared to ground state atoms, leading to many intriguing effects in Rydberg physics. Interactions will be at the root of the experiments presented in Ch. 4 and 5 and here we review their origin and their main properties.

2.2.1 Two-atom approximation

The classical interaction energy (in atomic units) of two dipoles $\vec{\mu}_1$ and $\vec{\mu}_2$ separated by a distance $\vec{R}$ is given by

$$V^{\mathrm{DD}} = \frac{\vec{\mu_1} \cdot \vec{\mu_2}}{|\vec{R}|^3} - 3\frac{(\vec{\mu_1} \cdot \vec{R})(\vec{\mu_2} \cdot \vec{R})}{|\vec{R}|^5} \tag{2.2}$$

The second term on the right hand side in (2.2) accounts for the angular dependence of the interaction energy and is neglected in the following discussion for the sake of clarity. In the quantum mechanical description the dipoles are replaced by dipole operators $\hat{\mu} = e\hat{r}$ with matrix elements $\mu = \langle \psi | \hat{\mu} | \psi' \rangle$ and the dipole interaction energy V^{DD} for two atoms in the internal states $|\psi_1\rangle$ and $|\psi_2\rangle$ becomes

$$V^{\mathrm{DD}}(R) \propto \frac{1}{R^3} \sum_{|\psi_1'\rangle, |\psi_2'\rangle} \langle \psi_1 | \hat{\mu}_1 | \psi_1' \rangle \, \langle \psi_2 | \hat{\mu}_2 | \psi_2' \rangle = \sum_{|\psi_1', \psi_2'\rangle} \langle \psi_1, \psi_2 | \frac{\hat{\mu}_1 \, \hat{\mu}_2}{R^3} | \psi_1', \psi_2' \rangle \ , \tag{2.3}$$

where the summation represents the coupling to all the internal states $|\psi_1'\rangle$ and $|\psi_2'\rangle$ of the atoms (see e.g. [Amthor *et al.*, 2009]). Typically this summation can be approximated to include only the few energetically close states that have a direct coupling, consequently contributing the most to the sum. For atoms in the states $|n_1 S\rangle$ and $|n_2 S\rangle$ the main contribution is from coupling to the energetically closest pair of states $|n_1' P\rangle$ and $|n_2' P\rangle$, as represented in Fig. 2.1 (a).

To calculate the dipole-dipole interaction strength it is convenient to change the description from the atomic basis to the pair state basis, as done in the second step of Eq. (2.3). The initial pair state $|n_1 S, n_2 S\rangle$ is coupled with a strength $V^{\mathrm{DD}}(R) = (\mu_1 \mu_2)/R^3 = V_0/R^3$ to the state $|n_1' P, n_2' P\rangle$, which has an energy difference expressed by the Förster defect $\Delta_F = [E(|n_1' P\rangle) + E(|n_2' P\rangle)] - [E(|n_1 S\rangle) + E(|n_2 S\rangle)]$, as
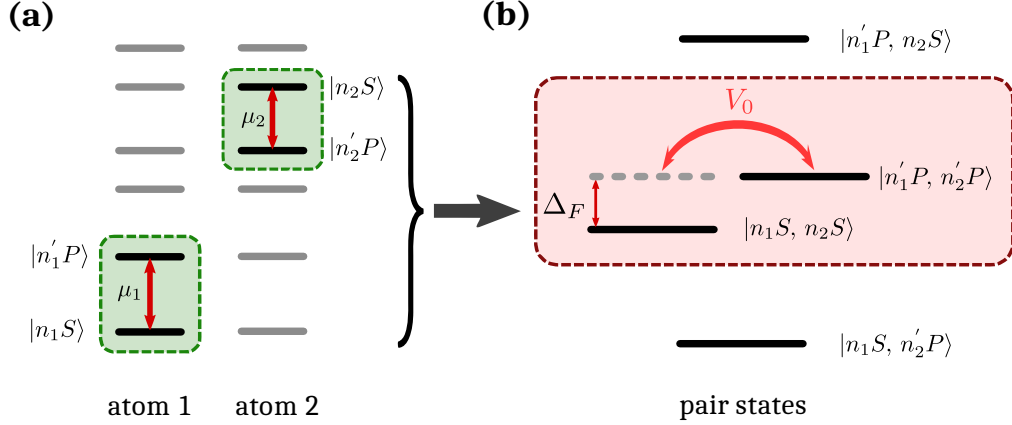
Figure 2.1: Origin of strong Rydberg-Rydberg interactions. (a) Schematic illustration of the bare atomic states of two atoms. The main contribution to the interaction between atoms in the states $|n_1 S\rangle$ and $|n_2 S\rangle$ is from coupling to the energetically closest pair of states $|n_1' P\rangle$ and $|n_2' P\rangle$. **(b)** Representation in the pair state basis of the four bare atomic states which are marked with green boxes in (a). Only the pair states $|n_1 S, n_2 S\rangle$ and $|n_1' P, n_2' P\rangle$ are coupled and they contribute the most to the interaction between the atoms. The strength of the coupling V_0 is determined by the dipole matrix elements μ_1 and μ_2 and by the Förster defect Δ_F which corresponds to the energy difference between the coupled pair states. Taken from [Günter, 2014].

represented in Fig. 2.1 (b). In the pair state basis, the complete Hamiltonian $\mathcal{H} = \mathcal{H}_{\psi_1} \otimes \mathbf{1} + \mathbf{1} \otimes \mathcal{H}_{\psi_2} + \mathcal{H}_{V\mathrm{DD}}$ describing the atomic system $\mathcal{H}_\psi$ and the off-diagonal interaction part $\mathcal{H}_{V\mathrm{DD}}$ can be written as

$$\mathcal{H} = \begin{pmatrix} 0 & V_0/R^3 \\ V_0/R^3 & \Delta_F \end{pmatrix} . \tag{2.4}$$

Solving for the eigenvalues of the coupled pair states we obtain

$$E_\pm = \frac{1}{2}\left(\Delta_F \pm \sqrt{\Delta_F^2 + 4(V_0/R^3)^2} \right) . \tag{2.5}$$

We observe that the pair energy depends on the inter-atomic separation R and on the Förster defect Δ_F, and consequently two regimes arise:

- **resonant dipole-dipole interaction** ($V_0/R^3 \gg \Delta_F$): for small distances or when the Förster defect is tuned to zero through the application of electric fields (reaching a so called Förster resonance [Gallagher *et al.*, 1982; Vogt *et al.*, 2006; Ryabtsev *et al.*, 2010]), the dipole-dipole coupling dominates and the energy shift reduces to

$$E_\pm = \pm\frac{\mu_1\,\mu_2}{R^3} := \pm\frac{C_3}{R^3} . \tag{2.6}$$

$E_\pm$ scales with $1/R^3$ indicating that in this regime Rydberg atoms exhibit resonant dipole-dipole interactions[1] with a strength expressed by $C_3 = \mu_1\mu_2 \propto \mathsf{n}^{\star 4}$. This description includes the case when the two initial states are directly strongly coupled, like an $|nS, n'P\rangle$ pair for which the dominant pair state is the exchange symmetric state $|n'P, nS\rangle$. In this case $\Delta_F = 0$ for any distance and field.

- **van der Waals interaction** ($V_0/R^3 \ll \Delta_F$): for long distances the dipole-dipole coupling is only perturbative and a second order Taylor expansion of Eq. (2.5) gives

$$E_+ \simeq \Delta_F + \frac{V_0^2/\Delta_F}{R^6} \quad \text{and} \quad E_- \simeq -\frac{V_0^2/\Delta_F}{R^6} := -\frac{C_6}{R^6}. \qquad (2.7)$$

  $E_\pm$ scales with $1/R^6$ and this corresponds to the van der Waals interaction energy, which strongly depends on the effective principal quantum number, because $\mu \propto \mathsf{n}^{\star 2}$ and $\Delta_F \propto \mathsf{n}^{\star -3}$ such that $C_6 = C_3^2/\Delta_F \propto \mathsf{n}^{\star 11}$, as listed in Tab. 2.1. Depending on the energy of the pair states $|\psi_1, \psi_2\rangle$ and $|\psi_1', \psi_2'\rangle$, the Förster defect can be either positive or negative, determining the sign of the interaction. Within our convention, $C_6 < 0$ corresponds to repulsive interactions and this will be the case for all experiments performed with $|nS\rangle$ states. This choice is beneficial because repulsively interacting states are more stable against ionizing collisions than attractively interacting states [Amthor *et al.*, 2007a; Amthor *et al.*, 2007b].

The crossover between the van der Waals and the dipole-dipole interaction regimes occurs when $V^{\mathrm{DD}}(R_{cr}) \approx \Delta_F$ which gives a crossover radius $R_{cr} = \sqrt[6]{|C_6|/\Delta_F} \propto \mathsf{n}^{\star 7/3}$ [Walker and Saffman, 2008]. Above this radius the system eigenstates are in good approximation the initial pair ones $|\psi_1, \psi_2\rangle$, while below R_{cr} dipole-dipole interactions induce a strong state mixing [Gallagher and Pillet, 2008; Comparat and Pillet, 2010]. Another important difference is that in a many atom system in the van der Waals regime the many-body dynamics are dominated by nearest neighbor interactions, allowing a two-body treatment, while in the dipolar regime the coupling is inherently long-range and a many-body description is necessary. A more detailed discussion of this fascinating topic is given in [Amthor, 2008].

---

[1]This is valid down to the LeRoy-radius, below which the electron clouds start to overlap and the electron exchange interaction has to be accounted for [Boisseau *et al.*, 2002].

2.2.2   State exchange process

Resonant dipole-dipole interactions not only affect the pair state energy, but also allow the two initial states to exchange their quantum state $|\psi_1, \psi_2\rangle \leftrightarrow |\psi_2, \psi_1\rangle$, causing an oscillatory dynamic between the two. This effect can be interpreted as an energy exchange between the two atoms.

Pairs of states that interact through direct dipolar coupling (i.e. for states that differ in $|\Delta\ell| = 1$, like $|nS, n'P\rangle$) realize the simplest single step state exchange mechanism

$$|\psi_1, \psi_2\rangle \Leftrightarrow |\psi_2, \psi_1\rangle \tag{2.8}$$

This simple mechanism is called Förster process [Förster, 1948] and is found in many research fields like semi-conductor physics [van Amerongen *et al.*, 2000; Williams, 2007; Govorov *et al.*, 2016] and biology [Clegg, 2009; Collini, 2013], and it has been observed in ultracold Rydberg atom experiments [Anderson *et al.*, 1998; Mourachko *et al.*, 1998; Anderson *et al.*, 2002].

A two step process

$$|\psi_1, \psi_2\rangle \Leftrightarrow |\psi_1', \psi_2'\rangle \Leftrightarrow |\psi_2, \psi_1\rangle \tag{2.9}$$

is also possible, with exchange probability dependent on all four involved dipole moments μ and on the Förster defect [Paris-Mandoki *et al.*, 2016]. Due to the quick reduction of the dipole moment for increasing difference in principal quantum number [Gallagher, 1994], pairs of states with small differences $n_2 - n_1$ and $n_2' - n_1'$ are the most favorable ones, as well as pair states near a Förster resonance. For a big difference in n the exchange process can be neglected. A more detailed discussion of state exchange processes between Rydberg atoms can be found in [Günter *et al.*, 2013; Schempp, 2014; Paris-Mandoki *et al.*, 2016].

2.2.3   Interaction of $|nS\rangle$ and $|nP\rangle$ states

In the experiments presented in this thesis $|nS, n'S\rangle$ and $|nS, nP\rangle$ pairs of Rydberg states of ^{87}Rb have been used. These two sets of states differ in the interaction type and strength that they exhibit and here we discuss more in detail this aspect.

The interaction between $|nS, n'S\rangle$ states is described in very good approximation by the van der Waals interaction, until the density of Rydberg atoms does not cross the level corresponding to a mean inter-particle distance smaller than the cross-over radius R_{cr}. In the simple discussion carried out in the previous section we neglected in Eq. (2.2) the second term which accounts for the angular dependence

of the interaction energy. This approximation is well justified for S-states since they interact isotropically [Walker and Saffman, 2008]. In order to estimate with high accuracy the interaction coefficents C_6, Eq. (2.3) can be evaluated numerically, including a large set of states in the summation. Tabulated values and approximate formulas for alkali atoms can be found in [Singer *et al.*, 2005; Reinhard *et al.*, 2007; Walker and Saffman, 2008]. In this work we use C_6 coefficents calculated via an effective Hamiltonian approach by R.M.W. van Bijnen [van Bijnen, 2013].
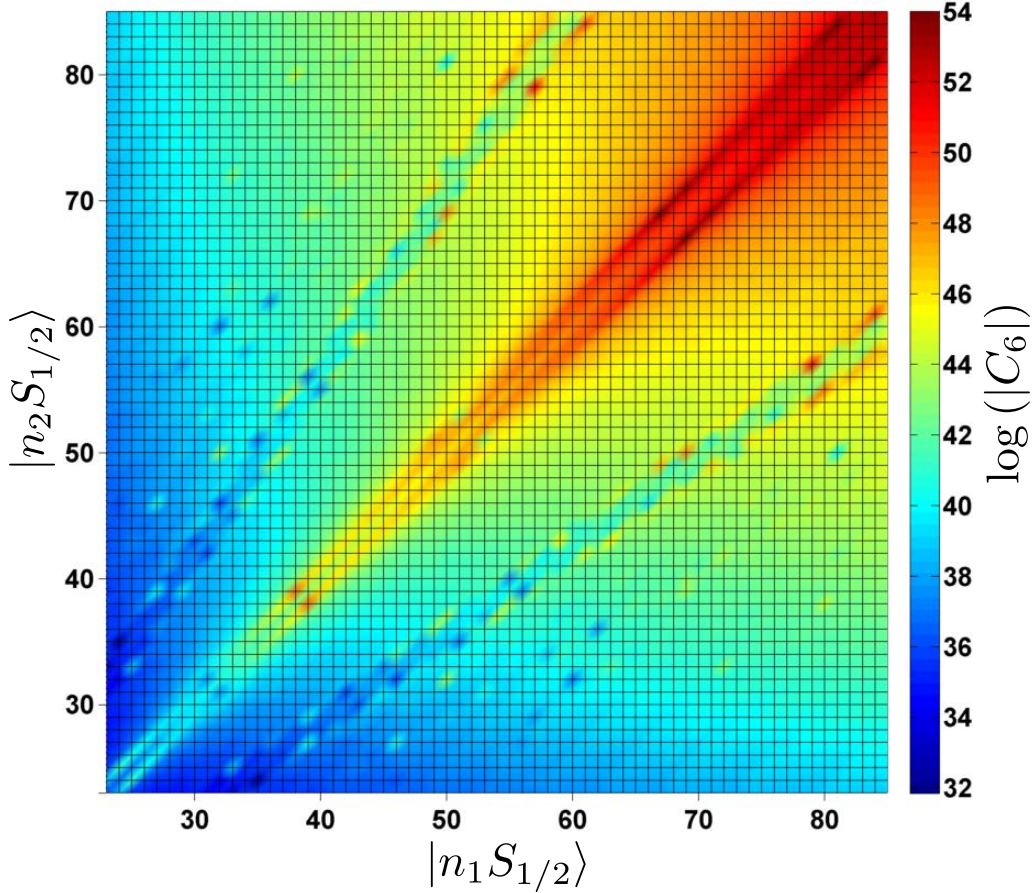
Figure 2.2: Map of C_6 interaction coefficients between $|n_1S_{1/2}\rangle$ and $|n_2S_{1/2}\rangle$ states of ^{87}Rb. The values shown are the $\log(|C_6^{n_1,n_2}|)$ with the C_6 expressed in atomic units $(E_h a_0^6/\hbar$ with E_h the Hartree energy) and are calculated using an effective Hamiltonian approach [van Bijnen, 2013]. Reproduced with permission from R.M.W. van Bijnen.

A map of C_6 interaction coefficients between $|n_1S_{1/2}\rangle$ and $|n_2S_{1/2}\rangle$ states is shown in Fig. 2.2. We can see that different Rydberg state pairs can have vastly different interaction strength, due to the different couplings V_0 and Förster defects, but the $n^{\star 11}$ scaling is respected. The state combinations that are predicted to interact

strongly have a small Δ_F. By applying an electric field it is possible to tune their pair energy difference to 0 and reach a Förster resonance [Gallagher *et al.*, 1982; Vogt *et al.*, 2006; Ryabtsev *et al.*, 2010; Nipper *et al.*, 2012a; Gurian *et al.*, 2012], where the interaction will become even stronger due to the transition from a van der Waals into a dipolar regime.
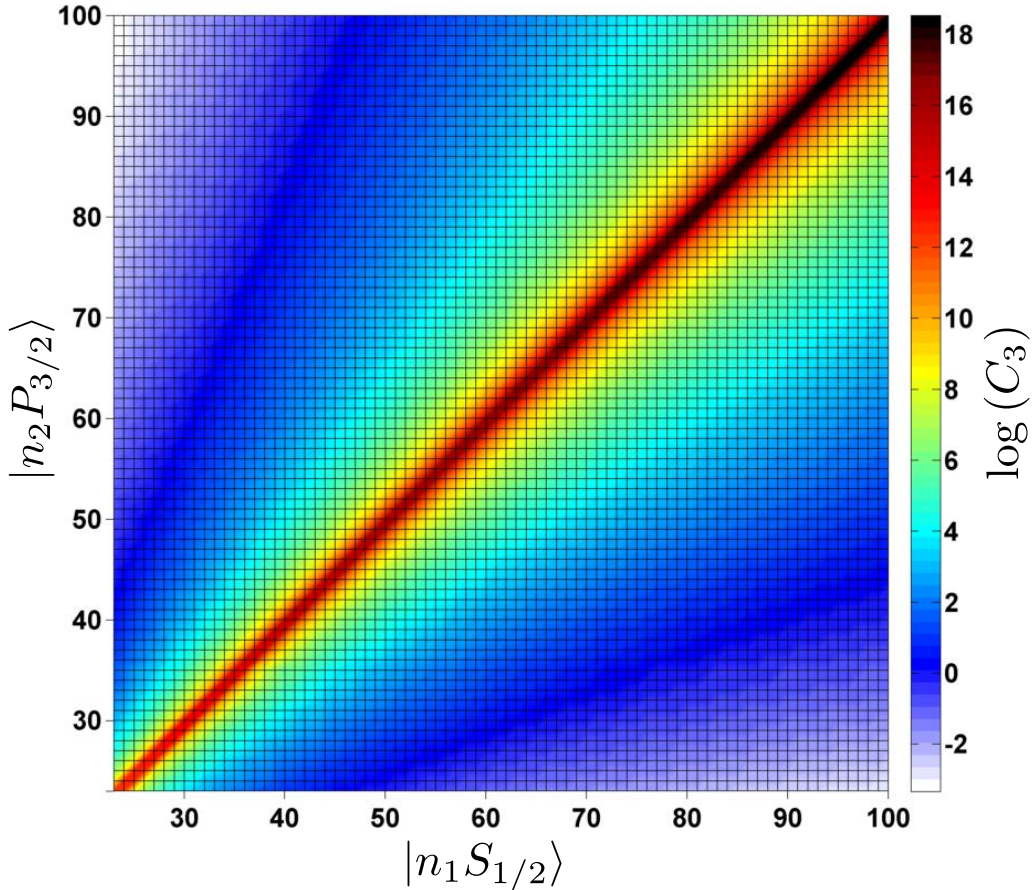
Figure 2.3: Map of the radial component of the C_3 interaction coefficients between $|n_1 S_{1/2}\rangle$ and $|n_2 P_{3/2}\rangle$ states of ^{87}Rb. The interaction strength decreases rapidly for increasing $|n_1 - n_2|$. The values shown are the $\log C_3^{n_1, n_2}$ with the C_3 expressed in atomic units ($E_h a_0^3 / \hbar$ with E_h the Hartree energy) and are calculated by numerically integrating an analytic approximation for the radial wavefunctions [Kostelecký *et al.*, 1988]. To estimate the interaction strength $C_3(\theta)$ between a specific pair of states the radial component has to be multiplied by the angular component [van Bijnen, 2013; Paris-Mandoki *et al.*, 2016].

The interaction between $|nS, n'P\rangle$ states is always of dipolar type. In this case the C_3 coefficient is simply the square of the dipole matrix element $\mu = \left\langle \psi_{n,\ell,j,m_j} \left| \hat{\mu} \right| \psi_{n',\ell',j',m'_j} \right\rangle$, whose calculation can be divided into a radial term and an

angular part that considers the orientation between the dipoles of the two atoms, expressed through the angle θ and the spherical harmonics. The peak amplitude of the dipole matrix element is determined by the integral of the radial matrix element $\langle n, \ell | \hat{\mu} | n', \ell' \rangle$ which can be calculated with the Numerov method [Zimmerman *et al.*, 1979; Singer, 2004; Pritchard, 2011] or from an analytic approximation for the radial wavefunctions [Kostelecký *et al.*, 1988], that is accurate on the 3% level. Using the latter approach, we show in Fig. 2.3 a map of the radial component of the C_3 interaction coefficients between $\left| n_1 S_{1/2} \right\rangle$ and $\left| n_2 P_{3/2} \right\rangle$. We observe the expected scaling with $\mathsf{n}^{\star 4}$ and that pairs of states with $n_1 - n_2 = -1, 0$ exhibit the strongest interactions due to the large overlap between their wavefunctions. In general, the angular component of the interaction cannot be neglected. It mainly reduces the peak amplitude of μ and leads to an anisotropic $C_3(\theta)$ coefficient. Furthermore, for an arbitrary θ it may not preserve the m_j quantum number, potentially leading to undesired population of additional states. A more detailed treatment of the problem is presented in [Comparat and Pillet, 2010; Paris-Mandoki *et al.*, 2016]. For the scope of this work, since the experiments are performed in a 3D geometry with random distribution of atoms and without a polarizing field, we estimate an effective C_3 considering an angular averaging [Walker and Saffman, 2008]. For increased accuracy in the theoretic estimations, we use C_3 coefficients calculated by R.M.W. van Bijnen.

2.3   Rydberg atom-light interactions

An important consequence of the strong Rydberg-Rydberg interactions is the dipole blockade of excitation from a ground state to a Rydberg state [Jaksch *et al.*, 2000; Lukin *et al.*, 2001; Tong *et al.*, 2004; Singer *et al.*, 2004; Comparat and Pillet, 2010]. This effect can be understood using the pair state basis, as illustrated in Fig. 2.4 (a). Each Rydberg atom is modeled as a two level atom with ground state $|g\rangle$ and Rydberg state $|r\rangle$. A laser, with excitation bandwidth $\hbar\mathcal{W}$, is resonant with the excitation frequency of a single Rydberg atom. When the first of the two atoms is excited, it does not significantly perturb the energies of the pair states $|gg\rangle$ and $|gr\rangle$, because of the small polarizability of the ground state, but the doubly excited state $|rr\rangle$ experiences a level shift $V(R)$ that depends on the separation R between the two atoms. For large distances both atoms can be excited to the Rydberg state, but when the separation becomes smaller than a critical value the interaction between them shifts the doubly excited state $|rr\rangle$ out of the excitation bandwidth $\hbar\mathcal{W}$ and inhibits the formation of close pairs of Rydberg atoms, introducing a natural length

scale to the system. The distance below which the doubly excited state is suppressed is called blockade radius R_{bl} and is defined as

$$R_{bl} = \left(\frac{C_6}{\hbar\mathcal{W}}\right)^{1/6} \qquad\qquad R_{bl} = \left(\frac{C_3}{\hbar\mathcal{W}}\right)^{1/3} \qquad\qquad (2.10)$$

for van der Waals and resonant dipole interactions, respectively. The excitation bandwidth $\hbar\mathcal{W}$ depends on the Rabi frequency Ω and on the dephasing associated with the laser excitation. Typically the blockade radius is on the order of few µm and this determines the density of Rydberg atoms $n_r \propto R_{bl}^{-3}$ at which the blockade effect would suppress the excitation of additional excitations. For nS-states the approximately isotropic interaction would lead to a spherical blockade volume with radius R_{bl}, as represented in Fig. 2.4 (b). nP or nD-states would have more complex anisotropic blockade volumes, like ellipsoids, and at certain angles there may not even be a blockade effect [Saffman *et al.*, 2010].
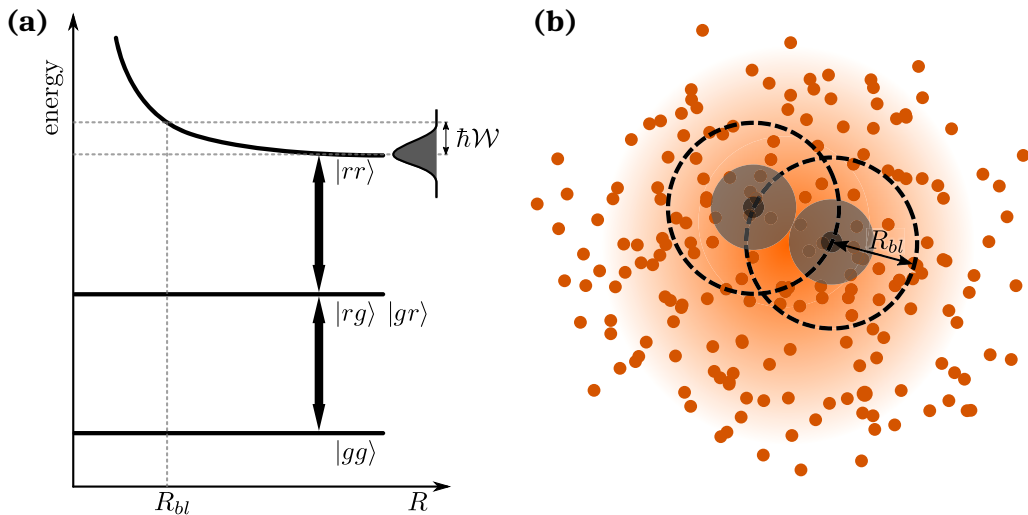
Figure 2.4: Rydberg blockade effect. (a) Pair state energies of two atoms as a function of inter-atomic separation R. For large distances both atoms can be excited to the Rydberg state, but when the separation becomes smaller than the blockade radius R_{bl} the interaction between them shifts the doubly excited state $|rr\rangle$ out of the excitation bandwidth $\hbar\mathcal{W}$ and inhibits the formation of close pairs of Rydberg atoms. **(b)** In an atomic cloud, in the case of resonant excitation and isotropic Rydberg-Rydberg interactions, the blockade effect leads to a forbidden spherical volume around each Rydberg atom, represented by the blockade spheres (dashed black lines). In each blockade sphere only a single Rydberg excitation is possible. Taken and adapted from [Hofmann, 2013; Günter, 2014].

This simple description of the Rydberg blockade effect can be extended to the

case of a gas of many atoms. The system can be imagined as made up of many blockade spheres, each with $N-1$ ground state atoms and one single Rydberg atom. If the excitation is coherent, then the Rydberg excitation cannot be assigned to a specific atom, but instead is shared by all of them, resulting in a collective quantum state of N atoms. This in turn leads to a collective enhancement of the excitation Rabi frequency by a factor $\sqrt{N}$, increasing consequently the excitation bandwidth. Since the blockade radius, which defines the size of the blockade sphere and the number of atoms it encompasses, depends on the excitation bandwidth, both N and the collectively enhanced Rabi frequency have to be determined self-consistently [Löw $et\ al.$, 2012]. A large enhancement factor leads to a reduction in the blockade radius and the impact of this collective effect increases with the atomic density.

2.4   Experimental setup and detection methods

The experiments described in this thesis are performed using the experimental setup presented in the following sections. First the preparation of the ultracold atomic cloud using optical dipole traps will be introduced, then the detection methods will be described. Emphasis will be made on the parts of the setup that were enhanced during the course of this thesis, while the main components were built by [Hofmann, 2013; Günter, 2014; Schempp, 2014; Hofmann $et\ al.$, 2014] where a more detailed description can be found.

2.4.1   Preparing ultracold and dense atomic samples

General features of our experimental setup are sketched in Fig. 2.5. We first apply common laser cooling and trapping techniques [Ketterle $et\ al.$, 1999] to create an ultracold gas of ^{87}Rb ground state atoms. A typical preparation cycle is shown in Fig. 2.6 (a)). The atoms are pre-cooled in a 2D-MOT, then loaded into a 3D-MOT in the science chamber [Dieckmann $et\ al.$, 1998; Schoser $et\ al.$, 2002] and directly transferred into a "reservoir" optical dipole trap (ODT). This trap is composed of two weakly-focused laser beams crossing at a small angle and generated by a 50 W single frequency fiber amplifier laser (Coherent Mephisto MOPA) at a wavelength of 1064 nm, resulting in an elongated cigar-shaped atomic cloud (Fig. 2.6 (b, 1)) of width of $\sim 40\,\mu\text{m} \times 40\,\mu\text{m} \times 800\,\mu\text{m}$ at $1/e^2$, tilted from the x probing direction by 45°. This geometry allows for efficient loading from the 3D-MOT, leading to large densities up to $5 \cdot 10^{11}\,\text{cm}^{-3}$ with typical temperatures of 40 μK. A second ODT, called "dimple", is oriented along the y direction at 45° relative to the reservoir and the
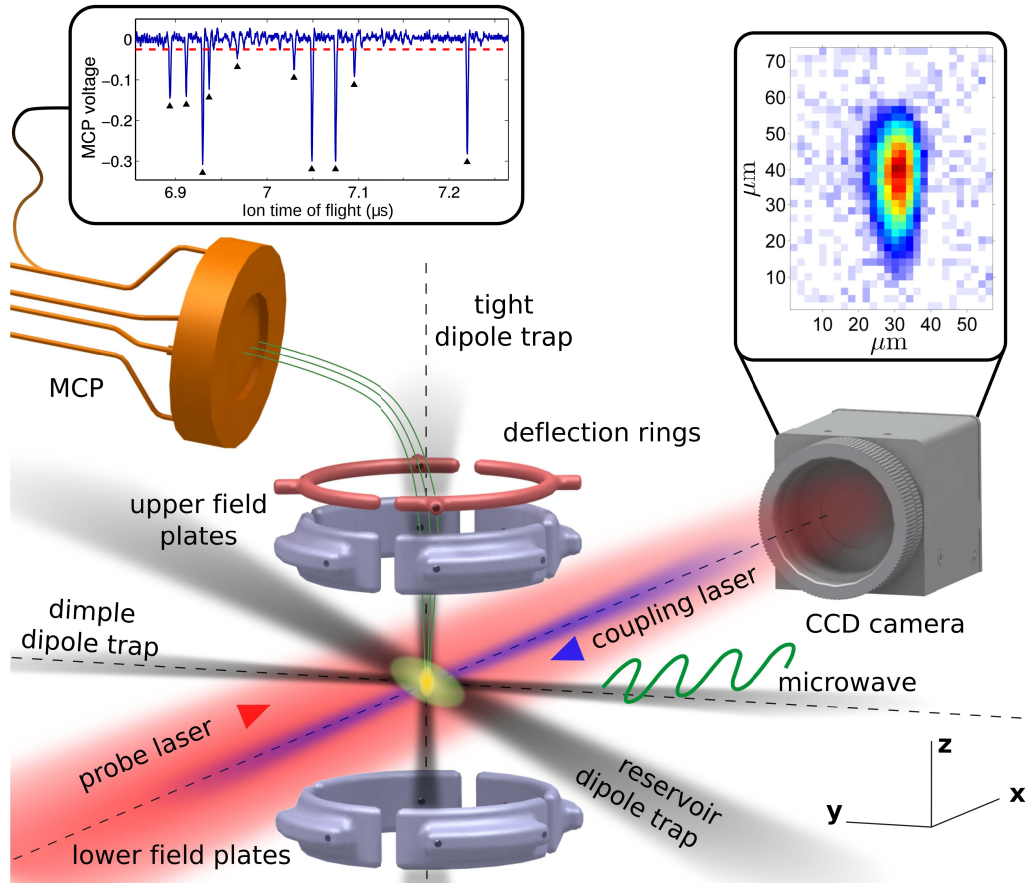
Figure 2.5: Experimental setup for excitation and detection of Rydberg atoms in an ultracold $^{87}\mathrm{Rb}$ gas. Pre-cooled atoms are transferred from a magneto-optical trap into the reservoir optical dipole trap (light yellow volume). Two additional tightly focused dipole traps are used to create small and dense samples (strong yellow volume). After being released from the trap, the atoms are excited to Rydberg states by a combination of a $780\,\mathrm{nm}$ probe laser, a counter-propagating $480\,\mathrm{nm}$ coupling laser and microwave radiation. An electrode structure composed of 8 field plates is used for precise electric field control and for field ionization of Rydberg atoms, whereas two deflection rings guide the ions (green trajectories) onto a micro-channel plate (MCP) detector. Complementary information on the spatial distribution of ground state atoms and on the optical response of the medium to the probe beam is acquired in parallel by absorption imaging with a CCD camera (imaging system not shown). The insets show examples of typical images of atoms released from the tight trap and of ion traces. Each voltage spike (indicated by the black triangles) above a certain threshold (red dashed line) corresponds to a single detection event.

(a)

	MOT loading (0.7 s)	compression (0.07 s)	dark MOT (0.15 s)	evaporation 1 (0.75 s)	evaporation 2 (3 s)	evaporation 3 (0.6 s)	tight trap loading (0.1 s)
2D MOT							
3D MOT power							
3D MOT red detuning							
3D MOT gradient							
repumper power				①			
reservoir power						②	
dimple power							
tight power							③

(b)
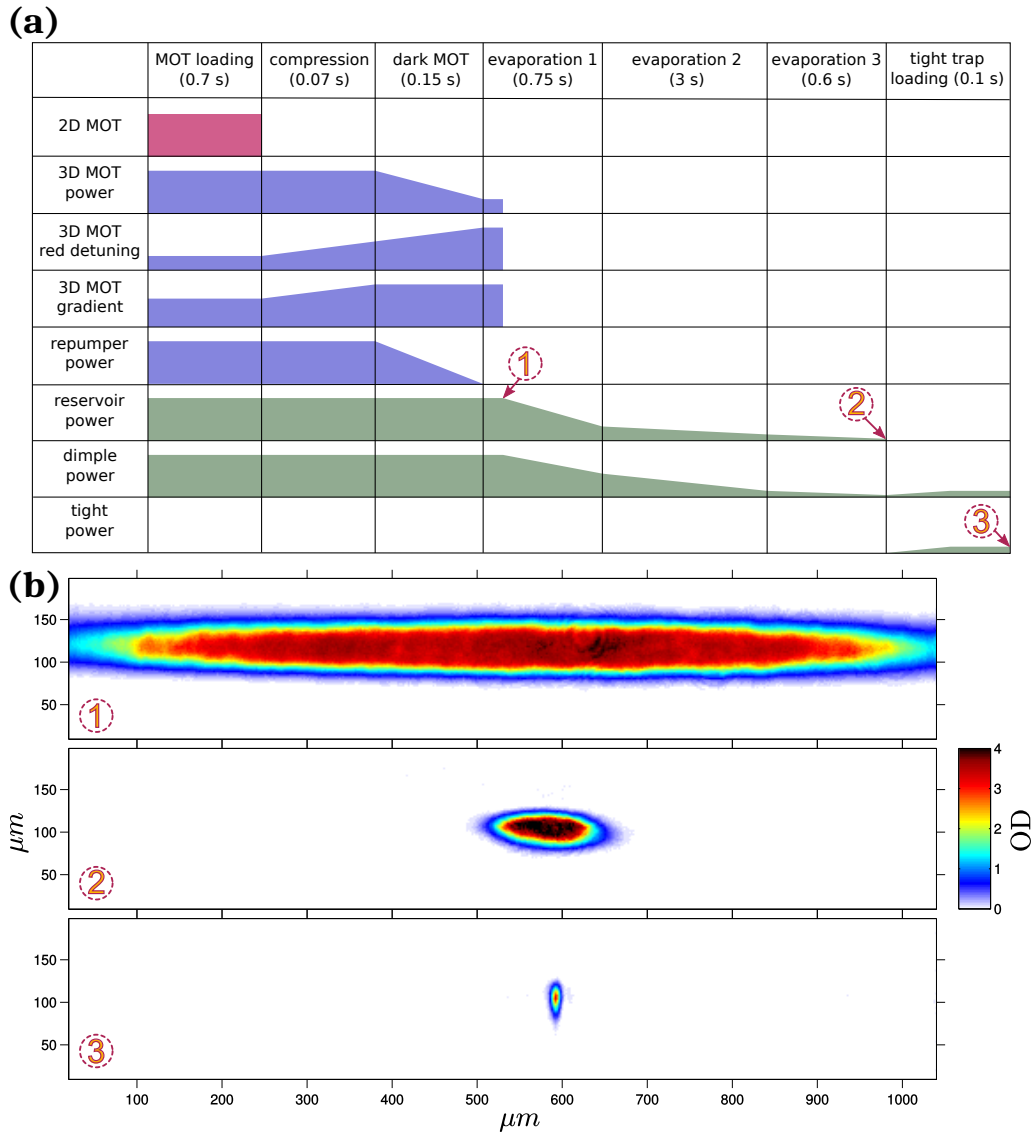
Figure 2.6: Preparation of cold and dense atomic clouds. (a) Typical experimental cycle for the preparation of cold and dense atomic clouds. The cycle starts with the 2D-MOT operation which loads the 3D-MOT, where the atoms are pre-cooled in three different stages, then evaporative cooling is performed in three phases and finally the sample is transferred into the tight trap. Taken and adapted from [Hofmann, 2013]. **(b)** Typical optical density and spatial profile of the atom cloud measured by absorption imaging at different stages of the evaporation in the optical dipole traps, respectively in the reservoir (1), dimple (2) and tight traps (3).

two are used together to perform all-optical evaporative cooling, in order to increase the phase-space density of the atoms whilst decreasing their temperature [Clément et al., 2009; Grimm et al., 2000]. Using two different ODT allows to decouple the trap loading from the evaporation process [Weber et al., 2002; Clément et al., 2009; Jacob et al., 2011] and to optimize independently the two steps. In the resulting crossed three-beam trap we typically produce a much smaller elongated cigar-shaped atomic cloud (Fig. 2.6 (b, 2)) of width of $\sim 22\,\mu\text{m} \times 22\,\mu\text{m} \times 150\,\mu\text{m}$ at $1/e^2$, oriented transversally to the x probing direction, with large densities up to $2 \cdot 10^{12}\,\text{cm}^{-3}$ and typical temperatures of $1\,\mu\text{K}$. With an optimized evaporation ramp it has been shown that Bose-Einstein condensation can be achieved [Hofmann, 2013].

2.4.2 Loading into a small dipole trap

We desire to have a trap where only very few Rydberg atoms can be excited before reaching the fully-blockaded regime (see Ch. 2.3), so the trap size has to be comparable to the typical Rydberg blockade volume. We create such small volume using an additional vertical "tight" ODT together with the "dimple" ODT. Starting from the last step of the evaporation (Fig. 2.6 (a)) we load the "tight" trap by increasing its potential depth, raising together the power of the "dimple" and "tight" laser beams, while reducing to zero the intensity of the "reservoir". The final cloud is shown in Fig. 2.6 (b, 3) and contains up to 3000 atoms in a volume of $\sim 8\,\mu\text{m} \times 22\,\mu\text{m} \times 8\,\mu\text{m}$ (width at $1/e^2$), providing densities up to $1.5 \cdot 10^{12}\,\text{cm}^{-3}$ as well as low temperatures of $\sim 1\,\mu\text{K}$.

2.4.3 Ground state preparation

After the loading of the atoms into one of the three dipole traps is complete, both the $F = 1$ and $F = 2$ manifolds of the ^{87}Rb ground state $\left|5S_{1/2}\right\rangle$ are populated. To prepare a clean initial ground state for the following experiments, we first remove the atoms in the $F = 2$ manifold by switching off the repumping light at the end of the MOT cooling stage. Then we apply a static magnetic field of 3 or 6 G along the x direction to define the quantization axis and to remove the m_F degeneracy of the hyperfine levels via the Zeeman effect. Next we transfer populations from the state $\left|5S_{1/2}, F = 1, m_F = 1\right\rangle$ to the selected ground state $\left|g\right\rangle = \left|5S_{1/2}, F = 2, m_F = 2\right\rangle$ by inducing a 6.8 GHz microwave transfer via a Landau-Zener sweep of a magnetic field (illustrated in Fig. 2.7). The atoms left in the other magnetic sublevels of the $F = 1$ manifold can be neglected because they are far off-resonant from the transitions

addressed by the laser fields, which are applied in the next step, due to the $h \cdot 6.8\,\mathrm{GHz}$ energy splitting between the $F = 2$ and $F = 1$ manifolds.

We control the density of the cloud, without affecting its size, by varying the duration of the magnetic field sweep to tune the level of adiabaticity of the transfer. Before probing, the trap is switched off and the atoms expand for a fixed time. The duration of the free expansion and of the MOT loading allow to further tune the cloud density.

2.4.4 Detection methods

After a set free expansion time, the ground state atoms are excited to the Rydberg state (see Ch. 2.5) and the desired experiment is performed. To probe the system we use combined measurements of both the Rydberg population and the transmitted light field, respectively by field ionization and charged particle detection on a micro-channel plate detector (MCP) and by recording the transmitted photons on a charge-coupled-device (CCD) camera, as sketched in Fig. 2.5.

The experimental apparatus has an electrode structure which allows to apply and control the electric fields in the three dimensions, which is necessary for Rydberg atoms due to their high atomic polarizability [Löw *et al.*, 2012; Saßmannshausen *et al.*, 2013; O'Sullivan and Stoicheff, 1985]. Moderate electric fields can be applied to DC-Stark shift the energy levels of the Rydberg atoms to tune their Förster defect and therefore the strength of the interactions [Vogt *et al.*, 2006; Westermann, S. *et al.*, 2006; Ryabtsev *et al.*, 2010; Nipper *et al.*, 2012b; Gurian *et al.*, 2012]. The electrodes also enable us to count the number of Rydberg atoms present in the sample by switching on at the end of the experiment a high electric field to ionize the Rydberg states (with amplitude $\mathcal{E} \propto \mathsf{n}^{\star\,-4}$). Due to the large polarizability of the Rydberg state, the ionizing field causes a sudden shift of the transition frequency by several linewidths in less than $10\,\mathrm{ns}$, which is fast compared to the criteria for adiabatic following[2], such that the Rydberg population is effectively frozen. The resulting ions are then guided to a micro-channel plate detector and a voltage trace is acquired on a fast oscilloscope. The guiding field is produced by several electrodes with applied voltages which have been optimized in order to maximize the number of ions reaching the MCP detector [Hofmann *et al.*, 2014], with an estimated overall detection efficiency of $\eta \approx 0.4$.

At low incoming ion count rates (typically for up to 20 ions) (a typical trace is shown in Fig. 2.5), each voltage spike crossing a chosen threshold above the noise

---

[2]For the experiments in Ch. 3 on Rydberg EIT the criteria is $\partial \Delta_c / \partial t \ll \Omega_c^2 / 2$

floor is assigned to correspond to a single Rydberg atom, since the probability for overlapping events is low. When the number of detected ions is large (> 20) the latter effect cannot be neglected and, therefore, we integrate the MCP signal over the distribution of arrival times and divide by the average area of a single detection event, measured at low excitation numbers, to obtain the number of detected ions [Schempp *et al.*, 2010; Hofmann *et al.*, 2013].

To optically image the ultracold gas we resonantly couple a $780\,\mathrm{nm}$ σ^+ polarized probe laser beam to the $|g\rangle \leftrightarrow |e\rangle = \left|5P_{3/2}, F = 3, m_F = 3\right\rangle$ transition, as illustrated in Fig. 2.7. The probe beam is collimated with a Gaussian beam waist of $1.5\,\mathrm{mm}$, so the cloud is illuminated with an approximately uniform Rabi frequency Ω_p, calibrated using the saturated absorption imaging method [Reinaudi *et al.*, 2007]. The transmitted light is collected onto an Andor iXon Ultra 897 EM-CCD camera (Fig. 2.5) via a nearly diffraction limited imaging system with a resolution of $4.8\,\mathrm{\mu m}$ (Rayleigh criterion). The imaging system magnification is a factor of 7.7 [Helmrich, 2013] and it leads to an effective single pixel area of $a_{px} = 4.3\,\mathrm{\mu m}^2$ in the object plane. The camera converts the incoming photons into electrons with a total photon detection efficiency of $44 \pm 4\%$, given by the product of the imaging system transmission T and the camera quantum efficiency Q_e. This EM-CCD camera has been implemented in the course of this thesis to replace and improve over the previous Andor iXon 887 EM-CCD which had a factor of two lower Q_e and much higher readout noise.

We use a mode of our CCD camera, called "fast kinetics", that allows to take multiple images within $100\,\mathrm{\mu s}$ from each other by using a masked part of the sensor as temporary storage for the sequence of images. The masking is done by inserting a narrow horizontal slit with a height of $200\,\mathrm{\mu m}$ in the intermediate focal plane of the imaging system and stray illumination is eliminated by carefully covering the imaging system. After each exposure, the acquired image is moved into the masked area of the CCD and the shift time sets the maximum acquisition rate.

Absorption imaging is performed by recording three images in a row [Ketterle *et al.*, 1999]: in the first image $N_{\mathrm{e}^-,a}$ the transmitted light in the presence of atoms is stored, then a second probe pulse without atoms is used to normalize out the intensity variations and to produce an reference image $N_{\mathrm{e}^-,r}$. In the last a background $N_{\mathrm{e}^-,b}$ without probing light is acquired to remove any stray light or CCD dark counts and many of these are averaged together to reduce their noise contribution. Three quantities can be calculated in each pixel from these images, the absorption A, the

cloud optical density OD and the number of atoms N_{atoms} (accounting for saturation):

$$A = 1 - \frac{N_{e^-,a} - \langle N_{e^-,b} \rangle}{N_{e^-,r} - \langle N_{e^-,b} \rangle} \tag{2.11}$$

$$\text{OD} = -\log\left(\frac{N_{e^-,a} - \langle N_{e^-,b} \rangle}{N_{e^-,r} - \langle N_{e^-,b} \rangle} \right) \tag{2.12}$$

$$N_{atoms} = \frac{a_{px}}{\sigma_0} \left[s \left(\frac{N_{e^-,r} - N_{e^-,a}}{N_{e^-,r}} \right) + \alpha\,\text{OD} \right] \tag{2.13}$$

where $\sigma_0 = 3\lambda^2/2\pi$ is the absorption cross section, $s = 2(\Omega_p/\Gamma_e)^2$ is the saturation parameter, Γ_e the decay rate of the addressed transition, and α is a dimensionless parameter which accounts for imperfections like state population of multiple $F = 2$ Zeeman sublevels or not perfect probe polarization. For our setup we measured $\alpha = 1.00 \pm 0.05$ via the saturated absorption imaging method [Reinaudi *et al.*, 2007].

From a single measurement, each of these quantities is known within an error given by the propagation of the detection noise:

$$\sigma(A) = \sqrt{\text{var}(N_{e^-,a})/N_{e^-,r}^2 + \text{var}(N_{e^-,r})\,N_{e^-,a}^2/N_{e^-,r}^4} \tag{2.14}$$

$$\sigma(\text{OD}) = \sqrt{\text{var}(N_{e^-,a})/N_{e^-,a}^2 + \text{var}(N_{e^-,r})/N_{e^-,r}^2} \tag{2.15}$$

$$\sigma(N_{atoms}) = \frac{a_{px}}{\sigma_0} \sqrt{\text{var}(N_{e^-,r}) \left(\frac{s+\alpha}{N_{e^-,r}} \right)^2 + \text{var}(N_{e^-,a}) \left(\frac{s\,N_{e^-,a} + \alpha\,N_{e^-,r}}{N_{e^-,a}N_{e^-,r}} \right)^2} \tag{2.16}$$

$$\overline{+ \text{var}(s) \left(\frac{N_{e^-,r} - N_{e^-,a}}{N_{e^-,r}} \right)^2 + \text{var}(\alpha)\,\text{OD}^2}$$

The noise sources that affect absorption imaging are investigated and discussed in detail in Ch. 5.2.1 and 5.2.2, while a noise model for our camera is presented in Appendix B.

2.4.5   Laser stabilization

The frequency stability of the laser sources that we use to image the ground state distribution and to excite the Rydberg states plays an important role in the experiments where Rydberg atom-light interactions are investigated. Fluctuations in the laser frequency around the set central value on the timescales of interest for the measurements, such as the exposure time to the beams, lead to a dephasing effect on the evolution of the coupled light-matter system's state [McDonnell *et al.*, 2004], which will be discussed in detail in Ch. 3.1.4. In particular it broadens the

observed spectra and causes an increased absorption under resonant two-photon EIT coupling, as illustrated in Fig. 3.2 (b). Rydberg states are more sensitive than ground state atoms to dephasing because of their small decay rate. Furthermore, under EIT coupling the atomic system is decoupled from the intermediate state, making the decay and dephasing terms that affect the Rydberg state relatively more important. To minimize these negative effects it is important to reduce the frequency fluctuations of the involved lasers.

In our setup the ground state distribution is probed using a laser beam generated by a 780 nm TOPTICA DL100 pro laser. Originally it was stabilized using the modulation transfer spectroscopy technique [Shirley, 1982; Camy *et al.*, 1982; McCarron *et al.*, 2008] in a thermal ^{87}Rb vapor cell with an estimated linewidth of ~ 300 kHz [Schnellbächer, 2010; Labuhn, 2013]. For the second step at 480 nm of the two-photon coupling to a Rydberg state we use two different frequency doubled lasers, a 960 nm TOPTICA TA-SHG for the off-resonant preparation and a 960 nm TOPTICA TA-SHG pro for the resonant EIT coupling (the different preparation schemes are discussed in the following Ch. 2.5). Both lasers were originally stabilized to an EIT resonance [Abel *et al.*, 2009] in a thermal ^{87}Rb vapor cell with estimated linewidths of ~ 1 MHz [Müller, 2010; Labuhn, 2013] and ~ 300 kHz, respectively.

In the course of this thesis a passive high finesse ultra-low-expansion glass Fabry-Pérot cavity [Aikawa *et al.*, 2011; Gregory *et al.*, 2015] was implemented in our setup [Kerst, 2014]. The cavity mirrors are dual-wavelength coated, allowing to stabilize all three lasers at the same time via the Pound-Drever-Hall method (PDH) [Black, 2001]. To generate the PDH error signal and to have a broad frequency tunability range we pass each beam through a broadband fibre-coupled electro-optic modulator to which we apply, by means of a power combiner, a modulation and an offset frequencies. We estimate the frequency stability of our lasers by measuring the root mean square instantaneous frequency deviation relative to a cavity mode of a reference active Fabry-Pérot cavity (Sirah Eagle Eye). For timescales longer than 3 µs we measure linewidths below 10, 30 and 10 kHz for the three lasers, which are much smaller than the Rydberg-state dephasing rates observed in our experiments. This improvement in linewidth has reduced the absorption under EIT for $\Omega_c = 2\pi \cdot 5$ MHz from $\sim 7\%$ to below 0.3%, allowing perfect transparency in absence of interactions. More details on the laser locking system are given in Appendix A.
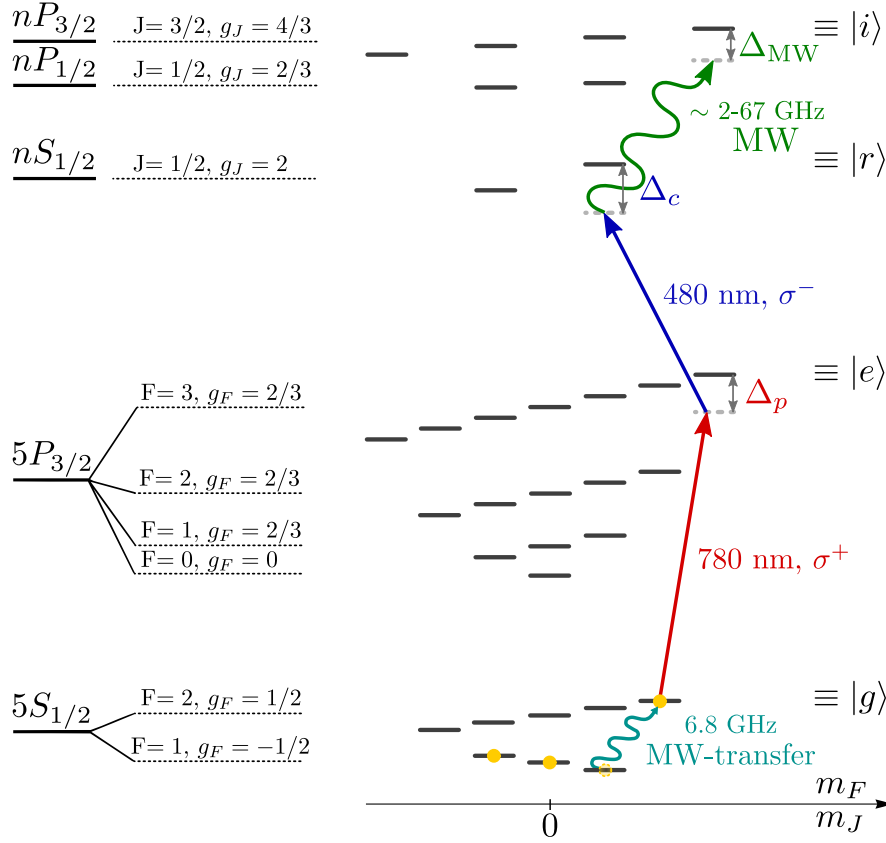
Figure 2.7: Rydberg state preparation scheme with relevant levels of ^{87}Rb in presence of a small magnetic field. After the evaporation the atoms are distributed over the $F = 1$ manifold. By means of a $6.8\,\text{GHz}$ microwave Landau-Zener adiabatic sweep we transfer populations from the state $\left|5S_{1/2}, F = 1, m_F = 1\right\rangle$ to the selected ground state $|g\rangle \equiv \left|5S_{1/2}, F = 2, m_F = 2\right\rangle$. A $780\,\text{nm}$ σ^+-polarized laser beam addresses the $|g\rangle \leftrightarrow |e\rangle \equiv \left|5P_{3/2}, F = 3, m_F = 3\right\rangle$ transition which is used for absorption imaging. A $480\,\text{nm}$ σ^--polarized laser couples $|e\rangle$ to the Rydberg state $|r\rangle \equiv \left|nS_{1/2}, m_J = 1/2\right\rangle$. These two laser couplings form the three-level system used in EIT experiments. A fourth state $|i\rangle \equiv \left|nP_J, m_J\right\rangle$ can be excited in the desired Zeeman level using a microwave photon with a frequency between 2 and $67\,\text{GHz}$, depending on the chosen n. Taken and adapted from [Günter, 2014]. More detailed information on the level scheme of Rubidium can be found in [Steck, 2001].

2.5 Rydberg state preparation

Starting from the prepared ground state, we can excite Rydberg $|nS\rangle$ states using a two-photon scheme or $|nP\rangle$ states via a three-photon transition, as shown in Fig. 2.7. In the first section a brief introduction to the preparation of $|nS\rangle$ states will be given, then in the following four sections more attention will be dedicated to the three photon excitation scheme that was developed and characterized during the course of this thesis.

2.5.1 Excitation of $|nS\rangle$ states

To excite a ground state atom to a Rydberg $|nS\rangle$ state a two-photon transition has to be used. A $780\,\mathrm{nm}$ σ^+-polarized laser beam addresses the $|g\rangle \leftrightarrow |e\rangle \equiv \left|5P_{3/2}, F = 3, m_F = 3\right\rangle$ transition which is also used for absorption imaging, leading to name it "probe" beam. A counter-propagating $480\,\mathrm{nm}$ σ^--polarized laser beam couples $|e\rangle$ to the chosed Rydberg state $|r\rangle \equiv \left|nS_{1/2}, m_J = 1/2\right\rangle$ and is called "coupling". When both probe Δ_p and coupling Δ_c detunings are zero, then these two laser couplings form the three-level system used in EIT experiments, which is discussed in detail in Ch. 3. For $\Delta_p = -\Delta_c$ a direct two-photon off-resonant excitation scheme is realized and a large detuning is chosen ($\Delta_p \gg \Gamma_e$) in order to avoid undesired population of the intermediate state.

2.5.2 Off-resonant excitation of $|nP\rangle$ states

To prepare the Rydberg P states we perform a three-photon excitation. The first stage of the excitation is done using another $780\,\mathrm{nm}$ laser beam propagating along the vertical direction (not shown in Fig. 2.5 for clarity) and linearly polarized such that it generates both σ^+ and σ^- polarization, only the σ^+ one being relevant for the excitation. The σ^--polarized light leads to off-resonant processes that can be neglected in good approximation. For the second stage we use the same blue beam that is involved in EIT. Additionally we employ an Anritsu MG3697C microwave synthesizer which allows to address transitions between Rydberg states with different angular momentum, e.g. $|nS\rangle \leftrightarrow |nP\rangle$ transitions. The microwave radiation is emitted in the science chamber by a simple antenna without any control of the polarization.

To prepare nP Rydberg states of ^{87}Rb a two-photon excitation is prohibited by the selection rules. Instead we use a three-photon excitation making use of two optical photons and an additional microwave photon. This approach allows us to

simultaneously excite nS and nP states, both required for the experiments presented in this work.

The excitation scheme is presented in figure 2.8 (a). The σ^+-polarization of a 780 nm laser beam couples the ground state $|g\rangle$ to the intermediate state $|e\rangle$. Hence, a 480 nm σ^--polarized laser couples $|e\rangle$ to the Rydberg state $|r\rangle = \left|nS_{1/2}, m_J = +1/2\right\rangle$. The third stage of the excitation to the state $|i\rangle = \left|nP_{3/2}, m_J = +3/2\right\rangle$ is done using a microwave photon with a frequency between 2 and 67 GHz, depending on the chosen n. This four-level system is then described by the Hamiltonian

$$
\begin{aligned}
\hat{H} = & - \Delta_e \, |e\rangle \, \langle e| - \Delta_r \, |r\rangle \, \langle r| - \Delta_{mw} \, |i\rangle \, \langle i| \\
& + \left(\frac{\Omega_e}{2} \, |e\rangle \, \langle g| + \frac{\Omega_r}{2} \, |r\rangle \, \langle e| + \frac{\Omega_{mw}}{2} \, |i\rangle \, \langle r| + h.c. \right)
\end{aligned}
\tag{2.17}
$$

with $\hbar = 1$, Δ_e, Δ_r, Δ_{mw} the one-photon, two-photon and three-photon detunings respectively, and Ω_e, Ω_r, Ω_{mw} the Rabi frequencies of each transition.
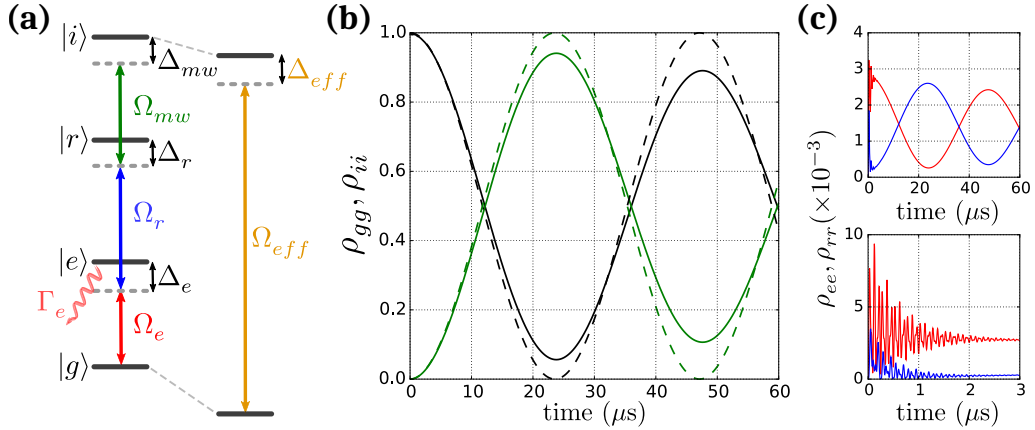
Figure 2.8: Excitation scheme of Rydberg P states. (a) Three-photon excitation scheme. The ground state $|g\rangle$ is off-resonantly coupled to the Rydberg state $|i\rangle$ by two optical fields and one microwave field with Rabi frequencies Ω_e, Ω_r and Ω_{mw}, respectively. Large intermediate detunings Δ_e and Δ_r prevent extensive populations of the two intermediate states $|e\rangle$ and $|r\rangle$. **(b)** Simulation of the time-evolution of the state populations ρ_{gg} and ρ_{ii} (resp. black and green lines), assuming the initial population in the ground state, with $\Delta_e = \Delta_r = -2\pi \cdot 100\,\mathrm{MHz}$, $\Omega_e = \Omega_{mw} = 2\pi \cdot 2.4\,\mathrm{MHz}$ and $\Omega_r = 2\pi \cdot 25\,\mathrm{MHz}$. The exact calculation is compared to the effective two-level model (dashed lines). The observed difference is due to the absence of the decay Γ_e in the latter. **(c)** Populations ρ_{ee} (red) and ρ_{rr} (blue) simulated in the same regime. With a maximum fraction of $3 \cdot 10^{-3}$ these states are weakly populated. On short timescales we observe very fast oscillations that are damped after $2\,\mu\mathrm{s}$, justifying the adiabatic elimination, then the populations follow a similar evolution to $|g\rangle$ and $|r\rangle$.

2.5.3 Effective two-level approximation of a four-level system

To avoid populating the two intermediate states we use large intermediate detunings Δ_e and Δ_r compared to the Rabi frequencies Ω_e, Ω_r and Ω_{mw}. In this regime, the four-level excitation can be described by an effective two-level system that we theoretically develop in the following. The model helps to derive the best strategy to efficiently excite Rydberg P states without any undesired additional effects.

To simulate the three-photon excitation one can use the optical Bloch equations in the four-level basis and numerically solve them for a set of the six experimental parameters given by Eq. (2.17). However, the numerical simulations do not give insight into the excitation process to find the optimal settings for efficient state preparation. Since the excitation is done in the off-resonant regime $\Delta_e, \Delta_r \gg \Omega_e, \Omega_r, \Omega_{mw}$, the evolution of the intermediate state populations exhibit two very different timescales, leading to a rapidly oscillating term at a frequency $\Delta_{e,r}$ and a slow-varying envelope that evolves together with the states $|g\rangle$ and $|i\rangle$. After a short-time, the fast oscillations average to zero due to the decay of the short-lived intermediate state $|e\rangle$. The time derivative of the $|e\rangle$ and $|r\rangle$ populations can then be set to zero as they are dominated by the fast-oscillating terms. By introducing the steady state solutions in the optical Bloch equations, one can eliminate all the terms involving $|e\rangle$ and $|r\rangle$ in order to write an effective equation valid in the limit of long timescales, which directly couples $|g\rangle$ to $|i\rangle$. This approximation is known as adiabatic elimination [Linskens *et al.*, 1996; Brion *et al.*, 2007]. With c_x the projection of the wavefunction to the state $|x\rangle$ ($x = g, e, r, i$), one obtains the following coupled equations

$$\dot{c}_g = -\mathrm{i}S_g c_g + \mathrm{i}\frac{\Omega_{eff}}{2}c_i \qquad (2.18)$$

$$\dot{c}_i = -\mathrm{i}(\Delta_{mw} - S_i)c_i + \mathrm{i}\frac{\Omega_{eff}}{2}c_g \qquad (2.19)$$

where S_g and S_i are the AC-Stark shifts of the states $|g\rangle$ and $|i\rangle$ defined by

$$S_g = \frac{\Omega_e^2}{4\Delta_e - \frac{\Omega_r^2}{\Delta_r}} \qquad\qquad S_i = \frac{\Omega_{mw}^2}{4\Delta_r - \frac{\Omega_r^2}{\Delta_e}} \qquad (2.20)$$

and Ω_{eff} is the effective Rabi frequency of the four-level system defined by

$$\Omega_{eff} = \frac{\Omega_e \Omega_r \Omega_{mw}}{4\Delta_e \Delta_r - \Omega_r^2}. \qquad (2.21)$$

Equation (2.20) simply shows that one can reduce the effect of the three off-resonant fields to AC-Stark shifts of the two outer states $|g\rangle$ and $|i\rangle$ and to an effective Rabi frequency Ω_{eff} coupling these states. The AC-Stark shifts are calculable in a

perturbative approach. By setting the ground-state energy to zero via a rotation in the rotating frame, the differential equations can be rewritten as

$$\dot{c}_g = \mathrm{i}\frac{\Omega_{eff}}{2}c_p \tag{2.22}$$

$$\dot{c}_i = -\mathrm{i}\Delta_{eff}c_i + \mathrm{i}\frac{\Omega_{eff}}{2}c_g. \tag{2.23}$$

with $\Delta_{eff} = \Delta_i + S_g - S_i$ the effective detuning. At this stage one can identify the Schrödinger equation of a two-level system with Rabi frequency Ω_{eff} and detuning Δ_{eff}. Therefore the whole system can be considered as an effective two-level system where conditions for the inversion of state populations are known.

This effective description is illustrated in Fig. 2.8 (b), where the populations of the four levels are plotted as a function of the excitation time and compared to full numerical solutions of the optical Bloch equations. It clearly shows that the two intermediate states are negligibly populated and that the two outer states behave like a two-level system, exhibiting an evolution similar to two-level Rabi oscillations. We notice that the effective model does not predict the decay of the oscillations which would be a consequence of the decay of the intermediate state, not considered in the current effective model. To take it into account we use an effective operator formalism for open quantum systems to derive an effective master equation [Reiter and Sørensen, 2012]. It results that the decay Γ_e effectively leads to various terms in the two-level model which can, on long timescales, either kill or enhance coherences. In the following discussion we neglect this decay since it has no crucial impact on the regime we are working on.

Using this approach we can derive an optimized excitation scheme of the Rydberg state $|i\rangle$. Due to the AC-Stark shifts, the intuitive resonance condition with $\Delta_{mw} = 0$ is not valid. From the effective two-level model we deduce a modified resonance condition that must be fulfilled to efficiently transfer an atom from $|g\rangle$ to $|i\rangle$

$$\Delta_{eff} = \Delta_i + \frac{\Omega_e^2}{4\Delta_e - \frac{\Omega_r^2}{\Delta_r}} - \frac{\Omega_{mw}^2}{4\Delta_r - \frac{\Omega_r^2}{\Delta_e}} = 0. \tag{2.24}$$

In addition, two other constraints must be considered before performing the experiment. On one hand we aim to excite the $|nP\rangle$ state on a timescale shorter than its lifetime, leading to the condition

$$\Omega_{eff} \leq \tau_i^{-1}. \tag{2.25}$$

On the other hand we want to avoid populations in both intermediate states. Populations in the Rydberg state $|r\rangle$ cannot be resolved by our field ionization setup

and would be mistaken for the desired state, while population in $|e\rangle$ could lead to scattering and heating of the cloud. In the far-detuned regime, c_e and c_r are very accurately approximated by $\Omega_e/\Delta_e \cdot c_g$ and $\Omega_{mw}/\Delta_{mw} \cdot c_i$, respectively. To satisfy both conditions, it is favourable to keep Ω_e and Ω_{mw} relatively small, while Ω_r can remain large as long as it satisfies the far-detuned condition $\Omega_r \ll \Delta_e, \Delta_r$.

Experiments presented in Ch. 4.5, aimed at optically revealing the presence of $|nP\rangle$ states, require a two-photon resonant EIT coupling to $|nS\rangle$ states. In the following we choose to use the same principal quantum number n for both the $|r\rangle$ and $|i\rangle$ states, such that the same 480 nm laser field is shared between the second step of the off-resonant excitation scheme and the EIT coupling. Hence $\Delta_r = 0$ and the detunings must fulfill $\Delta_e = \Delta_r$. In all experiments we set them to $\sim 2\pi \cdot 100$ MHz. In these conditions the red beam heating effect is negligible if the Rabi frequency Ω_e is below a critical value of typically $2\pi \cdot 2.5$ MHz. Hence, Ω_r and Ω_{mw} can be adjusted to respect the above-mentioned conditions. The simulations in Fig. 2.8 show an example of efficient excitation with populations in the intermediate states smaller than 3%.

2.5.4 Three-photon spectroscopy of $|42P\rangle$ Rydberg states

Now that we understood how to excite $|nP\rangle$ Rydberg states while avoiding population in the intermediate levels, we apply our three-photon off-resonant excitation scheme to prepare the $|i\rangle = |42P_{3/2}\rangle$ state, which will be used later on in the experiments presented in Ch. 4.5. As previously discussed, the two optical photons only address the Zeeman substate $|42S_{1/2}, m_J = +1/2\rangle$. The target state $|42P_{3/2}\rangle$ is addressed by a microwave field without control of the polarization, allowing for excitation of the $m_J = -1/2, +1/2, +3/2$ states. The magnetic field induces a Zeeman shift that lifts the degeneracy between these states. Scanning the microwave frequency ν_{mw} we record the spectrum shown in Fig. 2.9 (a) using field-ionization detection after the excitation pulse. Large numbers of ions are measured at three expected equally-spaced frequencies. In addition a fourth, smaller peak appears at the expected position of the $m_J = -3/2$ Zeeman substate, which can be explained by misalignment of the polarization of the 780 nm excitation beam with the vertical direction, resulting in a residual π-polarized component for which two additional σ^- photons allow to address the $m_J = -3/2$ state. We also observe small additional peaks with frequency separations exactly corresponding to the ground state Zeeman splitting. Such resonances are signature of transitions from the other hyperfine levels of the ground state $|5S_{1/2}, F = 2\rangle$ to the $|42P_{3/2}\rangle$ state. Population in these states
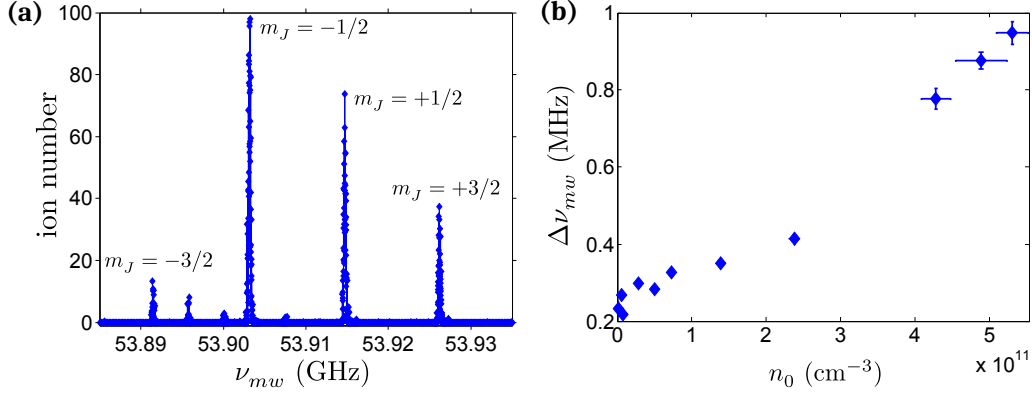
Figure 2.9: Three-photon spectroscopy of the $\left|42P_{3/2}\right\rangle$ states. (a) Microwave frequency scan around the three-photon resonance, at a peak density $n_0 = (3.30 \pm 0.18) \cdot 10^9 \, \mathrm{cm}^{-3}$ where interaction effects do not play a significant role. The atoms, initially prepared in $\left|g\right\rangle$, are off-resonantly driven to $\left|e\right\rangle$ and $\left|r\right\rangle = \left|42S_{1/2}, m_J = +1/2\right\rangle$. A detuned microwave radiation finally excites the state $\left|i\right\rangle$ by compensating the energy mismatch. Only the Zeeman substates $m_J = +3/2, +1/2, -1/2$ are addressed with σ^+, π, σ^- polarization components, respectively. The Rabi frequencies are calibrated to be $\Omega_e = 2\pi \cdot 9.7 \, \mathrm{MHz}$, $\Omega_r = 2\pi \cdot 25 \, \mathrm{MHz}$, $\Omega_{mw} = 2\pi \cdot 12 \, \mathrm{MHz}$. The spectrum shows a significant population of $\left|42P_{3/2}, m_J = -3/2\right\rangle$, coming from a residual π polarization component of Ω_e. The additional residual peaks come from a cycling process that populates different m_F sub-states of $\left|5S_{1/2}, F = 2\right\rangle$. A magnetic field $B_x = 6.43 \, \mathrm{G}$ is estimated from the fine splitting observed between the m_J peaks. **(b)** Density dependence of the width of the $\left|42P_{3/2}, m_J = +3/2\right\rangle$ resonance. In contrast to (a), many-body interaction effects play a major role on the lineshape at higher densities. The spectrum is acquired with $\Omega_e = 2\pi \cdot 5.6 \, \mathrm{MHz}$, $\Omega_r = 2\pi \cdot 25 \, \mathrm{MHz}$, $\Omega_{mw} = 2\pi \cdot 12 \, \mathrm{MHz}$.

cannot be explained by imperfections of the state preparation since we initially excite with high-efficiency the pure $m_F = +2$ hyperfine state. However, they could arise from coupling to the Rydberg state, for which the purity of the m_F quantum number is not preserved.

The spectrum in Fig. 2.9 (a) was taken under low-density conditions to minimize multi-particle interaction effects, which have been reported to strongly modify the width of the observed transitions [Anderson *et al.*, 2002; Park *et al.*, 2011; Afrousheh *et al.*, 2004; Afrousheh *et al.*, 2006; Goldschmidt *et al.*, 2016]. In our experiments, we perform the excitation of the $\left|42P_{3/2}, m_J = +3/2\right\rangle$ at various densities of ground state atoms and, as shown in Fig. 2.9 (b), we observe an increase of the width of the spectral line at higher densities, which constitutes a signature of van der Waals Rydberg-Rydberg interactions.

(a)

(b)
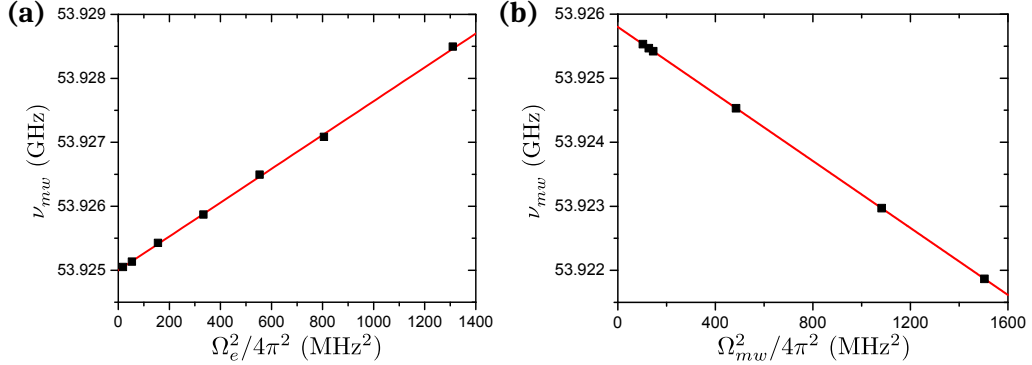
Figure 2.10: **Calibration of Ω_e and Ω_{mw} from the light shift of the resonance.** **(a)** For a given coupling of Ω_r and Ω_{mw} the intensity of the red beam Ω_e is varied. The resonant position of the peak $\left|42P_{3/2,+3/2}\right\rangle$ undergoes a quadratic light shift following Eq. 2.20. **(b)** Analogously, for given Ω_e and Ω_r, the same procedure can be applied to calibrate Ω_{mw}. We must rely on the fact that the AC-Stark Shift is linear with the power (Eq. 2.20) and therefore find the unperturbed central peak frequency.

Three-photon spectroscopy provides a powerful tool to calibrate the Rabi frequencies and the detunings of the fields involved in the excitation process because the resonance condition depends on all these parameters according to Eq. (2.24). Only the measurement of the coupling Rabi frequency $\Omega_r = \Omega_c$ is independently realized using a method based on a local fitting of the electromagnetically-induced transparency profile [Gavryusev *et al.*, 2016b], described in Ch. 3.2.4. By performing three-photon spectroscopy at different Ω_e (Fig. 2.10 (a)) while keeping the other settings constant, we observe that the resonance frequency exhibits a linear behavior with the laser power $P_e \propto \Omega_e^2$ (measured independently), in perfect agreement with Eq. (2.24). We determine the unshifted resonance frequency from a linear extrapolation to zero intensity and we can afterwards express the measured resonance frequencies in terms of light shifts S_g of the ground state, allowing us to use equation (2.20) to calculate the Rabi frequencies Ω_e. The calibration between P_e and Ω_e^2 is then used to plot figure 2.10 (a), revealing a linear relation as would have been expected from the two-level model, thus validating its use.

A similar procedure cannot be applied to calibrate the microwave Rabi frequency Ω_{mw} since the intensity of the microwave source at the position of the atoms is unknown. Therefore we rely on the same theoretical predictions for the AC-Stark shift, assuming a linear dependence with Ω_{mw}^2. From the variation of the spectral peak position for different microwave intensities, we infer the non-shifted three-photon resonance that leads to a linear relation of the resonance frequency with Ω_{mw}^2

(fig. 2.10b). From it we again calculate the AC-Stark shifts and therefore deduce a calibration of Ω_{mw}. We have checked the consistency of these measurements by measuring the non-shifted transition, setting $\Omega_e = \Omega_{mw}$. We obtain a resonance shifted by $-96\,\text{MHz}$, in agreement with the experimental calibration of the detuning within $0.5\,\text{MHz}$. In this way we obtain all the required parameters to perform an efficient and controllable excitation of Rydberg P-states.

2.5.5 Incoherent excitation of $|42P\rangle$ Rydberg states
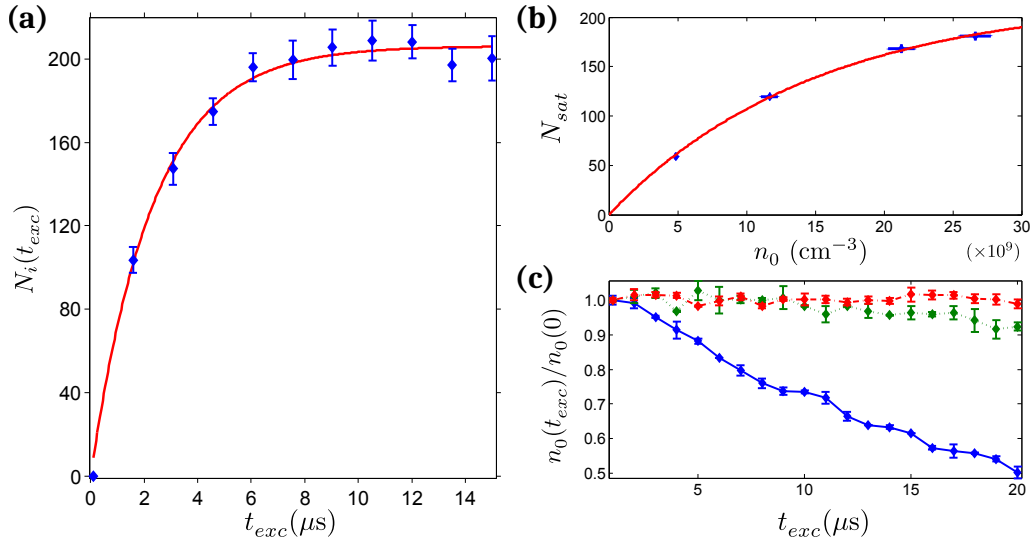
Figure 2.11: Excitation of $\left|42P_{3/2}, m_J = +3/2\right\rangle$ Rydberg atoms. (a) Excitation dynamics as a function of the excitation time t_{exc}. The measurement is done after a fixed time-of-flight of $1\,\text{ms}$, at a peak ground-state density $n_0 = (7.26 \pm 0.21) \cdot 10^9\,\text{cm}^{-3}$, with $\Omega_e = \Omega_{mw} = 2\pi \cdot 10\,\text{MHz}$, $\Omega_r = 2\pi \cdot 25\,\text{MHz}$. The data shows a saturation of the number of excitations N_i. A fit with the function $N_i(t_{exc}) = N_{sat}(1 - e^{-t_{exc}/\tau})$ gives $N_{sat} = 206.2 \pm 2.6$ and $\tau = (2.34 \pm 0.11)\,\mu\text{s}$. **(b)** Blockade effect on the excited states. Repeating the same experiment, we observe a saturation of N_{sat} while increasing the ground-state density. To reach high enough densities, the time-of-flight is reduced to $0.5\,\text{ms}$. **(c)** Heating induced by scattering on the $|g\rangle \leftrightarrow |e\rangle$ transition. The density is plotted at different excitation times t_{exc} for $\Omega_e = 2\pi \cdot [2.4, 7.1, 21]\,\text{MHz}$ (resp. dash-dotted red, dotted green and solid blue lines). The microwave is switched off to avoid density reduction due to Rydberg excitation. The error bars represent the standard deviation.

The imaging experiments performed with the $\left|42P_{3/2}, m_J = +3/2\right\rangle$ in Ch. 4.5 require a precise control of the number of excited Rydberg atoms. For this purpose it

is important to understand the evolution of the population in $|i\rangle$ with the excitation time t_{exc}. The theoretical model predicts coherent Rabi oscillations between the ground and the P-states with an effective Rabi frequency Ω_{eff} given by Eq. (2.21). Yet our measurements show the emergence of a saturation effect after typically 6 µs (Fig. 2.11 (a)), that we attribute to incoherent excitation of the $\left|42P_{3/2}, m_J = +3/2\right\rangle$ Rydberg state. We understand this to be a consequence of a large degree of dephasing introduced by the strong inhomogeneity of the effective Rabi frequency Ω_{eff}, due to the Gaussian profile of the coupling beam [Heidemann *et al.*, 2007].

Repeating the experiment for increasing ground-state atomic densities, we observe a similar behavior of the excitation dynamics on the same timescale, but with different saturated number of excitations N_{sat}. In figure 2.11 (b) this number is plotted versus the ground-state density n_0. As can be seen from the plot, we observe a second saturation effect that we attribute to the Rydberg blockade between P-states: due to their van der Waals interactions, the total number of Rydberg atoms in the finite volume of the cloud is limited. Given that the detection efficiency is not known with high accuracy, the value $N_{bl} = 218 \pm 6$ that we extract from the exponential fit is consistent with an estimation based on the van der Waals $P - P$ blockade radius ($R_{ii} = (C_6^{ii}/\Delta\nu_{mw})^{1/6} \sim 4$ µm with $\Delta\nu_{mw}$ the width of the resonance at low density extracted from Fig. 2.9 (b)) that would lead to ~ 230 Rydberg atoms in the excitation volume.

The final step to optimize the excitation of $\left|42P_{3/2}, m_J = +3/2\right\rangle$ Rydberg states consists in minimizing any heating effects due to large excitation Rabi frequency Ω_e, which lead to loss of atoms from the atomic cloud (Fig. 2.11 (c)). In order to avoid such an effect, we reduce the power of the 780 nm laser beam to $\Omega_e = 2\pi \cdot 2.4$ MHz and compensate it by increasing the microwave Rabi frequency Ω_{mw} to $2\pi \cdot 14$ MHz, such that the effective coupling is not significantly affected.

Chapter 3

Density matrix reconstruction of three-level atoms via Rydberg electromagnetically induced transparency

This chapter is partially based on the following publication, from which parts of the text are reproduced verbatim:

The interplay between Rydberg-Rydberg interactions and the non-linear optical response of a three-level atomic medium can allow to optically detect the presence of Rydberg atoms [Günter *et al.*, 2012; Olmos *et al.*, 2011], which in turn grants access to the dynamics and correlations present in these complex many-body systems. At the root of the Interaction Enhanced Imaging technique, that we discuss in Ch. 4, lies the use of a narrow optical transition that can be locally perturbed by the presence of a Rydberg atom, allowing to detect them. For this purpose, we use the steep optical response induced by a quantum interference effect called electromagnetically induced transparency (EIT), which renders transparent an otherwise absorptive medium. Thus, a comprehensive understanding of EIT is a prerequisite step for IEI studies.

The experimental and theoretical investigation of ensembles of Rydberg atoms driven by laser fields is currently attracting much interest [Comparat and Pillet, 2010; Löw *et al.*, 2012; Pritchard *et al.*, 2013; Firstenberg *et al.*, 2016]. For instance, the exceptional properties of Rydberg atoms, such as their tunable long-range interactions and the Rydberg blockade effect, allow to create atom-light interfaces operating at the single photon level [Dudin and Kuzmich, 2012; Peyronel *et al.*, 2012; Maxwell *et al.*, 2013; Tiarks *et al.*, 2014; Gorniaczyk *et al.*, 2014].

However, to fully explore the rich physics of these strongly coupled atom-light systems we require new ways to disentangle the different degrees of freedom which link single atom properties to many-body observables. We begin our investigation at low atomic densities, such that the effects of Rydberg interactions are negligible. The complete knowledge of the atomic ensemble is encoded in the single atom density matrix. Most often no prior information is possessed on the form of this quantity, requiring to apply the general method of Quantum Homodyne Tomography to reconstruct it [Vogel and Risken, 1989; Leonhardt, 1995; Leonhardt and Paul, 1995]. This approach has allowed to successfully investigate the quantum states of light [Smithey *et al.*, 1993; Ourjoumtsev *et al.*, 2006; Deléglise *et al.*, 2008], matter [Dunn *et al.*, 1995; Leibfried *et al.*, 1996; Gaëtan *et al.*, 2010] and of coupled light-matter systems [De Greve *et al.*, 2013]. A tomographic reconstruction is possible, given the limited number of states, but in practice it is experimentally difficult to measure all the populations and coherences. In contrast, if prior knowledge on the form of the density matrix is possessed, then a reconstruction is possible by measuring a reduced number of density matrix elements.

In this chapter we demonstrate the reconstruction of the single atom density matrix of an ultracold gas of three-level non-interacting atoms under electromagnetically induced transparency conditions involving high-lying Rydberg states. Traditionally, in a Rydberg atom experiment, either the Rydberg state population or the medium optical response are measured to obtain limited information on the coupled atom-light system. However, we show that combining measurements of both quantities in a single experiment allows to probe the underlying system with high spectral and spatial resolution and obtain nearly complete information on its properties. First steps towards this goal have already been achieved, with the observation of sub-Poissonian statistics of the matter-part of Rydberg dark state polaritons [Hofmann *et al.*, 2013] and the electrical readout of Rydberg EIT in thermal vapour cells [Barredo *et al.*, 2013]. Through time resolved measurements of the transparency signal it has been shown that it is possible to reconstruct the Rydberg population [Mack *et al.*, 2015; Karlewski *et al.*, 2015], but here we present the first demonstration of the full density

matrix reconstruction of a three-level system under Rydberg EIT.

This chapter is structured as follows: first in Ch. 3.1 we illustrate a semi-classical description of the interaction of light fields with non-interacting three-level atoms. This description allows to explain the origin and properties of EIT and, most importantly, constitutes the prior knowledge needed later on for the density matrix reconstruction. Then in Ch. 3.2 we present our combined measurements of the Rydberg population and of the spatially resolved transmission spectra in an ultracold gas of ^{87}Rb atoms, performed at low atomic densities, such that the effects of Rydberg interactions are negligible. Next we explain how the density matrix of the system is reconstructed from these two sets of measurements, leveraging the previously introduced theoretical model. This provides complete information on the system, which we use to reconstruct the spatial distributions of the Rydberg state population and of the medium optical response. Furthermore, we determine the spatial profile of the coupling beam.

3.1   Theory of electromagnetically induced transparency

Electromagnetically-induced-transparency is a quantum interference effect which arises in three-level systems composed of two long-lived states that are coherently coupled via a short-lived state [Harris, 1997; Marangos, 1998; Fleischhauer *et al.*, 2005]. The destructive interference of different excitation pathways driven by the radiation fields renders an otherwise absorbing medium transparent [Fano, 1961]. This is accompanied by the evolution of the atomic system into a dark-state that is a superposition of the long-lived states and is decoupled from the light field.

Using the ladder level scheme introduced in Ch. 2.5.1, $|g\rangle$ and $|r\rangle$ are the two long-lived states, while $|e\rangle$ is the short-lived state which is coupled to them, as illustrated in Fig. 3.1 (a). In our experiments, state $|r\rangle$ is a high lying Rydberg state of ^{87}Rb and it can be treated as meta-stable on the timescale of the experiment, since $\Gamma_r/2\pi \sim$ kHz $\ll \Gamma_e/2\pi = 6.067$ MHz. Under EIT conditions a transparency resonance arises for the $|g\rangle \leftrightarrow |e\rangle$ transition, which is sensitive to the properties of the Rydberg state. Strong laser coupling of the $|e\rangle \leftrightarrow |r\rangle$ transition with Rabi frequency Ω_c produces an Autler-Townes doublet of dressed states [Autler and Townes, 1955; Cohen-Tannoudji, 1996] (Fig. 3.1 (b)).
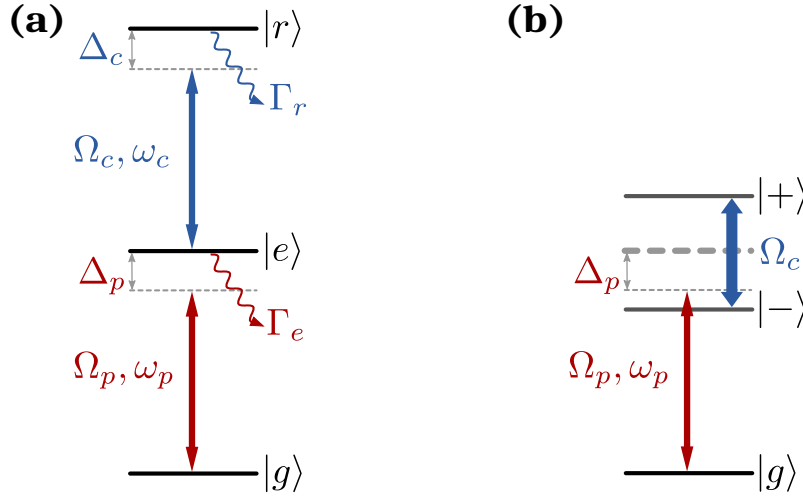
Figure 3.1: Level scheme of a three-level ladder system. (a) The atomic states $|g\rangle$, $|e\rangle$ and $|r\rangle$ are coherently coupled by two laser fields with frequencies $\omega_{p,c}$, coupling Rabi frequencies $\Omega_{p,c}$ and detunings $\Delta_{p,c}$. The excited state and the Rydberg state are subject to decay with decay constants Γ_e and Γ_r, respectively. **(b)** In the case of strong coupling $\Omega_c > \Gamma_e$ the intermediate state is split into two by the Autler-Townes effect and the system is more conveniently described in a dressed basis. Here the dressed-state level structure for $\Delta_c = 0$ with $|\pm\rangle = (|r\rangle \pm |e\rangle)/\sqrt{2}$ is shown. Taken and adapted from [Günter, 2014].

3.1.1 Optical Bloch equations

To describe the coupled atom-light system, we assume to be in a low density regime, such that Rydberg-Rydberg interaction effects can be neglected, and a semi-classical treatment with a quantized atomic system and classical light fields will be sufficient. The coupled atom-light system in the dipole and rotating wave approximations is described by the following Hamiltonian [Scully and Zubairy, 1997]

$$\hat{\mathcal{H}} = \frac{\hbar}{2} \begin{pmatrix} 0 & \Omega_p & 0 \\ \Omega_p & -2\Delta_p & \Omega_c \\ 0 & \Omega_c & -2(\Delta_p + \Delta_c) \end{pmatrix}. \tag{3.1}$$

Here $\Omega_{p,c}$ are the Rabi frequencies for the probe and coupling lasers respectively, and $\Delta_{p,c}$ are the detunings from the probe and coupling transitions.

The spontaneous decay of the intermediate state $|e\rangle$ and of the Rydberg state $|r\rangle$ with rates Γ_e and Γ_r, respectively, lead to decoherence and non-unitary evolution of the system. To account for decay and dephasing effects [Pritchard *et al.*, 2010; Gärttner and Evers, 2013], we use the density matrix formalism which describes the time evolution of incoherent or open systems and we derive a master equation for

the single atom density matrix ρ

$$\dot{\rho} = -\frac{i}{\hbar}[\hat{\mathcal{H}}, \rho] + \mathcal{L}_{\text{deph}}(\rho) + \mathcal{L}_{\text{dec}}(\rho), \tag{3.2}$$

with $\rho_{jk} = \rho_{kj}^*$ and where $\mathcal{L}(\rho)$ is the Lindblad superoperator [Lindblad, 1976].

$\mathcal{L}_{\text{dec}}(\rho)$ accounts for population decays and the resulting loss of coherence

$$\mathcal{L}_{\text{dec}}(\rho) = -\frac{1}{2}\sum_k (C_k^\dagger C_k \rho + \rho C_k^\dagger C_k) + \sum_k C_k \rho C_k^\dagger, \tag{3.3}$$

where the operators C_k express the decay strength and the involved states of the k-th decay channel. The sums are over all possible decay channels, which are just two for our system

$$C_{ge} = \sqrt{\Gamma_e}\,|g\rangle\langle e|\,, \qquad C_{er} = \sqrt{\Gamma_r}\,|e\rangle\langle r|\,. \tag{3.4}$$

The atomic coherences (off-diagonal terms) can be affected by phase fluctuations, leading to a dephasing, i.e. to a decay which does not perturb the populations [Sultana and Zubairy, 1994; Fleischhauer *et al.*, 2005]. The dephasing can be accounted for by using a phenomenological Lindblad operator $\mathcal{L}_{\text{deph}}(\rho)$

$$\mathcal{L}_{\text{deph}}(\rho) = -\frac{1}{2}\begin{pmatrix} 0 & \gamma_p \rho_{ge} & \gamma_{gr} \rho_{gr} \\ \gamma_p \rho_{eg} & 0 & \gamma_c \rho_{er} \\ \gamma_{gr} \rho_{rg} & \gamma_c \rho_{re} & 0 \end{pmatrix}, \tag{3.5}$$

where γ_p, γ_c and γ_{gr} are the dephasings affecting the three transitions. Often dephasings are induced by the laser sources that drive the system. Their emission fluctuates around a central frequency and, if these variations are caused by phase fluctuations, then they lead to dephasing. The frequency emission spectrum of a laser can usually be described by a Lorentzian distribution with a full width half-maximum γ (FWHM), called "linewidth"[1]. Another source of dephasing is represented by Fourier-transform-limited pulses, that has to be estimated on the timescale of the laser coupling duration (see Ch. 2.4.5).

Equation (3.2) yields the three-level optical Bloch equations (OBE) for the single

---

[1]For independently fluctuating probe and coupling lasers, as in our experiment, and without other contributions we can express $\gamma_{gr} = \gamma_p + \gamma_c$.

atom density matrix ρ

$$
\begin{aligned}
\dot{\rho}_{gg} &= -\Omega_p \mathrm{Im}[\rho_{ge}] + \Gamma_e \rho_{ee} \\
\dot{\rho}_{ee} &= +\Omega_p \mathrm{Im}[\rho_{ge}] - \Omega_c \mathrm{Im}[\rho_{er}] - \Gamma_e \rho_{ee} + \Gamma_r \rho_{rr} \\
\dot{\rho}_{rr} &= +\Omega_c \mathrm{Im}[\rho_{er}] - \Gamma_r \rho_{rr} \\
\dot{\rho}_{ge} &= -\Gamma_{ge} \rho_{ge}/2 + \mathrm{i}\Omega_c \rho_{gr}/2 + \mathrm{i}\Omega_p(\rho_{gg} - \rho_{ee})/2 \\
\dot{\rho}_{gr} &= -\Gamma_{gr} \rho_{gr}/2 - \mathrm{i}(\Omega_p \rho_{er} - \Omega_c \rho_{ge})/2 \\
\dot{\rho}_{er} &= -\Gamma_{er} \rho_{er}/2 - \mathrm{i}(\Omega_c \rho_{rr} + \Omega_p \rho_{gr} - \Omega_c \rho_{ee})/2 \,,
\end{aligned}
\tag{3.6}
$$

where $\mathrm{Im}[x]$ denotes the imaginary part of x, and we have defined the rates
$\Gamma_{ge} = \Gamma_{ge}^0 + 2\mathrm{i}\Delta_p$, $\Gamma_{er} = \Gamma_{er}^0 + \gamma_c + 2\mathrm{i}\Delta_c$ and $\Gamma_{gr} = \Gamma_{gr}^0 + 2\mathrm{i}(\Delta_p + \Delta_c)$
with $\Gamma_{ge}^0 = \Gamma_e + \gamma_p$, $\Gamma_{er}^0 = \Gamma_e + \Gamma_r + \gamma_c$, $\Gamma_{gr}^0 = \Gamma_r + \gamma_{gr}$.

3.1.2 Solutions of the optical Bloch equations in the weak probe approximation

The solutions of the OBEs describe the time evolution of the populations and coherences, providing therefore a complete knowledge of the density matrix of the coupled atom-light system, if all parameters present in the equations are known $(\Omega_p, \Omega_c, \Delta_p, \Delta_c, \Gamma_e, \Gamma_r, \gamma_p, \gamma_c)$. Assuming that the presented model captures all the key physical processes that affect a non-interacting three-level system under Rydberg EIT, if we find the solutions for Eqs. (3.6) we would know the exact form of the density matrix. This prior information allows to reconstruct ρ by measuring a reduced number of density matrix elements, specifically those from which all eight unknown parameters can be estimated.

We derive now the solutions of the OBEs. The decay rate of the intermediate state Γ_e sets a timescale for the evolution of the system. With typical Rabi frequencies of several MHz in the experiment, the atomic evolution reaches steady-state in less than a μs and this allows to work with the steady-state solutions of the OBEs.

Inspecting the OBEs in this regime ($\dot{\rho} = 0$), one finds the following relations

$$
\rho_{ee} = \frac{\Omega_p \mathrm{Im}[\rho_{ge}]}{\Gamma_e}, \quad \rho_{er} = \frac{\Omega_p \mathrm{Im}[\rho_{gr}]}{\mathrm{Re}[\Gamma_{er}]}, \quad \rho_{rr} = \frac{\mathrm{i}\Gamma_{er}\rho_{er} + \Omega_c \rho_{ee} - \Omega_p \rho_{gr}}{\Omega_c}.
\tag{3.7}
$$

Exact analytic solutions of the optical Bloch equations for the single atom density matrix ρ can be found without requiring any approximation (see Appendix C), but their form is cumbersome and does not give an intuitive insight on the system's properties. We work with small light intensities which allows to use the weak probe

limit ($\Omega_p \ll \Omega_c, \Gamma_e$), yielding two much simpler approximate analytic solutions for ρ_{ge} and ρ_{gr}

$$\rho_{ge} \approx \frac{\mathrm{i}\Gamma_{gr}\Omega_p}{\Gamma_{ge}\Gamma_{gr} + \Omega_c^2}, \quad \rho_{gr} \approx \frac{-\Omega_c\Omega_p}{\Gamma_{ge}\Gamma_{gr} + \Omega_c^2}, \tag{3.8}$$

which when substituted into equations (3.7) provide solutions for all elements of ρ.

In our experiment we cannot measure the density matrix elements directly, but only observables connected to them. In particular in each experimental run of our system we obtain information on ρ_{rr} and ρ_{ge} by measuring, respectively, the Rydberg state population, by means of field ionization and charged particle detection, and the medium optical response, by spatially resolved detection of the transmitted light field on a CCD camera (see Ch. 2.4.4). In the following we will show that the combined measurement of these two observables allows to extract all the unknown parameters in the OBEs and reconstruct the density matrix.

3.1.3 Light propagation in a two- and a three-level system

Exposing the atomic cloud to a probe light field, which addresses the $|g\rangle \leftrightarrow |e\rangle$ transition with Rabi frequency Ω_p, induces a response expressed by the optical susceptibility [Steck, 2007], which is related to the off-diagonal density matrix element that represents the atom-light coherence for the addressed transition,

$$\chi(\Delta_p) = -\frac{2\,n|\hat{\mu}_{eg}|^2}{\epsilon_0\hbar}\frac{\rho_{eg}}{\Omega_p} = -\chi_0\frac{\Gamma_e}{\Omega_p}\rho_{eg}\,, \tag{3.9}$$

where n is the local atomic density and ϵ_0 the vacuum permittivity. In the last step we grouped the specific medium properties that do not depend on the laser parameters in the term $\chi_0 = \sigma_0 n/k$, where σ_0 is the resonant scattering cross-section and $k = 2\pi/\lambda$ the wavevector of the probe light field.

For our experiments there are two important cases to consider:

- **two-level response** – if the coupling beam is absent ($\Omega_c = 0$), the three-level system reduces to a two-level system for which an exact solution for ρ_{eg} is known [Steck, 2007], leading to

$$\chi_{2lvl}(\Delta_p) = \chi_0\frac{\Gamma_e(-2\Delta_p + \mathrm{i}(\Gamma_e + \gamma_p))}{2\Omega_p^2(\Gamma_e + \gamma_p)/\Gamma_e + (\Gamma_e + \gamma_p)^2 + 4\Delta_p^2} \tag{3.10}$$

We observe that χ_0 is the resonant optical susceptibility of a perfect two-level system in absence of dephasing and power broadening.

- **three-level response** – in presence of the coupling beam and using the weak probe limit solution for ρ_{eg} (Eq. (3.8)), we obtain the first order susceptibility [Fleischhauer *et al.*, 2005]

$$\chi_{3lvl}(\Delta_p) = \frac{i\Gamma_e\Gamma_{gr}^*}{\Gamma_{ge}^*\Gamma_{gr}^* + \Omega_c^2} = \chi_0 \frac{\Gamma_e(\Gamma_r + \gamma_{gr} - 2i(\Delta_p + \Delta_c))}{(\Gamma_e + \gamma_p - 2i\Delta_p)(\Gamma_r + \gamma_{gr} - 2i(\Delta_p + \Delta_c)) + \Omega_c^2}.$$
(3.11)

For the following discussion it is convenient to define the scaled linear optical susceptibility

$$\tilde{\chi}(\Delta_p) = \frac{\chi(\Delta_p)}{\chi_0} = \frac{\Gamma_e}{\Omega_p}\rho_{ge}$$
(3.12)

In the experiment we measure the transmission of the probe beam through the cloud. Assuming a paraxial approximation, the propagation of a stationary probe field with initial Rabi frequency Ω_p through the medium along the x direction is described by the differential equation

$$\frac{\partial\Omega_p(x)}{\partial x} = i\frac{k}{2}\chi\Big(\Omega_p(x), n(x)\Big)\Omega_p(x),$$
(3.13)

where non-linear effects may arise due to the dependence on the local Rabi frequency and susceptibility. This equation shows that the imaginary part of the susceptibility is responsible for absorption, while the real part induces a phase shift during propagation. Provided that $|\chi| \ll 1$, as verified for low atomic densities, we can neglect refraction effects and assume a constant χ. In this linear regime, equation (3.13) can be easily integrated, giving the transmission through the cloud

$$T \approx \exp\Big(-k\int_{-\infty}^{+\infty}\mathrm{Im}[\chi]dx\Big) \approx \exp\Big(-\sigma_0\mathrm{Im}[\tilde{\chi}]n_{2d}\Big),$$
(3.14)

where n_{2d} is the atomic density integrated along the probe propagation direction.

Complementary information to the cloud transmission is provided by field ionization of the gas which gives a direct measure of the integrated Rydberg population $N_r = \int\rho_{rr}(r)n(r)dr$ over the whole cloud, where the spatial dependence enters through the atomic density profile $n(r)$ and the inhomogeneous profiles of the excitation beams.

3.1.4 Electromagnetically induced transparency

The scaled susceptibility and Rydberg population spectra, simulated as a function of the probe laser detuning Δ_p (with $\Delta_c, \Gamma_r, \gamma_p, \gamma_c = 0$ and $\Omega_p \ll \Omega_c, \Gamma_e$), show three different regimes depending on the laser coupling, as illustrated in Fig. 3.2 (a):
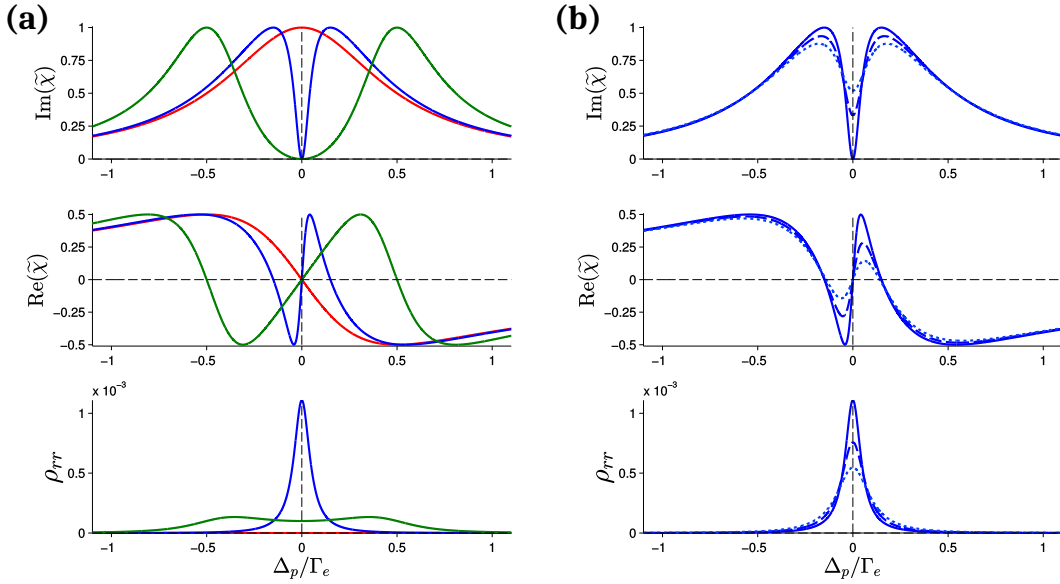
Figure 3.2: Electromagnetically Induced Transparency. Imaginary and real parts of the scaled linear optical susceptibility and Rydberg population as a function of the probe laser detuning Δ_p. **Column (a)** Spectra calculated using the analytic solutions of the OBEs (Eqs. (3.7-3.8)) with $\Delta_c, \Gamma_r, \gamma_p, \gamma_c = 0$, $\Omega_p = 0.01\,\Gamma_e$ for three different coupling Rabi frequencies. The case $\Omega_c = 0.0\,\Gamma_e$ describes the response of a two-level system (red), while for $\Omega_c = 0.3\,\Gamma_e$ we observe a narrow EIT resonance featuring a steep change in the susceptibility and a single Lorentzian shaped peak in the population (blue). In the case of strong coupling $\Omega_c = 1\,\Gamma_e$ we enter the Autler-Townes regime, characterized by a broad transparency window and by the splitting and suppression of population in the Rydberg state (green). **Column (b)** Both the optical response and the Rydberg state population are negatively affected by dephasing sources, such as finite laser linewidth $\gamma_p, \gamma_c = 0.04\,\Gamma_e$ (dashed blue) and fourier limited pulse width ($\gamma_p, \gamma_c = 0.10\,\Gamma_e$ for $t_{pulse} = 5\,\mu s$, dotted blue) with $\Omega_c = 0.3\,\Gamma_e$. An increasing ratio of γ/Ω_c reduces the transparency on EIT resonance, as well as the peak $\mathrm{Im}[\tilde{\chi}]$ off-resonance, and the population spectrum is lowered in amplitude and broadened.

- **two-level** $(\Omega_c = 0.0\,\Gamma_e)$ – (red) The imaginary part of the scaled susceptibility shows a Lorentzian profile with FWHM $\propto \Gamma_{ge}^0$, as expected for a two-level system. The real part follows the well known anomalous dispersion and crosses 0 at $\Delta_p = 0$. The Rydberg population is identically zero.

- **EIT** $(\Omega_c < \Gamma_e)$ – (blue) The imaginary part of the scaled susceptibility shows a narrow EIT resonance with FWHM $\propto (\Gamma_{gr}^0 + \Omega_c^2/\Gamma_{ge}^0)$, with complete suppression of absorption at $\Delta_p = 0$. The real part features a steep normal dispersion coinciding with the transparency window. This reduces greatly the group velocity of the light passing through the EIT medium, since it depends on the dispersion gradient [Harris, 1997; Hau *et al.*, 1999; Fleischhauer *et al.*, 2005]. In this regime the Rydberg population is described by a single Lorentzian peak.

- **Autler-Townes** $(\Omega_c \geq \Gamma_e)$ – (green) in presence of a strong coupling beam we enter the Autler-Townes regime [Autler and Townes, 1955; Cohen-Tannoudji, 1996], characterized by the splitting of the absorption profile into two distinct lines with FWHM separation $\propto \Omega_c$ and by the splitting and suppression of population in the Rydberg state. A detailed discussion of the differences between EIT and the Autler-Townes splitting can be found in [Anisimov *et al.*, 2011].

Figure 3.2 (b) shows the effect of dephasing sources, such as finite laser linewidth (dashed blue) and fourier limited pulse width (dotted blue), on the optical response and the Rydberg state population. An increasing ratio of γ/Ω_c reduces the transparency on EIT resonance, the peak $\mathrm{Im}[\tilde{\chi}]$ off-resonance and the normal dispersion, while the population spectrum is lowered in amplitude and broadened. The transparency reduction can be understood as follows: under laser coupling the atomic system is driven into a dark-state (a superposition of only $|g\rangle$ and $|r\rangle$, decoupled thus from the light field) with a rate Ω_c^2/Γ_{ge}^0. If the decay Γ_{gr}^0 of the atomic coherence is comparable to the driving rate, then there will be an admixture of the intermediate state $|e\rangle$ to the dark state which leads to absorption and, consequently, to a transparency reduction [Pritchard, 2011].

To describe the EIT properties it is convenient to introduce the EIT quality factor $C = \Omega_c^2/\Gamma_{gr}^0\Gamma_{ge}^0$. To have high transparency on resonance $(\Delta_p, \Delta_c = 0)$, we require $C \gg 1$, since the imaginary part of the susceptibility has a minimum equal to

$$\chi_{eit}^0 = \chi_0 \frac{1}{1+C}. \tag{3.15}$$

This is achieved using a strong coupling Rabi frequency Ω_c and by reducing as much as possible the linewidths of the lasers, which motivated the improvement of the

laser stabilization system presented in Ch. 2.4.5 that allowed to decrease χ_{eit}^0 for $\Omega_c = 2\pi \cdot 5\,\text{MHz}$ from $\sim 7\,\%$ to below $0.3\,\%$.

The EIT resonance has a width σ_{eit} (FWHM) which in the weak probe approximation is

$$\sigma_{eit} = \begin{cases} \Gamma_{gr}^0(1+C) & \text{for} \quad \Delta_c = 0, \ \Omega_c < \Gamma_e \\ \Omega_c & \text{for} \quad \Delta_c = 0, \ \Omega_c \geq \Gamma_e \\ \Gamma_{gr}^0(1+C) & \text{for} \quad \Delta_p = 0, \ \forall\,\Omega_c \end{cases} \qquad (3.16)$$

The width scaling with Ω_c differs when scanning the probe or coupling laser detuning.
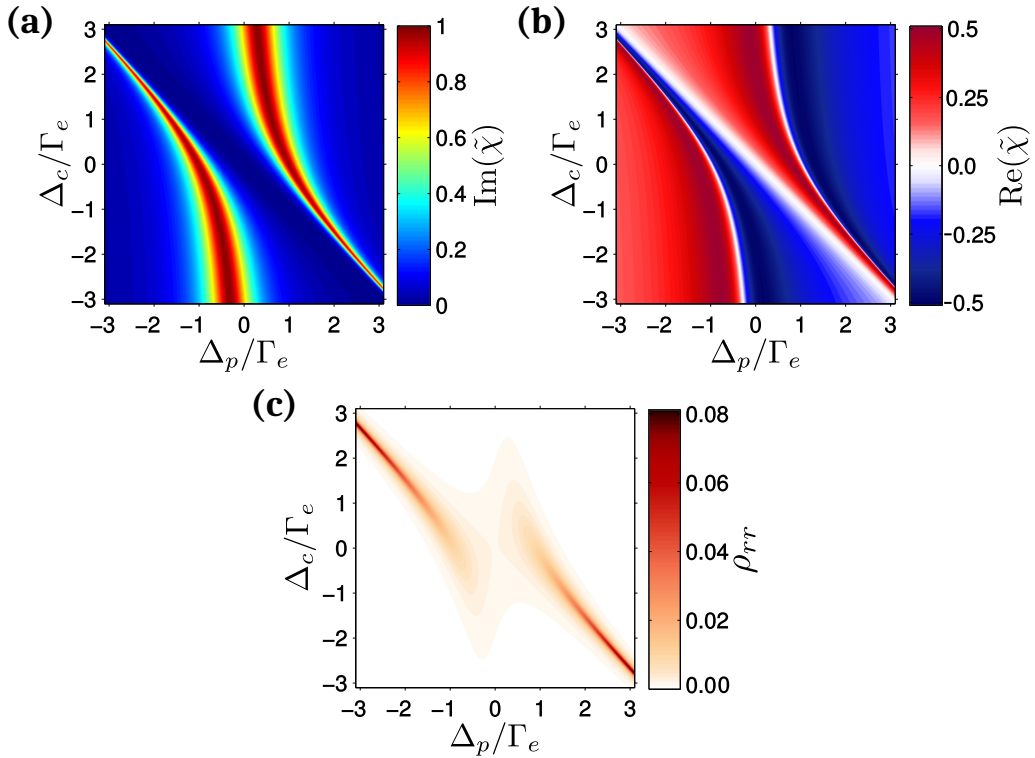
Figure 3.3: Electromagnetically Induced Transparency as a function of the single photon detunings Δ_p and Δ_c. Imaginary **(a)** and real **(b)** parts of the scaled linear optical susceptibility and Rydberg population **(c)**. Both parts of $\tilde{\chi}$ are equal to zero when the two photon resonance condition $\Delta_p + \Delta_c = 0$ is fulfilled and are insensitive to the single photon detunings, instead the width of the induced transparency region shows a strong dependency and asymmetry for $|\Delta_c| > 0$. ρ_{rr} changes from a single Lorentzian profile into an Autler-Townes damped and broadened double peak structure when $\Delta_p, \Delta_c = 0$. Parameters as in Fig. 3.2 (a) with $\Omega_c = 2\,\Gamma_e$.

In the experiments presented in this chapter we vary the probe laser detuning Δ_p, treating it as a known parameter, while staying on resonance with the coupling beam ($\Delta_c = 0$). This choice allows to extract the most information on the medium

under EIT coupling from the measurements of the transmission $T(\Delta_p)$ and integrated Rydberg population $N_r(\Delta_p)$, since for such scan $\text{Im}[\tilde{\chi}](\Delta_p)$ and $\rho_{33}(\Delta_p)$ show clear EIT signatures, as can be seen from Fig. 3.3 (a) and (c). In contrast, in the next two chapters we will want to keep the medium transparent in a wide bandwidth, without affecting the amplitude of the two-level response, so the opposite choice with $\Delta_p = 0$ will be used. It is of interest then to discuss how the imaginary and real parts of the scaled linear optical susceptibility and the Rydberg population depend on the single photon detunings Δ_p and Δ_c, as shown in Fig. 3.3. Both parts of $\tilde{\chi}$ are equal to zero when the two photon resonance condition $\Delta_p + \Delta_c = 0$ is fulfilled and are insensitive to the single photon detunings, instead the width of the induced transparency region shows a strong dependency and asymmetry for $|\Delta_c| > 0$. The Rydberg population follows a similar trend with the two photon detuning, with the spectrum changing from a single Lorentzian profile into an Autler-Townes damped and broadened double peak structure in the vicinity of $\Delta_p, \Delta_c = 0$.

3.2   Density matrix reconstruction

In the previous section we have introduced a semi-classical model for the density matrix that we expect to describe our system of non-interacting three-level atoms coupled under Rydberg EIT. Using the weak probe approximation we have found analytic solutions for all the density matrix elements and this prior knowledge allows to reduce the number of elements that have to be measured. By inspecting Eqs. (3.7, 3.8) we learn that the two observables that we can experimentally access, the Rydberg state population and the spatially resolved transmission, form a complete set of measurements because they provide information on ρ_{rr} and ρ_{ge}, which depend in turn on all unknown parameters that govern the OBEs ($\Omega_p, \Omega_c, \Delta_p, \Delta_c, \Gamma_e, \Gamma_r, \gamma_p, \gamma_c$). A combined measurement of these two observables, as a function of the probe laser detuning Δ_p, and a joint data analysis allow to estimate these quantities and reconstruct the full density matrix of the system.

3.2.1   Reconstruction strategy

In our experiments, the coupling beam doesn't cover the whole cloud and the measured transmission in the regions where the coupling Rabi frequency vanishes ($\Omega_c = 0$) provides information on the susceptibility of the two-level system composed by the states $|g\rangle$ and $|e\rangle$. The study of $\text{Im}[\chi_{2lvl}(\Delta_p)]$ allows to extract $\Gamma_e + \gamma_p$ and the optical density for the probe transition $\sigma_0 n_{2d}$. The latter is used as a fixed

parameter to extract $\text{Im}[\tilde{\chi}_{3lvl}(\Delta_p)]$ from the transmission measured for the three-level system where the coupling beam is present. From the Rydberg population spectrum we determine Δ_c and $\Gamma_r + \gamma_c$. Ω_p can be calibrated on the two-level optical response [Reinaudi et $al.$, 2007], so the only remaining quantity is Ω_c which is extracted from $\text{Im}[\tilde{\chi}]$ using a spatially resolved approach and Eq. (3.11).

Before performing the experiments we can further simplify our problem by reducing the number of parameters to be estimated, thanks to few considerations. The decay of the long-lived Rydberg state is estimated to contribute with a rate on the order of few kHz which is three orders of magnitude smaller than the typical Rabi frequencies we use, so it can be safely neglected. The dephasing on the probing transition caused by laser linewidth is negligible $\gamma_p \ll \Gamma_e$, while for the Rydberg state we consider a dephasing term γ_{deph} to take into account the experimentally observed properties.

3.2.2 Combined measurement of transmission and Rydberg population

The experiment is performed with a three-level ladder scheme coupling to the $|r\rangle \equiv \left|42S_{1/2}, m_J = 1/2\right\rangle$ Rydberg state (see Ch. 2.5.1). Approximately $3 \cdot 10^6$ ground state atoms are prepared in the "reservoir" ODT and an expansion time of $2\,\text{ms}$ is used, leading to an ellipsoidal Gaussian shaped cloud with $e^{-1/2}$ radii of $\sigma_{\text{radial}} = 90 \pm 7\,\mu\text{m}$, $\sigma_{\text{axial}} = 380 \pm 13\,\mu\text{m}$ and a peak atomic density of $n_0 = 7 \cdot 10^9\,\text{cm}^{-3}$. The expected peak Rydberg density is $\rho_{rr}n_0 \leq 2 \cdot 10^9\,\text{cm}^{-3}$, corresponding to a Wigner Seitz radius of $4.9\,\mu\text{m}$. The anticipated blockade radius for the $\left|42S_{1/2}\right\rangle$ state is $\approx 2.3\,\mu\text{m}$, a factor of two smaller than the mean inter-particle distance, therefore the effects of Rydberg-Rydberg interactions can be safely neglected [Pritchard et $al.$, 2010; Schempp et $al.$, 2010; Sevinçli et $al.$, 2011a; Ates et $al.$, 2011].

A homogeneous magnetic field of $3\,\text{G}$ is applied along the probe beam direction to define a quantization axis. We use a probe Rabi frequency $\Omega_p/2\pi = (1.03 \pm 0.05)\,\text{MHz}$ which we independently measure using the saturated absorption imaging method [Reinaudi et $al.$, 2007]. For this experiment the coupling laser is focused into the center of the cloud with a waist of approximately $15\,\mu\text{m}$ and an intensity of approximately $0.9\,\text{kW cm}^{-2}$.

To measure the optical response we record 93 absorption images (see Ch. 2.4.4) for different probe detunings $\Delta_p/2\pi$ ranging from $-8.1\,\text{MHz}$ to $8.1\,\text{MHz}$. We first exclude the pixels illuminated by the coupling beam and perform a fit of each image to a 2D Gaussian distribution reflecting the expected atomic distribution. Interpolating

the Gaussian fit into the excluded area allows us to infer the two-level absorption and the local atomic 2D density n_{2d} of the atom cloud at the position of the coupling beam. Using this information and equation (3.14) we are then able to extract from the measured transmission T the scaled optical susceptibility $\tilde{\chi}(\Delta_p)$ for each pixel comprising the image of the cloud. In parallel, at the end of the laser pulse, we measure the Rydberg-state population. Since the number of detected ions is large (> 100), the signal is integrated and calibrated as described in Ch. 2.4.4, in order to quantify the number of detected ions.
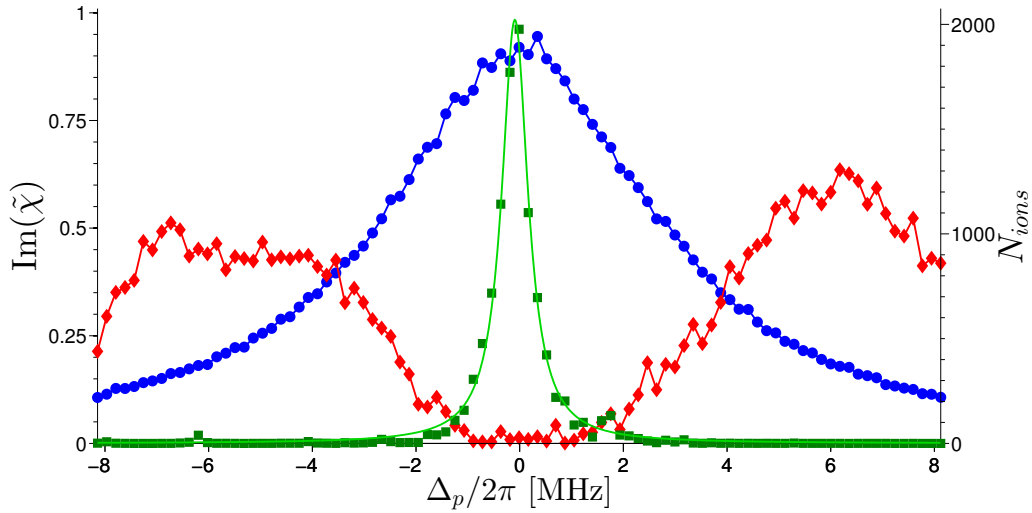
Figure 3.4: Scaled optical susceptibility and population spectrum as a function of the probe laser detuning. The three measured curves show: three-level optical response averaged over the center of the coupling laser beam (red diamonds), two-level optical response (blue circles) and integrated Rydberg population (green squares - corresponding to the right axis). The green solid line represents the Rydberg population spectrum estimated by numerically solving the OBEs. The slight asymmetry of the absorption spectrum is most likely caused by residual lensing effects due to the non-negligible optical thickness of the sample [Han *et al.*, 2015].

Figure 3.4 shows the imaginary part of the scaled optical susceptibility $\propto \mathrm{Im}[\rho_{ge}]$ measured at the center of the coupling laser beam (red diamonds). This is compared with the two-level susceptibility (blue circles) and the Rydberg population spectrum (green squares) measured in the same experimental sequence. On two-photon resonance, and for the parameters given above, we observe an almost complete suppression of absorption ($> 99\%$) as compared to the two-level absorption. While the absorption spectrum shows the characteristic double peak shape reflecting the Autler-Townes doublet, the corresponding Rydberg population spectrum is much

narrower and shows no evidence for the double peak structure that we would have expected to observe according to the discussion in Ch. 3.1.4. In the following we will exploit the spatially resolved detection of the transparency feature to elucidate the connection between the transparency resonance and the Rydberg population resonance.

3.2.3 Spatially resolved electromagnetically-induced-transparency
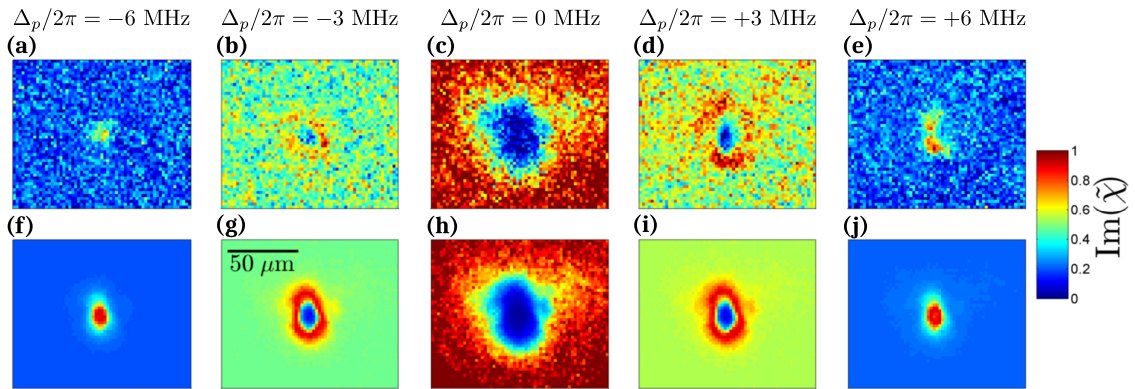
Figure 3.5: Spatially resolved scaled optical susceptibility $\mathrm{Im}[\tilde{\chi}]$ **near the center of the cloud as a function of the probe laser detuning.** **(a-e)** Measured cloud response for various probe laser detunings (respectively $-6, -3, 0, +3, +6\,\mathrm{MHz}$) under the same conditions as Fig. 3.4. The region illuminated by the coupling laser is aligned at the center of the region of interest. **(f-j)** Reconstructed spatial response from the OBE steady state solution (from Eqs. (3.8, 3.12)), combined with the fitted coupling Rabi frequencies beam profile using the procedure described in the text. The horizontal bar in **(g)** indicates the spatial scale of $50\,\mu\mathrm{m}$.

Figures 3.5 (a-e) show a selection of extracted scaled optical susceptibilities for different probe detunings, showing the transparency spot at the center of each frame. We find that as a function of detuning the shape and size of the transparency spot varies and exhibits ring-like structures, indicating that the spatial shape of the coupling laser beam plays an important role. To account for this we analyze the optical susceptibility on a pixel-by-pixel basis and construct a series of absorption spectra, one for each position of the cloud. These spectra can then be fit to Eqs. (3.8, 3.12) using the procedure outlined in the following paragraphs which allows for the extraction of the key system parameters in a spatially resolved manner.

A typical dataset involves several thousand pixels which would be prohibitively slow to fit one-by-one. Furthermore the signal-to-noise ratio for a single pixel

spectrum is typically quite low. Therefore, we use a two-step fitting algorithm which gives reliable results by minimizing the number of free fit parameters. In the first step we use the two-level peak absorption inferred from the interpolated Gaussian fit to calibrate the two-level optical response including the width of the probe resonance via a fit to a Lorentzian lineshape. For the data shown in Fig. 3.5 the resonance width is found to be (6.21 ± 0.03) MHz which is in good agreement with the power broadened intermediate state natural decay rate $\Gamma_e/2\pi \cdot \sqrt{1 + 2(\Omega_p/\Gamma_e)^2} = 6.23$ MHz, confirming that the role of dephasing (e.g. due to laser fluctuations) on this transition is negligible. Analogously, we fit a Lorentzian lineshape to the measured Rydberg population spectrum to determine the coupling laser detuning $\Delta_c/2\pi = (0.10 \pm 0.01)$ MHz and the width of the resonance $W/2\pi = (0.63 \pm 0.01)$ MHz. This width can be attributed to several effects, but for the coupling Rabi frequency determination we assume it originates entirely from dephasing of the Rydberg state ($\gamma_{\mathrm{deph}} = W$).
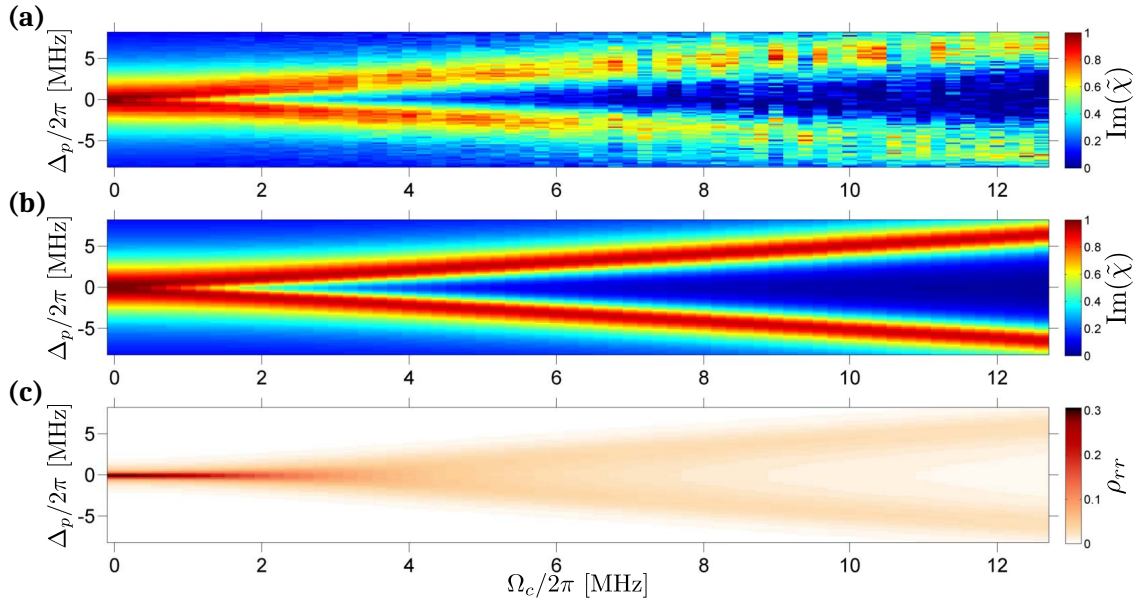
Figure 3.6: **(a)** Measured three-level absorption spectra (under same conditions as Fig. 3.4) for each pixel, sorted according to the fitted coupling Rabi frequencies with 0.2 MHz binning. From left to right shows the transition from the EIT regime towards the Autler-Townes regime. **(b)** Fitted absorption spectra using Eqs. (3.8, 3.12) as described in the text. **(c)** Corresponding Rydberg population spectrum calculated analytically using Eq. (3.7).

After the first step all global parameters are fixed and the only remaining free parameter is the value of Ω_c which differs for each pixel. Using the fitted local two-level resonant optical susceptibility and equations (3.12, 3.14) we extract the
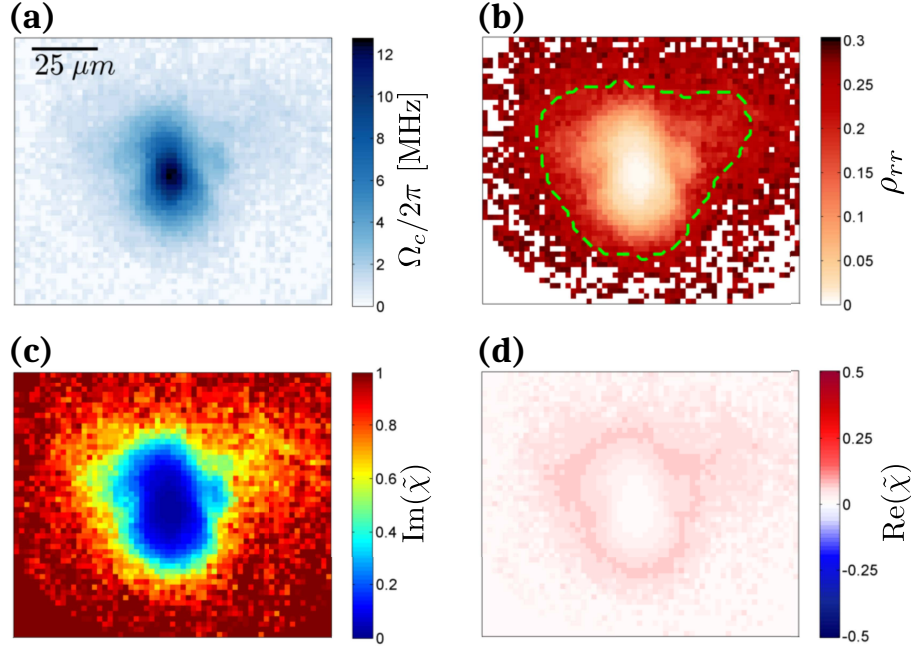
scaled optical susceptibility $\tilde{\chi}(\Delta_p)$. Fig. 3.6 (a) shows the measured absorption spectra with each column corresponding to a single pixel in the vicinity of the transparency spot. In order to estimate $\Omega_c(x, y)$ we pre-calculate a set of model absorption spectra corresponding to different values of $\Omega_c/2\pi$ between 0 and 15 MHz in steps of 0.05 MHz (Fig. 3.6 (b)). Minimizing the least-squares difference between each single-pixel spectrum and the model spectra gives an estimate of the local coupling Rabi frequency which best matches the data at each pixel location. The result yields extracted values for $\Omega_c/2\pi$ in the range between 0 MHz and 12.8 MHz. Compared to the analytic solutions of the OBEs, we observe an unexplained slight broadening and reduction of amplitude of the Autler-Townes peaks for large Ω_c. However we find that this discrepancy does not significantly influence the coupling Rabi frequency determination.

3.2.4 Reconstructed spatial distributions of ρ_{rr} and $\tilde{\chi}$

Figure 3.7 (a) shows the spatial distribution of coupling beam Rabi frequencies as extracted from the fits to the single-pixel optical spectra. The observed shape closely reflects the elliptical shape of the coupling beam which we independently confirm using a beam profiler external to the vacuum system. The measured beam profile is close to a Gaussian with a peak Rabi frequency of $\Omega_c/2\pi = (12.8 \pm 0.5)$ MHz. This is close to the theoretical expectation of $\Omega_c/2\pi = 10.7$ MHz taking into account the power of the coupling laser, the dipole matrix element for the $\left|5P_{3/2}\right\rangle$ to $\left|42S_{1/2}\right\rangle$ transition, and the spatial extent of the excitation region. The fitted one-sigma radii in the semi-minor and semi-major axes are evaluated to have a size of 11.8 μm and 15.4 μm respectively.

Using the spatially-resolved distribution of Rabi frequencies (Fig. 3.7 (a)) and the global parameters constrained by the two-level absorption and the total Rydberg population spectrum, we can reconstruct the full density matrix of the system at each position using the analytical solution derived in equations (3.7) and (3.8). As practical examples we show the spatial distribution of the real and imaginary parts of the scaled optical susceptibility $\tilde{\chi} \propto \rho_{ge}$ and the Rydberg population ρ_{rr} (Fig. 3.7 (b-d)) which demonstrates how both optical and atomic spatially-dependent properties can be reconstructed.

Using the results of this reconstruction procedure we also show the Rydberg population as a function of Ω_c and Δ_p in Fig. 3.6 (c). For large coupling strengths ($\Omega_c > \Gamma_e$) the Rydberg population resembles the Autler-Townes doublet resonance structure with two maxima at $\Delta_p = \pm\Omega_c/2$, while in the limit of weak coupling

Figure 3.7: Reconstructed spatial distribution of **(a)** the coupling Rabi frequency $\Omega_c(x, y)$, **(b)** the Rydberg population distribution and **(c-d)** the imaginary and real parts of the scaled optical susceptibility, under the same conditions as the previous figures. For (b-d) we use analytic solutions of the OBE (Eqs. (3.7-3.8)) for $\Delta_p=0$. The green dashed line in (b) marks the limit of validity of the analytic reconstruction of ρ_{rr} using Eq. (3.7). Outside of the coupling beam region $\text{Im}[\tilde{\chi}] \to 1$ (consistent with the two-level response), while $\text{Re}[\tilde{\chi}]$ is approximately zero over the region of interest. The slight increase of $\text{Re}[\tilde{\chi}]$ towards the edges of the coupling beam is due to the relatively steep dispersion for $\Omega_c \ll \Gamma_e$ and the small detuning $\Delta_c/2\pi = 0.1\,\text{MHz}$.

$\Omega_c \ll \Gamma_e$ the population is concentrated in a single spectrally narrow resonance with maximum at $\Delta_p = -\Delta_c \approx 0$. The peak population is found for small Ω_c which can be understood considering that on two photon resonance $\rho_{rr} \approx \Omega_p^2/(\Omega_p^2 + \Omega_c^2)$ (neglecting dephasing). This is also visible in Fig. 3.7 (b) which shows the maximum Rydberg population outside of the coupling beam region. This spatial distribution also explains the spectrally narrow resonance in Fig. 3.4 as a consequence of spatially averaging over the entire excitation volume in the field ionization detection. Here we note that at the edges, where ρ_{rr} is largest, the validity of the analytic solution for ρ_{rr} provided by equations (3.7, 3.8) is compromised since the condition $\Omega_p \ll \Omega_c$ is not fulfilled. By comparing with numerical solutions of the time-dependent OBEs which are not restricted to the weak probe limit we find that the discrepancy between the approximate and the full numerical solutions remains smaller than 25% for coupling Rabi frequencies $\Omega_c \geq \Omega_p$. This criteria defines an approximate range of validity of

the analytic reconstruction, marked by the region inside the green dashed line in Fig. 3.7 (b). Furthermore the numerical simulation allows to quantitatively reproduce the measured population spectrum (solid green line in Fig. 3.4) by spatially integrating for each detuning the reconstructed $\rho_{rr}(x, y)$. To achieve the best agreement we had to adapt $\gamma_{\text{deph}}/2\pi$ to the value $(0.20 \pm 0.02)\,\text{MHz}$. The extra broadening seen in Fig. 3.4 can be attributed to power broadening of the $|g\rangle \leftrightarrow |e\rangle$ transition and spatial averaging over the excitation volume. This dephasing rate is still much larger than the sum of the coupling and probe lasers linewidths, therefore we conclude that it originates from effects associated with atomic motion or residual Rydberg-Rydberg interactions [Pritchard *et al.*, 2010; Gärttner and Evers, 2013; Zhang *et al.*, 2014]. In order to approximately reproduce the measured spectrum using the analytic solution of ρ_{rr} (which neglects power broadening), we had to introduce a larger effective dephasing rate $\gamma_{\text{eff}}/2\pi = 0.37\,\text{MHz}$ and a cut-off coupling Rabi frequency $\Omega_c^{cut} = 0.35\,\Omega_p$, below which we assume the Rydberg population to be zero.

The above considerations only weakly influence the determination of the coupling Rabi frequency Ω_c since dephasing has a minimal effect on the Autler-Townes splitting. We also verify that it has a small effect on the reconstructed components of the density matrix and optical susceptibility in the considered range. The reconstructed imaginary and real parts of the scaled optical susceptibility $\tilde{\chi}$ using the analytical formulas in Sec. 3.1 are shown for $\Delta_p = 0$ (for $\gamma_{\text{deph}}/2\pi = 0.63\,\text{MHz}$) in Fig. 3.7 (c-d). As expected, $\text{Im}[\tilde{\chi}]$ shows almost full transparency $\text{Im}[\tilde{\chi}] \approx 0$ at the center of the coupling beam, whereas it approaches the two-level response outside of the coupling beam region. The reconstructed $\text{Im}[\tilde{\chi}]$ is also plotted for different detunings in figures 3.5 (f-j), showing good qualitative agreement with the experimental measurements. However we note a slight asymmetry in the detuning dependence of the experimental data which could be attributed to lensing effects which are not accounted for in our simple model. In contrast, $\text{Re}[\tilde{\chi}]$, which is responsible for light dispersion, is nearly zero across the whole spatial profile for $\Delta_p = 0$. The small observed deviation at the edges of the coupling beam region is due to the relatively steep dispersion for $\Omega_c \ll \Gamma_e$, combined with the slight detuning of the coupling beam $\Delta_c/2\pi = 0.1\,\text{MHz}$. For larger detunings $\Delta_p \approx \Omega_c/2$ the amplitude of $\text{Re}[\tilde{\chi}]$ can increase significantly, which could be responsible for the lensing effects seen in Figs. 3.5 (a-e). Analogous effects have been recently studied in Ref. [Han *et al.*, 2015].

3.3   Tool for new atom-light studies

By combining field ionization detection with optical spectroscopy under Rydberg EIT conditions, we have reconstructed the full single-atom density matrix of the system, thereby obtaining nearly full information about the coupled atom-light ensemble. Spatially resolving the absorption spectra and analyzing hundreds of camera pixels in parallel gives information on hundreds of mesoscopic Rydberg ensembles, each with different densities or laser parameters. The extracted spatially-dependent profile of Rabi coupling frequencies explains the observed spectral shape and width of the Rydberg population resonance as a consequence of spatially averaging over the entire excitation volume in the field ionization detection.

The combination of optical and population-based probing of coherently driven three-level atomic systems as realised in these experiments offers new avenues for studying multilevel interference effects such as electromagnetically-induced-transparency, coherent population trapping and stimulated-Raman adiabatic passage with simultaneous access to all degrees of freedom. Furthermore, the reconstructed spatially-dependent Rabi frequency, Rydberg population and optical susceptibility serve as valuable input for modeling light propagation in interacting Rydberg ensembles [Ates *et al.*, 2011; Gorshkov *et al.*, 2013; Gärttner *et al.*, 2014b; Bienias *et al.*, 2014] and realizing new non-destructive imaging techniques for strongly-interacting particles, with single atom sensitivity [Günter *et al.*, 2012; Günter *et al.*, 2013; Gavryusev *et al.*, 2016a; Olmos *et al.*, 2011]. Ultimately, these efforts, complemented by the technique described here, will enable new studies of the correlations between atoms and photons induced by Rydberg-Rydberg interactions, relevant for example to current and future studies of nonlinear light propagation in strongly interacting media [Peyronel *et al.*, 2012; Sevinçli *et al.*, 2011b; Stanojevic *et al.*, 2013; Tresp *et al.*, 2015; Moos *et al.*, 2015] and Rydberg dressed quantum fluids [Helmrich *et al.*, 2016; Gaul *et al.*, 2016; DeSalvo *et al.*, 2016] which exploit strong-atom light coupling in three-level atomic systems.

Chapter 4

Interaction Enhanced Imaging of Rydberg atoms

This chapter is partially based on the following publications, from which parts of the text are reproduced verbatim:

Interaction-Enhanced Imaging of Rydberg P states
V. Gavryusev, M. Ferreira-Cao, A. Kekić, G. Zürn and A. Signoles
arXiv:1602.04143 (2016), accepted for publication in Eur. Phys. J. ST

Controlled coherent and incoherent motion of dipolar interacting Rydberg excitations
H. Schempp, G. Günter, V. Gavryusev, M. Ferreira-Cao, S. Whitlock, M. Weidemüller
in preparation

Observing the dynamics of dipole-mediated energy transport by interaction enhanced imaging
G. Günter, H. Schempp, M. Robert-de-Saint-Vincent, V. Gavryusev, S. Helmrich, C. S. Hofmann, S. Whitlock, M. Weidemüller
Science **342**, 953-956 (2013)

Ultracold Rydberg atoms with their strong and long-range interactions [Saffman *et al.*, 2010] offer many possibilities to study equilibrium and non-equilibrium properties of complex many-body systems [Hazzard *et al.*, 2014] and to realize strongly correlated atom-light interfaces [Pritchard *et al.*, 2013; Firstenberg *et al.*, 2016]. Over the last few years we have witnessed an explosion of interest in these sys-

tems for studying diverse phenomena including the formation of spatially correlated crystalline-like structures [Pohl *et al.*, 2010; Schauß *et al.*, 2012; Levi *et al.*, 2015] or ultracold plasmas [Vanhaecke *et al.*, 2005; Vrinceanu *et al.*, 2009; Pohl *et al.*, 2011], the emergence of extreme nonlinear optical effects [Pritchard *et al.*, 2010; Peyronel *et al.*, 2012; Firstenberg *et al.*, 2013; Tiarks *et al.*, 2014] and the transport of energy through Rydberg aggregates [Schönleber *et al.*, 2015; Schempp *et al.*, 2015; Fahey *et al.*, 2015]. However, until recently, optical techniques for state-resolved detection of Rydberg atoms with high spatial and temporal resolution have been missing. Here we present a detailed study of a technique called Interaction Enhanced Imaging (IEI) [Günter *et al.*, 2012], that has been successfully used to optically image Rydberg S-states and observe dipole-mediated energy transport under the influence of a controlled environment [Günter *et al.*, 2013; Günter, 2014; Schempp, 2014]. Rydberg P-states embedded in a gas of atoms coupled to Rydberg S-states are even better candidates for future time resolved studies of coherent and incoherent transport of Rydberg excitations, due to their direct strong dipolar exchange interactions [Westermann, S. *et al.*, 2006; Schönleber *et al.*, 2015; Schempp *et al.*, 2015]. As a first step towards this goal, we apply IEI to demonstrate the state resolved detection of Rydberg P-states with high spatial resolution. To understand the main aspects of the imaging technique and increase its sensitivity, we develop a quantitative hard-sphere model of the coupled atom-light system [Faraoni, 2014], finding good agreement with experimental data.

This chapter is structured as follows: first in Ch. 4.1 we give an overview of the detection method and compare it to state-of-the-art cold Rydberg gas experiments. Then in Ch. 4.2 we briefly describe the observed transport dynamics of Rydberg S-states. In Ch. 4.3 we present an intuitive model that captures the main physical principles of the imaging technique and provides a quantitative estimation of the optical response of the coupled atom-light system. Finally, the first results on the optical detection of Rydberg P-states using IEI are presented in section 4.5.

4.1   Imaging methods for Rydberg atoms

4.1.1   State-of-the-art of Rydberg atom imaging

Direct optical detection of Rydberg atoms with common techniques based on the scattering of light, like absorption or fluorescence imaging, is hardly applicable because the light scattering rate for the transition from the ground to a Rydberg state is much smaller than the one between the ground and the first excited state

(used to probe the ground state atoms), due to the longer lifetime of the Rydberg state (for alkali atoms $\approx 10\,\mu s - 1\,ms$ and $\approx 26 - 30\,ns$, respectively). Furthermore there are no closed, cycling transitions starting from or going to a Rydberg state, which would decrease even further the number of photons that can be collected on a detector before the Rydberg state decays into a dark state [Gibble *et al.*, 1992; Mhaskar *et al.*, 2006; Wang *et al.*, 2010]. Due to these problems, alternative methods had to be developed.

So far there are only a few techniques suited to spatially image Rydberg atoms. An early example is based on field ion microscopy demonstrated by Schwarzkopf *et al.* [Schwarzkopf *et al.*, 2011]. Here Rydberg atoms excited from a magneto-optical trap are ionized by applying a large voltage onto a needle with a tiny, rounded tip, which creates a strong inhomogeneous electric field. Following the divergent field lines, the resulting ions are guided towards a fluorescent multichannel plate (MCP). Each ion is revealed by a bright spot of light on a charge-coupled-device (CCD) camera, allowing for a resolution of the order of a few µm. Nevertheless, the detection efficiency is limited to $\leq 50\%$ by the quantum efficiency of the MCP. Using this technique, spatial correlations through the pair correlation function and van der Waals interactions between Rydberg atoms have been measured [Schwarzkopf *et al.*, 2013; Thaicharoen *et al.*, 2015; Weber *et al.*, 2015; Manthey *et al.*, 2015].

Spatially resolved detection of Rydberg atoms trapped in an optical lattice has also been achieved using an optical approach [Schauß *et al.*, 2012; Schauß *et al.*, 2015; Zeiher *et al.*, 2015]. Rydberg atoms are de-excited via stimulated emission by laser light towards a short-lifetime intermediate state and are captured in an optical lattice. Their position is then revealed by high-resolution fluorescence imaging using a lower transition. With this technique, strong spatial correlations have been observed with nearly single-site resolution and a detection efficiency of $\sim 75\%$. A similar technique allows to detect Rydberg atoms trapped in small arrays with nearly a 97% efficiency [Labuhn *et al.*, 2016]. Although the detection sensitivity is very good, this technique is best suited to two-dimensional lattices or optical tweezers and the detection method destroys the Rydberg atoms.

Other methods have been introduced for alkaline-earth atomic species, taking advantage of the state-dependent optical transition of the core electron to probe the presence of Rydberg atoms. By shining laser light resonant to a transition of the core electron in Strontium with one electron excited in a Rydberg state, the fluorescence light can be measured, revealing the presence of Rydberg atoms [McQuillen *et al.*, 2013]. The technique provides very good temporal resolution of $\sim 10\,ns$, but low spatial resolution ($\sim 200\,\mu m$) and is most sensitive to high-ℓ states. For low-ℓ states,

a more sophisticated technique allowing for larger spatial resolution consists in exciting the core electron to an intermediate state, which has a large probability of leading to autoionization of the Rydberg state. Using a focused laser beam, one can then locally ionize the atoms and record the Rydberg distribution with a spatial resolution of $10\,\mu m$ [Lochead *et al.*, 2013].

4.1.2   Review of Interaction Enhanced Imaging (IEI)
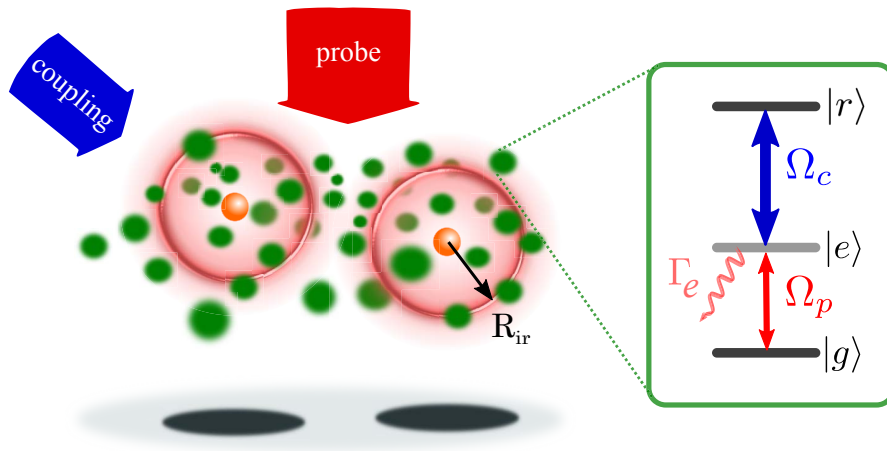
Figure 4.1: Scheme for interaction-enhanced absorption imaging of individual impurities (orange spheres) within a dense gas of probe atoms (green spheres). Two coherent resonant light fields called *probe* and *coupling*, with Rabi frequencies Ω_p and Ω_c, couple the ground state $|g\rangle$ of the probe atoms to a Rydberg state $|r\rangle$, inducing the transparency condition for the probe light field for atoms far from any impurity. However, the impurities and the surrounding atoms interact strongly within a critical distance R_{ir}, leading to an energy shift of the Rydberg state $|r\rangle$ which locally breaks the EIT condition. Consequently the probe atoms become absorptive in these regions. The presence of an impurity is revealed by a shadow on the camera which collects the probe light after its propagation through the atomic cloud.

To study dipole-mediated transport dynamics, we recently implemented a new type of detection method which combines single particle sensitivity and high spatial and temporal resolution. We experimentally apply an absorption technique to detect Rydberg atoms, so-called impurities, embedded in an atomic gas, with a spatial resolution below the Rydberg blockade radius. This IEI technique, based on the original proposal of our group [Günter *et al.*, 2012] and also related to a similar proposal by Olmos *et al.* [Olmos *et al.*, 2011], consists of measuring the absorption of a probe light propagating through the gas, which acts as a contrast medium, in such

a way that the absorption is modified by the presence of the Rydberg impurities. The method has been demonstrated in our experiment with rubidium Rydberg atoms, but it can be potentially applied for any particle that exhibits strong coupling to a medium, like ions via Coulomb interactions and polar molecules via dipole-dipole interactions. The key to IEI is to use the background atoms to reveal the presence of impurities. To do so, the gas is coupled under electromagnetically-induced transparency (EIT) conditions to an auxiliary "probe" Rydberg state by a weak probe field and a strong coupling field, being therefore transparent to the probe light [Fleischhauer *et al.*, 2005; Pritchard *et al.*, 2011; Sevinçli *et al.*, 2011a] (see Ch. 3.1.4). However, atoms close to an impurity experience dipole-dipole interactions that energetically shift this probe Rydberg state and break the EIT [Hofmann *et al.*, 2013; Gärttner *et al.*, 2014b]. This effect thus casts a shadow in the spatial absorption profile that allows to map the position of the impurities (Fig. 4.1).

This method exhibits numerous advantages that are of fundamental importance for the investigation of the dynamics of Rydberg excitations in ultracold gases. Since the detection signal is generated from background atoms surrounding the Rydberg impurities, the signal can be strongly enhanced, allowing to detect the impurity with high efficiency. Those background atoms act like an amplifier with an enhancement factor equal to the number of additional absorbers per impurity

$$A^{\mathrm{IEI}} = \frac{N_{add.abs}}{N_i}\,. \tag{4.1}$$

In the blockade picture, one can define a critical distance R_{ir} from an impurity below which probe atoms are considered as absorbers. The amplification factor, defined now as the number of probe atoms within the blockade sphere, can be tuned to strongly enhance absorption around a single impurity. Therefore, the detection is potentially single-impurity sensitive, as soon as the detected signal is larger than the imaging noise. This topic will be investigated in detail in Ch. 5. Furthermore, one experimental snapshot might be enough to reveal the presence of the impurities with a good spatial resolution. Finally, the detection keeps the number of impurities constant and should allow for multiple measurements similarly to quantum non-destructive measurements [Grangier *et al.*, 1998; Guerlin *et al.*, 2007].

### 4.1.3 Connection to similar experiments

The IEI technique uses the optical absorption spectrum to map out atomic properties. From a complementary point of view, it is possible to use Rydberg gases

to modify an optical field. Many studies have been recently done to investigate how dipole-dipole interactions affect propagation of light, for instance leading to non-linear absorption [Ates *et al.*, 2011; Sevinçli *et al.*, 2011a], dephasing of Rydberg polaritons [Tresp *et al.*, 2015] and photon-photon interactions [Gorshkov *et al.*, 2011; Peyronel *et al.*, 2012]. IEI differs from these experiments because it exploits strong inter-state interactions between the Rydberg impurities and Rydberg polaritons to imprint information on the spatial distribution directly onto the light field.

In Rydberg gases coupled under EIT, the strong change of optical susceptibility due to the presence of impurities opens interesting perspectives to engineer control on the quantum state of optical photons. Recent developments towards a single-photon optical transistor have been done, where a single "control" photon is used to substantially change an optical signal [Baur *et al.*, 2014; Tiarks *et al.*, 2014; Gorniaczyk *et al.*, 2014; Gorniaczyk *et al.*, 2016]. In practice, a resonant light signal propagates through a gas of Rubidium atoms under EIT condition, where previously a single photon could be stored in the form of a Rydberg polariton [Fleischhauer and Lukin, 2000; Hofmann *et al.*, 2013; Maxwell *et al.*, 2013]. As in IEI, the transparency of the gas depends on the state ($|0\rangle$ or $|1\rangle$) of the control photon. In this way, the storage of a single control photon affects the propagation of many other photons, constituting a first step in the realization of a photon transistor. Although the purpose is different, these experiments exhibit strong similarities with IEI: the absorption of a signal (resp. probe) light is strongly enhanced by the presence of a Rydberg polariton (resp. impurity) in an EIT medium. The efficiency of the transistor will then be measured by a gain, characterizing the number of signal photons affected by the presence of a polariton. In IEI we define an amplification factor which represents the number of atoms affected by the presence of an impurity. Both can be enhanced by increasing the interaction strength, for instance by tuning two S states into a Förster resonance [Tiarks *et al.*, 2014; Gorniaczyk *et al.*, 2016].

4.1.4 First experimental realization of IEI

We successfully implemented Interaction Enhanced Imaging to measure the spatial distribution of Rydberg impurities in a gas of Rubidium [Günter *et al.*, 2013]. The atoms were initially prepared in the ground state $|g\rangle$ in the "reservoir" ODT at a temperature of few µK. From $|g\rangle$ they were resonantly coupled to the probe $|r\rangle = |37S_{1/2}\rangle$ Rydberg state, inducing an EIT condition on the probing transition (see Chs. 2.5.1 and 3.1.4). The blue coupling laser beam was focused in a smaller region, considered as the region of interest (Fig. 4.2 (c)). Therefore, atoms in this
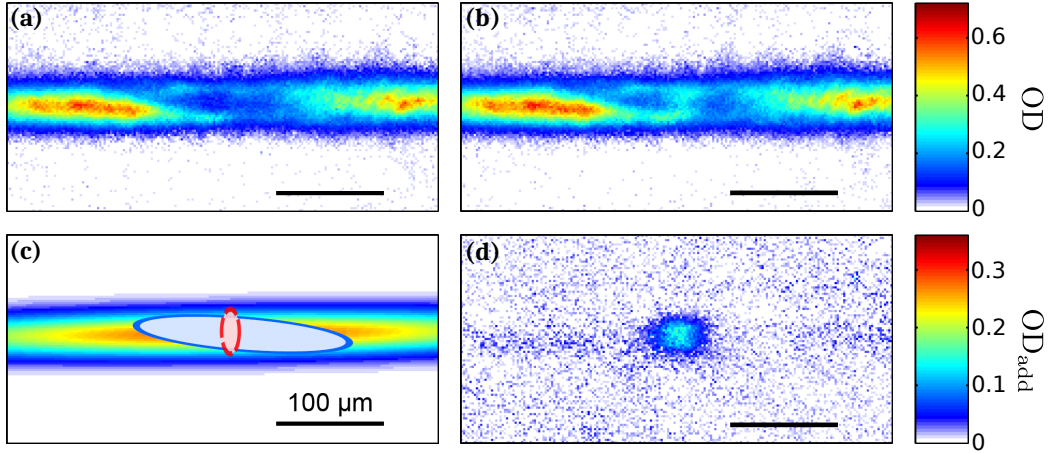
Figure 4.2: Absorption images acquired during an interaction-enhanced imaging experiment. (a) In a large region in the center of the cloud, atoms are illuminated by a strong coupling beam with $\Omega_c \sim 2\pi \cdot 9\,\mathrm{MHz}$, which renders them transparent to the probe light. **(b)** A second absorption image is acquired with Rydberg impurities pre-excited in the center of the cloud. They locally break the EIT condition, rendering the atoms absorptive again. **(c)** Sketch of the atomic cloud and of the positions of the EIT-coupling (blue) and excitation (red) beams. The ellipses indicate the regions corresponding to $1.5 \cdot \sigma$ of the intensity profiles. **(d)** The difference in absorption between (a) and (b) reveals the additional absorbers and contains information about the number and the spatial distribution of the Rydberg impurities. The images are averaged over 150 repetitions, with an exposure time of $5\,\mathrm{\mu s}$. For this data, we estimated a number of ~ 300 impurities. Adapted from [Günter, 2014].

region were rendered transparent to the probe light (Fig. 4.2 (a)). In a second experimental repetition, impurities in the state $|i\rangle = \left|50S_{1/2}\right\rangle$ were first excited in the very center of the trap by means of a two-photon off-resonant transition (with $\Delta_p = -2\pi \times 65\,\mathrm{MHz}$, see Chs. 2.5.1), then the EIT coupling was turned on. The transparency contrast in this region drops because of the presence of these impurities (Fig. 4.2 (b)) which break the EIT condition. A typical pulse sequence for these experiments is presented in Ch. 4.4. The final signal is obtained by calculating the difference between the two transmission images, extracting the additional absorption induced by the impurities (Fig. 4.2 (d)). This experiment illustrates how IEI allows to map the distribution of Rydberg impurities embedded in an atomic gas.

4.2 Imaging transport phenomena with Rydberg S state atoms

After the first proof-of-principle experiments demonstrated the capability of IEI to image $|nS\rangle$ Rydberg states, this technique has been applied to investigate a fascinating effect induced by dipole-dipole interactions [Günter *et al.*, 2013]. As introduced in Ch. 2.2.2, resonant dipole-dipole interactions allow two atoms to swap their quantum states, potentially giving rise to a diffusion process, which can be interpreted as an energy transport. Dipolar state-exchange processes have been observed before, also with cold Rydberg gases [Mourachko *et al.*, 1998; Anderson *et al.*, 1998; Anderson *et al.*, 2002; Westermann, S. *et al.*, 2006; van Ditzhuijzen *et al.*, 2008; Nipper *et al.*, 2012a]. However, using IEI, we have been able for the first time to observe the dynamics of this process in a spatially resolved way. Here I will give a brief overview of the outcomes, while a more detailed discussion of these transport experiments can be found in [Günter *et al.*, 2013; Günter, 2014; Schempp, 2014].

4.2.1 Transport with Rydberg $|38S\rangle$-$|37S\rangle$ atoms

The experiment was performed in the "reservoir" ODT, coupling to the impurity $|i\rangle = \left|38S_{1/2}\right\rangle$ and probe $|r\rangle = \left|37S_{1/2}\right\rangle$ Rydberg states, which exhibit strong dipolar interactions due to the Förster resonance $\left|38S_{1/2}, 37S_{1/2}\right\rangle \leftrightarrow \left|37P_{3/2}, 37P_{3/2}\right\rangle$. Thanks to the small $\Delta n = 1$, this pair state combination allows for the two step state exchange $|38S, 37S\rangle \leftrightarrow |37S, 38S\rangle$ to occur (Eq. (2.9)). The impurities were excited in a small central region of the cloud (as shown in Fig. 4.3 (a)) using a two-photon off-resonant transition. The probe and coupling beams were tuned to the single-photon resonances, and the latter was focused onto the atoms to an elongated Gaussian intensity profile which defined the transparency region, as illustrated in Fig. 4.3 (a) (for additional experimental parameters see Supplementary Material of [Günter *et al.*, 2013]).

A first set of measurements is taken on the Förster resonance, by applying a small electric field such that $\Delta_F = 0$. The top row in Fig. 4.3 (a) shows snapshots of the detected impurity distribution after different exposure times. We can clearly see that the distribution is expanding along the horizontal direction, indicating the presence of a diffusion process (expansion along the vertical direction is not observed since the EIT region is smaller than the impurity one). To rule out that the increase in the distribution width is caused by processes affecting only the impurities, like mechanical forces, we repeated the IEI measurement at fixed $t_{exp} = 2\,\mu s$, but with

variable delay between the excitation of impurities and the imaging pulse (bottom row in Fig. 4.3 (a)). No growth is observed as a function of delay time, only the total number of additional absorbers decays slightly, which can be attributed to the decay of the impurity state ($\tau \approx 30\,\mu\text{s}$ [Beterov *et al.*, 2009]). This experiment confirms that the diffusion process must be related to the interaction between the impurity and probe Rydberg states.

Figure 4.3 (b) shows the squared width of the measured impurity distribution $\sigma_x^2(t_{exp})$, which increases approximately linearly for continuous probing (full blue circles) and is constant as a function of delay time (open blue circles). A third IEI measurement is taken in the regime of off-resonant exchange interactions, by applying a detuning $\Delta_F = 2\pi \cdot 100\,\text{MHz}$ from the Förster resonance. This changes the interaction character from resonant dipole-dipole into the van der Waals type and reduces the interaction strength. Consequently a slow down of the state exchange process is expected, in agreement with the observed slower diffusion (full red circles).

The diffusion process can be understood using a simple heuristic model that considers the evolution of a single impurity atom embedded in a bath of background atoms under EIT coupling (a more rigorous model is developed and presented in [Schempp, 2014; Schempp *et al.*, 2015]). The coherent state exchange between the impurity and probe states depends on the interaction strength V_{ir} between them and on the density of exchange partners, which is dominated by the steady state population ρ_{rr} of the probe Rydberg state. These quantities depend on the distance between the impurity and the probe atom such that the coherent exchange rate can be approximated by $\omega_{coh}(r) \simeq 2V_{ir}(r)\rho_{rr}(r)$. At short distances below R_{ir} the impurity-probe interaction shifts the probe Rydberg state out of resonance with the coupling beam, consequently suppressing the population $\rho_{rr}(r < R_{ir}) \to 0$. At the same time the interaction strength falls with the distance, either as $1/r^3$ in the dipolar regime or as $1/r^6$ in the van der Waals case. The competition between these scalings leads to a maximum of the coherent exchange rate ω_{coh} at $r \approx R_{ir}$.

Another process is at play in this system. The presence of the impurity not only affects $\rho_{rr}(r)$, but also makes the surrounding atoms absorptive, causing a finite population in the excited state $\rho_{ee}(r < R_{ir})$. The scattering of light by the background atoms surrounding the impurity causes a measurement-induced environmental decoherence γ_{env}, since information on the impurity position is acquired on the detector, in analogy with a projective measurement of the quantum state of the many-body system. The decoherence rate per impurity is assumed to equal the sum over all additional absorbers of their individual light scattering rates, leading to $\gamma_{env} = \sum_i \Gamma_e \rho_{ee}^{(i)}(r)$.
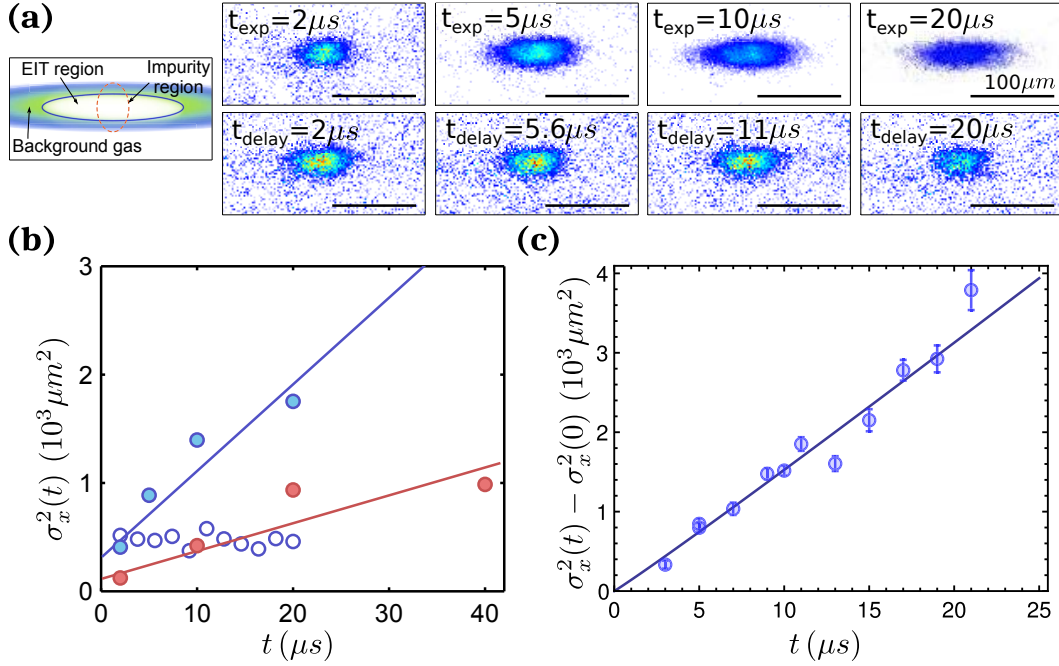
Figure 4.3: Expansion of additional absorption distribution during imaging. (a) The sketch shows the experimental geometry indicating the initial position of the $|38S_{1/2}\rangle$ impurities and the imaging region where probe atoms coupled to the $|37S_{1/2}\rangle$ state are present. Panels next to it show snapshots of the impurity distribution after different exposure times (top row) and delay times at fixed $t_{exp} = 2\,\mu s$ (bottom row). It is apparent that the distribution widens with increasing exposure time, while showing no growth with delay time. The images are averaged over 50 and 30 realizations respectively and taken on the Förster resonance. **(b)** The squared width of the measured impurity distribution σ_x^2 increases approximately linearly with exposure time and the diffusion is faster on the Förster resonance (full blue circles) than off resonance (full red circles). For comparison the blue empty circles show the distribution size at fixed $t_{exp} = 2\,\mu s$ for different delay times between impurity excitation and the actual imaging. **(c)** Analogous experiment performed with impurities in the state $|50S_{1/2}\rangle$ and probe atoms coupled to the $|48S_{1/2}\rangle$ state. Like in (b), the second moment of the impurity distribution (with the initial size subtracted) shows a linear increase with exposure time. A fit with a power law (solid line) yields an exponent of 1.04 ± 0.08, supporting the hypothesis that the observed dynamics follows a classical diffusion process. Errorbars are standard errors of the mean (100 realizations) and are estimated using the bootstrap method [Efron and Tibshirani, 1994]. Adapted from [Schempp, 2014].

For the used experimental parameters, we estimated that the environmental decoherence rate γ_{env} was about 150 times larger than ω_{coh}. Treating γ_{env} as a dephasing, the coherences in the four-level density matrix of the system can be neglected, leading to an effective classical rate equation which gives a hopping rate $\Gamma_{hop}(r) \approx \omega_{coh}^2(r)/\gamma_{env}(r)$. For classical hopping, a diffusive transport process is expected, with a diffusion law (considering time integration over the measurement time t_{exp})

$$\sigma_x(t_{exp})^2 = \sigma_x^2(0) + D \cdot t_{exp}, \tag{4.2}$$

where $D(\Gamma_{hop})$ is the diffusion coefficient. The diffusion is expected to scale linearly with the exposure time to the probe and coupling beams, since this is the time during which the impurities can exchange state with the probe Rydberg atoms, present only during the EIT coupling. Using this simple model, diffusion coefficents can be estimated for the resonant dipole-dipole and van der Waals interaction regimes (a derivation is presented in [Günter *et al.*, 2013; Günter, 2014])

$$D^{\mathrm{DD}} \simeq \frac{5}{18}(R_{ir}^{\mathrm{DD}})^2\frac{\Omega_p^2}{\Gamma_e} \qquad D^{\mathrm{vdW}} \simeq \frac{1}{14}(R_{ir}^{\mathrm{vdW}})^2\frac{\Omega_p^2}{\Gamma_e}. \tag{4.3}$$

The two rates differ by the numerical pre-factor and the strongly reduced blockade radius for the latter. In presence of a Förster defect Δ_F, these are related by $R_{ir}^{\mathrm{vdW}}/R_{ir}^{\mathrm{DD}} = (\Omega_c^2/4\Gamma_e\Delta_F)^{1/6} \approx 0.6$ for our parameters.

We fitted Eq. (4.2) to the measured $\sigma_x^2(t_{exp})$ to extract the diffusion coefficient D. On the Förster resonance we expected diffusion with $D^{\mathrm{DD}} = (55 \pm 23)\,\mu\mathrm{m}^2\,\mu\mathrm{s}^{-1}$ which is fair agreement with the measured $D = (80 \pm 13)\,\mu\mathrm{m}^2\,\mu\mathrm{s}^{-1}$. In the van der Waals regime ($\Delta_F = 2\pi \cdot 100\,\mathrm{MHz}$) we found $D = (26 \pm 6)\,\mu\mathrm{m}^2\,\mu\mathrm{s}^{-1}$, which is an order of magnitude larger than the expected $D^{\mathrm{vdW}} = (3.0 \pm 0.9)\,\mu\mathrm{m}^2\,\mu\mathrm{s}^{-1}$. This discrepancy was attributed to the always resonant direct single step state exchange $|37S, 37P\rangle \leftrightarrow |37P, 37S\rangle$ (Eq. (2.8)) that can occur once the $|37P\rangle$ is off-resonantly populated. Similar processes have been considered in [Mourachko *et al.*, 1998; Anderson *et al.*, 1998] to explain the broadening of Förster resonances.

4.2.2 Transport with Rydberg $|50S\rangle$-$|48S\rangle$ atoms

The first energy transport experiment with $|38S_{1/2}\rangle$ impurity and $|37S_{1/2}\rangle$ probe states indicated that the dynamics were classical, but, given the small number of measurements, we could not exclude a possible deviation from linear diffusion for longer probing times. To address this question, we performed a similar experiment with impurities in the state $|50S_{1/2}\rangle$ and probe atoms coupled to the $|48S_{1/2}\rangle$

state. This state combination is also close to a Förster resonance $|50S_{1/2}, 48S_{1/2}\rangle \leftrightarrow |49P_{1/2}, 48P_{1/2}\rangle$, but the probability of the two step exchange process $|50S, 48S\rangle \leftrightarrow |50S, 48S\rangle$ (Eq. (2.9)) is much lower due to $\Delta n = 2$. Nonetheless, fast exchange can happen as soon as the pair state $|49P_{1/2}, 48P_{1/2}\rangle$ is off-resonantly populated, leading to an always resonant direct single step process $|48P, 48S\rangle \leftrightarrow |48S, 48P\rangle$ (Eq. (2.8)), similarly to the van der Waals case discussed at the end of Ch. 4.2.1.

The IEI measurements are performed with $\Delta_F = 2\pi \cdot 103\,\text{MHz}$ and the second moment of the impurity distribution (with the initial size of $10\,\mu\text{m}$ subtracted) shows a linear increase with exposure time, like in the previous experiment and as illustrated in Fig. 4.3 (c). A fit with a power law (solid line) yields an exponent of 1.04 ± 0.08, supporting the hypothesis that the observed dynamics follows a classical diffusion process. Fixing the exponent to 1 we extract a diffusion coefficient $D = (153 \pm 5)\,\mu\text{m}^2\,\mu\text{s}^{-1}$. A more complete analysis of these measurements with an improved theoretical model is presented in [Schempp, 2014].

4.2.3 Towards $|nP\rangle$-$|nS\rangle$ transport experiments

In this section we presented the first spatially resolved investigations via IEI of energy transport processes induced by dipole-dipole interactions. Our imaging method gave insight into the classical diffusion regime, but many more questions can be addressed in the future, concerning e.g. the transport mechanisms, the transition between quantum and classical transport, the effect of disorder and the role of dissipation.

These experiments revealed that $|n'S\rangle$-$|nS\rangle$ state combinations allow for at least two state exchange processes to occur, the two step (Eq. (2.9)) and the single step (Eq. (2.8)). This makes the theoretical description of the transport dynamics more complex, because at least 4 Rydberg states are involved, and even more can become coupled due to the state mixing induced by dipole-dipole interactions (see Ch. 2.2.3).

A promising approach to minimize the number of excitation pathways would be to perform experiments directly with $|n'P\rangle$ impurity and $|nS\rangle$ probe states. Such pair state choice is always resonantly coupled, leading to the simplest single step state exchange dynamics. Furthermore, resonant dipole-dipole interactions are much stronger than van der Waals interactions for the same principal quantum numbers and the states with $|n' - n| \leq 1$ exhibit the highest couplings, as discussed in Ch. 2.2.3. This should lead to an improvement of the IEI sensitivity, which was estimated to be around 6 impurities in a single-shot measurement [Günter *et al.*, 2013; Günter, 2014].

Motivated by this insight, we added to our experimental setup the capability to

excite Rydberg $|n'P\rangle$ states. Direct single-photon laser excitation from the ground state to a Rydberg P-state [Thoumany *et al.*, 2009; Manthey *et al.*, 2014; Manthey *et al.*, 2015; Zeiher *et al.*, 2016] is possible, but it would require a whole new laser system with wavelength in the UV, with limited power output and increased technical complexity. An alternative route, implemented in the course of this thesis, is to prepare Rydberg $|n'P\rangle$ states using microwave radiation, starting either from a energetically close $|nS\rangle$ state [Li *et al.*, 2003; Afrousheh *et al.*, 2004; Afrousheh, 2006] or from the ground state via a three-photon off-resonant transition. The latter scheme allows for a clean preparation of the initial impurity state $|i\rangle$ by avoiding population of the intermediate states. To minimize the number of laser beams required to prepare the impurity and probe Rydberg states, the same principal quantum number is chosen for both $n' = n$. The preparation scheme is explained and characterized in detail in Ch. 2.5.2.

Once the desired initial states are prepared, it is necessary to prove the capability of IEI to image $|nP\rangle$ states. In Ch. 4.5 we demonstrate the first experimental spatially resolved optical imaging of $\left|42P_{3/2}\right\rangle$ Rydberg atoms. For these first proof-of-principle measurements it is desirable to suppress the transport process because the diffusion of the impurities may severely constrain the signal accumulated on the detector per each impurity, by spreading it over a large area. We circumvent this problem by introducing the "tight" ODT. The volume of a cloud prepared in this small trap is limited to few blockade spheres with radius R_{ir}, such that the number of potential hopping partners per impurity is severely restricted, leading to a negligible hopping rate. Moreover, only very few impurities can be excited in this tight trap before reaching the fully-blockaded regime, where the exchange dynamic is inhibited.

Future transport experiments with $|nP\rangle$-$|nS\rangle$ state pairs would require very short exposure times in order to track with high temporal resolution the fast energy transport dynamics expected from their strong resonant dipole-dipole coupling. This calls for a quantitative description of IEI that would be able to predict the signal per impurity. In the following section we develop a simple model of our imaging method and of the underlying coupled atom-light system [Faraoni, 2014]. This hard-sphere model captures the interplay between EIT and interactions, which determines the optical response, and is in good agreement with experimental data.

4.3   Model for Interaction Enhanced Imaging of Rydberg atoms

Interaction-enhanced imaging is based on the different optical responses of an atomic cloud with and without the impurities it is aimed to detect. To determine optimal conditions for imaging we develop a simple model which captures the main features of IEI [Faraoni, 2014], especially the impurity-probe interactions and the probe-probe interactions that naturally arise in the gas. This model describes the medium as composed of three inter-dispersed sub-volumes: a first region where transparency is preserved, a second region in which transparency is reduced due to probe-probe interactions and a third one in which transparency is affected by impurity-probe interactions. To account for the relative size of each volume we employ a simple hard-sphere approach to quantify each region.

The atom-light interaction is treated semi-classically and we will consider the system to be in the steady state, since the imaging pulses of few µs are much longer than the typical decay time Γ_e^{-1}. Additionally we will assume in the following that the atoms are cooled to temperatures low enough to neglect thermal motion and mechanical effects on the Rydberg atoms [Amthor *et al.*, 2007b; Teixeira *et al.*, 2015].

4.3.1   Light propagation under ideal EIT conditions

In our system, the probe atoms are coupled under electromagnetically induced transparency conditions in order to make them initially transparent to a weak probe field of Rabi frequency Ω_p resonant on the $|g\rangle \leftrightarrow |e\rangle$ transition (see Fig. 4.1). A description of the EIT properties and requirements has been given in Ch. 3.1. The optical response of the medium is determined by its susceptibility, expressed by Eq. (3.9). In our case, the density is a function of position $n(r)$ due to the Gaussian profile of the atomic cloud, while ρ_{eg} depends in particular on the probe Rabi frequency Ω_p. Assuming for the moment that interactions between atoms can be fully neglected, which is reasonably valid in a dilute gas, from Eq. (3.11) we find that on the single photon resonance ($\Delta_p, \Delta_c = 0$) the ideal first order susceptibility is expressed by Eq. (3.15)

$$\chi_{eit}^0 = \chi_0 \frac{1}{1+C} \simeq \chi_0 \frac{\mathrm{i}\Gamma_e^2}{\Gamma_e^2 + \Omega_c^2 \Gamma_e/\Gamma_{gr}^0 + 2\Omega_p^2} \,, \tag{4.4}$$

where the term $2\Omega_p^2$ is introduced to account for intensity saturation effects, that were neglected in the weak probe approximation. Here we suppose that the sources

of dephasing acting on the intermediate level $|e\rangle$ are negligible compared to Γ_e, which is experimentally verified (Ch. 2.5), while we account for an effective dephasing rate $\Gamma_{gr}^0/2$ of the coherence density matrix element ρ_{gr}, including contributions of the decay rate of $|r\rangle$ and of additional dephasing rates. Equation (4.4) shows that $\chi_{eit}^0 \ll \chi_0$ as soon as $C \gg 1$, which is satisfied in our experiment for coupling Rabi frequencies Ω_c on the order of few MHz. Since the absorption is related to the imaginary part of the susceptibility, such conditions lead to transparency of the cloud for the probing beam.

### 4.3.2 Inclusion of probe-probe interactions

The validity of equation (4.4) breaks down as soon as the Rydberg atomic density is large enough such that the van der Waals interaction between the Rydberg states of the probe atoms becomes significant. Experimentally, the change in transparency as function of Rydberg density has already been observed in Rydberg media [Sevinçli *et al.*, 2011a; Pritchard *et al.*, 2010; Pritchard *et al.*, 2011; Hofmann *et al.*, 2013; DeSalvo *et al.*, 2016; Han *et al.*, 2016]. Moreover it has been shown from a semi-analytic rate equation (RE) approach that the effect of these interactions can be approximated by an energy shift $\Delta_{int} = V_{rr}$ of the Rydberg state when we want to estimate the optical response of the gas [Gärttner *et al.*, 2014b; Ates *et al.*, 2011] (Fig. 4.6 (b)). This shift effectively introduces a detuning $\Delta_c = \Delta_{int}$ of the coupling light that modifies the effective dephasing $\Gamma_{gr}^0 \rightarrow \Gamma_{gr}^0 + 2\,\mathrm{i}\,\Delta_{int}$ in Eq. (4.4), leading to a loss of transparency. For large energy shift V_{rr} the susceptibility approaches the resonant two-level susceptibility χ_{2lvl} which is given by Eq. 3.10 for $\Delta_p = 0$

$$\chi_{2lvl} = \chi_0 \frac{\mathrm{i}\Gamma_e^2}{\Gamma_e^2 + 2\Omega_p^2}. \tag{4.5}$$

The dependence on Ω_p takes into account the saturation of the atomic transition in contrast to the weak probe limit. Figure 4.4 (a) shows a plot of the ratio between the scaled imaginary part of χ_{eit}^0 as a function of the single-photon detuning Δ_c between the coupling field and the atomic transition $|e\rangle \leftrightarrow |r\rangle$. It shows that the transparency is preserved in a window around the resonance with a FWHM given by Eq. 3.16 $C \gg 1 \rightarrow \sigma_{eit} \approx \Omega_c^2/\Gamma_e$ which defines the EIT bandwidth.

Using a rate equation model and Monte-Carlo simulations Ates *et al.* [Ates *et al.*, 2011] has found that the optical response including probe-probe interactions can be related to the Rydberg atomic density through the relation

$$\chi_{eit} = f_{rr}\chi_{2lvl} + (1 - f_{rr})\,\chi_{eit}^0, \tag{4.6}$$
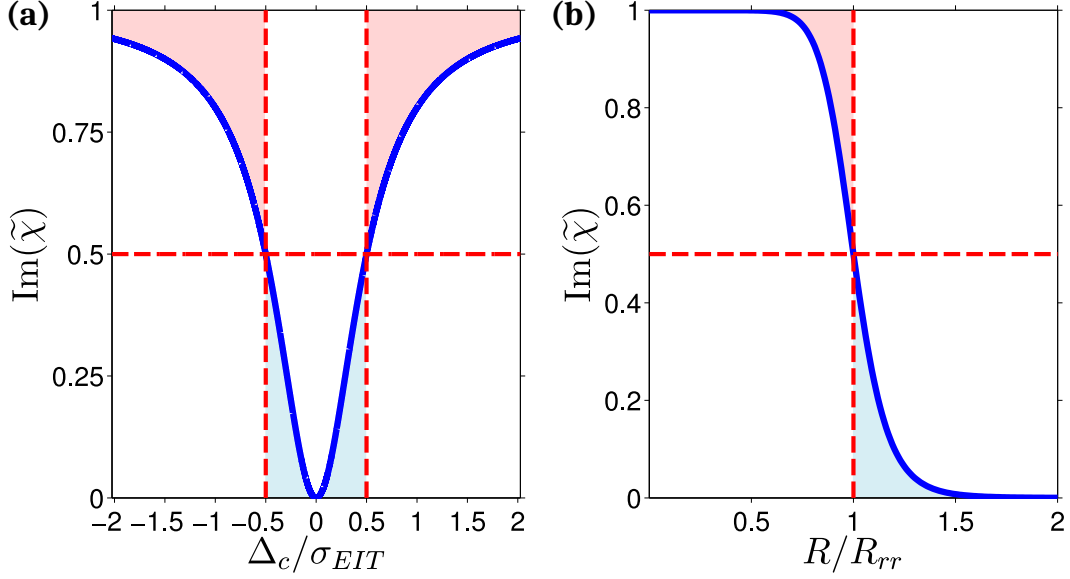
Figure 4.4: Hard-sphere description of EIT with interactions. (a) Imaginary part of the scaled susceptibility under EIT as a function of the detuning Δ_c of the $|e\rangle \leftrightarrow |r\rangle$ transition, normalized by the FWHM of the EIT transparency window. At $\Delta_c = \sigma_{eit}/2$ the susceptibility is half of the two-level one. For larger detunings atoms are considered as two-level absorbers (filled red area). **(b)** Imaginary part of the scaled susceptibility as a function of the inter-atomic separation normalized by the probe-probe blockade radius R_{rr}. Atoms within $R \leq R_{rr}$ are treated as two-level absorbers, and as under perfect EIT while outside this range. This hard-sphere approach is supported by the fact that the integrals of $\mathrm{Im}[\tilde{\chi}]$ and $\mathrm{Im}[\tilde{\chi}_{\text{hard-sphere}}]$ over the approximated regions (red and blue areas) are equal.

where f_{rr} is the effective fraction of volume blockaded by the probe-probe interactions, expressed as

$$f_{rr} = \frac{n\rho_{rr}^0 - n\rho_{rr}}{n\rho_{rr}^0} = 1 - \frac{\rho_{rr}}{\rho_{rr}^0}. \tag{4.7}$$

Here ρ_{rr}^0 is the density matrix element in the non-interacting regime (single atom case, equal to Ω_p^2/Ω_c^2 in the steady state, see Ch. 3.1.4) and ρ_{rr} the one in the interacting regime. The blockaded volume fraction is represented by the fraction of atoms that are not excited to the Rydberg state $|r\rangle$ because of the probe-probe interactions. Therefore f_{rr} is expressed through the normalized difference between $n\rho_{rr}^0$, the density of Rydberg atoms that would have been excited without interactions, and $n\rho_{rr}$, the density of Rydberg atoms that are effectively excited. Nevertheless, eqs. (4.6) and (4.7) do not allow to calculate the optical susceptibility since they do not provide the expression of ρ_{rr} which requires a self-consistent solution to properly

take into account collective effects present in the system.

To determine the fraction f_{rr} we use a hard-sphere approximation [Petrosyan *et al.*, 2011; Sevinçli *et al.*, 2011a; Parigi *et al.*, 2012] in which atoms that experience an energy shift V_{rr} larger than half of the EIT bandwidth $\sigma_{eit}/2$ will be considered as two-level absorbers, while the others are assumed to be coupled under ideal EIT conditions (Ch. 4.3.1), as illustrated in Fig. 4.4 (b). Hence probe atoms surrounding any given atom experience the interaction only if their distance R is smaller than the probe-probe Rydberg blockade radius R_{rr}

$$R < R_{rr} = \left(\frac{2C_6^{rr}}{\sigma_{eit}} \right)^{\frac{1}{6}}, \tag{4.8}$$

where C_6^{rr} is the van der Waals coefficient of the $|r\rangle$ state determining $V_{rr} = C_6^{rr}/R^6$. Within this approach the fraction f_{rr} can be expressed as the number of atoms contained in each blockaded volume $V_{bl} = 4/3 \cdot \pi R_{rr}^3$ over the total number of atoms, leading to

$$f_{rr} = n\rho_{rr}V_{bl}. \tag{4.9}$$

By substituting Eq. (4.9) in Eq. (4.7) we can extract the density matrix element ρ_{rr}

$$\frac{\rho_{rr}}{\rho_{rr}^0} = \frac{1}{1 + n\rho_{rr}^0 V_{bl}} \tag{4.10}$$

and obtain an analytical expression for the optical susceptibility in the presence of probe-probe interactions. For negligible $\tilde{\chi}_{eit}^0 \to 0$, we observe that $\text{Im}[\tilde{\chi}_{eit}] = f_{rr}$ and, consequently, both quantities scale together as a function of $n\rho_{rr}^0 V_{bl}$. The imaginary part of the scaled susceptibility reaches half of its possible peak value at $n\rho_{rr}^0 V_{bl} = 1$, as illustrated in Fig. 4.5. This happens when the mean inter-particle distance becomes equal to the blockade radius, entering thus the blockaded regime discussed in Ch. 2.3.

4.3.3 Effect of impurities

We follow a very similar approach to incorporate the optical response in the presence of impurities $|i\rangle$, which have been independently excited. When $|n'S\rangle$ Rydberg impurities are imaged using $|nS\rangle$ probe atoms, the van der Waals interaction between the two states leads to a frequency shift $\Delta_{int} = V_{ir}^{\text{vdW}} = C_6^{ir}/R^6$ on $|r\rangle$ that modifies the optical response of the medium (Fig. 4.6 (b)). The eigenstates of the system are in good approximation the single atom ones, $|i\rangle$ and $|r\rangle$. In contrast, when $|nP\rangle$ Rydberg impurities are imaged using $|nS\rangle$ probe atoms, the two states
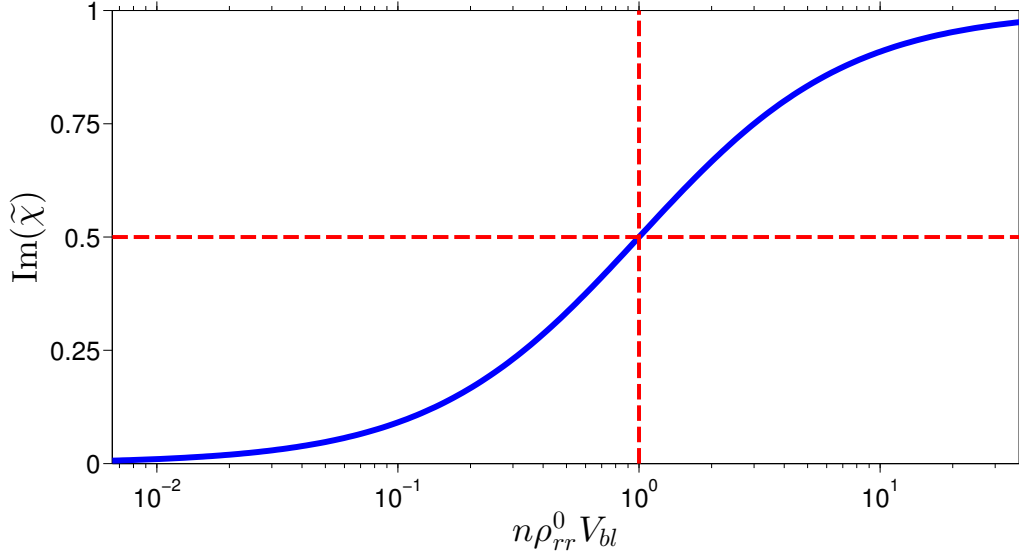
Figure 4.5: Imaginary part of EIT scaled susceptibility in presence of interactions, as a function of $n\rho_{rr}^0 V_{bl}$. At $n\rho_{rr}^0 V_{bl} = 1$ the susceptibility reaches half of its possible peak value.

experience a dipole-dipole exchange interaction and the system eigenstates become the symmetric and antisymmetric combinations $(|ri\rangle \pm |ir\rangle)/\sqrt{2}$ of the unbound pair states, split in energy by $\pm\Delta_{int} = \pm V_{ir}^{\mathrm{DD}} = \pm C_3^{ir}/R^3$ (Fig. 4.6 (b)). In analogy to the probe-probe interactions, we define a critical radius R_{ir} for the two interaction types

$$R_{ir}^{\mathrm{DD}} = \left(\frac{2C_3^{ir}}{\sigma_{eit}}\right)^{\frac{1}{3}} \qquad R_{ir}^{\mathrm{vdW}} = \left(\frac{2C_6^{ir}}{\sigma_{eit}}\right)^{\frac{1}{6}}, \qquad (4.11)$$

beyond which the energy splitting is smaller than the EIT bandwidth σ_{eit}, allowing to address the Rydberg $|r\rangle$ state. Above this critical distance we assume that the gas behaves as a three level system, while below this distance the susceptibility is approximated by the behavior of a two level system. In the $|nP\rangle$-$|nS\rangle$ case, since the interactions are anisotropic and the experiment is performed with 3D random positions of the atoms, we consider an effective isotropic reduced interaction strength C_3^{ir} that is obtained by averaging over the total solid angle.

With this hard-sphere model it becomes possible to express the optical susceptibility of a medium under EIT coupling in the presence of impurities as the weighted combination of the two-level susceptibility (Eq. (4.5)) and the EIT susceptibility with probe-probe interactions (Eq. (4.6))

$$\chi_{imp} = f_{ir}\chi_{2lvl} + (1 - f_{ir})\chi_{eit}, \qquad (4.12)$$

where f_{ir} is the fraction of volume blockaded by the impurity-probe interactions.
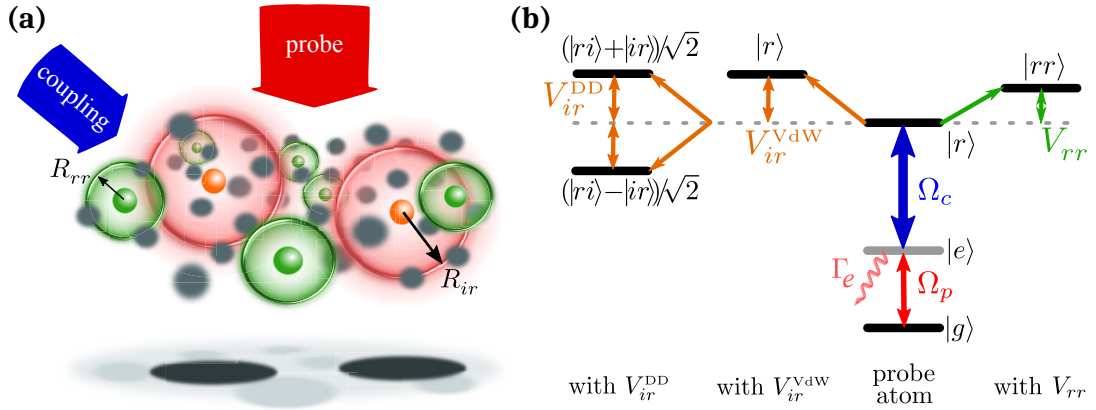
Figure 4.6: Hard-sphere description of IEI. (a) Description of interactions with a hard-sphere approach: the impurities (orange dots) interact with the surrounding probe atoms (grey and green dots when respectively in $|g\rangle$ or $|r\rangle$). They induce a level shift V_{ir} that, within a distance R_{ir}, breaks the EIT condition. The probing laser beam is imaged on a CCD camera and an absorption spot is expected around the position of each impurity. Within a distance R_{rr} around each $|r\rangle$ Rydberg state, probe-probe interactions reduce the transparency as well. **(b)** Without interactions the three states $|g\rangle$, $|e\rangle$, $|r\rangle$ of the probe atoms are coherently coupled by two resonant light fields with Rabi frequencies Ω_p and Ω_c (probe atom case). The probe-probe interactions induce a level shift of V_{rr} on $|r\rangle$ (right). The presence of a Rydberg impurity $|i\rangle$ (left) in an $|n'S\rangle$ state causes a level shift of $|r\rangle$ due to the van der Waals interaction V_{ir}^{VdW}, while if it is in an $|n'P\rangle$ state, which interacts through the dipolar exchange with $|r\rangle$, the new eigenstates are split by an energy $2V_{ir}^{\mathrm{DD}}$. Effectively all three types of interaction lead to a vanishing probability to excite $|r\rangle$ when their strength exceeds the EIT bandwidth and to absorption on the $|g\rangle \leftrightarrow |e\rangle$ transition.

At low impurity density n_i this fraction can be estimated by geometric arguments assuming no overlap between the blockade sphere around each impurity. Each impurity blockades a volume $V_{bl,i} = 4/3 \cdot \pi R_{ir}^3$, so that N_i impurities blockade a total volume $N_i V_{bl,i}$, leading to a blockaded fraction $f_{ir} = n_i V_{bl,i}$. In the opposite case of large impurity densities f_{ir} is equal to 1 since the whole volume is blockaded. In analogy to Ch. 4.3.2, we extrapolate the relation to $f_{ir} = 1 - 1/(1 + n_i V_{bl,i})$.

4.3.4   Model limitations

The hard-sphere model that we presented in this section is a simplified description of the interplay between the Rydberg-Rydberg interactions and the non-linear optical response of the three-level atomic system under EIT conditions. First the interaction

potential is not hard-core, but scales monotonically with distance, nonetheless this approximation should hold well since the integrals of $\mathrm{Im}[\tilde{\chi}]$ and $\mathrm{Im}[\tilde{\chi}_{\text{hard-sphere}}]$ over the approximated regions (red and blue areas) are equal, as shown in Fig. 4.4 (b). Then we assume a spherical blockade volume, while for P-states it has an angular dependence (see Ch. 2.2.3). Another assumption is that interactions between Rydberg atoms lead only to energy shifts, while models based on a mean field and local density approximations [Goldschmidt *et al.*, 2016; DeSalvo *et al.*, 2016; Aman *et al.*, 2016; Han *et al.*, 2016] present also a dephasings term that represents the variance of the induced shifts over the cloud. Furthermore, our approach neglects all collective effects [Gärttner *et al.*, 2014b], as well as photon-photon correlations and interactions [Petrosyan *et al.*, 2011; Ates *et al.*, 2011; Gorshkov *et al.*, 2011; Gorshkov *et al.*, 2013; Bienias *et al.*, 2014; Bienias and Büchler, 2016; Bienias, 2016; Murray and Pohl, 2016]. Förster resonances are not described, nor the change in interaction type from the van der Waals to the dipole-dipole interaction regimes, that occurs when the mean inter-particle distance between Rydberg atoms becomes smaller than R_{cr} (see Ch. 2.2.3). We also neglect the effects of energy transport that spread the signal over an area on the detector due to the ongoing diffusion during the imaging time. In Ch. 4.5.1 we will compare the predictions of our IEI hard-sphere model with experimental measurements to study its validity range.

4.4   Detection method

To probe the impurity distribution we measure the probe light transmitted through the atomic cloud under EIT conditions in presence and absence of impurities. A typical IEI experimental pulse sequence is shown in Fig. 4.7. First, the impurities are excited during a time t_{exc} to either an $|n'S\rangle$ or an $|nP\rangle$ state using the two-photon (Ch. 2.5.1) or the three-photon (Ch. 2.5.2) off-resonant excitation schemes. After a short delay time t_{delay}, the imaging and coupling pulses are turned on together for a variable exposure time t_{exp} to make the cloud transparent and a first image $N_{\mathrm{e}^-,imp}$ is acquired on the CCD, where the transmitted light in presence of impurities is converted into electrons. Immediately after the pulses end, the Rydberg atoms are field ionized and counted (see Ch. 2.4.4). In order to obtain a reference image of EIT without impurities we apply the same pulse sequence, but with the microwave and the blue impurity excitation laser pulses turned off, recording a second image $N_{\mathrm{e}^-,eit}$.

This spatially resolved detection process can be modeled by calculating the transmission of the cloud, expressed by Eq. (3.13), using the susceptibilities predicted
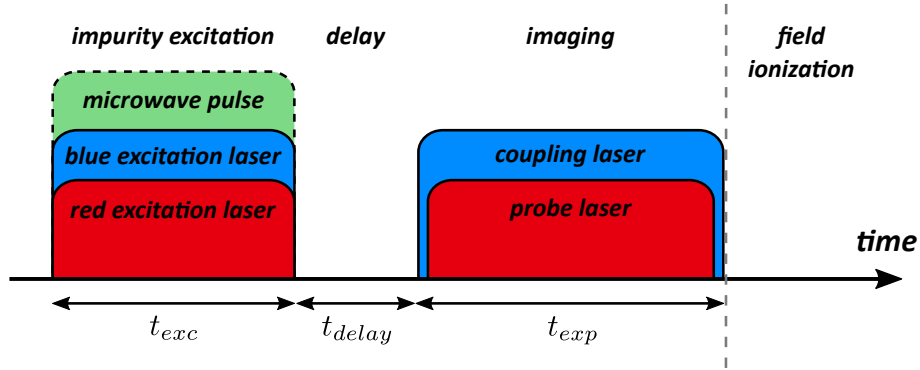
Figure 4.7: Typical pulse sequence for Interaction Enhanced Imaging. The impurities are excited during a time t_{exc} to either an $|n'S\rangle$ or an $|n'P\rangle$ state using the two-photon (Ch. 2.5.1) or the three-photon (Ch. 2.5.2) off-resonant excitation schemes. After a short delay time t_{delay}, the imaging and coupling pulses are turned on together for a variable exposure time t_{exp} and an image is acquired on the CCD. Immediately after the pulses end, a high electric field is quickly ramped up on the electrode structure surrounding the cloud and the Rydberg atoms are field ionized. The resulting ions are guided to the MCP detector and counted from a trace acquired on a fast oscilloscope. To obtain a reference image of EIT without impurities we apply the same pulse sequence, but with the microwave and the blue impurity excitation laser pulses turned off.

by the hard-sphere model. In general χ can be a complicated function of the local medium density and probe Rabi frequency, leading to non-linear propagation of light, and this would require to solve the differential equation (3.13) taking into account the local parameters. Nevertheless, here we will neglect non-linear light propagation effects by assuming a constant probe Rabi frequency experienced by the atoms, resulting in $\chi(\Omega_p, n(x))$. This approximation is justified since we observe the cloud under transparency conditions where $|\chi| \ll 1$, but small deviations might be observed for large absorption levels [Hofmann *et al.*, 2013; Gärttner and Evers, 2013]. Considering a Gaussian profile for the density $n(x) = n_0 \exp\{(-x^2/2\sigma_x^2)\}$, we can numerically solve equation (3.14) to calculate the normalized intensity along the propagation through the cloud. As an example, Fig. 4.8 shows the normalized light intensity $(\Omega_p(x)/\Omega_{p,in})^2$ in the three considered cases, the two-level one using χ_{2lvl} from Eq. (4.5), the response under EIT conditions using χ_{eit} from Eq. (4.6), and the response in the presence of impurities using χ_{imp} from Eq. (4.12). The impurity *signal* is given by the difference between the two latter cases. This observable will be useful for the discussion on the IEI sensitivity carried out in Ch. 5, while here we will focus on two other quantities that represent the signal emerging from the impurities.

The presence of impurities embedded in the atomic gas causes an additional
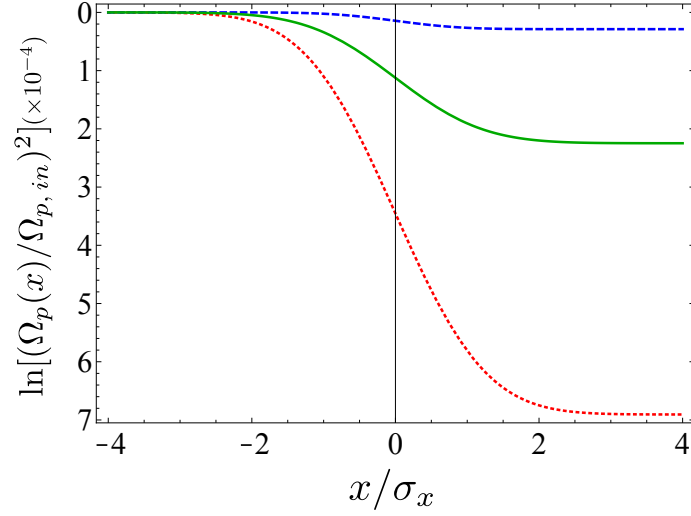
Figure 4.8: Light propagation under EIT in presence of impurities. (a) Simulation of light propagation through a one-dimensional Gaussian cloud of atoms of width σ_x as a function of the rescaled distance x/σ_x. The red dotted line describes the two level system response with $\Omega_{p,in} = 2\pi \cdot 1\,\text{MHz}$ and $n_0 = 1 \cdot 10^{11}\,\text{cm}^{-3}$, while the blue dashed line refers to the one under EIT ($\Omega_c = 2\pi \cdot 10\,\text{MHz}$). The stray absorption is induced by probe-probe interactions between $|r\rangle = |42S_{1/2}\rangle$ states, estimated here with $C_6^{rr} = 2\pi \cdot 1.8\,\text{GHz}\,\mu\text{m}^6$. The green solid line represents the case of EIT with impurities in the $|i\rangle = |42P_{3/2}\rangle$ states at a density of $n_i = 5 \cdot 10^8\,\text{cm}^{-3}$, assuming an interaction strength $C_3^{ir} = 2\pi \cdot 1.7\,\text{GHz}\,\mu\text{m}^3$.

absorption

$$A_{add} = \frac{N_{e^-,eit} - N_{e^-,imp}}{N_{e^-,eit}} = 1 - e^{-\Delta\text{OD}} \quad \text{with} \quad \Delta\text{OD} = \text{OD}_{imp} - \text{OD}_{eit} \quad (4.13)$$

that we can experimentally access. It changes from 0 when transparency is not affected by their presence to A_{2lvl} when impurity-probe interactions fully break the transparency. To get more insight into this quantity it is convenient to rewrite it using eqs. (4.6) and (4.12) into

$$\Delta\text{OD} = \int_{-\infty}^{+\infty} k f_{ir}(1 - f_{rr})\text{Im}\left[\chi_{2lvl} - \chi_{eit}^0\right] dx \quad (4.14)$$

Under our assumptions only the density is spatially-dependent and it comes into play in the fractions f_{rr} and f_{ir}. Measuring the additional absorption A_{add} allows to determine the impurity density n_i which is included in f_{ir}, under the assumption of knowing the other parameters involved in Eq. (4.14). In order to physically interpret this equation, a first consideration can be done at low probe-probe interactions when

$f_{rr} \to 0$: the presence of the impurities blockades a volume fraction f_{ir} in which each probe atom will become an additional absorber, leading to a change of the susceptibility from χ^0_{eit} to χ_{2lvl}. Then ΔOD would be the optical density of these additional absorbers. In the general case, some of these probe atoms would already behave as additional absorbers due to the probe-probe interactions, leading to a reduction of the signal by a factor $1 - f_{rr}$.

From the spatially resolved additional absorption we can calculate the number of additional absorbers N_{add} for each pixel of the CCD camera, given by

$$N_{add} = \frac{a_{px}(1+s)}{\sigma_0} \Delta\text{OD} = \frac{a_{px}(1+s)}{\sigma_0} \ln\left[(1 - A_{add})^{-1})\right], \qquad (4.15)$$

where $s = 2\Omega_p^2/\Gamma_e^2$ is the saturation parameter of the probe transition. This equation converts the measured signal into an effective number N_{add} of atoms that would be absorptive instead of fully transparent due to the presence of impurities and allows to measure the amplification factor per impurity A^{IEI}.

4.5 Imaging of Rydberg $|42P\rangle$ atoms

We discuss in this last section the first spatially resolved imaging of Rydberg $|i\rangle = |42P_{3/2}, m_J = +3/2\rangle$ impurities embedded in a gas of atoms and prepared using the excitation scheme introduced in section 2.5.2. IEI is performed by coupling the probe atoms to the Rydberg state $|r\rangle = |42S_{1/2}, m_J = +1/2\rangle$. For the first experimental realization we work in a large volume trap which allows for good statistics in order to validate our hard-sphere model. We then image Rydberg impurities within a small volume to avoid transport effects.

4.5.1 Testing the validity of the hard-sphere model

To test the validity of the hard-sphere model presented in Sec. 4.3, we first perform an IEI experiment in the large and dense "reservoir" optical dipole trap (see Ch. 2.4.1) where we can tune the density over more than an order of magnitude ($n_0 = (0 - 15) \cdot 10^{10}\,\text{cm}^{-3}$), transitioning from a dilute non-interacting gas into a strongly interacting regime. At a given time, we release the trap and probe the response of the atomic cloud by measuring the absorption in three different configurations: without coupling light nor impurities (two-level response), with the coupling light turned on but no impurities (EIT response), and finally with both the coupling light and the impurities present. To measure the probe light absorption
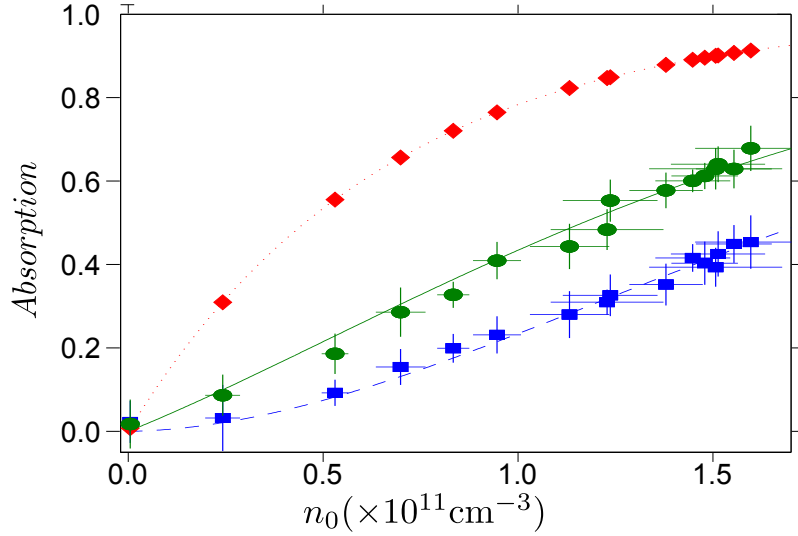
Figure 4.9: Validation of IEI hard-sphere model. Comparison between the measured and theoretical absorptions A of the probe beam through the atomic cloud as a function of the peak density n_0 using the $|42P_{3/2}\rangle$ impurity and $|42S_{1/2}\rangle$ probe states. We measure the two-level response (red diamonds), the EIT response (blue squares) and the one with pre-excited impurities (green circles). The absorption is averaged over an area of 3x3 pixels at the center of the cloud. Error bars represent the measured standard deviation obtained from 10 repetitions. The data is compared to the hard-sphere model developed in section 4.3: the absorption is calculated from the two-level susceptibility χ_{2lvl} (red dotted line), the EIT susceptibility χ_{eit} (blue dashed line), and the susceptibility with impurities χ_{imp} (green solid line).

A defined by Eq. (2.11), we record on the CCD camera the transmitted number of photons $N_{e^-,a}$, converted into electrons, just after switching off the optical dipole trap, as well as the reference initial number of photons $N_{e^-,r}$ after 10 ms when all the atoms felt below the light path because of gravity.

We first measure the two-level response of the ground state atoms by turning off the coupling light field (red diamonds in Fig. 4.9 (a)). The measured absorption A_{2lvl} allows us to extract the peak density of the cloud using Eq. (4.5), taking into account the small saturation effect due to the non-zero probe Rabi frequency $\Omega_p = 2\pi \cdot (1.14 \pm 0.02)$ MHz, which leads to a correction of about 7%. Since it is used to calibrate the peak density axes, the data coincides exactly with the theoretical two-level absorption (red dotted line).

We then turn on the coupling light field to reach the conditions for EIT and perform the same acquisition (blue squares). We analyse only the probe absorption A_{eit} in an area corresponding to the center of the coupling laser beam, which

allows us to assume Ω_c as constant. Independent measurements relying on Autler-Townes spectra (see Ch. 3.2.4) are used to calibrate the strength of the coupling $\Omega_c = 2\pi \cdot (9.5 \pm 0.7)\,\text{MHz}$. The observed loss of transparency when the atomic density increases is the signature of van der Waals interaction between probe atoms. The data is compared to the hard-sphere model (blue dashed line) using Eq. (4.6). We obtain good agreement assuming a Rydberg blockade of $R_{rr} = 3.6 \pm 0.3\,\mu\text{m}$, while the theoretical prediction is $2.5\,\mu\text{m}$, meaning that the effect of interactions appears to be stronger than predicted from the dipole moment of the used state. This discrepancy can be potentially explained by the presence of additional Rydberg states, populated via black-body radiation induced transitions, as suggested by measurements presented in Ch. 5.2.3. In these conditions the blockaded fraction f_{rr} changes with the density from 0 to 0.31 ± 0.03.

In the last realization we pre-excite some impurities during a fixed excitation time $t_{exc} = 5\,\mu\text{s}$ and we record the optical response (green circles). The larger absorption compared to the previous case is caused by additional absorbing probe atoms due to the presence of impurities. The evolution of the optical response measured from the absorption A_{imp} is again compared to the hard-sphere model using Eq. (4.12). The anisotropic interaction strength is estimated to be $C_3^{ir} = 2\pi \cdot 1.7\,\text{GHz}\,\mu\text{m}^3$ considering an angular averaging [Walker and Saffman, 2008], leading to a blockade radius of $R_{ir} = 6.1\,\mu\text{m}$, roughly 2 times larger than R_{rr}. The model reproduces the data very well assuming a constant fraction of volume blockaded by the impurities of $f_{ir} = 0.24 \pm 0.02$, resulting in 26 ± 5 Rydberg impurities embedded in the whole sample. From the field ionization we estimate the number of impurities to be ~ 12, which is consistent within the large uncertainty of the ion detection efficiency.

The agreement with the data justifies the use of a hard sphere model to describe IEI. In the density range we have explored, Figure 4.9 shows that the signal increases with the atomic peak density, indicating that the amplification factor per impurity A^{IEI} is also raising. Nevertheless, we expect that the signal will saturate at higher densities and then decrease due to the incrementing impact of probe-probe interactions.

## 4.5.2 Imaging few Rydberg P state atoms

After testing the model with experiments in the "reservoir" ODT, we perform a new set of IEI experiments in the "tight" optical dipole trap. Due to its restricted volume, diffusion of the Rydberg impurities is negligible, as discussed in Ch. 4.2.3. Moreover the maximum number of impurities remains relatively small due to the

blockade effect, which allows us to investigate the detection of up to ~ 10 impurities in the sample.

We prepare the atoms in the ground state $|g\rangle$ with a peak density of $n_0 = (1.4 \pm 0.3) \cdot 10^{11} \, \text{cm}^{-3}$. The average number of impurities $\langle N_i \rangle$ is changed by varying the duration time t_{exc} of the three-photon excitation and can be separately determined via field-ionization detection (see Ch. 2.4.4). For each t_{exc} we record the optical response under EIT conditions and compare it to the one in absence of impurities to deduce the additional absorption A_{add} and extract N_{add}. In Fig. 4.10 (a) we plot the spatial distribution of the number of additional absorbers N_{add} for increasing $\langle N_i \rangle$ and we clearly see that the cloud becomes progressively more absorptive for higher average numbers of impurities. The integrated number of additional absorbers along the vertical axis is plotted in Fig. 4.10 (b) (red solid line) and is compared to a Gaussian fit (blue dashed line) where the scale of the different plots has been fixed. This representation helps to observe how large the signal is compared to the residual noise in the region outside the cloud.

In order to distinguish the signal coming from different numbers of impurities, we have increased the EIT bandwidth σ_{eit} by strongly raising the coupling Rabi frequency Ω_c. Because of the small size of the sample compared to the extension of the coupling beam, we assume Ω_c to be constant, equal to $2\pi \cdot (26.2 \pm 2.3) \, \text{MHz}$ according to the beam profile estimated from a density matrix reconstruction in the dilute regime (see Ch. 3.2 for the method). To characterize how the impurities affect the optical response, we extract the total number of additional absorbers $\sum N_{add}$ for each realization through a 2D Gaussian fit over the absorption area, which allows to remove the contribution of noise outside the sample region. The plot in Figure 4.11 shows the evolution of $\sum N_{add}$ with respect to the mean number of impurities $\langle N_i \rangle$ measured by field ionization (blue points). It can be seen that ΣN_{add} linearly increases for small $\langle N_i \rangle$, before reaching a saturated value of ~ 35 additional absorbers for $\langle N_i \rangle > 5$.

Within the large coupling Rabi frequency Ω_c regime in which the experiment is performed, we can reasonably assume that $\chi_{eit}^0 \approx 0$ and we can also neglect the correction due to probe-probe interactions in equation (4.14), since $f_{rr} \approx 0.02 \ll 1$. We can then simply express the total number of additional absorbers as $\sum N_{add} = f_{ir} N$ where N is the total number of ground-state atoms in the sample. This formula shows that under our assumptions any atom within the impurity blockade volume will behave as an additional absorber. Since $\sum N_{add}$ saturates around 35 atoms, while N is on the order of 400 in the experiment, f_{ir} remains smaller than 10%, meaning that only part of the total volume is blockaded by the impurity-probe interactions,
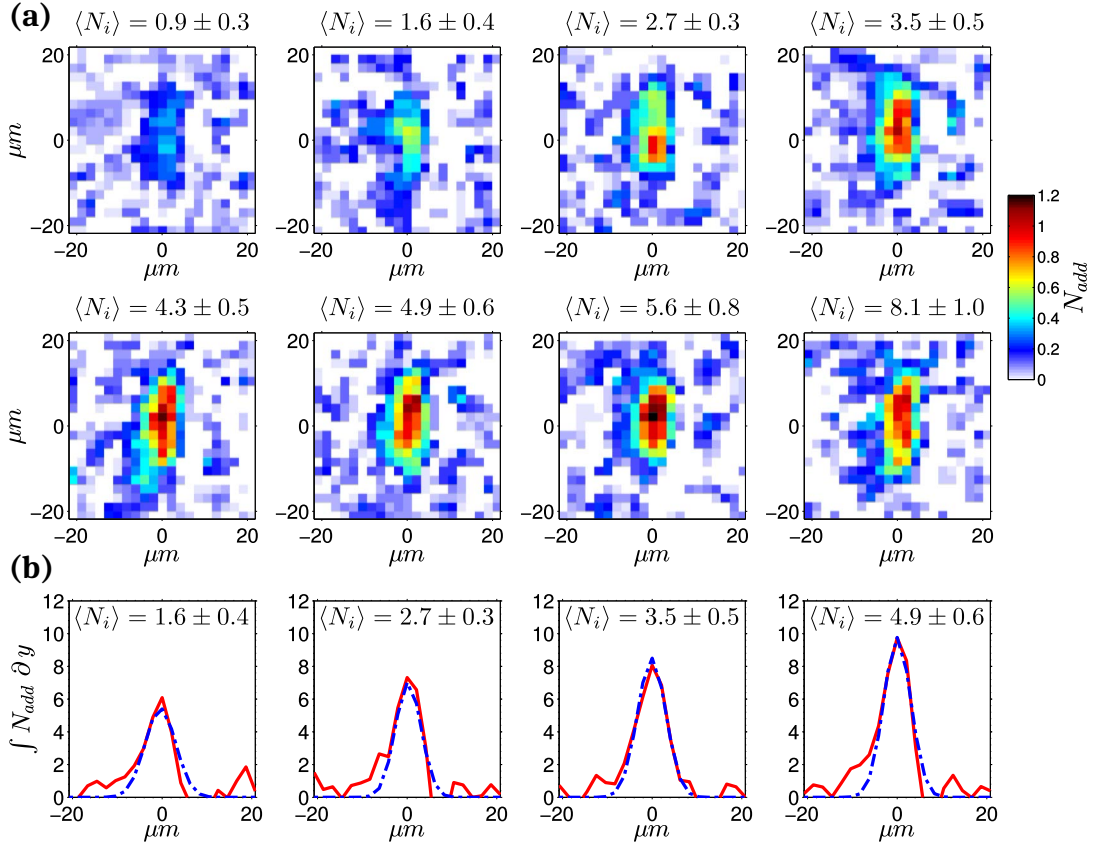
Figure 4.10: Interaction-enhanced imaging of $42P_{3/2}$ Rydberg atoms in a small atomic sample. (a) Spatial distribution of the additional absorbers per pixel N_{add} for increasing average number of impurities $\langle N_i \rangle$, as measured by field ionization. Each measurement is averaged over 50 repetitions with an exposure time of $t_{exp} = 30\,\mu\text{s}$. **(b)** Integral along the picture's vertical direction of the measured number of additional absorbers (solid red) and of a 2D Gaussian fit to the data (blue dashed line). The fit integral allows us to extract $\sum N_{add}$ from the data, while removing the noise outside of the sample region.

which is consistent with the estimated blockade radii $R_{ii} \gg R_{ir}$. We can then express $\sum N_{add}$ in an even simpler form $\sum N_{add} = \langle N_i \rangle \cdot n_0 V_{bl,i}$ (see Sec. 4.3.3).

Hence our model predicts a linear dependence of the total number of additional absorbers with the number of impurities. The amplification factor per impurity, as defined in Sec. 4.1.2, would be given here by $A^{\text{IEI}} = n_0 V_{bl,i}$. Although we observe a nearly linear increase for few impurities, our data shows an exponentially decaying growth of $\sum N_{add}$ at larger numbers $\langle N_i \rangle > 3$. This can be interpreted as a Rydberg blockade effect between the impurities during their excitation. Impurities cannot be excited in the center of the sample, while it would be still possible in the tails, where
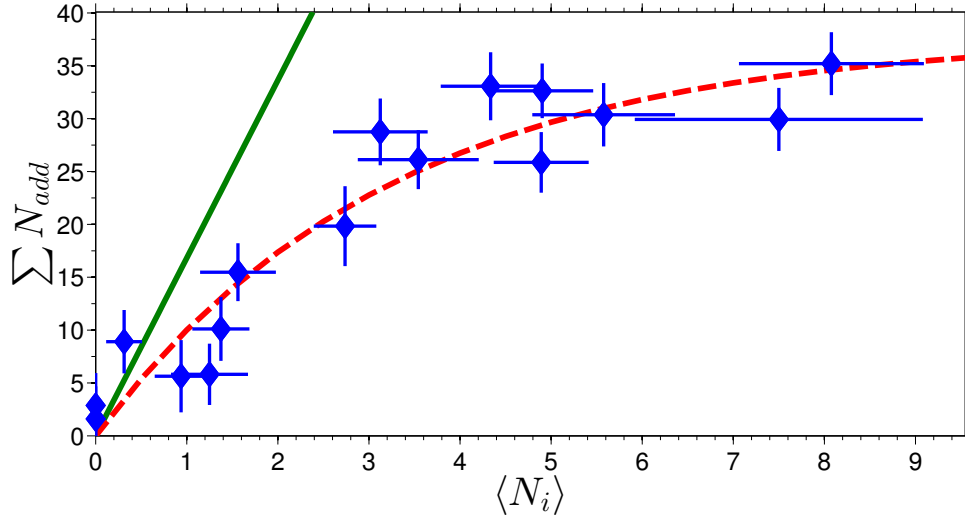
Figure 4.11: Number of total additional absorbers $\sum N_{add}$ as a function of the mean number of impurities $\langle N_i \rangle$ in the $42P_{3/2}$ state. We first observe a nearly linear growth of the additional absorbers as expected from the hard-sphere model. Then the growth decays exponentially, reaching a saturated level of around 35 absorbers, that we interpret as a signature of the Rydberg blockade effect between the impurities. We fit the experimental data to Eq. 4.16 (dashed red), obtaining an amplification factor $A^{IEI} = 17 \pm 4$ (green line) and saturation at $\langle N_i \rangle_{sat} = 2.7 \pm 0.9$, in excellent agreement with our hard-sphere model that predicts an amplification factor of 17.1. The errors are the standard errors of the mean.

the density is low and thus the change in the optical response negligible.

To measure the amplification factor, we fit our data to a model that accounts for the Poissonian excitation statistics of the impurities and the saturation induced by the Rydberg blockade effect between impurities

$$\sum N_{add}(\langle N_i \rangle) = \sum_{k=0}^{+\infty} N_{add}(k) \cdot \frac{(\langle N_i \rangle)^k}{k!} e^{-\langle N_i \rangle} \text{ with } N_{add}(k) = \sum_{j=0}^{k} A^{IEI} \cdot e^{-j/\langle N_i \rangle_{sat}},$$
(4.16)

where $N_{add}(k)$ is the total number of additional absorbers for $N_i = k$ (with $N_{add}(0) \equiv 0$) that saturates exponentially for $N_i \geq \langle N_i \rangle_{sat}$ due to the reduction of the effective amplification factor per impurity. This simple model is motivated by more advanced work on the statistics of hard rods [Ji *et al.*, 2013; Gorniaczyk *et al.*, 2014] and fits very well to the experimental data, as shown by the dashed red line in Fig. 4.11. From the fit we extract $A^{IEI} = 17 \pm 4$ and $\langle N_i \rangle_{sat} = 2.7 \pm 0.9$, in excellent agreement with our hard-sphere model that predicts an amplification factor of 17.1.

These measurements demonstrate that IEI is suitable to detect individual Rydberg

impurities with a sensitivity of 1 impurity on average. Moreover in the regime of strong EIT coupling and few impurities, the number of additional absorbers changes linearly with the number of impurities and depends only on the atomic density n_0 and the EIT bandwidth σ_{eit} through the blockade volume. This relationship allows to directly estimate the number of impurities without considering the microscopic details of the imaging.

4.6 Prospects

Interaction Enhanced Imaging has proved a powerful method to optically image Rydberg $|nS\rangle$ states and to investigate with high spatial and temporal resolution energy transport dynamics of pairs of Rydberg S-state atoms, driven by strong dipole-dipole interactions. These first studies have motivated further work towards the realization of $|nP\rangle$-$|nS\rangle$ transport experiments.

Here we have demonstrated optical imaging of Rydberg P-states via IEI. To prepare the atom sample, we have implemented and characterized a well-controlled excitation scheme that allows us to reliably excite a chosen average number of atoms in a Rydberg P-state, without perturbing the cloud. The scheme is based on a three-photon off-resonant excitation, which avoids population of any other Rydberg state. A theoretical analysis has allowed us to introduce a simple description of the excitation scheme in terms of an effective two-level system which provides accessible tools to fully optimize the excitation dynamics.

To gain insight into the imaging process, we have extended an analytic hard-sphere model, first introduced to describe interactions within the EIT medium, to include Rydberg impurity-medium interactions and we have used it to predict the optical response of the system. Then, using our technique, we have successfully imaged Rydberg atoms prepared in the $\left|42P_{3/2}\right\rangle$ state in a large atomic sample and we have compared the estimated signal with experimental data, finding good agreement. Furthermore, measurements in a small atomic sample with dimensions comparable to the impurity-impurity blockade radius R_{ii} have shown that we can reach a sensitivity of few Rydberg atoms with IEI, close to the best competing methods [Schwarzkopf *et al.*, 2011; Schauß *et al.*, 2012; McQuillen *et al.*, 2013; Lochead *et al.*, 2013], with the important benefit that we do not destroy the Rydberg atoms under observation. A further improvement of IEI will consist in reaching single-impurity sensitivity on single-shot measurements and this will be the subject of the next chapter.

One of the main advantages of the IEI method is that the spatial resolution is

given by the impurity-probe blockade radius R_{ir}, convolved with the optical resolution of the imaging system. Consequently it can be engineered to be smaller than the typical impurity-impurity distance R_{ii}, allowing for spatially-resolved single-impurity imaging. Combined with a high sensitivity, the IEI technique might be promising for spatial correlation measurements of Rydberg ensembles in bulk atomic gases, opening perspectives to study energy transport mechanisms in open systems [Schönleber *et al.*, 2015; Schempp *et al.*, 2015] or the formation of Rydberg aggregates [Malossi *et al.*, 2014; Schempp *et al.*, 2014; Urvoy *et al.*, 2015].

Chapter 5

Improving the sensitivity of Interaction Enhanced Imaging

In the last chapter we discussed the Interaction Enhanced Imaging method and we demonstrated optical detection of Rydberg P atoms in the $|i\rangle = \left|42P_{3/2}, m_J = +3/2\right\rangle$ state. By averaging over many repetitions we could measure the amplification factor per impurity and observe the increase of the spatially resolved absorption together with the mean number of excited P states. Averaging was used to improve the signal to noise ratio in the optical detection.

Reaching single impurity sensitivity in single-shot IEI measurements would allow to directly observe the dynamics and correlations of a strongly interacting Rydberg gas without destroying the sample [Günter *et al.*, 2012], allowing potentially to track the evolution of the system in time, which is not possible for inherently destructive methods like fluorescence imaging [Schauß *et al.*, 2012; Labuhn *et al.*, 2016] or field ionization [Schwarzkopf *et al.*, 2011; Schwarzkopf *et al.*, 2013]. With single impurity sensitivity new studies of energy transport dynamics induced by dipolar interactions would become possible, e.g. by following the dynamics of a single Rydberg impurity in a system with highly controllable geometry and dimensionality [Günter *et al.*, 2013; Schempp *et al.*, 2015; Schönleber *et al.*, 2015; Fahey *et al.*, 2015; Yu and Robicheaux, 2016]. IEI could also become an alternative method to fluorescence imaging to probe the spatial correlations of crystalline states of higly excited Rydberg atoms arranged in an optical lattice and prepared via an adiabatic frequency sweep protocol [Pohl *et al.*, 2010; van Bijnen *et al.*, 2011; Schauß *et al.*, 2012; Schauß *et al.*, 2015; Vermersch *et al.*, 2015; Petrosyan *et al.*, 2016]. Recently it has been shown that Rydberg atoms can be used to engineer spin models with long-range interactions [Hazzard *et al.*, 2014; Glaetzle *et al.*, 2015; van Bijnen and Pohl, 2015; Barredo *et al.*, 2015; Labuhn

et al., 2016; Whitlock *et al.*, 2016] and many Hamiltonians can be implemented using different state combinations. The possibility to image S or P Rydberg states with IEI could prove a powerful method to investigate the evolution and correlations of such systems, both in ordered geometries or random samples.

The most detailed studies of a quantum system require single particle sensitivity [Bakr *et al.*, 2009; Bakr *et al.*, 2010; Sherson *et al.*, 2010; Cheuk *et al.*, 2015; Greif *et al.*, 2016; Ott, 2016] which in turn demands an IEI SNR far above 1, while probing the system within a short time compared to the dynamics of the impurities, typically few µs. In this chapter we perform a detailed analysis of the signal and noise contributions in IEI and we formulate and test a strategy to reach the desired sensitivity. We start first by introducing appropriate observables to quantify our current sensitivity level in Ch. 5.1. Then in Ch. 5.2 we identify which factors contribute to the noise of our detection method and in Ch. 5.3 we formulate strategies to address them. In Ch. 5.4 we test the impact of the proposed methods on the detection sensitivity and in Ch. 5.5 we investigate how single particle sensitivity can be reached.

5.1   Fidelity and sensitivity

To quantify the sensitivity achievable in a single Interaction Enhanced Imaging measurement we will use a statistical approach. A measurement of a quantity X, formally defined "measurand" [JCGM, 2012], is performed to learn its true value. However, the measurement outcome x would never correspond to the quantity itself, nor would it be exact, instead it would represent an estimate of the measurand's true value. Repeated measurements would normally give a distribution of values, assuming that the measuring system has sufficient resolution to distinguish between the different outcomes [JCGM, 2009]. The properties of this distribution quantify how precisely we believe to know the true value of the studied quantity and express this concept quantitatively through the measurement uncertainty. This uncertainty reflects our incomplete knowledge on the measurand and brings the study into the probability and statistical analysis domain.

There are two types of uncertainty associated with a measurement, systematic and random errors [JCGM, 2008]. A systematic error (also called measurement bias) introduces an offset in the measured quantity relative to the expected true value. If the causes of a systematic error are known, then a correction can be applied to compensate the offset. A random error represents the fact that a new measurement

will give a different value which cannot be predicted from previous observations.

The analysis of the statistical properties of the measured distribution [Cowan, 1998] allows to obtain detailed information on the measurand. The first property that can be estimated is the average value of the distribution $\mu(x) = \langle x \rangle$ and it provides an estimate of the true value of the quantity of interest. The dispersion of the measured values, expressed through the standard deviation $\sigma(x)$, is connected both to how well the measurement is performed and to the statistical properties of the measurand. It quantifies the probability of observing a certain value different from the distribution mean. For example, for a normal distribution a measurement will give a value within $1\,\sigma$ from the mean μ in 68.26% of the repetitions. The square of the standard deviation, called variance $\text{var}(x) = \sigma^2(x)$, can also be of interest. For example, a Poisson distribution, which describes random processes, has the characteristic property of having equal variance and mean $\text{var}(x) = \mu(x)$.

The mean, standard deviation and variance are examples of descriptive statistics, in other words they quantify properties of the observed distribution. Since we always estimate them using a finite number of measurements, we perform in practice a random sampling of the underlying distribution. A legitimate question arises: how does the sample size affect the calculation? How far are these quantities likely to be from estimations done on an ideal infinite size sample? For each estimator it is possible to provide a bound on its $1\,\sigma$ confidence interval by computing its standard deviation. In the following we will focus on the mean and variance of the measured distributions, for which the standard deviations are [Cowan, 1998; Brandt, 2014]:

$$\sigma_{sem} = \sigma(\mu(x)) = \frac{\sigma(x)}{\sqrt{n}}, \quad \sigma_{var} = \sigma(\text{var}(x)) = \sqrt{\frac{n-1}{n^3}\left[(n-1)\mu_4 - (n-3)\mu_2^2\right]}$$

(5.1)

where n is the sample size and μ_i is the unbiased central moment of order i. These two estimators are called respectively standard error of the mean σ_{sem} and standard error of the variance σ_{var}. If the standard deviation is finite, with increasing sample size these standard errors will tend to zero, while the standard deviation will tend to approximate the "true" standard deviation of the distribution.

Now we turn to the question of having two sets of measurements and wanting to compare them. We have to define which quantity represents the signal of interest and decide the error associated with it. By making this choice we construct a test statistic t with a so called "null" hypothesis H_0 that we want to verify and one or more alternative hypotheses $H_1, ...H_i$. Now we have to choose a critical region of the test statistic parameter space where the null hypothesis would be rejected. This region has to be chosen such that the probability ϵ of incorrectly rejecting H_0 while

it was true would equal a certain value that defines the test significance level.

The simplest criterion which can be applied as a test statistic is to calculate the signal to noise ratio (SNR). A SNR higher than 1 means that the signal is bigger than its error. Crossing a chosen threshold SNR value would define when to accept or reject the null hypothesis.

In an IEI experiment we shine a probe laser beam through the atom cloud and record on the CCD camera two distributions of the number of transmitted photons (converted into electrons), one under EIT conditions and a second one under EIT in presence of impurities (see Ch. 4.4). A natural choice for the signal would be the difference between the means of these distributions

$$\langle N_{e^-, add} \rangle = \langle N_{e^-, eit} \rangle - \langle N_{e^-, imp} \rangle. \tag{5.2}$$

If we take as noise the root of the sum of the squares of the two standard errors of the mean $\sqrt{\sigma_{sem, eit}^2 + \sigma_{sem, imp}^2}$, we test the null hypothesis that the two means are distinguishable and, considering Eq. (5.1), arbitrarily high SNRs are reachable by increasing the sample size through averaging over many repetitions. This was the approach followed in Ch. 4.5 to optically detect few Rydberg P state impurities with spatial resolution. Choosing instead as noise the root of the sum of the squares of the standard deviations $\sqrt{\sigma_{eit}^2 + \sigma_{imp}^2}$ we test a different null hypothesis, asking if the two distributions are distinguishable. It is this null hypothesis that we want to study in this chapter and for this goal a test statistic other than the SNR, called detection fidelity $\mathcal{F}$, can provide a better estimation.

To define the detection fidelity $\mathcal{F}$ for the null hypothesis that impurities are present in the cloud we follow the conservative definition of [Bochmann *et al.*, 2010] which states that the fidelity is the minimum probability of inferring the correct hypothesis from any value measured in a single experiment. The fidelity is then expressed as

$$\mathcal{F} = 1 - \epsilon_{max} \tag{5.3}$$

where ϵ_{max} is the maximum of the probabilities to incorrectly assign each possible hypothesis, considering errors in the detection as well as in the initial state preparation. This test statistic is often used to discriminate between two or more outcomes of an experiment and is the method of choice for quantum computation experiments realized with single ions [Cirac and Zoller, 1995; Leibfried *et al.*, 2003; Roos *et al.*, 2004; Acton *et al.*, 2006; Myerson *et al.*, 2008; Harty *et al.*, 2014; Debnath *et al.*, 2016] or with neutral atoms trapped in an optical cavity [Bochmann *et al.*, 2010; Gehr *et al.*, 2010]. It has also found application in the Rydberg atom domain

in experiments that realized single-photon optical transistors leveraging EIT and strong Rydberg-Rydberg interactions [Tiarks *et al.*, 2014; Gorniaczyk *et al.*, 2014; Gorniaczyk *et al.*, 2016]. In these experiments a non-destructive detection of a single impurity in a single shot has been reported with detection fidelities up to $\mathcal{F} = 0.86$ [Tiarks *et al.*, 2014], after removing the systematic effect of the probabilistic impurity excitation.

When we perform an IEI experiment we measure the mean number of excited impurities $\langle N_i \rangle$ through the field ionization detection. For a given $\langle N_i \rangle$ we take as null hypothesis H_{imp} the presence of this average impurity number and as alternative hypothesis H_{eit} that there are none. We employ the threshold method [Cowan, 1998] to define the critical parameter region for the fidelity test statistic. We set an initial arbitrary threshold on the number of detected electrons $N_{e^-, thr}$ and for each single measurement we accept H_{imp} if $N_{e^-, imp} < N_{e^-, thr}$, otherwise we reject it. We proceed similarly for H_{eit}, accepting it if $N_{e^-, eit} > N_{e^-, thr}$, otherwise we reject it. The threshold position defines the two probabilities ϵ_{imp} and ϵ_{eit} that we incorrectly reject H_{imp} and H_{eit} when $\langle N_i \rangle \neq 0$ and $\langle N_i \rangle = 0$, respectively. Then the total probability of incorrectly assigning the hypothesis is $\epsilon_{max} = \max(\epsilon_{imp}, \epsilon_{eit})$. Finally the threshold position has to be varied to find the optimum position that maximizes the fidelity $\mathcal{F}$.

It is evident now that the fidelity provides a more precise test of a hypothesis than the SNR because it considers the whole measured distribution of values, and not only its variance, thus avoiding any assumption on the distribution form. If the measured distributions are well described by a normal distribution, it is possible to make a direct connection between the two statistical tests. As we noted at the beginning of this section, an SNR = 1 means that 68.26% of the measured values will fall within 1σ from the mean μ and the corresponding fidelity would be $\mathcal{F} = 1 - 0.6826/2 = 0.8413$, while for SNR = 2 the probability is 95.45% leading to $\mathcal{F} = 0.9773$ and for SNR = 3 we get $\mathcal{F} = 0.99865$.

The last observable we are interested in is the sensitivity S. Sensitivity is commonly defined for measurement instruments as the smallest change in an input signal that can cause the measuring device to respond. Such definition can be straightforwardly applied to our imaging method where it would correspond to the smallest number of impurities that lead to a change in the medium optical response distinguishable from the noise background in a single shot measurement. This coincides with $\mathcal{F} = 0.8413$ and, for a normal distribution, with SNR = 1.

We can now quantify our current sensitivity level by estimating the detection fidelity on a set of IEI experiments performed with $|43S_{1/2}\rangle$ impurity and $|42S_{1/2}\rangle$
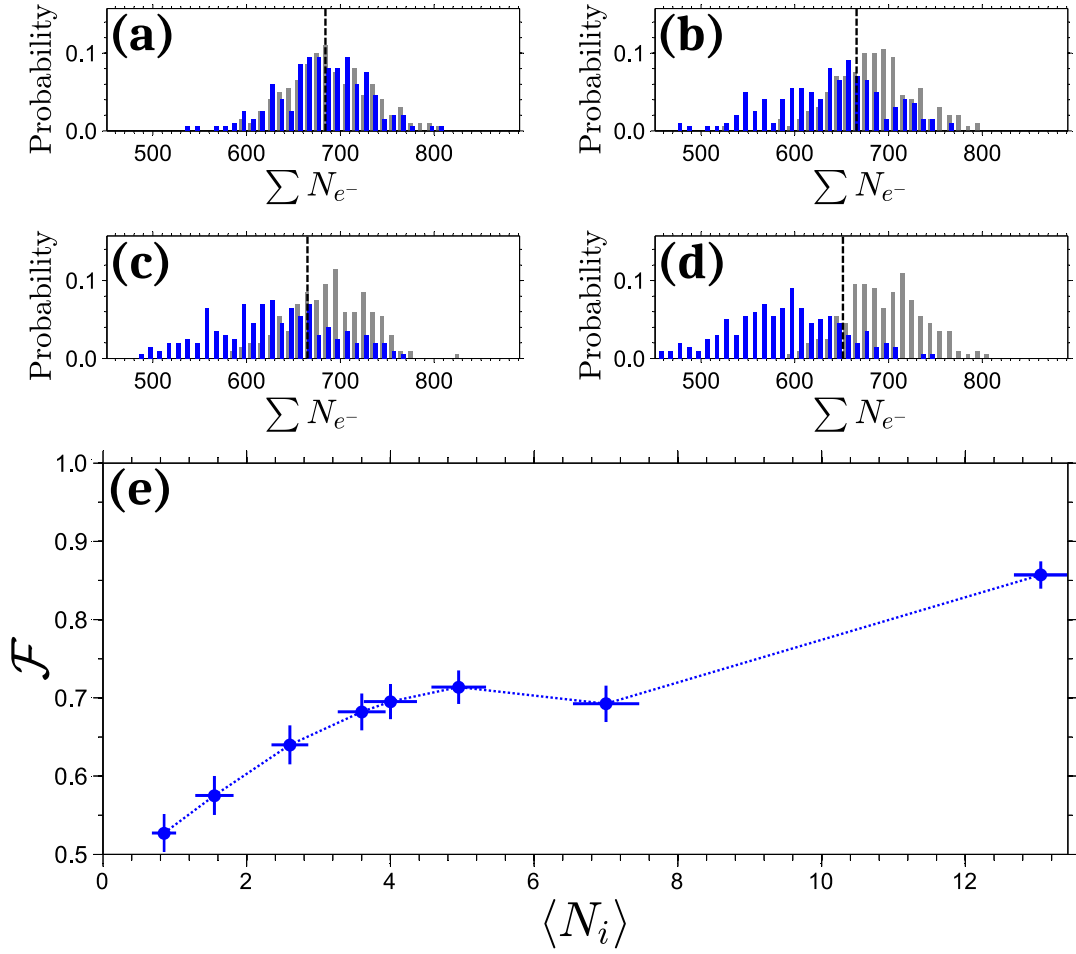
Figure 5.1: Histograms of measured electron distributions on the CCD camera and single-shot IEI detection fidelity for increasing mean number of impurities. The IEI experiment is performed with $\left|43S_{1/2}\right\rangle$ impurity and $\left|42S_{1/2}\right\rangle$ probe states in the "tight" dipole trap. The number of detected electrons in presence of impurities (blue) and without (grey) is summed over the cloud and the normalized probability distribution is calculated over 200 repetitions, shown respectively for 0.8 ± 0.2 **(a)**, 3.6 ± 0.3 **(b)**, 5.0 ± 0.4 **(c)** and 13.1 ± 0.4 **(d)** average impurities. **(e)** We apply the photon threshold method to each probability distribution to estimate the single-shot detection fidelity (vertical black lines indicate the optimum threshold). For $\langle N_i \rangle = 3.6 \pm 0.3$ we reach $\mathcal{F} = 0.68 \pm 0.2$, while for $\langle N_i \rangle = 13.1 \pm 0.4$ we achieve $\mathcal{F} = 0.86 \pm 0.2$. Error bars are statistical standard errors of the mean.

probe states for increasing $\langle N_i \rangle$, with 200 repetitions each. We prepare the atoms in the ground state $|g\rangle$ in the "tight" dipole trap at a temperature of $T = 1\,\mu\text{K}$ with a peak density of $n_0 = (7.0 \pm 0.2) \cdot 10^{11}\,\text{cm}^{-3}$ and we probe the system during $t_{exp} = 10\,\mu\text{s}$ using $\Omega_p = 2\pi \cdot (0.30 \pm 0.05)\,\text{MHz}$ and $\Omega_c = 2\pi \cdot (20 \pm 1)\,\text{MHz}$. To

improve the SNR at this small probe Rabi frequency we apply directly on the CCD camera a hardware binning of $N_{bin} = 20$ pixels, placing almost the whole cloud in two "super-pixels".

The number of detected electrons is summed over the cloud and the normalized probability distribution in presence of impurities (blue) and without (grey) is shown in figure 5.1 (a-d) for increasing $\langle N_i \rangle$. We observe that at first the two distributions overlap completely and then they start to diverge, appearing well separated for $\langle N_i \rangle = 13.1 \pm 0.4$, so we intuitively would expect that the detection fidelity will be initially close to 0.5 and then reach higher values. We now apply the photon threshold method to each probability distribution (vertical black lines indicate the found optimum threshold) to estimate the single-shot detection fidelity, shown in Fig. 5.1 (e). The analysis confirms our expectation and shows that for $\langle N_i \rangle = 3.6 \pm 0.3$ we reach $\mathcal{F} = 0.68 \pm 0.2$, while for $\langle N_i \rangle = 13.1 \pm 0.4$ we achieve $\mathcal{F} = 0.86 \pm 0.2$. Both error bars are standard errors of the mean and the fidelity ones are estimated using the bootstrap method [Efron and Tibshirani, 1994].

Using the previously defined criterion for the sensitivity, we estimate the current level to be $S = 12$ for the investigated $\left|43S_{1/2}\right\rangle$-$\left|42S_{1/2}\right\rangle$ impurity-probe state combination. The measured sensitivity is far from the desired level of 1 and to improve it we have to understand which error sources affect IEI.

5.2 Error sources in Interaction Enhanced Imaging

As discussed in Ch. 4.1.2, Interaction Enhanced Imaging is a method based on an absorption technique where the atom cloud acts as a contrast medium in such a way that the absorption is modified by the presence of the Rydberg impurities. Consequently, the technique is affected by two types of noise, one coming from the light and the second from the absorption process.

5.2.1 Camera photon transfer curve

The first source of error arises from the detection process of light on the CCD camera. The latter converts the incoming photons on each pixel of area a_{px} into electrons with a quantum efficiency Q_e such that the number of electrons per pixel N_{e^-} is proportional to $I \cdot t_{exp} \cdot Q_e$, with t_{exp} the exposure time of the imaging and I the intensity of the beam. The properties of CCD cameras have been extensively studied [Janesick, 2001; Robbins and Hadwen, 2003; Basden *et al.*, 2003; Hirsch *et al.*, 2013] and a reliable method to characterize their noise contribution is the

photon transfer technique [Janesick *et al.*, 1985; Janesick, 2007]. For each pixel we measure the mean $\langle N_{e-}\rangle$ and the variance $\mathrm{var}(N_{e-})$ of the detected electron number over many images acquired at a fixed incident beam power and we repeat this measurement for many power levels. Then we plot the observed variance as a function of the mean, constructing the camera photon transfer curve, as shown in Fig. 5.2.
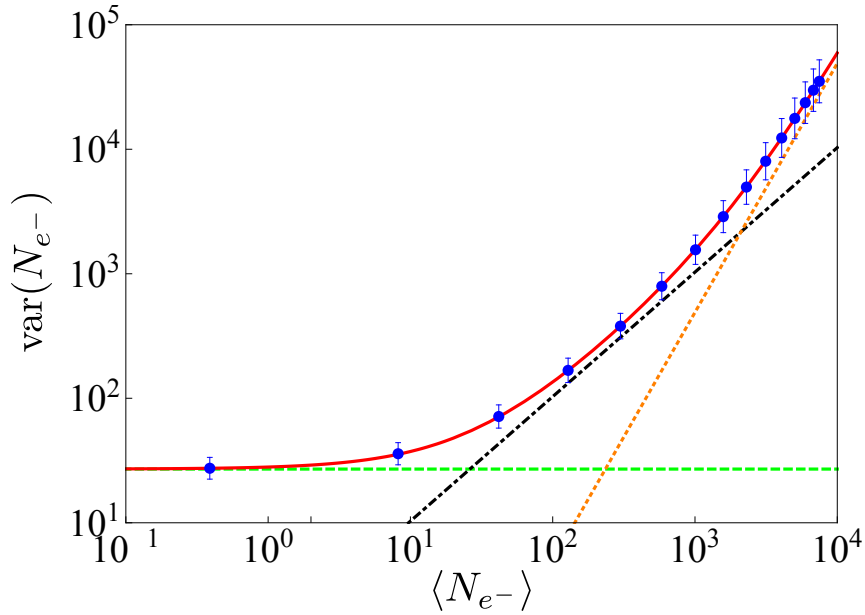
Figure 5.2: CCD photon transfer curve. Variance $\mathrm{var}(N_{e-})$ vs. mean value $\langle N_{e-}\rangle$ of the electron number detected on our camera (blue points). The mean values and its variances are calculated for each pixel over 50 repetitions, then fitted with a second order polynomial (Eq. (5.4)) whose parameters are in agreement with the expected ones. At low signal the noise is dominated by the readout noise of the camera (green dotted line, $\sigma_{rd}^2 = 27.0 \pm 0.1$), at intermediate levels by the photon shot noise (black dash-dotted line, best fitting slope $= 1.031 \pm 0.004$), while above $10^3\,\mathrm{e}^-/\mathrm{px}$ the noise scales quadratically with the signal (orange dotted line, $\sigma_{gf}^2 = (4.90 \pm 0.02) \cdot 10^{-4}$).

We identify three regions, each dominated by one main error source. For very low signal the electronic noise σ_{rd} introduced by the charge readout dominates (constant at each chosen camera setting, green dotted line). Between ~ 20 and $10^3\,\mathrm{e}^-/\mathrm{px}$ we are limited by the photon statistics of the incident light. Since we use a laser source, we expect the emitted photons to follow a Poisson distribution [Glauber, 1963], which is confirmed by the data (the black dash-dotted line has unity slope). For $\langle N_{e-}\rangle > 10^3\,\mathrm{e}^-/\mathrm{px}$ we observe a quadratic scaling of the variance with the mean (orange dotted line). The exact origin of this error contribution is not known, but,

since we analyse each pixel indipendently, we can exclude that it is caused by fixed pattern noise which represents the non-uniformity between pixels [Mooney *et al.*, 1989; Joseph and Collins, 2002]. A drift of the mean light intensity in a single dataset could contribute to enhance the noise in the quadratic region, but this has been verified not to be a significant/dominant effect. A detailed error propagation of the noise sources present in a CCD detector (see App. B) shows that a quadratic term affecting each pixel may originate from fluctuations of the gain factor σ_{gf} applied in the camera pre-amplification stage.

We can now express the expected noise level for a given number of electrons N_{e^-} through a simple second order polynomial model

$$\mathrm{var}(N_{e^-}) = \sigma_{rd}^2 + N_{e^-} + \sigma_{gf}^2 N_{e^-}^2 \tag{5.4}$$

The lowest impact of noise on the signal is in the photon shot-noise limited regime, while for high intensities the SNR will saturate. To reduce the contribution of readout noise we use the slowest camera readout speed which has the smallest σ_{rd} and we can apply hardware binning on the pixels at the expense of spatial resolution. If we assume for simplicity a constant signal per pixel, hardware binning will increase the SNR linearly with the number of binned pixels N_{bin}, in contrast to binning done in software where the improvement would scale with $\sqrt{N_{bin}}$.

5.2.2 Atom number fluctuation

We now investigate the noise contribution of the atom cloud. Considering first the case of a two-level system, we expect from Eq. (3.14) that the medium will transmit only a fraction of the incident light. If the number of absorbing atoms fluctuates between experiments, then the transmission will also vary, leading to an increased variance of the detected electron number. To experimentally confirm our expectation, we prepare a cloud in the "tight" dipole trap with a peak density of $n_0 = (2.0 \pm 0.4) \cdot 10^{11}\,\mathrm{cm}^{-3}$ and we probe the system for a variable exposure time $t_{exp} = 2 - 40\,\mu\mathrm{s}$ using $\Omega_p = 2\pi \cdot (1.20 \pm 0.05)\,\mathrm{MHz}$ and a hardware binning of $N_{bin} = 20$. In the pixel with the peak density we calculate the mean and the variance of the measured electron number (blue points in Fig. 5.3 (a)) and we find that the variance is few orders of magnitude higher than the photon transfer curve (red), confirming our expectation that fluctuations in the cloud absorption play an important role.

We now model the observed effect. Using Eq. (2.13) we calculate the atom number in each image and we fit it with a 2D Gaussian function, finding that the total atom
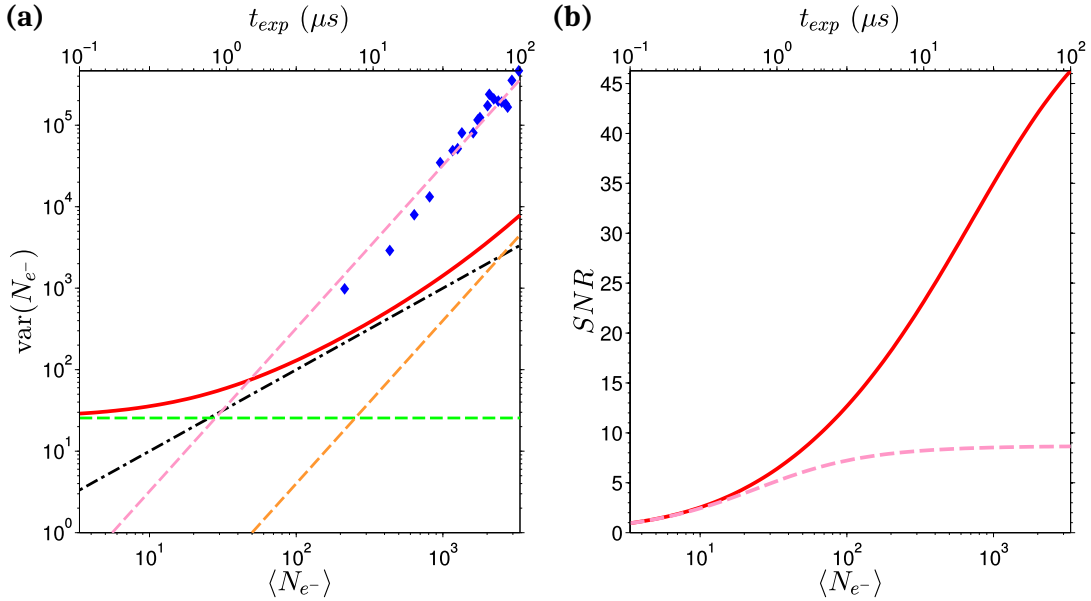
Figure 5.3: Impact of atom number fluctuations. (a) Variance $\text{var}(N_{e^-})$ vs. mean value N_{e^-} of the electron number on our camera in presence of an atomic cloud (blue points). The previously measured photon transfer curve (solid red) does not describe the observed variance. The deviation can be accounted for by including the effect of shot to shot variations in the cloud absorption (dashed pink), originating from an atom number fluctuation of $\approx 20\%$. **(b)** Expected SNR for absorption imaging as a function of exposure time. Atom number fluctuations (dashed pink) strongly reduce the SNR in comparison to the photon shot noise limited case (solid red).

number varied during the experiment by $\approx 20\%$. Including the transmission term $e^{-\tilde{\chi}\frac{\sigma_0}{a_{px}}N_{atoms}}$ in the error propagation of the noise sources affecting a CCD detector (see App. B) we obtain a model for the detection noise in presence of absorption:

$$\text{var}(N_{e^-}) = \sigma_{rd}^2 + N_{e^-} + \sigma_{gf}^2 N_{e^-}^2 + \tilde{\chi}^2 \frac{\sigma_0^2}{a_{px}^2 Q_e} N_{e^-}^2 \text{var}(N_{atoms}) \tag{5.5}$$

The contribution of the atom number fluctuation scales quadratically with N_{e^-} and can potentially become the dominant error source. In such a regime the atomic noise contribution can be easily separated from the light contribution. Considering for $\text{var}(N_{atoms})$ the square of the product between the measured total atom number fluctuation and the atom number measured in the selected pixel, we estimate the excess variance caused by atom fluctuation and we obtain a fair agreement with the observed values (pink dashed line). Using equations $(2.13, 2.16, 5.5, 5.4)$ we can calculate the expected SNR with and without the contribution of atom number fluctuations and we find a strong reduction of the peak achievable value, as shown

in Fig. 5.3 (b). We conclude that this effect has a detrimental impact on statistical measurements, like the IEI fidelity determination, and in Ch. 5.3.2 we will discuss a method to compensate it.

5.2.3 Population of additional states under EIT

We now consider the case of a cloud of atoms under EIT coupling. At densities below $n_0 = 10^{10}\,\mathrm{cm}^{-3}$, as investigated in Ch. 3.2, the interaction effects between probe Rydberg states can be safely neglected and the scaled susceptibility is $\tilde{\chi} \approx 0$, consequently the contribution of atom number fluctuations should be completely suppressed according to Eq. (5.5). For higher ground state densities, like in IEI experiments, the probe Rydberg state density increases, conforming to Eq. (4.10), and the absorption caused by probe-probe Rydberg interactions becomes significant, as observed in Ch. 4.5.1. In this regime we expect that cloud absorption fluctuations will be caused by global atom number fluctuations like in the two-level system case, but an additional contribution may arise from fluctuations in the scaled susceptibility induced by variations in the Rydberg state population. Using our combined detection we can access both the optical response of the cloud and the Rydberg state population and correlate them (see Ch. 3.2).

To experimentally confirm our expectation, we perform a new set of measurements under EIT coupling to the $\left|42S_{1/2}, m_J = +1/2\right\rangle$ state with $\Omega_c = 2\pi \cdot (10 \pm 2)\,\mathrm{MHz}$, varying the density $n_0 = 1.0 - 2.0 \cdot 10^{11}\,\mathrm{cm}^{-3}$ and the exposure time $t_{exp} = 2 - 40\,\mathrm{\mu s}$, with other parameters as in Ch. 5.2.2. Since the imaging pulses are much longer than the typical decay time Γ_e^{-1}, we consider the system to be in the steady state. Before investigating the variances of the observed electron number and Rydberg state population, we check if the means of the optical density and of the detected number of ions are stationary in time.

Figure 5.4 shows the optical density (blue) and number of detected ions (red) as a function of exposure time for $n_0 = (1.2 \pm 0.1) \cdot 10^{11}\,\mathrm{cm}^{-3}$. The initial values are compatible within $1\,\sigma_{sem}$ with the ones expected from the hard-sphere model (OD = 0.14 and $N_{ions} = \eta N_{ryd} = 12.4$), but, in stark contrast to our expectation, we observe that both quantities undergo an evolution in time. The same dynamic is found for all the investigated densities, with different increase rates that we extract through a linear fit (solid lines). We have checked the variance of the detected electron number and it also increases as a function of the exposure time.

We find that the OD and ion number increase rates scale linearly with the cloud density and that the measured increase rate of the ion number is consistent within
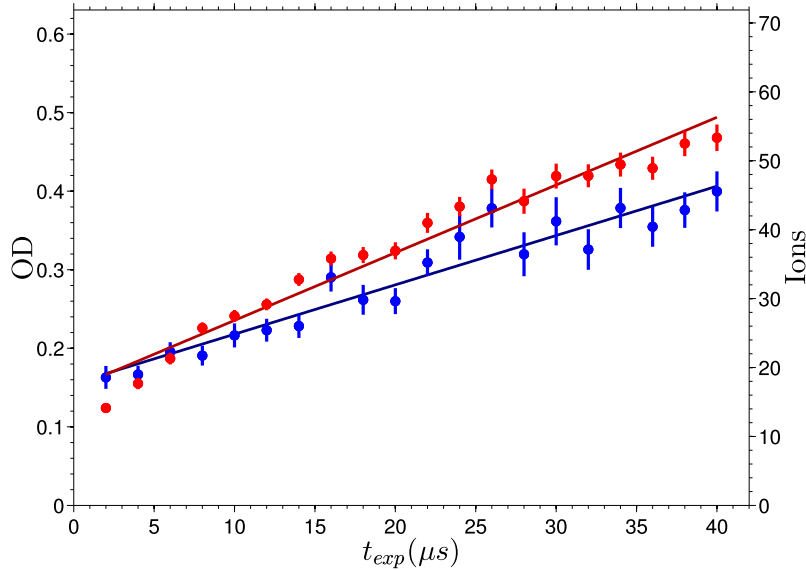
Figure 5.4: Optical density under EIT condition (blue) and number of detected ions (red) as a function of exposure time. Both quantities increase with t_{exp}, instead of being stationary (Ch. 3.1). The solid lines are linear fits used to extract the increase rates and the errors are standard errors of the mean. The OD is measured in the pixel corresponding to the cloud center.

a factor of 2 with the rate expected for black body radiation induced population of states neighboring the $|42S\rangle$ probe state [Gallagher, 1994; Branden *et al.*, 2010] ($\tau_{42S,BBR} = 84\,\mu s$ [Beterov *et al.*, 2009]). We lack state selective field ionization detection capability to confirm the population of additional Rydberg states, so other processes, like population of the Rydberg Zeeman sublevel $m_J = -1/2$ [Hofmann *et al.*, 2013] or plasma formation by spontaneous ionization [Robert-de Saint-Vincent *et al.*, 2013], cannot be excluded. If black body radiation induced population of additional states occurs, we can also explain the linear increase of the optical density with exposure time. $|n'P\rangle$ states have the highest probability to be populated and, once present, they would act as impurities, interacting strongly with the probe Rydberg state $|r\rangle$ through resonant dipole-dipole interactions. The population in $|r\rangle$ is constantly repumped by the laser coupling, so the population in P and other states will increase linearly over time, enhancing the interaction effects and consequently leading to a gradual increase in the medium susceptibility and absorption.

Similar effects have been recently observed in other experiments. Han *et al.* [Han *et al.*, 2016] measured the EIT spectrum of a gas of ^{87}Rb Rydberg atoms within a range of densities $n_0 = 0.1 - 3.0 \cdot 10^{11}\,\mathrm{cm}^{-3}$ for different states $|27S\rangle \leq |nS\rangle \leq |43\rangle$ and modeled it using a hard-sphere approach very similar to ours. The spectra showed

a blue shift compatible with the effect of probe-probe interactions, but required an additional exposure time dependent dephasing term to account for changes in the optical response. Experiments aimed at demonstrating Rydberg-dressing with $|nS\rangle$ states of ^{87}Rb [Goldschmidt *et al.*, 2016] and ^{84}Sr [DeSalvo *et al.*, 2016; Aman *et al.*, 2016] observed a broadening and time dependent dephasing rate of the two-photon excitation spectra for increasing atomic density and excitation strength that could not be accounted for by van der Waals interactions, while a model with strong dipole-dipole interactions caused by black body radiation induced population of $|n'P\rangle$ states could describe the measurements.

In conclusion we have found that an additional effect under EIT conditions causes an increase of the optical response over time and we have identified a potential mechanism which can explain the data. This process impacts negatively both the separation and the width of the number of electrons detected under EIT and in presence of impurities. To avoid this effect it is necessary to perform IEI experiments at exposure times shorter than the timescale of the black body induced transitions, with the drawback of severely limiting the total number of photons detected on the CCD. Another method could be to cool the experimental apparatus down to few K in order to strongly reduce the black body transitions rates [Beterov *et al.*, 2009], but this would require major changes in the setup.

5.2.4 Probabilistic impurity excitation

At last, we consider the case of a cloud of atoms under EIT coupling in presence of impurities. We expect that this system will be affected by all error sources discussed in Ch. 5.2.3 and that one more process will contribute to fluctuations in the cloud absorption. To prepare the impurities we use a probabilistic protocol (see Ch. 2.5) and through field ionization detection we verify that in good approximation it follows a Poisson distribution, as long as the impurity-impurity Rydberg blockade effect can be neglected [Hofmann *et al.*, 2013; Gavryusev *et al.*, 2016a]. When we perform multiple repetitions of an IEI experiment we can control only the average impurity number $\langle N_i \rangle$, but in each shot there will be a different discrete number of them, down to none, and each will revert to being absorptive a number of surrounding ground state atoms, given by the amplification factor. This represents a source of systematic error in the fidelity. If we could model the effect of this process on the detected number of electrons, then it would be possible to remove its contribution, as done in [Tiarks *et al.*, 2014; Gorniaczyk *et al.*, 2014]. A candidate model could be the one used in Ch. 4.5 to extract the amplification factor, knowing the $\langle N_i \rangle$ for each

set of experiments. A first problem is that the measured amplification factor and the saturation number are affected by a significant error, even after averaging the data over many repetitions, and furthermore the current sensitivity level does not allow us to distinguish the means of electron number distributions for few to zero impurities which is required to decompose them into the underlying contributions. Due to these considerations the development and application of a model is not justified.

We also check if post-selection based on the number of ions measured at the end of each IEI repetition can be applied, but a cross-correlation of this quantity with the number of additional absorbers shows only a weak relation, leading to a negative answer. The potential presence of additional states with an unknown distribution may partially explain this finding.

5.3   Error contribution reduction

Now that the main error sources that affect IEI have been identified we develop two methods to reduce the variance contribution of light intensity drifts and of global atom number fluctuations in the cloud, with the aim of narrowing the width of the electron distributions under EIT, with and without impurities.

5.3.1   Light intensity fluctuation compensation

The photon shot noise contribution of light is a fundamental limitation affecting absorption imaging, while drifts of the mean light intensity between experiments or single images are not. For example, if the mean light intensity fluctuates between the absorption and reference images, then an offset would appear in the atom number determination with Eq. (2.13). We can easily remove this systematic effect by rescaling each image by the ratio between the global mean of the electron number over the whole measurement set and the average number in each image, measuring them in a region of interest outside the cloud,

$$N_{\mathrm{e}^-,i}^{lfc} = N_{\mathrm{e}^-,i} \cdot \frac{\langle N_{\mathrm{e}^-,i} \rangle_{\forall i}^{roi}}{\langle N_{\mathrm{e}^-,i} \rangle^{roi}} \tag{5.6}$$

Another contribution can arise from the propagation of the probing light through the imaging system. When imaging with coherent laser light, fringes can appear on the recorded images due to diffraction effects, e.g., caused by small dust particles on the optical components [Ockeloen *et al.*, 2010; Muessel *et al.*, 2013]. Ideally we would expect that the division of the absorption image for the reference one would

completely remove them because both should exhibit the same fringe structure. However, external perturbations affecting the imaging system, such as air movement or mechanical vibrations of the optics, may shift the fringe position between the two images, leading to a remaining fringe structure on the deduced atomic density.

The impact of this error source can be minimized by applying the fringe removal algorithm described in [Ockeloen *et al.*, 2010]. The algorithm constructs for each absorption image $N_{\mathrm{e}^-, a, i}$ an optimal reference image $N^{opt}_{\mathrm{e}^-, r, i} = \sum_k c_k N_{\mathrm{e}^-, r, k}$ from a linear combination of many different reference images $N_{\mathrm{e}^-, r, k}$ within a set. The coefficients c_k are found through a least squares minimization of $\mid N_{\mathrm{e}^-, r, i} - N^{opt}_{\mathrm{e}^-, r, i} \mid$ in a region of interest which excludes the cloud. If the reference image set size is big, then it is likely that there will be one or many images with fringes appearing in the same positions as in the target image. Their linear combination with optimized weights into $N^{opt}_{\mathrm{e}^-, r, i}$ will suppress the fringes and also reduce the photon shot noise contribution of the reference image to the atom number measurement.

## 5.3.2 Atom number fluctuation compensation

Multiple complementary approaches to reduce atom fluctuations are possible. First of all, a passive improvement of the tight trap loading stability has been achieved by stabilizing the power of the dipole trap beams and by reducing mechanical drifts in the alignment of the trap optics, caused by temperature fluctuations. An active real-time control and preparation of an ultracold cloud below the atom number shot noise level has been recently demonstrated [Gajdacz *et al.*, 2016], but it requires an implementation of a feedback mechanism and an important change in the detection method to probe the sample in a non-destructive way. Here we use an approach that requires one more image of the cloud to measure the atom number and only few assumptions and technical developments.

The main idea is to perform first the desired experiment, then to measure in a consecutive image the atom number present in each repetition. A high SNR measurement of $N_{atoms, i}$ is important to make the impact of light noise negligible on this determination. Now the optical response measured in the first image has to be associated with the atom number measured in the second. If random atom losses between the images are negligible (systematic ones can be accounted for), we can model the transmission with Eq. (3.14) using the atom number measured in the second image and an appropriate scaled susceptibility based on the performed experiment. Now we can compensate the absorption fluctuations induced by variations of the atom number by rescaling the electron number measured in the experiment by the

ratio between the modeled mean optical response at the mean atom number and the modeled response at the atom number measured in each repetition:

$$N_{\mathrm{e}^-,i}^{afc} = N_{\mathrm{e}^-,i}\, e^{-\tilde{\chi}\frac{\sigma_0}{a_{px}}(\langle N_{atoms}\rangle - N_{atoms,i})} \qquad (5.7)$$

This compensation method can be implemented either by retrapping the cloud in between the images and making sure that there are no significant losses or by taking a second image during free time-of-flight expansion within few hundreds of µs from the first, in order to have the same cloud density and size. We follow the latter strategy and we acquire multiple images within 100 µs from each other using the "fast kinetics" mode of our CCD camera, introduced in Ch. 2.4.4.
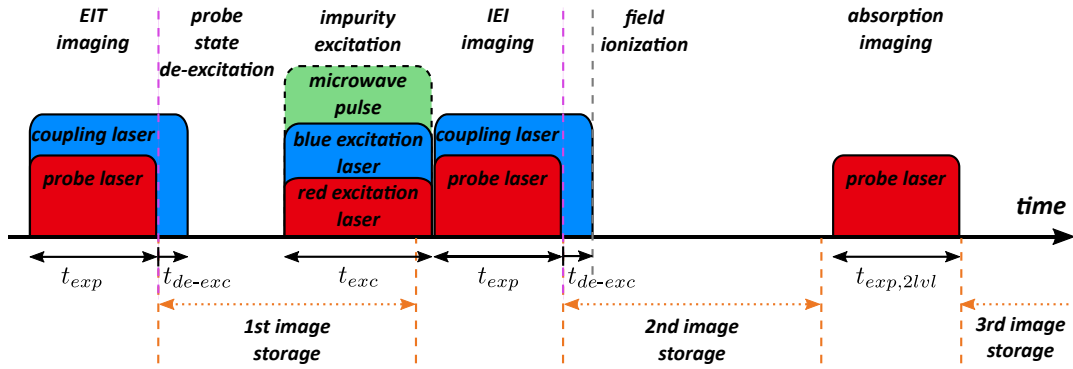

Figure 5.5: Triple imaging pulse sequence for Interaction Enhanced Imaging. First a reference image under EIT conditions is acquired, then impurities are excited and an IEI experiment is performed. The blue laser pulse lasts longer to de-excite the probe Rydberg atoms, preserving the total atom number. The few impurity Rydberg states are field ionized and counted on the MCP detector. A third image is acquired to extract with high SNR the atom number from the two-level response. After each exposure, the acquired image is moved into the masked area of the CCD and the shift time sets the maximum acquisition rate. The relative timings between pulses are not in scale.

To take full advantage of the fast multiple imaging we implement a new pulse sequence for IEI, depicted in Fig. 5.5. First a reference image under EIT conditions is taken and stored in the masked area of the CCD. The blue laser pulse lasts 2 µs longer than the red to de-excite the probe Rydberg state, such that the ground state atom number is preserved. Then impurities are excited to the chosen state using an off-resonant excitation scheme (Ch. 2.5) and the Interaction Enhanced Imaging experiment is performed. The probe Rydberg state is again de-excited in 2 µs to avoid being field ionized together with the few impurity states when a high electric field is ramped up on the electrode structure surrounding the cloud immediately after

the laser pulses end. For the third image only the red imaging laser is turned on for a longer exposure time $t_{exp,\,2lvl}$ to measure the cloud two-level response with a higher SNR. An important advantage of this sequence over the preceding one (see Ch. 4.4) is that the two images required to observe the impurity effect are acquired during one experimental realization, rather than two. This can potentially help to reduce systematic effects arising under EIT from atom number fluctuations. Another benefit of the triple imaging sequence is a strongly reduced impact of fringes, compared to older measurements, because the set of absorption images is now taken on a timescale short compared to the external perturbations affecting the imaging system.

The atom number in each run is extracted from the third image using Eq. (2.13) with an associated error given by Eq. (2.16), where the main error source is the photon transfer curve. We aim to compensate the atom number fluctuations down to a $\approx 2\%$ level and this requires a SNR≥ 50, which can be reached by tuning the exposure time $t_{exp,\,2lvl}$ and the probe Rabi frequency Ω_p. To establish the relation between the optical responses in the three images we need to consider an important collateral effect of absorption imaging which is the recoil heating of the cloud [Ketterle *et al.*, 1999; Wolf *et al.*, 2000]. Each time an atom absorbs or emits a photon it receives a small recoil which after many scattering events translates into a significant increase in temperature and even loss. Consequently after each image the cloud will expand in size with an increased rate due to the incurred heating and the effect will cumulate across images. The magnitude of the effect scales with t_{exp} and Ω_p, if both are small then it can be neglected, otherwise the atom number has to be measured by integrating in the third image over all pixels that contain the expanded cloud. Hardware binning of the whole cloud in one "super-pixel" increases the SNR at the expense of spatial resolution and allows to neglect the motion of atoms between pixels.

To validate the proposed compensation method we start from the simpler case of a two-level cloud and we acquire 1000 times three consecutive absorption images, with $\Omega_p = 2\pi \cdot (1.03 \pm 0.05)\,\mathrm{MHz}$ and $t_{exp} = (5, 30, 30)\,\mathrm{\mu s}$ respectively. A hardware binning of $N_{bin} = 160$ is applied, placing the whole cloud in one "super-pixel" with total atom number $N_{atoms} = 640 \pm 160$. The scaled susceptibility is the same for all three images, so an atom number can be measured in each. Figure 5.6 (a) shows the ratio between the atom number measured in the first or the second image and the third (blue and green, respectively) and we find that they are both compatible with unity within $1\,\sigma$. The small systematic deviation of the second ratio is consistent with atom loss due to heating between the second and third images, while for the first ratio the shorter exposure time limits the atom number determination SNR and explains the observed
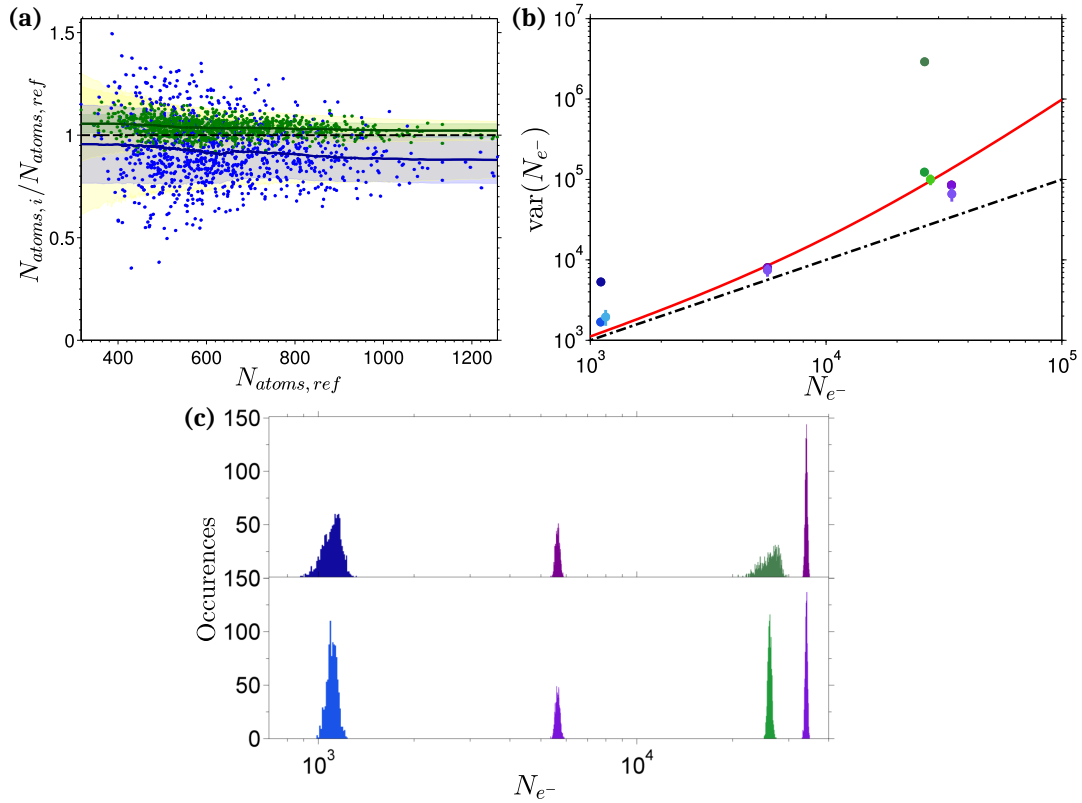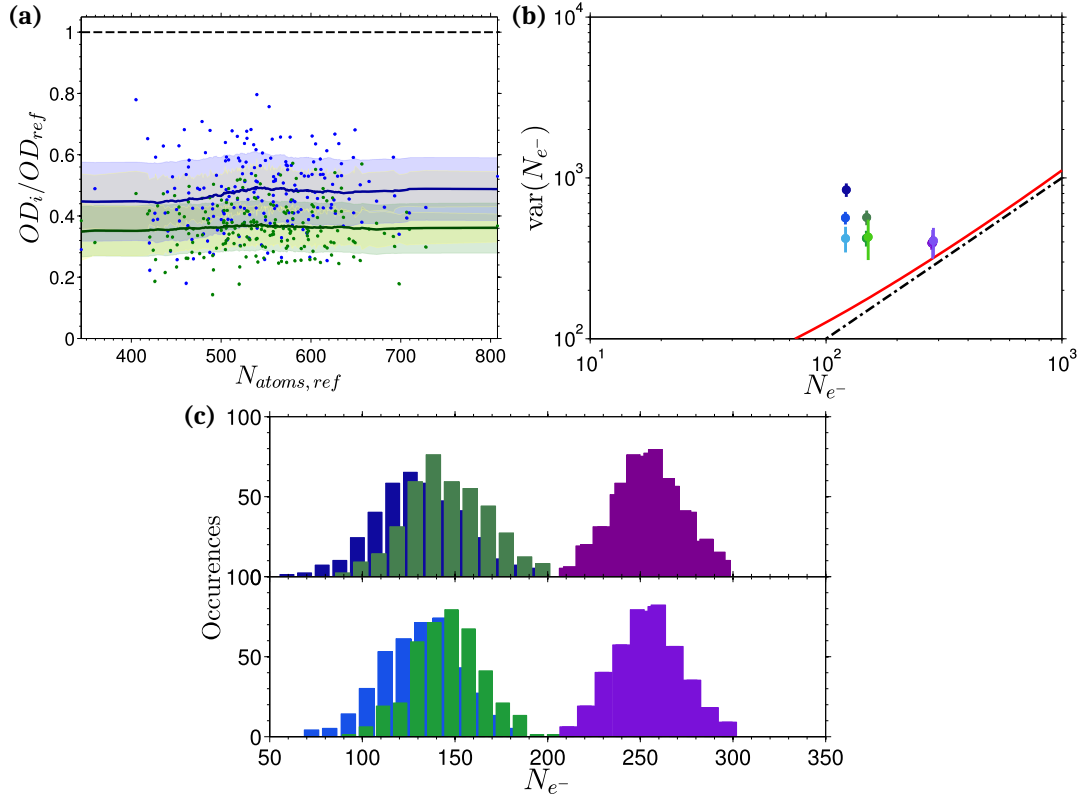
Figure 5.6: Atom number fluctuation compensation for a two-level system. Three consecutive images of a two-level cloud are taken, with $t_{exp} = (5, 30, 30)\,\mu$s respectively. **(a)** Ratio between the atom number measured in the first or the second image and the third (blue and green, respectively), both are compatible with unity within $1\,\sigma$. The two solid lines are running averages and the colored areas around each are running standard deviations. The latter are in agreement with the standard deviation expected for absorption imaging using the photon transfer curve (yellow areas). **(b)** Variance $\mathrm{var}(N_{\mathrm{e}^-})$ observed within the cloud in the first two absorption images without any compensation (dark blue and dark green), with applied intensity and atom number fluctuation compensations (lighter colors) and after post-selection (lightest colors with increased errorbars due to sample size reduction). The variance in the respective reference images (dark purple) is close to the calibrated photon transfer curve (solid red). **(c)** Histograms of detected electrons without (top) and with intensity and atom number fluctuation corrections (bottom). The narrowing of the distributions width is evident and corresponds to the smaller variances shown in (b).

spread in values. Figure 5.6 (b) shows that the variance $\mathrm{var}(N_{\mathrm{e}^-})$ observed within the cloud in the first two absorption images (dark blue and dark green) is dominated by atom number fluctuations, while in the respective reference images (dark purple) it is close to the calibrated photon transfer curve (solid red). The joint application of the intensity and atom number fluctuation compensations (eqs. (5.6, 5.7)) allows to suppress these sources of variance and approach the photon transfer curve (lighter colors). The reduction in variance leads to a narrowing of the detected electrons distributions (Fig. 5.6 (c) without (top) and with the corrections (bottom)).

This positive outcome demonstrates that the compensation method we developed and applied addresses the correct source of fluctuations and is capable of removing its contribution. As a further test of our method, we compare it with a post-selection approach that does not require any prior assumption on the cloud optical response. The first and second image measurements are post-selected based on the atom number measured in the third within a bin of $\langle N_{atoms} \rangle \pm 2\%$ and a new mean and variance is calculated for these reduced samples (lightest colors with increased errorbars due to sample size reduction, according to Eq. (5.1)). We observe that post-selection also leads to suppression of the atom number fluctuation contribution, giving a variance consistent with our method.

The next step is to apply the atom fluctuation compensation method to a three-pulse IEI experiment and to verify its impact. We perform 200 repetitions, acquiring three consecutive images with hardware binning of 20 pixels, respectively under EIT with impurities ($t_{exp} = 5\,\mu s$), under EIT without impurities ($t_{exp} = 5\,\mu s$) and as two-level system ($t_{exp,\,2lvl} = 30\,\mu s$). The peak density is $n_0 = (7.0 \pm 0.2) \cdot 10^{11}\,\mathrm{cm}^{-3}$ and the Rabi frequencies are $\Omega_p = 2\pi \cdot (0.60 \pm 0.05)\,\mathrm{MHz}$ and $\Omega_c = 2\pi \cdot (20 \pm 1)\,\mathrm{MHz}$. As before, we measure the total number of atoms in the cloud using the third image, but now the medium optical response in the first two images is strongly modified by EIT and impurities. Assuming that the total atom number was conserved, the scaled medium susceptibilities $\tilde{\chi}_{imp}$ and $\tilde{\chi}_{eit}$ can be estimated in a model independent way and are given directly by the ratio between the measured optical densities in the first or the second image and the third. We verify that thermal cloud expansion and atom number losses induced by photon recoil heating during imaging are negligible thanks to the short duration of our imaging sequence ($\simeq 300\,\mu s$ in total).

Figure 5.7 (a) shows for each single acquisition the ratios between the optical density measured under EIT with impurities (blue) or under EIT only (green) and the optical density of a two-level system. The presence of impurities causes an increase in absorption, as expected. The running averages over the data (solid lines) indicate that $\tilde{\chi}_{imp}$ and $\tilde{\chi}_{eit}$ are almost constant within the observed atom

Figure 5.7: Atom number fluctuation compensation for a three-pulse IEI experiment. Three consecutive images of a cloud are taken, respectively under EIT with impurities (blue, $t_{exp} = 5\mu s$), under EIT without impurities (green, $t_{exp} = 5\mu s$) and as a two-level system ($t_{exp, 2lvl} = 30\mu s$). The color coding is identical to Fig. 5.6. **(a)** Ratio between the optical density measured in the first or the second image and the third. Due to EIT, the medium response is lower than χ_{2lvl} and the presence of impurities in the first image results in an increased absorption. **(b)** Variance $var(N_{e-})$ observed within the cloud in the first two images without compensation (dark blue and dark green), with applied intensity and atom number fluctuation compensations (lighter colors) and after post-selection (lightest colors with increased errorbars due to sample size reduction). The compensation methods reduce the variance, but do not account for all sources of fluctuation. **(c)** Histograms of detected electrons without (top) and with intensity and atom number fluctuation corrections (bottom). The distribution width narrowing is less efficient than for a pure two-level system.

number fluctuation range ($\approx 10\%$). This relation allows us to approximate the optical response for increasing atom number N_{atoms} with a linear scaling given by $\tilde{\chi}_{imp} = \langle OD_{imp}/OD_{2lvl}\rangle$ and $\tilde{\chi}_{eit} = \langle OD_{eit}/OD_{2lvl}\rangle$. Figure 5.7 (b) shows that the variance $var(N_{e-})$ observed within the cloud in the first two images (dark blue and dark green) is higher than expected from the photon transfer curve (red). The joint

application of the light intensity and atom number fluctuation compensations (lighter colors) or of post-selection (lightest colors) reduces the variance, but does not account for all sources of fluctuation. Correspondingly the detected electron distributions narrow less significantly than for a pure two-level system (Fig. 5.7 (c)).

Our method removed approximately 1/3 of the excess variance originated by fluctuations in the cloud absorption. This fraction can be attributed to the atom number fluctuation error contribution, while the remaining part may be caused by the additional process that we discussed in Ch. 5.2.3. We note that in presence of impurities the variance is higher than under EIT and this could be connected with the impurity excitation statistics, as outlined in Ch. 5.2.4.

5.4 Improved single-shot detection of few impurities

Now that the main error sources in IEI have been identified and with two validated methods to reduce their effect at hand, we come back to the investigation of the detection fidelity. We analyze once more the data presented in Ch. 5.1 for the $\left|43S_{1/2}\right\rangle$-$\left|42S_{1/2}\right\rangle$ impurity-probe state combination, applying the light intensity and atom number fluctuation compensations in order to test their impact on the fidelity. A hardware binning of $N_{bin} = 20$ was used to increase the SNR and to place most of the cloud into two bins in the first image, while in the image used for the atom number measurement the cloud expanded into 10 bins, over which we integrate. This set of data was acquired using both the two repetition pulse sequence (detailed in Ch. 4.4), with the addition of an image to measure the atom number, and the triple imaging sequence introduced in the previous section, allowing for a comparison between the two. In the triple imaging sequence we reduce by 1.2% the electron number measured in the second image to compensate for a susceptibility reduction due to cloud thermal expansion.

Figure 5.8 (e) shows the original fidelity (blue) and the fidelities achieved by applying the two compensations with the two repetition sequence (green) and with the triple pulse sequence (red). The light intensity and atom number fluctuations improve the fidelity for both pulse sequences, but for small average numbers of impurities the improvement is rather small and within the estimation statistical error, while for $\langle N_i \rangle = 13.1 \pm 0.4$ we observe a clear benefit. The triple pulse sequence performs generally better than the older one and we achieve $\mathcal{F} = 0.89 \pm 0.02$, up from 0.86 ± 0.02, which allows to improve the sensitivity from 12 to 11 impurities.

Considering a photon shot noise limited measurement, we use the photon transfer
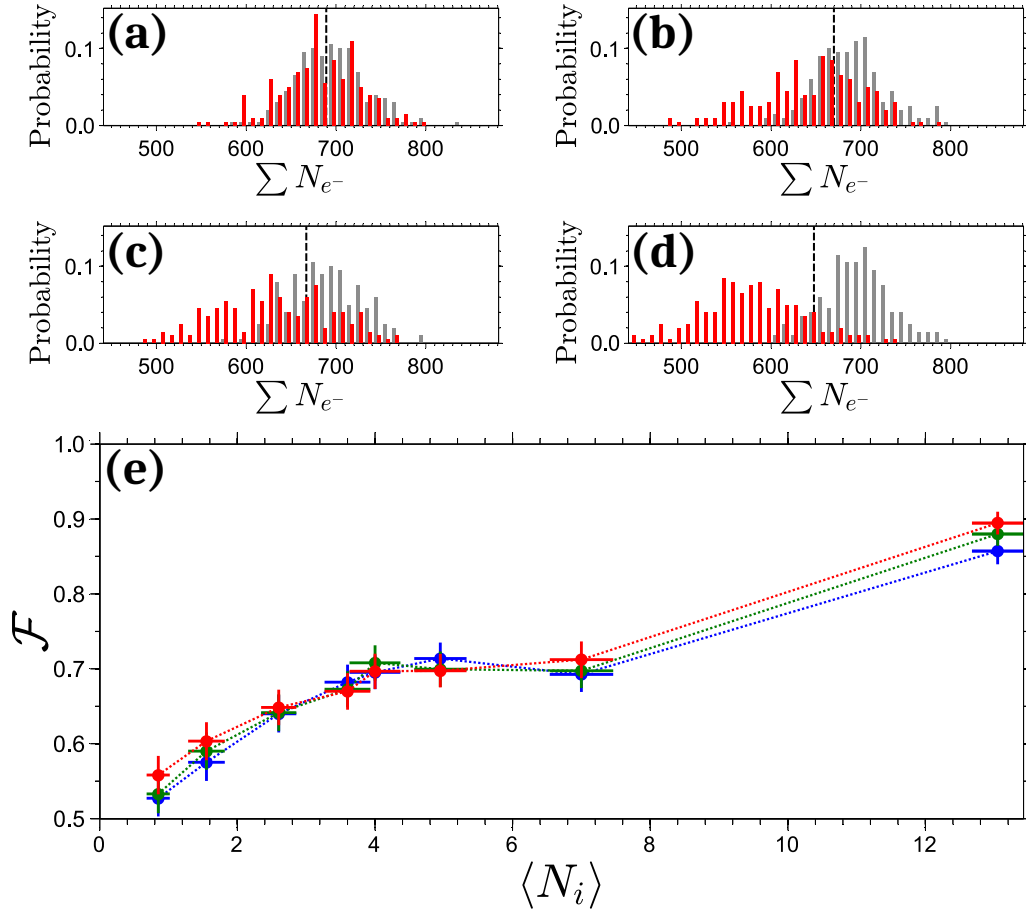
Figure 5.8: Histograms of measured electron distributions on the CCD camera and single-shot IEI detection fidelity for increasing mean number of impurities with applied the error reduction methods. In **(e)** are shown for comparison the original fidelity (blue) and the fidelities achieved by applying the light intensity and atom number fluctuation compensations with the two repetition (green) and the triple pulse (red) sequences. For the latter case the normalized probability distribution of the number of detected electrons in presence of impurities (red) and without (grey) is shown, respectively for $\langle N_i \rangle = 0.8 \pm 0.2$ **(a)**, 3.6 ± 0.3 **(b)**, 5.0 ± 0.4 **(c)** and 13.1 ± 0.4 **(d)**.

curve and our hard-sphere model to predict the achievable SNR with the used experimental parameters. Assuming for simplicity a gaussian distribution of the electron number, we estimate from the SNR that the corresponding single-shot sensitivity should be ~ 4, a factor of three higher than what we measure using the fidelity. The neglected noise contribution of the impurity excitation statistics and of the additional process observed under EIT may partially explain this discrepancy.

We apply the fidelity analysis described for the $\left| 43S_{1/2} \right\rangle$-$\left| 42S_{1/2} \right\rangle$ to two other impurity-probe combinations, $\left| 42P_{3/2} \right\rangle$-$\left| 42S_{1/2} \right\rangle$ and $\left| 50S_{1/2} \right\rangle$-$\left| 37S_{1/2} \right\rangle$, for which IEI

Impurity-probe states	A^{IEI}_{meas}	$A^{\mathrm{IEI}}_{theory}$	S_{meas}	S_{theory}
$\lvert 50S\rangle$-$\lvert 37S\rangle$	19 ± 2		13	
$\lvert 43S\rangle$-$\lvert 42S\rangle$	48 ± 12	56	12	3
$\lvert 42P\rangle$-$\lvert 42S\rangle$	17 ± 4	17.1	5	4

Table 5.1: Measured and estimated amplification factors A^{IEI} and sensitivities S for the investigated impurity-probe state combinations. The observed amplification factors are compatible within one σ with the expected values, while the measured sensitivities are worse than predicted by the hard-sphere model, indicating the presence of additional noise contributions.

data as a function of $\langle N_i \rangle$ was previously acquired (other results from this data were presented in Ch. 4.1.4 and 4.5.2). As listed in Table 5.1, we find that the measured amplification factors (Eq. (4.1)) are in good agreement with the expected values, while the sensitivities extracted from the fidelity are worse than predicted by the hard-sphere model, confirming the presence of additional noise contributions. The best single-shot sensitivity is measured for the $\lvert 42P_{3/2}\rangle$, corresponding to 5 impurities, while for $\lvert 50S_{1/2}\rangle$ and $\lvert 43S_{1/2}\rangle$ states we are restricted to ≈ 12. This confirms our expectation, presented in Ch. 4.2.3, that with Rydberg $\lvert nP\rangle$ impurities a higher sensitivity could be achieved than for $\lvert (n+1)S\rangle$ impurities, since resonant dipole-dipole interactions are much stronger than van der Waals interactions for the same principal quantum numbers.

For the $\lvert 42P\rangle$-$\lvert 42S\rangle$ pair state the intensity and atom number fluctuation compensation do not lead to a statistically significant improvement of the fidelity (from a peak value of 0.84 ± 0.03 to 0.86 ± 0.03), most probably because the data was taken without using hardware binning nor the triple pulse sequence. For the $\lvert 50S\rangle$-$\lvert 37S\rangle$ pair the atom number fluctuation compensation could not be applied, missing a second image for a precise measurement, and theoretical expectations are not provided because the experiment was performed at a Förster resonance and this situation is not accounted for by our model for the moment.

5.5 Increasing the signal per impurity

The improvement in sensitivity achieved by applying the light intensity and atom number fluctuation compensations is clearly not sufficient to reach single shot single impurity sensitivity with the pairs of Rydberg states investigated so far. A change

of strategy seems necessary to reach the desired goal.

In the previous sections we investigated and addressed only the error sources that influence the detection fidelity by widening the electron distributions (with and without impurities). Another important contribution to $\mathcal{F}$ which determines the potential separation between the distribution means is the signal per single impurity.

We will now investigate how the single impurity response can be magnified for a given choice of states and which impurity-probe states are the most promising for experiments with spatially resolved single-shot single impurity sensitivity. For this study we will use the hard-sphere model that we introduced in Ch. 4.3 to estimate the expected signal. Furthermore, the search for the optimum experimental parameters and states will use the SNR as test statistic because it allows a simple and intuitive interpretation. The measured electron number distributions can be described in good approximation by normal probability distributions, so a simple and direct mapping between the SNR and the detection fidelity is possible.

5.5.1   Signal in Interaction Enhanced imaging

In the first section we chose as signal the difference between the means of the electron distributions with and without impurities. To get an insight on how it can be increased, we rewrite Eq. (5.2) using the expected transmission (Eq. (3.14)) with the susceptibilities predicted by the hard-sphere model (Eqs. (4.6, 4.12))

$$\langle N_{e^-,\,add}\rangle = \langle N_{e^-,\,r}\exp\left\{-k\int_{-\infty}^{+\infty}\mathrm{Im}[\chi_{eit}]dx\right\}\rangle - \langle N_{e^-,\,r}\exp\left\{-k\int_{-\infty}^{+\infty}\mathrm{Im}[\chi_{imp}]dx\right\}\rangle$$
$$(5.8)$$
$$= \langle N_{e^-,\,r}\rangle\exp\left\{-k\int\mathrm{Im}[\chi_{eit}]dx\right\}\left[1-\exp\left\{-k\int f_{ir}(1-f_{rr})\mathrm{Im}[(\chi_{2lvl}-\chi_{eit}^0)]dx\right\}\right]$$

Equation (5.8) contains all the information needed to optimize the signal. The initial probe Rabi frequency determines the number of photons incident on the cloud, which partially transmits them. The photons are converted into electrons by the camera with a total light collection efficiency that should be as high as possible (see Ch. 2.4.4). Longer exposure times allow to collect more photons, but t_{exp} is constrained by the timescale at which additional noise contributions arise, like the one identified in Sec. 5.2.3, and by the lifetime of the impurity state. To compensate this limitation one would intuitively increase Ω_p, but this may negatively affect the second term in the equation.

The transmission contrast between the two images with and without impurities is set by the difference between the corresponding susceptibilities and can span a

maximum dynamic range between the ideal EIT χ^0_{eit} and the two-level χ_{2lvl}. To enlarge this range, χ^0_{eit} should be minimized by reducing the effective decay rate γ_{gr}, for example by decreasing the laser linewidths (as discussed in Ch. 2.4.5), while χ_{2lvl} should be maximized by avoiding any saturation effect.

To leverage this dynamic range, the impurities have to blockade a large fraction of the volume ($f_{ir} \to 1$) and this is possible if the EIT bandwidth σ_{eit} is smaller than the impurity-probe interaction strength V_{ir}. σ_{eit} and V_{ir} determine the blockade radius R_{ir}, which in turn is related to the amplification factor per impurity A^{IEI} that we would like to maximize. Higher ground state densities n_0 increase A^{IEI}, but unfortunately influence as well the degree of EIT transparency.

The non-ideal EIT susceptibility χ_{eit} is determined by the effective fraction f_{rr} of volume blockaded by the probe-probe interactions (see Ch. 4.3.2) and it directly limits the contrast. Consequently we aim for $f_{rr} \ll 1$ and this requires to increase the EIT bandwidth σ_{eit}, either by using a large coupling Rabi frequency Ω_c or by reducing the non-interacting Rydberg population ρ^0_{rr}. In the weak probe limit the latter is $\propto \Omega_p^2/\Omega_c^2$ and can be minimized using low probe intensities.

It is clear that multiple effects affect the signal, as well as the noise, and compete with each other. Furthermore most of them depend and share many parameters, like the cloud density n_0 and the probe and coupling Rabi frequencies. Finding the optimum conditions for an IEI experiment by looking only at the signal or the noise is impossible, so we have to consider them together and optimize the SNR.

5.5.2 Signal to noise ratio for a defined pair of states

The signal to noise ratio for a single shot IEI experiment, as defined in Sec. 5.1, is given by the ratio between the signal expressed by Eq. (5.8) and the root of the sum of the variances of the two involved distributions

$$\mathrm{SNR} = \frac{\langle N_{\mathrm{e}^-,r} \exp\{-k \int \mathrm{Im}[\chi_{eit}]dx\}\rangle - \langle N_{\mathrm{e}^-,r} \exp\{-k \int \mathrm{Im}[\chi_{imp}]dx\}\rangle}{\sqrt{\mathrm{var}(N_{\mathrm{e}^-,r} \exp\{-k \int \mathrm{Im}[\chi_{eit}]dx\}) + \mathrm{var}(N_{\mathrm{e}^-,r} \exp\{-k \int \mathrm{Im}[\chi_{imp}]dx\})}}$$

(5.9)

To model the variances we use the photon transfer curve measured in Ch. 5.2.1 and we do not include atom number induced fluctuations in the cloud absorption, because we can efficiently suppress their impact, as demonstrated in Ch. 5.3.2. The effects of the probabilistic impurity excitation and of additional error sources present under EIT cannot be accounted for without having a model for them.

The SNR given by Eq. (5.9) cannot be expressed analytically. Furthermore the optimization parameter space is huge because it depends on many variables and

consequently the SNR has to be optimized numerically. Nonetheless, assuming a weak probe approximation, linear light propagation and being photon shot noise limited, we can greatly simplify the problem and obtain a simple analytic expression that reveals the key aspects of the SNR optimization:

$$\text{SNR} = \sqrt{\frac{2\Omega_p^2}{\Gamma_e^2} \frac{I_{sat} t_{exp} a_{px} Q_e T}{\hbar \omega_p}} \frac{1 - \exp\{-\varepsilon \text{OD}_{bl}\}}{\sqrt{1 + \exp\{-\varepsilon \text{OD}_{bl}\}}} \exp\left\{\frac{(\varepsilon - 1)}{2} \text{OD}\right\} \qquad (5.10)$$

with the transparency degree under EIT $\varepsilon = (1 - f_{rr}) C/(1 + C)$ and $\text{OD}_{bl} = f_{ir}\text{OD}$ representing the fraction of cloud made absorptive by the impurities [Adams *et al.*, 2013; Gorshkov *et al.*, 2011]. The analytic SNR is made of three parts, the first groups all the properties of the absorption imaging detection method (for our system with $\Omega_p = \Omega_{sat}$ and $t_{exp} = 1\,\mu\text{s}$ it would be ≈ 10), the second expresses the difference in absorption with and without impurities, while the last term represents the loss of transparency in the cloud due to probe-probe interactions. The optimum is found for a high EIT quality factor $C \propto \Omega_c^2$, negligible probe-probe interaction induced blockaded fraction f_{rr} ($\varepsilon \to 1$) and large OD_{bl} ($f_{ir} \to 1$). In these conditions the second and third term saturate at 1, corresponding to a complete absorption of the incoming light in presence of impurities and full transparency without. This makes the SNR depend only on the initial number of photons incident on the cloud, per unit detector area a_{px}. The latter is the only free parameter remaining, since the exposure time and probe Rabi frequency are constrained to reach this regime, and it can be increased through hardware or software binning of the images, at the price of reduced spatial resolution.

The numerical optimization of the SNR is carried out by solving the light propagation equation (3.13) for a cloud with Gaussian density profile $n(x) = n_0 \exp\{(-x^2/2\sigma_x^2)\}$, prepared in the "tight" trap ($\sigma_x = 4\,\mu\text{m}$, see Ch. 2.4.2), and with a local impurity density $n_i(x) \propto n(x)$ such that only one impurity is present in the cloud volume. The imaginary part of χ, which is responsible for the absorption of the probe field by the atomic cloud, is modeled using the susceptibilities predicted by the hard-sphere model, neglecting collective effects. χ_{2lvl} and χ_{eit}^0 are calculated from exact analytic solutions of the steady state optical Bloch equations for the full density matrix ρ for a single three-level atom (see Appendix C). These solutions are valid for arbitrary Rabi frequencies and account for the decay of the $|e\rangle$ and $|r\rangle$ states and for the presence of dephasing on both transitions, caused by Fourier-transform-limited pulses. This allows to model the system outside the weak probe approximation (see Ch. 3.1.2). To solve equation (3.13), we neglect non-linear light propagation effects by assuming a constant susceptibility evaluated at the peak density n_0 and at the

initial Ω_p. This approximation is justified as soon as we observe the cloud under transparency conditions where $|\chi| \ll 1$ [Han *et al.*, 2016; Gavryusev *et al.*, 2016a], but deviations might be observed for large absorption levels [Hofmann *et al.*, 2013; Gärttner and Evers, 2013]. For a limited parameter range we verified that including non-linear light propagation changes the SNR by up to 30%, but has a minor impact on the parameters at which the peak value is found, which is acceptable for the purpose of optimization.

We investigate first which density and Rabi frequencies give the highest SNR for single impurity detection with the $\left|43S_{1/2}\right\rangle$-$\left|42S_{1/2}\right\rangle$ impurity-probe state combination. For this pair the interactions are $C_6^{ir} = 2\pi \cdot 12.255\,\text{GHz}\,\mu\text{m}^6$ and $C_6^{rr} = 2\pi \cdot 1.806\,\text{GHz}\,\mu\text{m}^6$. As exposure time we choose $t_{exp} = 5\,\mu\text{s}$ to safely neglect the additional noise contribution to EIT discussed in Ch. 5.2.3. Figure 5.9 (a) shows that at small Rabi frequencies the SNR calculated for a single pixel is dominated by the detector readout noise σ_{rd} and photon shot noise contributions. The probe and coupling Rabi frequencies should be increased together, with an optimum ratio $\Omega_p/\Omega_c \approx 9\%$, in order to raise the signal per impurity, while preserving the cloud transparency and suppressing the progressively increasing effect of probe-probe interactions. The reduction in SNR for high Ω_p is attributed to the saturation of the two-level susceptibility (of the additional absorbers). The density affects linearly the amplification per impurity, but also contributes to f_{rr}, and an optimum between the two effects is reached for $n_0 = 2 \cdot 10^{12}\,\text{cm}^{-3}$ at fixed Ω_c (Fig. 5.9 (b)). The SNR can be increased further if n_0 and Ω_c are scaled together, such that f_{rr} is kept constant while A^{IEI} raises (Fig. 5.9 (c)). Unfortunately we cannot proceed in this direction because densities above $2 \cdot 10^{12}\,\text{cm}^{-3}$ cannot be reached in the "tight" dipole trap and the peak Ω_c is limited by the available laser power.

The last parameter left to optimize is the binning size, at the price of spatial resolution. We model the application of hardware binning on the CCD camera by constructing a discrete 2D distribution of densities in different pixels, corresponding to the cloud transverse profile, and, starting from the center, we integrate the estimated number of transmitted photons over an increasing number of pixels. From this total number we calculate the new error using the photon transfer curve. Fig. 5.10 (a) shows a linear growth of SNR with increasing binning size until $\sim 68.3\%$ of the cloud surface is contained in the "super-pixel" (vertical black line). Then the SNR saturates and after integrating over the whole cloud (red line) it drops down because there is no further signal contribution, only noise is added from the additional pixels. A new SNR map can be calculated including hardware binning (Fig. 5.10 (b)) and for $\Omega_p = 2\pi \cdot 1.25\,\text{MHz}$, $\Omega_c = 2\pi \cdot 14.0\,\text{MHz}$ we observe a five fold improvement in
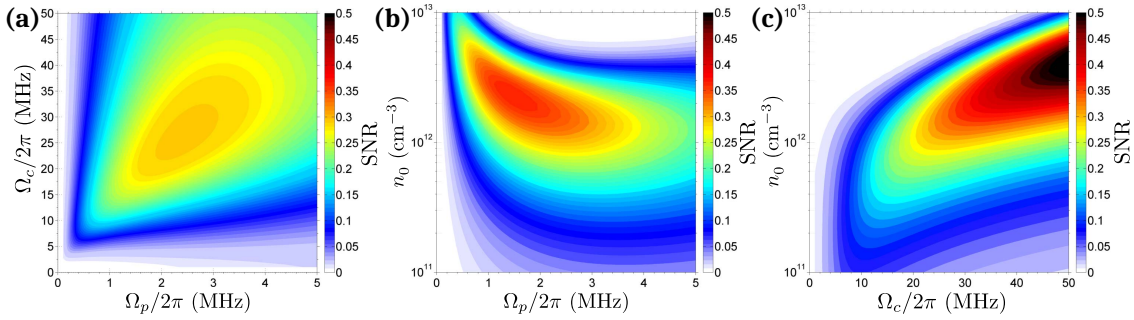
Figure 5.9: Estimated signal to noise ratio for the $|43S\rangle$-$|42S\rangle$ impurity-probe state combination using the IEI hard-sphere model. (a) For $t_{exp} = 5\,\mu$s and a peak density $n_0 = 1 \cdot 10^{12}\,\mathrm{cm}^{-3}$ the SNR is found to scale approximately linearly with increasing probe and coupling Rabi frequencies, with an optimum along the line $\Omega_p/\Omega_c \approx 9\%$. **(b)** Varying the density and Ω_p, for $\Omega_c = 2\pi \cdot 26.5\,\mathrm{MHz}$, we observe that the optimum SNR is found for smaller probe intensities and higher densities, conditions that maximize the amplification factor per impurity and minimize the loss of contrast due to probe-probe interactions. **(c)** At fixed $\Omega_p = 2\pi \cdot 2.5\,\mathrm{MHz}$ we find that raising together the density and coupling Rabi frequency leads to a continuous SNR improvement.

the peak SNR compared to Fig. 5.9 (a).

Hardware binning has a major impact on the SNR, at the expense of spatial resolution, because it allows both to reduce the noise and to acquire more signal, since the latter is spread over multiple pixels as soon as the impurity-probe blockade radius exceeds the pixel size. Unfortunately for the $|43S_{1/2}\rangle$-$|42S_{1/2}\rangle$ impurity-probe state combination investigated so far it seems not possible to reach a SNR much higher than 1 in a single shot measurement even using this method and optimizing all other parameters. This is not sufficient to experimentally observe single impurities. Consequently, in order to reach a single impurity sensitivity, we need to explore other impurity-probe state combinations.

5.5.3   Choice of states for Interaction Enhanced Imaging

In this last section we investigate which impurity-probe states are the most promising for IEI experiments with single-shot single impurity sensitivity. Two different types of impurity states $|i\rangle = |nS\rangle$, $|nP\rangle$ have been used so far, as discussed in Ch. 4.2 and 4.5, and it is interesting to compare the expected SNR between them since they interact differently with the probe Rydberg state $|r\rangle$, either via van der Waals or through resonant dipole-dipole interactions.

Assuming that only one impurity is present in the cloud, we apply the numerical
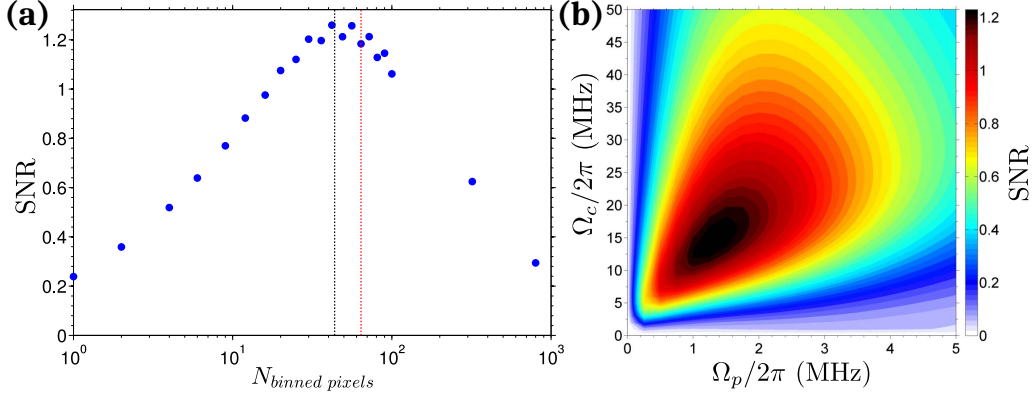
Figure 5.10: Impact of binning on the SNR of the $|43S\rangle$-$|42S\rangle$ impurity-probe state combination. **(a)** Applying a hardware binning on the CCD camera allows to increase the SNR at the expense of spatial resolution until $\sim 68.3\%$ of the cloud surface is contained in the "super-pixel" (vertical black line). Then the SNR saturates and after integrating over the whole cloud (red line) it drops down because the additional pixels contribute only noise. **(b)** SNR map with hardware binning of 42.

SNR optimization, introduced in the previous section, to calculate the peak SNR expected for IEI experiments performed with $\left|n_2 S_{1/2}, m_J = +1/2\right\rangle$-$\left|n_1 S_{1/2}, m_J = +1/2\right\rangle$ or $\left|n_2 P_{3/2}, m_J = +3/2\right\rangle$-$\left|n_1 S_{1/2}, m_J = +1/2\right\rangle$ state combinations. Both principal quantum numbers are varied in the range $n = 27 - 85$ which is easily accessible in our experiment. The C_3 and C_6 interaction coefficients are taken respectively from Fig. 2.3 (with the appropriate angular component for $\theta = 0$ [van Bijnen, 2013; Paris-Mandoki *et al.*, 2016]) and Fig. 2.2. For each pair of states and assuming $t_{exp} = 5\,\mu s$, we optimize the SNR over a broad range of densities $n_0 = 1 - 20 \cdot 10^{11}\,\text{cm}^{-3}$, probe Rabi frequencies $\Omega_p = 2\pi \cdot (0.2 - 3)\,\text{MHz}$, coupling Rabi frequencies $\Omega_c = 2\pi \cdot (1 - 30)\,\text{MHz}$ and binning sizes $N_{bin} = 1, 20, 40, 80$.

Figure 5.11 shows the expected SNR map for the $|n_2 S\rangle$-$|n_1 S\rangle$ impurity-probe state pairs. Not surprisingly it follows the map of C_6 interaction coefficients very closely, since the interaction effects are at the root of the IEI detection method. Interestingly the symmetry present in Fig. 2.2 is broken here, because $n_2 - n_1 \geq 1$ allows to have an impurity-probe blockade radius R_{ir} higher than the probe-probe blockade radius R_{rr}, which in turn leads to a higher amplification factor A^{IEI} per impurity. The same consideration explains why the state pairs which show the highest inter-state interactions due to a small Förster defect, like $|39S\rangle$-$|38S\rangle$, $|69S\rangle$-$|67S\rangle$ or $|79S\rangle$-$|57S\rangle$, are also the ones promising the highest achievable SNR, although our model prediction is less accurate because the mean inter-atomic distance is below the critical radius that represents the cross-over between the van der Waals and
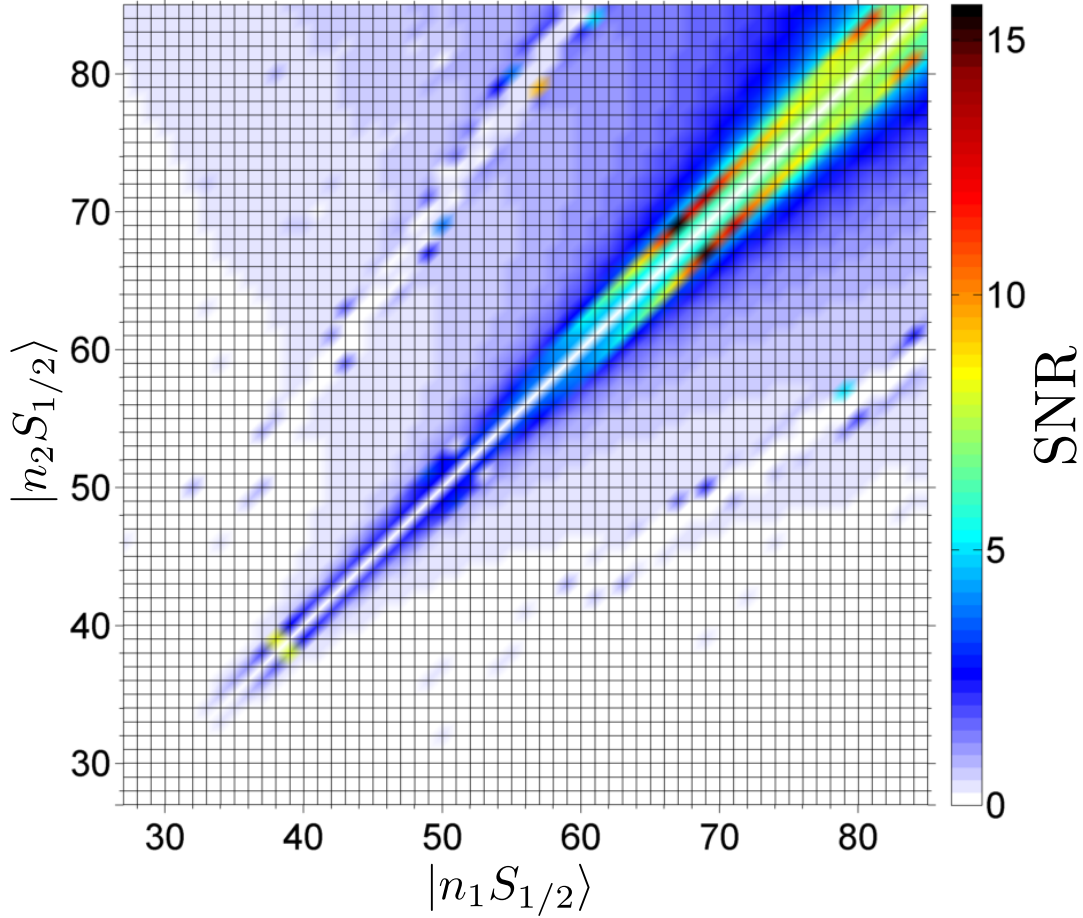
Figure 5.11: SNR map for impurity-probe state pairs with van der Waals interaction. For each $\left|n_2 S_{1/2}, m_J = +1/2\right\rangle$ impurity and $\left|n_1 S_{1/2}, m_J = +1/2\right\rangle$ probe state combination the optimum SNR is shown, which is found through a global optimization over n_0, Ω_p, Ω_c and hardware binning size, performed by numerically solving equation (3.13) using the susceptibilities predicted by the hard-sphere model and neglecting non-linear propagation effects. Pairs of states with a small Förster defect, like $\left|39S\right\rangle$-$\left|38S\right\rangle$, $\left|69S\right\rangle$-$\left|67S\right\rangle$ or $\left|79S\right\rangle$-$\left|57S\right\rangle$, show the most favorable ratio between the strength of impurity-probe and probe-probe interactions and are promising candidates for experiments that would benefit from single particle sensitivity.

the resonant dipole-dipole interactions (see Ch. 2.2.3). We expect that with these states an even higher SNR may be obtained by tuning their interaction from a van der Waals into a dipolar regime via a Förster resonance [Gallagher and Pillet, 2008; Günter *et al.*, 2013; Günter, 2014; Tiarks *et al.*, 2014; Gorniaczyk *et al.*, 2016]. The optimum parameters for each state are found to follow a common trend for increasing n_1: the best Ω_p decreases from 1.5 to 0.6 MHz, instead Ω_c raises from 10 to 30 MHz, while the optimum density for all states is the highest considered $n_0 = 2 \cdot 10^{12}\,\mathrm{cm}^{-3}$.

In summary, many $|n_2 S\rangle$-$|n_1 S\rangle$ state combinations show a SNR≥ 8 which is more than enough to realistically achieve a high fidelity for single impurity detection, even in presence of additional noise contributions.

Figure 5.12 shows the expected SNR map for the $|n_2 P\rangle$-$|n_1 S\rangle$ impurity-probe state pairs and, similarly to the previous case, it follows very closely the map of C_3 interaction coefficients. Only states with $n_2 - n_1 = -1$, 0 are suitable for experiments, due to the quickly vanishing radial wave-function overlap for increasing difference in principal quantum number. Resonant dipole-dipole interactions are much stronger than van der Waals interactions for $\Delta(n) \leq 1$ and this allows to have an impurity-probe blockade radius R_{ir} higher than the probe-probe blockade radius R_{rr} even for states with low principal quantum number, in contrast to the $|n_2 S\rangle$-$|n_1 S\rangle$ case. Although beneficial, this condition has the drawback that the ratio between these two radii does not show local optima, unlike near spontaneous Förster resonances for $|i\rangle = |nS\rangle$, and does not scale favorably with principal quantum number $\propto \mathsf{n}^{\star -7}$, leading to a similar SNR for the two cases for $n \geq 70$. We find that the optimum parameters for each state follow the same trend described for the $|n_2 S\rangle$-$|n_1 S\rangle$ case with a smaller Ω_p from 0.8 to 0.6 MHz.

The presented SNR map for the $|n_2 P\rangle$-$|n_1 S\rangle$ impurity-probe state pairs has weaker predictive power than the one for the $S - S$ combination because in our modeling the angular dependence of the dipole-dipole interactions (see Ch. 2.2) was neglected, arbitrarily choosing $\theta = 0$. A more accurate treatment would require to consider the anisotropy of the blockade volume and to simulate a realistic 3D distribution of Rydberg atoms with random orientation of the dipole moment. An additional consequence of the interaction angular dependency is that it allows couplings of the initially prepared $|i\rangle$ and $|r\rangle$ states with well defined m_J with other Zeeman states with different m'_J, potentially leading to undesired population of additional states.

In summary we find that $|n_2 P\rangle$-$|n_1 S\rangle$ state combinations allow to use much lower principal quantum numbers than $|n_2 S\rangle$-$|n_1 S\rangle$ pairs for IEI experiments, but the peak achievable SNR is lower than 6.5 in the considered parameter range, making high fidelity single impurity sensitive detection less likely to be successful in presence of additional noise contributions.

5.6 Towards single impurity imaging

Achieving single impurity sensitivity in single-shot IEI measurements has proven a challenging goal because many effects compete with each other in determining the
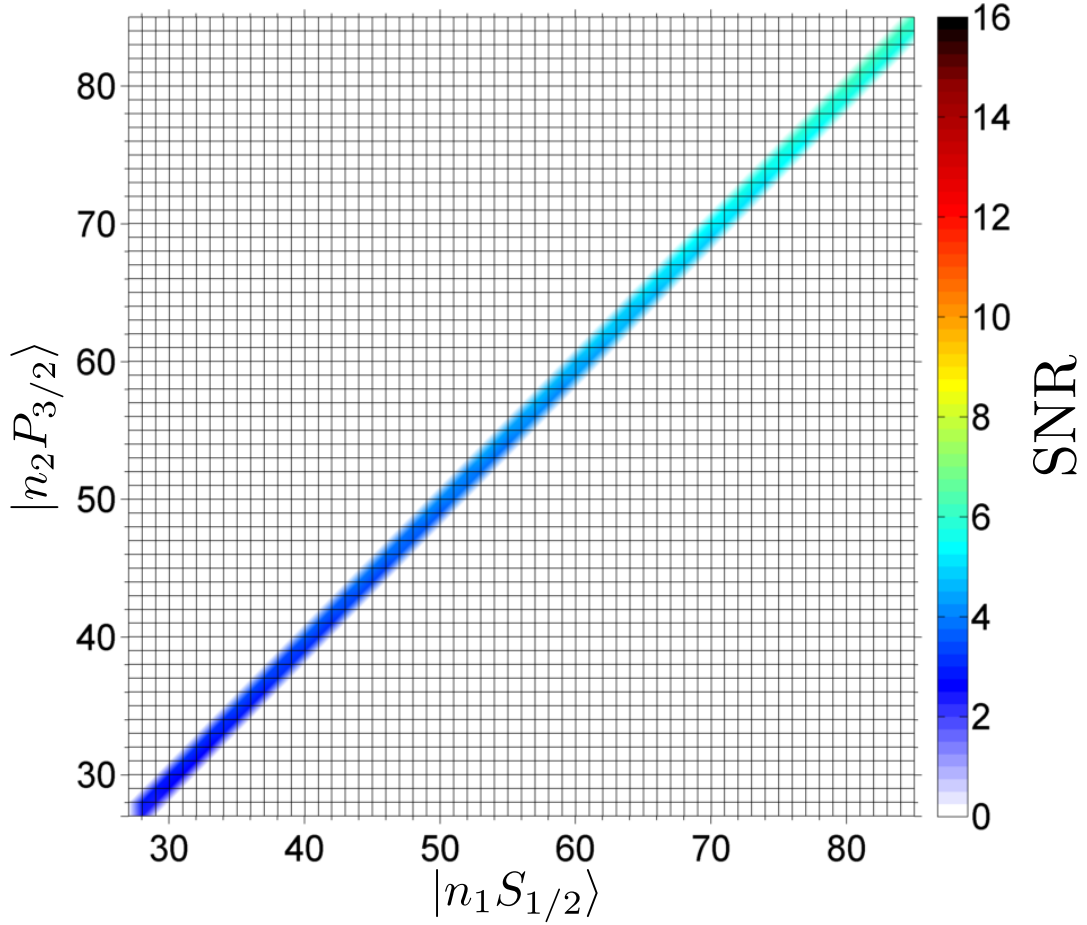
Figure 5.12: SNR map for impurity-probe state pairs with resonant dipole-dipole interaction. For each $\left|n_2 P_{3/2}, m_J = +3/2\right\rangle$ impurity and $\left|n_1 S_{1/2}, m_J = +1/2\right\rangle$ probe state combination the optimum SNR is shown, which is found through a global optimization over n_0, Ω_p, Ω_c and hardware binning size, performed by numerically solving equation (3.13) using the susceptibilities predicted by the hard-sphere model and neglecting non-linear propagation effects. Only states with $n_2 - n_1 = -1, 0$ are suitable for experiments, due to the quickly vanishing radial wave-function overlap for increasing difference in principal quantum number.

signal to noise ratio of Interaction Enhanced Imaging. After carefully exploring each of them, we have developed a robust procedure to predict the optimum experimental conditions that would allow to strike a delicate balance between competing effects and to reach a high signal to noise ratio.

The numeric SNR optimization program, based at its core on the hard-sphere model introduced in Ch. 4.3, is a powerful tool at our disposal to perform future experiments under the best experimentally achievable conditions. Furthermore it

can be used as a first theoretical comparison with the SNR and detection fidelity $\mathcal{F}$ extracted from the measurements.

The estimation of the realistically achievable SNR for a broad range of impurity-probe state pairs has allowed us to identify which Rydberg state combinations are the most suitable for future experiments. We expect that single impurity sensitivity can be reached with states that naturally have a small Förster defect, like $|39S\rangle$-$|38S\rangle$, $|69S\rangle$-$|67S\rangle$ or $|79S\rangle$-$|57S\rangle$. Furthermore, with these states an even higher SNR may be obtained by tuning their interaction from a van der Waals into a dipolar regime via a Förster resonance with the help of a small external electric field.

Once single impurity sensitivity is achieved and if the SNR is significantly higher than 1, it may be possible to reduce the binning size on the camera in order to recover spatial resolution. For a given pair state combination the optimum binning size is expected to correspond to the transverse size of the volume blockaded by the impurity-probe interaction, which in first approximation is a sphere with radius R_{ir}. Impurities in states with high principal quantum number exhibit typically a large impurity-impurity distance R_{ii}, caused by the Rydberg blockade effect between them (see Ch. 2.3), which may easily exceed R_{ir}, allowing spatially resolved single impurity detection and imaging.

The impact of total atom number variations on the cloud absorption fluctuations can be removed using the atom number fluctuation compensation method developed and demonstrated in Ch. 5.3.2. The limitations arising from the probabilistic excitation protocol that we use to prepare the initial impurity state can be overcome by using a different method to deterministically prepare a set number of impurities, like a two-photon adiabatic rapid passage [Deiglmayr *et al.*, 2006; Beterov *et al.*, 2011; Kuznetsova *et al.*, 2014] or other optimal control techniques [van Frank *et al.*, 2016]. Furthermore, in the regime of linear amplification per impurity, i.e. when saturation effects induced by the Rydberg blockade effect between impurities are negligible (see Ch. 4.5.2), we expect that a high enough SNR would correspond to a high detection fidelity such that the number of impurities present in each single shot measurement could be determined simply by distinguishing between the different electron number distributions.

This new level of sensitivity and resolution would allow to directly observe with IEI the dynamics and correlations of a strongly interacting Rydberg gas, enabling new studies of energy transport [Schönleber *et al.*, 2015; Schempp *et al.*, 2015; Fahey *et al.*, 2015; Yu and Robicheaux, 2016], formation of Rydberg aggregates [Malossi *et al.*, 2014; Schempp *et al.*, 2014; Urvoy *et al.*, 2015] or spin models [Hazzard *et al.*, 2014; Glaetzle *et al.*, 2015; van Bijnen and Pohl, 2015; Barredo *et al.*, 2015; Labuhn

et al., 2016; Whitlock *et al.*, 2016].

Chapter 6

Conclusion and outlook

In this thesis I have investigated how a single Rydberg atom can be optically imaged. Probing at the single particle level a cloud of strongly interacting Rydberg atoms would give access to the microscopic properties of the ensemble and allow the most detailed studies of these correlated many-body quantum systems [Weimer *et al.*, 2008; Pohl *et al.*, 2010; van Bijnen *et al.*, 2011; Viteau *et al.*, 2012; Hofmann *et al.*, 2013; Schempp *et al.*, 2014; Malossi *et al.*, 2014; Schauß *et al.*, 2015; Zeiher *et al.*, 2015].

Since direct optical detection of a Rydberg atom with techniques based on light scattering is hardly applicable due to the small scattering rate of the ground to Rydberg state transition, we have had to find an alternative route. The strong interactions between Rydberg atoms and the narrow optical transition provided by a three-level atomic cloud under electromagnetically induced transparency coupling (EIT) [Fleischhauer *et al.*, 2005] have lent us the two elements that, combined together, allow to map the presence of a Rydberg "impurity" state on a strong optical transition [Mohapatra *et al.*, 2007; Pritchard *et al.*, 2010; Tauschinsky *et al.*, 2010]. A cloud of ground state atoms, normally absorptive, is rendered transparent using EIT and a crucial step in our scheme is to use an auxiliary "probe" Rydberg state as one of the two stable states involved in the coupling. This turns the cloud into a contrast medium, whose optical response is locally perturbed by the strong Rydberg-Rydberg interaction between the probe Rydberg state and the Rydberg impurity which we want to detect. This perturbation restores absorption within a blockade volume around the impurity, which is readily detected and spatially resolved on a charge-coupled-device (CCD) camera, thereby exposing the impurity position. These are the key elements of the Interaction Enhanced Imaging (IEI) technique [Günter *et al.*, 2012; Olmos *et al.*, 2011].

Our first experiments focused on the properties of the EIT contrast medium in absence of interactions, in order to later disentangle its response from the effects of the impurity presence. By combining field ionization detection with optical spectroscopy under Rydberg EIT conditions, we reconstructed the full single-atom density matrix of the system, thereby obtaining nearly full information about the coupled atom-light ensemble. We used this knowledge to reconstruct the spatial distributions of the Rydberg state population and of the medium optical response. Furthermore, we determined the spatial profile of the coupling beam which explains the observed spectral shape and width of the Rydberg population resonance as a consequence of spatially averaging over the entire excitation volume in the field ionization detection. This experimental method serves as a tool to extract the single-atom spatially dependent parameters and as valuable input for modeling light propagation in interacting Rydberg ensembles [Ates *et al.*, 2011; Gorshkov *et al.*, 2013; Gärttner *et al.*, 2014b; Bienias *et al.*, 2014] and for IEI.

After characterizing the contrast medium, we performed first IEI experiments with Rydberg $|50S\rangle$ impurities, demonstrating their spatially resolved optical detection. Then using IEI we studied the $|38S\rangle$-$|37S\rangle$ and $|50S\rangle$-$|48S\rangle$ impurity-probe state pairs and we observed dipolar energy transport due to state-exchange interactions between the Rydberg impurity and the probe Rydberg state, which was shared by the surrounding bath of optically dressed atoms.

The experiments with $|n'S\rangle$ impurities indicated that the IEI sensitivity was limited by the van der Waals interaction strength between $|n'S\rangle$-$|nS\rangle$ pairs and by the transport dynamics. To overcome these problems we set to excite $|nP\rangle$ impurities, which have stronger resonant dipole-dipole interactions with the probe $|nS\rangle$ state, and we implemented and characterized a three-photon off-resonant excitation. We described this four-level scheme in terms of an effective two-level system which provides accessible tools to fully optimize the excitation dynamics. Then we inhibited transport by constraining the cloud volume to dimensions comparable to the impurity-impurity blockade radius and we demonstrated for the first time optical detection of Rydberg $|42P_{3/2}\rangle$ states with high spatial resolution and improved sensitivity, but still not on the single Rydberg atom level.

To quantify the sensitivity achieved in the experiments performed during this thesis work, we measured the detection fidelity $\mathcal{F}$ via the threshold method. We found that for $|42P_{3/2}\rangle$ states we reached a single-shot sensitivity of 5 impurities, while for $|50S_{1/2}\rangle$ and $|43S_{1/2}\rangle$ states we were restricted to ≈ 12. To identify the limiting factors, we investigated in detail the signal and noise contributions in IEI, devising methods to reduce the influence of the latter. In particular we developed a

technique to remove the impact of total atom number variations on the fluctuations in the cloud absorption. We also found signatures of the presence of an additional effect to EIT that causes an increase over time of the medium optical response. This data can be explained by a population of additional states induced by black-body radiation, although further measurements are needed to confirm this hypothesis. Similar effects have been recently observed in other experiments [Goldschmidt *et al.*, 2016; DeSalvo *et al.*, 2016; Aman *et al.*, 2016; Han *et al.*, 2016].

Finally, we developed a model to predict the signal to noise ratio (SNR) to be expected in an IEI experiment, by extending a hard-sphere model that was first introduced to describe a strongly interacting Rydberg EIT medium [Petrosyan *et al.*, 2011; Ates *et al.*, 2011; Gärttner *et al.*, 2014b; DeSalvo *et al.*, 2016; Han *et al.*, 2016]. We compared its predictions with experimental data, finding good agreement, and we used it to calculate the achievable SNR for a broad range of impurity-probe state pairs and laser coupling parameters, allowing us to identify which Rydberg state combinations are the most suitable for future experiments with single-shot single Rydberg atom sensitivity.

The combination of optical and population-based probing of coherently driven three-level atomic systems, as realized for the first time in this experiment, can be used in the future not only to provide the single-atom parameters for more advanced models that study non-linear light propagation or interacting Rydberg systems, but also to experimentally test their predictions with high spatial and spectral resolution. Although the analytic treatment that we used to reconstruct the single-atom density matrix is not easily extendable to two or more body interactions, a possible approach could be to include their effect as an additional detuning and dephasing calculated through a mean field and local density approximations [DeSalvo *et al.*, 2016; Han *et al.*, 2016]. The hard-sphere model that we used to describe IEI could be straightfforwardly applied in a spatially resolved way to predict the susceptibility of an interacting medium under Rydberg EIT. We expect that these simple effective descriptions would approximate well the coupled atom-light system until the collective Rydberg excitation regime is reached [Gärttner *et al.*, 2014a].

Such studies may pave the way for more advanced investigations. Recent theoretical works [Sevinçli *et al.*, 2011b; Gorshkov *et al.*, 2013; Zhang and Evers, 2016; Murray and Pohl, 2016] have studied how the medium susceptibility is modified by atom-atom interactions and have predicted regimes where a non-linear and non-local response would emerge. These studies could be experimentally realized by illuminating the cloud with structured light [Lu *et al.*, 2015], created using a spatial light modulator (SLM) [van Bijnen, 2013; Bowman *et al.*, 2015; Naber *et al.*, 2015], and

observing the transmitted light field. Then, knowing the input and output fields and using an appropriate inversion method, a reconstruction of the optical susceptibility of such complex medium may be attempted.

The results obtained using IEI have proven that this optical detection technique is suitable for observing Rydberg dynamics with high spatial and temporal resolution. The work presented here has shown that single-shot single particle sensitivity is within reach if optimum laser parameters and impurity-probe state pairs are chosen. Furthermore, the state choice plays a key role because the interaction strength affects not only the sensitivity, but also the dynamics of the system.

For pairs of states with small Δn or tuned to Förster resonances we expect that fast state exchange processes would happen, with transport character determined by the interplay between interaction strength, dephasing sources and laser couplings [Schempp *et al.*, 2015]. In the case of large difference in principal quantum numbers it may be possible to find state combinations with a small exchange rate, but still a large enough interaction [Paris-Mandoki *et al.*, 2016], that would allow IEI experiments in a quasi-static regime.

Finally, impurities in states with a high principal quantum number exhibit typically a large impurity-impurity distance R_{ii}, caused by the Rydberg blockade effect between them, which may easily exceed the spatial resolution of the IEI (given by the convolution of impurity-probe blockade radius R_{ir} with the optical resolution of the imaging system), allowing for spatially resolved single impurity detection and imaging. Such new levels of sensitivity and resolution would enable improved studies of energy transport at the single particle level [Robicheaux and Gill, 2014; Schönleber *et al.*, 2015; Schempp *et al.*, 2015; Fahey *et al.*, 2015; Yu and Robicheaux, 2016], where many open questions remain, like the role of disorder and dephasing and the possibility to observe a transition from incoherent to coherent state exchange. Furthermore, IEI could be used to directly observe the formation of Rydberg aggregates [Malossi *et al.*, 2014; Schempp *et al.*, 2014; Urvoy *et al.*, 2015] and to follow the dynamics of spin systems realized with Rydberg atoms [Hazzard *et al.*, 2014; Glaetzle *et al.*, 2015; van Bijnen and Pohl, 2015; Barredo *et al.*, 2015; Labuhn *et al.*, 2016; Whitlock *et al.*, 2016].

Appendices

Appendix A

Laser frequency stabilization on a high Finesse Fabry-Pérot cavity

Here complementary details to Ch. 2.4.5 are presented on the laser locking system developed in the course of this thesis. The setup allows to stabilize with the Pound-Drever-Hall (PDH) method [Black, 2001] two 780 nm and two 960 nm lasers to a single, passive, dual-wavelength coated, high finesse ultra-low-expansion glass Fabry-Pérot cavity, characterized in [Kerst, 2014].

The electronic and optical setup for stabilizing the Toptica TA-SHG pro is shown in Fig. A.1 (a). The laser emits at 960 nm and a small fraction of this power is coupled into a fiber that goes to the stabilization breadboard, while the frequency doubled output at 480 nm is also fiber coupled and sent to the experiment's optical table. In order to have a broad frequency tunability range that could cover the cavity free spectral range (FSR = 1.5 GHz), the 960 nm light passes through a broadband fiber-coupled electro-optic modulator (EOM, NIR-MPX-LN-05 for this wavelength and NIR-MPX800-LN-05 for the infrared) [Aikawa $et\ al.$, 2011; Gregory $et\ al.$, 2015] to which we apply, by means of a power combiner (ZESC-2-11+), two modulation frequencies generated by direct-digital-synthesis (DDS) sources (Toptica PDD110f or home-built DDS and AD-9914 PCBZ). The first frequency ν_{mod} is used for the PDH modulation, while the second one ν_{offset} generates a frequency offset relative to a cavity mode, allowing for detunings up to the cavity FSR. The power combiner output is amplified in order to reach an RF power for ν_{offset} corresponding to a 1.35 radian phase shift ($V = 0.43V_{\pi}$) that leads to maximum power transfer from the laser carrier frequency to the first sideband generated by ν_{offset} (the sidebands are described by Bessel functions). The ν_{mod} power is experimentally optimized to give the highest error signal amplitude.

Figure A.1: (a) Locking scheme of the Toptica TA-SHG Pro $480\,\mathrm{nm}$ laser (frequency doubled from $960\,\mathrm{nm}$) to the high finesse Fabry-Pérot cavity. **(b)** Comparison between measured instantaneous linewidths at different timescales for the free running case (black dash-dotted line), locked to EIT spectroscopy (blue dotted line) and locked to the cavity (red line). The shaded grey areas represent the standard deviation of the linewidth estimation.

On the stabilization breadboard the laser beam is first polarized horizontally and then optically aligned and mode-matched using a single lens to the cavity TEM_{00} mode. Right before entering the cavity vacuum housing, the beam is circularly polarized using a $\lambda/2$ and a $\lambda/4$ waveplates (needed to achieve a very clean polarization), such that the signal reflected by the cavity is detected on a photodiode and fed into the electronic part of the setup. The 780 nm light of the DL100 pro follows an identical optical setup and is overlapped with the 960 nm beam right before the cavity vacuum housing using a dichroic mirror (Thorlabs DMLP900). The TA-SHG laser is coupled employing an identical optical setup to the TA-SHG pro, but with opposite polarization. A second 780 nm laser can be added in the future.

The electronic part of the locking setup is conceptually identical for the three lasers, but differs in few components. The signal detected on the photodiode is demodulated on a mixer (Toptica PDD110f or home-built) using ν_{mod}, generating an error signal for the proportional-integral-derivative controller (Toptica FALC or home-built) that applies feed-back on the laser current and on the voltage of the piezo-electric that holds the grating of the laser's Littrow extended cavity.

The open-loop frequency response for all the components of each locking setup has been measured by applying a sinusoidal frequency and measuring the amplitude and relative phase of the frequency response, obtaining a Bode plot. This allowed to estimate the delay times introduced by each component, which in turn determines the locking bandwidth as the frequency at which a π phase delay occurs. These measurements are listed in Table A.1.

We estimate the frequency stability of our lasers by measuring the root mean square instantaneous frequency deviation [Kerst, 2014] relative to a cavity mode of a reference active Fabry-Pérot cavity (Sirah Eagle Eye). The measured RMS linewidths of the three laser systems are shown in Table A.2 on the 10 μs timescale for three situations: when free-running and by stabilizing on an EIT spectroscopy lock or on the cavity (both with the same optimized PID parameters). In Fig. A.1 (b) is shown a linewidth measurement over three orders of magnitude in time for the TA-SHG pro laser (identical measurements for the other two lasers display the same behavior). The improvement achieved with the cavity lock over the EIT lock is evident.

Component	DL100 pro t_{delay} (ns)	DL100 pro ϕ (°)	TA-SHG pro t_{delay} (ns)	TA-SHG pro ϕ (°)	TA-SHG t_{delay} (ns)	TA-SHG ϕ (°)
Laser MOD DC	61	22	61	22	112	40
Fiber EOM + Photodiode	28	10	28	10	28	10
Frequency Mixer	33	12	42	15	44	15
PID	50	18	50	18	40	15
Filter	0	0	0	0	20	7
Cables	25	9	25	9	25	9
Total	197	71	206	74	267	96
Locking BW (MHz)	≈ 1.6		≈ 1.5		≈ 0.9	

Table A.1: Delay times introduced by the locking system components and locking bandwidth. The phase delay ϕ (°) is calculated at an offset frequency from the carrier of $1\,\mathrm{MHz}$.

Laser	RMS Linewidth at $10\,\mu s$ (kHz) Free running	EIT spectroscopy lock	Cavity lock
DL100 pro $780\,\mathrm{nm}$	310	195	10
TA-SHG pro $960\,\mathrm{nm}$	210	45	10
TA-SHG $960\,\mathrm{nm}$	210	110	30

Table A.2: RMS linewidth of the laser systems on the $10\,\mu s$ timescale. For comparison are shown the free-running linewidth and those obtained by stabilizing on an EIT spectroscopy lock and on the cavity (both with the same optimized PID parameters).

Appendix B

EM-CCD camera noise model

Here we present a derivation of the signal and noise contributions in the detection process of an Electron Multiplying Charge Coupled Device (EM-CCD) camera in presence of absorption from an atom cloud.

A number of photons N_ν^0 propagates through a cloud with optical density $\text{OD} = (\sigma_0 \tilde{\chi}/a_{px}) \cdot N_{atoms}$ and is partially absorbed. We assume that the incoming light follows a Poisson distribution and that the absorption process is binomial (either a photon is absorbed or not). The number of transmitted photons is

$$N_\nu = N_\nu^0 e^{-\text{OD}} + N_\nu^{stray} \tag{B.1}$$

$$\text{var}(N_\nu) = \langle N_\nu^0 e^{-\text{OD}} \rangle + (N_\nu^0 e^{-\text{OD}})^2 \cdot \left(\frac{\sigma_0 \tilde{\chi}}{a_{px}}\right)^2 \text{var}(N_{atoms}) + \text{var}(N_\nu^{stray}) \tag{B.2}$$

where N_ν^{stray} represents background light (which typically can be made negligible) and a_{px} is the area of one camera pixel.

The transmitted photons N_ν are detected on an EM-CCD camera, which converts them into a number of detected electrons N_{e^-} with total quantum efficiency Q_e, property of the camera,

$$N_{\text{e}^-} = Q_e N_\nu \tag{B.3}$$

$$\text{var}(N_{\text{e}^-}) = Q_e \text{var}(N_\nu) + N_\nu^2 \text{var}(Q_e) \tag{B.4}$$

The detection process is binomial and preserves the distribution of the detected photons, consequently the number of detected electrons also follows a Poisson distribution (a derivation can be found in [Johnson, 2008]). If a single pixel is considered, $\text{var}(Q_e)$ originates from single pixel response fluctuations (typically negligible), while if a region of interest of size N_{pix}^{ROI} pixels is binned together, then it includes also fixed pattern noise (the non-uniformity in response between pixels [Mooney *et al.*, 1989; Joseph and Collins, 2002]).

The electric charges are shifted through the sensor into the readout register. This process adds clock-induced charges $N_{e^-}^{cic} = \alpha_{cic} N_{pix}^{ROI}$ (with rate α_{cic} per pixel) and charges produced by dark current $N_{e^-}^{dark} = \alpha_{dark} N_{pix}^{ROI} t_{exp}$ (with rate α_{dark} per pixel per second, t_{exp} the exposure time)

$$N_{e^-}^{shifted} = N_{e^-} + N_{e^-}^{cic} + N_{e^-}^{dark} \tag{B.5}$$

$$\text{var}(N_{e^-}^{shifted}) = \text{var}(N_{e^-}) + \text{var}(N_{e^-}^{cic}) + \text{var}(N_{e^-}^{dark}) \tag{B.6}$$

These two additional noise sources are described by a Poisson distribution.

The electric charges are amplified in the Electron Multiplier (EM) gain register (if present) with gain G_{em}

$$N_{e^-}^{amp} = G_{em} N_{e^-}^{shifted} \tag{B.7}$$

$$\text{var}(N_{e^-}^{amp}) = G_{em}^2 F^2 \, \text{var}(N_{e^-}^{shift}) \tag{B.8}$$

This type of amplification is stochastic [Hirsch *et al.*, 2013], since it is based on the same principle of photo-multiplier tubes, and can introduce excess noise that depends on the camera mode, quantified by the parameter F: $F = 1$ for conventional, $F = \sqrt{2}$ for EM mode at high gain, $F = \sqrt{3}$ for EM mode at low gain [Robbins and Hadwen, 2003].

This amplified charge is magnified again by a pre-amplifier with gain G_{gf} and finally it is read-out by an analog-to-digital converter (ADC) which outputs a digital number N_{counts}

$$N_{counts} = (G_{gf} N_{e^-}^{amp} + N_{e^-}^{bias})/s \tag{B.9}$$

$$\text{var}(N_{counts}) = (G_{gf}/s)^2 \, \text{var}(N_{e^-}^{amp}) + (1/s)^2 \, \text{var}(N_{e^-}^{bias}) \tag{B.10}$$

$$+ (N_{e^-}^{amp}/s)^2 \, \sigma_{gf}^2 + \sigma_{rd}^2 + \text{var}(\text{ADC}) \tag{B.11}$$

where s is the conversion factor, commonly called "sensitivity", between electrons and counts with units e^-/ADU and $N_{e^-}^{bias}$ is an offset charge. The amplification process, the charge readout and the discretization introduce additional noise contributions, respectively σ_{gf}^2, σ_{rd}^2 (normally distributed) and $\text{var}(\text{ADC}) = (N_{pix}^{ROI})^2 \sigma_{ADC}^2 = (N_{pix}^{ROI})^2 \text{LSB}^2/12$ (uniformly distributed, LSB is the least significant bit), with final variance derived through standard error propagation.

Equations (5.4) and (5.5) presented in Ch. 5.2 are derived from this noise model, with most contributions to variance neglected due to being small compared to σ_{rd}^2.

Appendix C

Optical Bloch Equations analytic solutions for a three-level system

Exact analytic solutions of the steady state optical Bloch equations (OBE) for the full density matrix ρ for a single three-level atom have been found by leveraging the program "Mathematica", version 9.0 [Wolfram Research Inc., 2012]. The OBEs were written exactly as discussed in Ch. 3.1.1 and the solutions have been obtained using the commands "FullSimplify", "CoefficientArrays", "NullSpace" and "Total", imposing the stationary state condition $\partial\rho/\partial t = 0$. In the OBEs were included the presence of decay of the $|e\rangle$, $|r\rangle$ states, dephasing on both transitions and arbitrary Rabi frequencies, consequently the presented solutions have a much broader validity range than the analytic solutions obtained with the weak probe approximation (see Eq. (3.8)). To validate the result, the analytic solutions have been compared with numeric solutions at a time which insured being in the steady state of the latter and the two approaches agreed within numeric precision on the 10^{-12} level.

The notation follows the one used in Ch. 3.1.1 with the following changes:

- $\Gamma_{ge} = \Gamma_e + \gamma_p$, $\Gamma_{gr} = \Gamma_r + \gamma_c + \gamma_p$, $\Gamma_{er} = \Gamma_r + \Gamma_e + \gamma_c$ (all three on resonance)

- for a "ladder" level configuration $\Delta_{gr} = \Delta_p + \Delta_c$

- for a "lambda" level configuration $\Delta_{gr} = \Delta_p - \Delta_c$

The following conditions reduce the number of independent matrix elements from 9 to 5:

$$\rho_{gg} + \rho_{ee} + \rho_{rr} = 1$$
$$\rho_{ab} = \rho_{ba}^*$$

All the density matrix elements have a common denominator:

$$
\begin{aligned}
\rho_d = & \Big[\Gamma_e(\Gamma_{er}^2\Gamma_r + 4\Gamma_r\Delta_c^2 + \Gamma_{er}\Omega_c^2)(4\Gamma_{gr}^2\Delta_p^2 + (-4\Delta_{gr}\Delta_p + \Omega_c^2)^2) \\
& + (-(4\Delta_{gr}\Delta_p - \Omega_c^2)(8\Gamma_e\Gamma_r\Delta_c\Delta_p + \Gamma_{er}(\Gamma_e - \Gamma_r)\Omega_c^2) \\
& + \Gamma_{gr}(8\Gamma_{er}\Gamma_e\Gamma_r\Delta_p^2 + 2(\Gamma_{er}^2\Gamma_r + 2\Gamma_e\Delta_p(-\Delta_c + \Delta_p) + 2\Gamma_r\Delta_c(2\Delta_c + \Delta_p))\Omega_c^2 + 3\Gamma_{er}\Omega_c^4))\Omega_p^2 \\
& + 2\Gamma_r(2\Gamma_e\Delta_p^2 + \Gamma_{er}\Omega_c^2)\Omega_p^4 + \Gamma_{ge}^2\Gamma_e((\Gamma_{gr}^2 + 4\Delta_{gr}^2)(\Gamma_{er}^2\Gamma_r + 4\Gamma_r\Delta_c^2 + \Gamma_{er}\Omega_c^2) \\
& + (-8\Gamma_r\Delta_c\Delta_{gr} + \Gamma_{gr}(2\Gamma_{er}\Gamma_r + \Omega_c^2))\Omega_p^2 + \Gamma_r\Omega_p^4) + \Gamma_{ge}(2\Gamma_{gr}\Gamma_e\Omega_c^2(\Gamma_{er}^2\Gamma_r + 4\Gamma_r\Delta_c^2 + \Gamma_{er}\Omega_c^2) \\
& + (2\Gamma_r(\Gamma_{er}^2 + 4\Delta_c^2)(\Gamma_{gr}^2 + 4\Delta_{gr}^2) + (\Gamma_{er}(3\Gamma_{gr}^2 + \Gamma_{gr}(\Gamma_e - \Gamma_r) + 2\Gamma_e\Gamma_r) \\
& + 4(-\Gamma_e + \Gamma_r)\Delta_c\Delta_{gr} + 12\Gamma_{er}\Delta_{gr}^2)\Omega_c^2 + \Gamma_e\Omega_c^4)\Omega_p^2 \\
& + (4\Gamma_r(\Gamma_{gr}\Gamma_{er} - 4\Delta_c\Delta_{gr}) + (3\Gamma_{gr} + \Gamma_e - \Gamma_r)\Omega_c^2)\Omega_p^4 + 2\Gamma_r\Omega_p^6)\Big]
\end{aligned}
$$
$$(C.1)$$

For the populations we find:

$$
\begin{aligned}
\rho_{gg} = & \Big[\Gamma_e(\Gamma_r^2\Gamma_r + 4\Gamma_r\Delta_c^2 + \Gamma_r\Omega_c^2)(4\Gamma_{gr}^2\Delta_p^2 + (-4\Delta_{gr}\Delta_p + \Omega_c^2)^2) \\
& + (8\Gamma_e\Gamma_r(\Gamma_{gr}\Gamma_r - 4\Delta_c\Delta_{gr})\Delta_p^2 + (\Gamma_{gr}\Gamma_r(\Gamma_r^2 + 4\Delta_c^2) \\
& + 4\Gamma_r(\Gamma_{gr}\Delta_c + 2\Gamma_e\Delta_c + \Gamma_r\Delta_{gr})\Delta_p + 4\Gamma_{gr}\Gamma_e\Delta_p^2)\Omega_c^2 + \Gamma_r(\Gamma_{gr} - \Gamma_r)\Omega_c^4)\Omega_p^2 \\
& + \Gamma_r(4\Gamma_e\Delta_p^2 + \Gamma_r\Omega_c^2)\Omega_p^4 + \Gamma_{ge}^2\Gamma_e((\Gamma_{gr}^2 + 4\Delta_{gr}^2)(\Gamma_r^2\Gamma_r + 4\Gamma_r\Delta_c^2 + \Gamma_r\Omega_c^2) \\
& + (-8\Gamma_r\Delta_c\Delta_{gr} + \Gamma_{gr}(2\Gamma_r\Gamma_r + \Omega_c^2))\Omega_p^2 + \Gamma_r\Omega_p^4) \\
& + \Gamma_{ge}(2\Gamma_{gr}\Gamma_e\Omega_c^2(\Gamma_r^2\Gamma_r + 4\Gamma_r\Delta_c^2 + \Gamma_r\Omega_c^2) + (\Gamma_r(\Gamma_r^2 + 4\Delta_c^2)(\Gamma_{gr}^2 + 4\Delta_{gr}^2) \\
& + (\Gamma_r(\Gamma_{gr}^2 - \Gamma_{gr}\Gamma_r + 2\Gamma_e\Gamma_r) + 4\Gamma_r\Delta_c\Delta_{gr} + 4\Gamma_r\Delta_{gr}^2)\Omega_c^2 + \Gamma_e\Omega_c^4)\Omega_p^2 \\
& + (\Gamma_{gr}(2\Gamma_r\Gamma_r + \Omega_c^2) - \Gamma_r(8\Delta_c\Delta_{gr} + \Omega_c^2))\Omega_p^4 + \Gamma_r\Omega_p^6)\Big]/\rho_d
\end{aligned}
$$
$$(C.2)$$

$$
\begin{aligned}
\rho_{ee} = & \Big[(\Gamma_{ge}(\Gamma_{gr}^2 + 4\Delta_{gr}^2) + \Gamma_{gr}\Omega_c^2)(\Gamma_{er}^2\Gamma_r + 4\Gamma_r\Delta_c^2 + \Gamma_{er}\Omega_c^2)\Omega_p^2 \\
& + (2\Gamma_{ge}\Gamma_r(\Gamma_{gr}\Gamma_{er} - 4\Delta_c\Delta_{gr}) + (\Gamma_{ge}\Gamma_{gr} + \Gamma_{er}\Gamma_r)\Omega_c^2)\Omega_p^4 + \Gamma_{ge}\Gamma_r\Omega_p^6\Big]/\rho_d
\end{aligned}
$$
$$(C.3)$$

$$
\begin{aligned}
\rho_{rr} = & \Big[\Omega_c^2\Omega_p^2(-4\Gamma_e(\Gamma_{gr}\Delta_c + \Gamma_{er}\Delta_{gr})\Delta_p + \Gamma_{er}(\Gamma_{gr} + \Gamma_e)\Omega_c^2 \\
& + \Gamma_{ge}(\Gamma_{gr}^2\Gamma_{er} + \Gamma_{gr}\Gamma_{er}\Gamma_e - 4\Gamma_e\Delta_c\Delta_{gr} + 4\Gamma_{er}\Delta_{gr}^2 + (\Gamma_{gr} + \Gamma_e)\Omega_p^2))\Big]/\rho_d
\end{aligned}
$$
$$(C.4)$$

For the coherences we find:

$$
\begin{aligned}
\rho_{ge} = \Big[\Big(& 2\Gamma_{gr}^2\Gamma_{er}^2\Gamma_e\Gamma_r\Delta_p\Omega_p + 8\Gamma_{gr}^2\Gamma_e\Gamma_r\Delta_c^2\Delta_p\Omega_p + 8\Gamma_{er}^2\Gamma_e\Gamma_r\Delta_{gr}^2\Delta_p\Omega_p + 32\Gamma_e\Gamma_r\Delta_c^2\Delta_{gr}^2\Delta_p\Omega_p \\
& - 2\Gamma_{er}^2\Gamma_e\Gamma_r\Delta_{gr}\Omega_c^2\Omega_p - 8\Gamma_e\Gamma_r\Delta_c^2\Delta_{gr}\Omega_c^2\Omega_p + 2\Gamma_{gr}^2\Gamma_{er}\Gamma_e\Delta_p\Omega_c^2\Omega_p + 8\Gamma_{er}\Gamma_e\Delta_{gr}^2\Delta_p\Omega_c^2\Omega_p \\
& - 2\Gamma_{er}\Gamma_e\Delta_{gr}\Omega_c^4\Omega_p + 4\Gamma_{gr}\Gamma_{er}\Gamma_e\Gamma_r\Delta_p\Omega_p^3 - 16\Gamma_e\Gamma_r\Delta_c\Delta_{gr}\Delta_p\Omega_p^3 + 2\Gamma_{gr}\Gamma_r\Delta_c\Omega_c^2\Omega_p^3 \\
& + 2\Gamma_e\Gamma_r\Delta_c\Omega_c^2\Omega_p^3 + 2\Gamma_{er}\Gamma_r\Delta_{gr}\Omega_c^2\Omega_p^3 + 2\Gamma_{gr}\Gamma_e\Delta_p\Omega_c^2\Omega_p^3 + 2\Gamma_e\Gamma_r\Delta_p\Omega_p^5 \Big) \\
+ \mathrm{i} \Big(& \Gamma_{ge}\Gamma_{gr}^2\Gamma_{er}^2\Gamma_e\Gamma_r\Omega_p + 4\Gamma_{ge}\Gamma_{gr}^2\Gamma_e\Gamma_r\Delta_c^2\Omega_p + 4\Gamma_{ge}\Gamma_{er}^2\Gamma_e\Gamma_r\Delta_{gr}^2\Omega_p + 16\Gamma_{ge}\Gamma_e\Gamma_r\Delta_c^2\Delta_{gr}^2\Omega_p \\
& + \Gamma_{ge}\Gamma_{gr}^2\Gamma_{er}\Gamma_e\Omega_c^2\Omega_p + \Gamma_{gr}\Gamma_{er}^2\Gamma_e\Gamma_r\Omega_c^2\Omega_p + 4\Gamma_{gr}\Gamma_e\Gamma_r\Delta_c^2\Omega_c^2\Omega_p + 4\Gamma_{ge}\Gamma_{er}\Gamma_e\Delta_{gr}^2\Omega_c^2\Omega_p \\
& + \Gamma_{gr}\Gamma_{er}\Gamma_e\Omega_c^4\Omega_p + 2\Gamma_{ge}\Gamma_{gr}\Gamma_{er}\Gamma_e\Gamma_r\Omega_p^3 - 8\Gamma_{ge}\Gamma_e\Gamma_r\Delta_c\Delta_{gr}\Omega_p^3 + \Gamma_{ge}\Gamma_{gr}\Gamma_e\Omega_c^2\Omega_p^3 \\
& + \Gamma_{er}\Gamma_e\Gamma_r\Omega_c^2\Omega_p^3 + \Gamma_{ge}\Gamma_e\Gamma_r\Omega_p^5 \Big) \Big] / \rho_d
\end{aligned}
\tag{C.5}
$$

$$
\begin{aligned}
\rho_{gr} = \Big[\Big(& - \Gamma_{ge}\Gamma_{gr}\Gamma_{er}^2\Gamma_e\Gamma_r\Omega_c\Omega_p - 4\Gamma_{ge}\Gamma_{gr}\Gamma_e\Gamma_r\Delta_c^2\Omega_c\Omega_p + 4\Gamma_{er}^2\Gamma_e\Gamma_r\Delta_{gr}\Delta_p\Omega_c\Omega_p \\
& + 16\Gamma_e\Gamma_r\Delta_c^2\Delta_{gr}\Delta_p\Omega_c\Omega_p - \Gamma_{ge}\Gamma_{gr}\Gamma_{er}\Gamma_e\Omega_c^3\Omega_p - \Gamma_{er}^2\Gamma_e\Gamma_r\Omega_c^3\Omega_p - 4\Gamma_e\Gamma_r\Delta_c^2\Omega_c^3\Omega_p \\
& + 4\Gamma_{er}\Gamma_e\Delta_{gr}\Delta_p\Omega_c^3\Omega_p - \Gamma_{er}\Gamma_e\Omega_c^5\Omega_p + \Gamma_{ge}\Gamma_{gr}\Gamma_{er}\Gamma_r\Omega_c\Omega_p^3 - \Gamma_{ge}\Gamma_{er}\Gamma_e\Gamma_r\Omega_c\Omega_p^3 \\
& - 4\Gamma_{ge}\Gamma_r\Delta_c\Delta_{gr}\Omega_c\Omega_p^3 - 4\Gamma_e\Gamma_r\Delta_c\Delta_p\Omega_c\Omega_p^3 - \Gamma_{ge}\Gamma_e\Omega_c^3\Omega_p^3 + \Gamma_{er}\Gamma_r\Omega_c^3\Omega_p^3 + \Gamma_{ge}\Gamma_r\Omega_c\Omega_p^5 \Big) \\
+ \mathrm{i} \Big(& 2\Gamma_{ge}\Gamma_{er}^2\Gamma_e\Gamma_r\Delta_{gr}\Omega_c\Omega_p + 8\Gamma_{ge}\Gamma_e\Gamma_r\Delta_c^2\Delta_{gr}\Omega_c\Omega_p + 2\Gamma_{gr}\Gamma_{er}^2\Gamma_e\Gamma_r\Delta_p\Omega_c\Omega_p \\
& + 8\Gamma_{gr}\Gamma_e\Gamma_r\Delta_c^2\Delta_p\Omega_c\Omega_p + 2\Gamma_{ge}\Gamma_{er}\Gamma_e\Delta_{gr}\Omega_c^3\Omega_p + 2\Gamma_{gr}\Gamma_{er}\Gamma_e\Delta_p\Omega_c^3\Omega_p - 2\Gamma_{ge}\Gamma_{gr}\Gamma_r\Delta_c\Omega_c\Omega_p^3 \\
& - 2\Gamma_{ge}\Gamma_e\Gamma_r\Delta_c\Omega_c\Omega_p^3 - 2\Gamma_{ge}\Gamma_{er}\Gamma_r\Delta_{gr}\Omega_c\Omega_p^3 + 2\Gamma_{er}\Gamma_e\Gamma_r\Delta_p\Omega_c\Omega_p^3 \Big) \Big] / \rho_d
\end{aligned}
\tag{C.6}
$$

$$
\begin{aligned}
\rho_{er} = \Big[\Big(& 2\Gamma_{ge}\Gamma_{gr}^2\Gamma_r\Delta_c\Omega_c\Omega_p^2 + 2\Gamma_{ge}\Gamma_{gr}\Gamma_e\Gamma_r\Delta_c\Omega_c\Omega_p^2 + 2\Gamma_{ge}\Gamma_{er}\Gamma_e\Gamma_r\Delta_{gr}\Omega_c\Omega_p^2 \\
& + 8\Gamma_{ge}\Gamma_r\Delta_c\Delta_{gr}^2\Omega_c\Omega_p^2 + 2\Gamma_{gr}\Gamma_{er}\Gamma_e\Gamma_r\Delta_p\Omega_c\Omega_p^2 - 8\Gamma_e\Gamma_r\Delta_c\Delta_{gr}\Delta_p\Omega_c\Omega_p^2 + 2\Gamma_{gr}\Gamma_r\Delta_c\Omega_c^3\Omega_p^2 \\
& + 2\Gamma_e\Gamma_r\Delta_c\Omega_c^3\Omega_p^2 + 2\Gamma_{ge}\Gamma_e\Delta_{gr}\Omega_c^3\Omega_p^2 + 2\Gamma_{gr}\Gamma_e\Delta_p\Omega_c^3\Omega_p^2 - 2\Gamma_{ge}\Gamma_r\Delta_{gr}\Omega_c\Omega_p^4 + 2\Gamma_e\Gamma_r\Delta_p\Omega_c\Omega_p^4 \Big) \\
+ \mathrm{i} \Big(& \Gamma_{ge}\Gamma_{gr}^2\Gamma_{er}\Gamma_r\Omega_c\Omega_p^2 + \Gamma_{ge}\Gamma_{gr}\Gamma_{er}\Gamma_e\Gamma_r\Omega_c\Omega_p^2 - 4\Gamma_{ge}\Gamma_e\Gamma_r\Delta_c\Delta_{gr}\Omega_c\Omega_p^2 + 4\Gamma_{ge}\Gamma_{er}\Gamma_r\Delta_{gr}^2\Omega_c\Omega_p^2 \\
& - 4\Gamma_{gr}\Gamma_e\Gamma_r\Delta_c\Delta_p\Omega_c\Omega_p^2 - 4\Gamma_{er}\Gamma_e\Gamma_r\Delta_{gr}\Delta_p\Omega_c\Omega_p^2 + \Gamma_{gr}\Gamma_{er}\Gamma_r\Omega_c^3\Omega_p^2 + \Gamma_{er}\Gamma_e\Gamma_r\Omega_c^3\Omega_p^2 \\
& + \Gamma_{ge}\Gamma_{gr}\Gamma_r\Omega_c\Omega_p^4 + \Gamma_{ge}\Gamma_e\Gamma_r\Omega_c\Omega_p^4 \Big) \Big] / \rho_d
\end{aligned}
\tag{C.7}
$$

Bibliography

(1997). *The Nobel Prize in Physics 1997*.

(2001). *The Nobel Prize in Physics 2001*.

(2003). *The Nobel Prize in Physiology or Medicine 2003*.

(2012). *The Nobel Prize in Physics 2012*.

(2014). *The Nobel Prize in Chemistry 2014*.

Abel, R. P., Mohapatra, A. K., Bason, M. G., Pritchard, J. D., Weatherill, K. J., Raitzsch, U., and Adams, C. S. (2009). *Laser frequency stabilization to excited state transitions using electromagnetically induced transparency in a cascade system*. Appl. Phys. Lett, **94**, 071107.

Acton, M., Brickman, K.-A., Haljan, P. C., Lee, P. J., Deslauriers, L., and Monroe, C. (2006). *Near-perfect Simultaneous Measurement of a Qubit Register*. Quantum Info. Comput., **6**, 465.

Adams, C. S., Weatherill, K. J., and Pritchard, J. D. (2013). *Nonlinear Optics Using Cold Rydberg Atoms*, chapter 8, , pp. 301–350. World Scientific Publishing Co.

Afrousheh, K. (2006). *Observation of Resonant Electric Dipole-Dipole Interactions Between Cold Rydberg Atoms Using Microwave Spectroscopy*. PhD thesis, University of Waterloo.

Afrousheh, K., Bohlouli-Zanjani, P., Carter, J. D., Mugford, A., and Martin, J. D. D. (2006). *Resonant electric dipole-dipole interactions between cold Rydberg atoms in a magnetic field*. Phys. Rev. A, **73**, 063403.

Afrousheh, K., Bohlouli-Zanjani, P., Vagale, D., Mugford, A., Fedorov, M., and Martin, J. D. D. (2004). *Spectroscopic Observation of Resonant Electric Dipole-Dipole Interactions between Cold Rydberg Atoms*. Phys. Rev. Lett., **93**, 233001.

Aikawa, K., Kobayashi, J., Oasa, K., Kishimoto, T., Ueda, M., and Inouye, S. (2011). *Narrow-linewidth light source for a coherent Raman transfer of ultracold molecules.* Opt. Express, **19**, 14479.

Aman, J. A., DeSalvo, B. J., Dunning, F. B., Killian, T. C., Yoshida, S., and Burgdörfer, J. (2016). *Trap losses induced by near-resonant Rydberg dressing of cold atomic gases.* Phys. Rev. A, **93**, 043425.

Amthor, T. (2008). *Interaction-Induced Dynamics in Ultracold Rydberg Gases: Mechanical Effects and Coherent Processes.* PhD thesis, Fakultät für Mathematik und Physik, Albert-Ludwigs-Universität Freiburg.

Amthor, T., Denskat, J., Giese, C., Bezuglov, N. N., Ekers, A., Cederbaum, L. S., and Weidemüller, M. (2009). *Autoionization of an ultracold Rydberg gas through resonant dipole coupling.* Eur. Phys. J. D, **53**, 329.

Amthor, T., Reetz-Lamour, M., Giese, C., and Weidemüller, M. (2007a). *Modeling many-particle mechanical effects of an interacting Rydberg gas.* Phys. Rev. A, **76**, 054702.

Amthor, T., Reetz-Lamour, M., Westermann, S., Denskat, J., and Weidemüller, M. (2007b). *Mechanical Effect of van der Waals Interactions Observed in Real Time in an Ultracold Rydberg Gas.* Phys. Rev. Lett., **98**, 023004.

Anderson, W., Veale, J., and Gallagher, T. (1998). *Resonant dipole-dipole energy transfer in a nearly frozen Rydberg gas.* Phys. Rev. Lett., **80**, 249.

Anderson, W. R., Robinson, M. P., Martin, J. D. D., and Gallagher, T. F. (2002). *Dephasing of resonant energy transfer in a cold Rydberg gas.* Phys. Rev. A, **65**, 063404.

Anisimov, P. M., Dowling, J. P., and Sanders, B. C. (2011). *Objectively Discerning Autler-Townes Splitting from Electromagnetically Induced Transparency.* Phys. Rev. Lett., **107**, 163604.

Ates, C., Sevinçli, S., and Pohl, T. (2011). *Electromagnetically induced transparency in strongly interacting Rydberg gases.* Phys. Rev. A, **83**, 041802.

Attwood, D. (2007). *Soft x-rays and extreme ultraviolet radiation: principles and applications.* Cambridge University Press.

Autler, S. H. and Townes, C. H. (1955). *Stark Effect in Rapidly Varying Fields.* Phys. Rev., **100**, 703.

Bakr, W. S., Gillen, J. I., Peng, A., Folling, S., and Greiner, M. (2009). *A quantum gas microscope for detecting single atoms in a Hubbard-regime optical lattice.* Nature, **462**, 74.

Bakr, W. S., Peng, A., Tai, M. E., Ma, R., Simon, J., Gillen, J. I., Fölling, S., Pollet, L., and Greiner, M. (2010). *Probing the Superfluid–to–Mott Insulator Transition at the Single-Atom Level.* Science, **329**, 547.

Barredo, D., Kübler, H., Daschner, R., Löw, R., and Pfau, T. (2013). *Electrical Readout for Coherent Phenomena Involving Rydberg Atoms in Thermal Vapor Cells.* Phys. Rev. Lett., **110**, 123002.

Barredo, D., Labuhn, H., Ravets, S., Lahaye, T., Browaeys, A., and Adams, C. S. (2015). *Coherent Excitation Transfer in a Spin Chain of Three Rydberg Atoms.* Phys. Rev. Lett., **114**, 113002.

Basden, A. G., Haniff, C. A., and Mackay, C. D. (2003). *Photon counting strategies with low-light-level CCDs.* Monthly Notices of the Royal Astronomical Society, **345**, 985.

Baur, S., Tiarks, D., Rempe, G., and Dürr, S. (2014). *Single-Photon Switch Based on Rydberg Blockade.* Phys. Rev. Lett., **112**, 073901.

Bendkowsky, V., Butscher, B., Nipper, J., Shaffer, J. P., Löw, R., and Pfau, T. (2009). *Observation of ultralong-range Rydberg molecules.* Nature, **458**, 1005 .

Beterov, I. I., Ryabtsev, I. I., Tretyakov, D. B., and Entin, V. M. (2009). *Quasiclassical calculations of blackbody-radiation-induced depopulation rates and effective lifetimes of Rydberg nS, nP, and nD alkali-metal atoms with $n <= 80$.* Phys. Rev. A, **79**, 052504.

Beterov, I. I., Tretyakov, D. B., Entin, V. M., Yakshina, E. A., Ryabtsev, I. I., MacCormick, C., and Bergamini, S. (2011). *Deterministic single-atom excitation via adiabatic passage and Rydberg blockade.* Phys. Rev. A, **84**, 023413.

Bienias, P. (2016). *Few-body quantum physics with strongly interacting Rydberg polaritons.* arXiv:1608.01629.

Bienias, P. and Büchler, H. P. (2016). *Quantum theory of Kerr nonlinearity with Rydberg slow light polaritons.* arXiv:1604.05125.

Bienias, P., Choi, S., Firstenberg, O., Maghrebi, M. F., Gullans, M., Lukin, M. D., Gorshkov, A. V., and Büchler, H. P. (2014). *Scattering resonances and bound states for strongly interacting Rydberg polaritons.* Phys. Rev. A, **90**, 053804.

Black, E. D. (2001). *An introduction to Pound-Drever-Hall laser frequency stabilization.* American Journal of Physics, **69**, 79.

Bloch, I., Dalibard, J., and Nascimbène, S. (2012). *Quantum simulations with ultracold quantum gases.* Nature Physics, **8**, 267.

Bloch, I., Dalibard, J., and Zwerger, W. (2008). *Many-body physics with ultracold gases.* Rev. Mod. Phys., **80**, 885.

Bochmann, J., Mücke, M., Guhl, C., Ritter, S., Rempe, G., and Moehring, D. L. (2010). *Lossless State Detection of Single Neutral Atoms.* Phys. Rev. Lett., **104**, 203601.

Boisseau, C., Simbotin, I., and Côté, R. (2002). *Macrodimers: Ultralong Range Rydberg Molecules.* Phys. Rev. Lett., **88**, 133004.

Bowman, D., Ireland, P., Bruce, G. D., and Cassettari, D. (2015). *Multi-wavelength holography with a single spatial light modulator for ultracold atom experiments.* Opt. Express, **23**, 8365.

Branden, D. B., Juhasz, T., Mahlokozera, T., Vesa, C., Wilson, R. O., Zheng, M., Kortyna, A., and Tate, D. A. (2010). *Radiative lifetime measurements of rubidium Rydberg states.* Journal of Physics B: Atomic, Molecular and Optical Physics, **43**, 015002.

Brandt, S. (2014). *Data Analysis: Statistical and Computational Methods for Scientists and Engineers.* SpringerLink : Bücher. Springer International Publishing.

Brion, E., Pedersen, L. H., and Mølmer, K. (2007). *Adiabatic elimination in a lambda system.* Journal of Physics A: Mathematical and Theoretical, **40**, 1033.

Camy, G., Bordé, C., and Ducloy, M. (1982). *Heterodyne saturation spectroscopy through frequency modulation of the saturating beam.* Optics Communications, **41**, 325 .

Cheuk, L. W., Nichols, M. A., Okan, M., Gersdorf, T., Ramasesh, V. V., Bakr, W. S., Lompe, T., and Zwierlein, M. W. (2015). *Quantum-Gas Microscope for Fermionic Atoms.* Phys. Rev. Lett., **114**, 193001.

Choi, J.-H., Knuffman, B., Liebisch, T. C., Reinhard, A., and Raithel, G. (2006). *Cold Rydberg Atoms.* Vol. 54 of *ADVANCES IN ATOMIC, MOLECULAR AND OPTICAL PHYSICS*, , pp. 131–202. Academic Press.

Cirac, J. I. and Zoller, P. (1995). *Quantum Computations with Cold Trapped Ions.* Phys. Rev. Lett., **74**, 4091.

Cirac, J. I. and Zoller, P. (2012). *Goals and opportunities in quantum simulation.* Nature Physics, **8**, 264.

Claudon, M., Dietrich, C. F., Choi, B. I., Cosgrove, D. O., Kudo, M., Nolsøe, C. P., Piscaglia, F., Wilson, S. R., Barr, R. G., Chammas, M. C., Chaubal, N. G., Chen, M.-H., Clevert, D. A., Correas, J. M., Ding, H., Forsberg, F., Fowlkes, J. B., Gibson, R. N., Goldberg, B. B., Lassau, N., Leen, E. L., Mattrey, R. F., Moriyasu, F., Solbiati, L., Weskott, H.-P., and Xu, H.-X. (2013). *Guidelines and Good Clinical Practice Recommendations for Contrast Enhanced Ultrasound (CEUS) in the Liver – Update 2012: A WFUMB-EFSUMB Initiative in Cooperation with Representatives of AFSUMB, AIUM, ASUM, {FLAUS} and {ICUS}.* Ultrasound in Medicine & Biology, **39**, 187 .

Clegg, R. M. (2009). *Forster resonance energy transfer – FRET what it is, why do it, and how it's done.* FRET and FLIM Techniques, **1**, 1.

Clément, J.-F., Brantut, J.-P., Robert-de Saint-Vincent, M., Nyman, R. A., Aspect, A., Bourdel, T., and Bouyer, P. (2009). *All-optical runaway evaporation to Bose-Einstein condensation.* Phys. Rev. A, **79**, 061406.

Cohen-Tannoudji, C. (1996). *Amazing Light: A Volume Dedicated To Charles Hard Townes On His 80th Birthday*, chapter The Autler-Townes effect revisited. Springer.

Collini, E. (2013). *Spectroscopic signatures of quantum-coherent energy transfer.* Chem. Soc. Rev., **42**, 4932.

Comparat, D. and Pillet, P. (2010). *Dipole blockade in a cold Rydberg atomic sample.* J. Opt. Soc. Am. B, **27**, A208.

Cowan, G. (1998). *Statistical data analysis*. Oxford University Press.

De Greve, K., McMahon, P. L., Yu, L., Pelc, J. S., Jones, C., Natarajan, C. M., Kim, N. Y., Abe, E., Maier, S., Schneider, C., Kamp, M., Höfling, S., Hadfield, R. H., Forchel, A., Fejer, M. M., and Yamamoto, Y. (2013). *Complete tomography of a high-fidelity solid-state entangled spin-photon qubit pair*. Nat Commun, **4**, .

Debnath, S., Linke, N. M., Figgatt, C., Landsman, K. A., Wright, K., and Monroe, C. (2016). *Demonstration of a small programmable quantum computer with atomic qubits*. Nature, **536**, 63.

Deiglmayr, J., Reetz-Lamour, M., Amthor, T., Westermann, S., de Oliveira, A., and Weidemüller, M. (2006). *Coherent excitation of Rydberg atoms in an ultracold gas*. Optics Communications, **264**, 293 .

Deléglise, S., Dotsenko, I., Sayrin, C., Bernu, J., Brune, M., Raimond, J.-M., and Haroche, S. (2008). *Reconstruction of non-classical cavity field states with snapshots of their decoherence*. Nature, **455**, 510.

DeSalvo, B. J., Aman, J. A., Gaul, C., Pohl, T., Yoshida, S., Burgdörfer, J., Hazzard, K. R. A., Dunning, F. B., and Killian, T. C. (2016). *Rydberg-blockade effects in Autler-Townes spectra of ultracold strontium*. Phys. Rev. A, **93**, 022709.

Dieckmann, K., Spreeuw, R. J. C., Weidemüller, M., and Walraven, J. T. M. (1998). *Two-dimensional magneto-optical trap as a source of slow atoms*. Phys. Rev. A, **58**, 3891.

Dudin, Y. O. and Kuzmich, A. (2012). *Strongly Interacting Rydberg Excitations of a Cold Atomic Gas*. Science, **336**, 887 .

Dunn, T. J., Walmsley, I. A., and Mukamel, S. (1995). *Experimental Determination of the Quantum-Mechanical State of a Molecular Vibrational Mode Using Fluorescence Tomography*. Phys. Rev. Lett., **74**, 884.

Efron, B. and Tibshirani, R. (1994). *An Introduction to the Bootstrap*. Chapman & Hall/CRC Monographs on Statistics & Applied Probability. Taylor & Francis.

Fahey, D. P., Carroll, T. J., and Noel, M. W. (2015). *Imaging the dipole-dipole energy exchange between ultracold rubidium Rydberg atoms*. Phys. Rev. A, **91**, 062702.

Fano, U. (1961). *Effects of Configuration Interaction on Intensities and Phase Shifts.* Phys. Rev., **124**, 1866.

Faraoni, G. (2014). *Nonlinear light propagation through a strongly interacting Rydberg gas.* Master's thesis, Facoltà di Scienze Matematiche, Fisiche e Naturali, Università di Pisa.

Firstenberg, O., Adams, C. S., and Hofferberth, S. (2016). *Nonlinear quantum optics mediated by Rydberg interactions.* Journal of Physics B: Atomic, Molecular and Optical Physics, **49**, 152003.

Firstenberg, O., Peyronel, T., Liang, Q.-Y., Gorshkov, A. V., Lukin, M. D., and Vuletic, V. (2013). *Attractive photons in a quantum nonlinear medium.* Nature, **502**, 71.

Fleischhauer, M., Imamoglu, A., and Marangos, J. P. (2005). *Electromagnetically induced transparency: Optics in coherent media.* Rev. Mod. Phys., **77**, 633.

Fleischhauer, M. and Lukin, M. D. (2000). *Dark-State Polaritons in Electromagnetically Induced Transparency.* Phys. Rev. Lett., **84**, 5094.

Förster, T. (1948). *Zwischenmolekulare Energiewanderung und Fluoreszenz.* Annalen der Physik, **437**, 55.

Gaëtan, A., Evellin, C., Wolters, J., Grangier, P., Wilk, T., and Browaeys, A. (2010). *Analysis of the entanglement between two individual atoms using global Raman rotations.* New Journal of Physics, **12**, 065040.

Gaj, A., Krupp, A. T., Balewski, J. B .and Löw, R., Hofferberth, S., and Pfau, T. (2014). *From molecular spectra to a density shift in dense Rydberg gases.* Nature Communications, **5**, 4546.

Gajdacz, M., Hilliard, A. J., Kristensen, M. A., Pedersen, P. L., Klempt, C., Arlt, J. J., and Sherson, J. F. (2016). *Preparation of Ultracold Atom Clouds at the Shot Noise Level.* Phys. Rev. Lett., **117**, 073604.

Gallagher, T. F. (1994). *Rydberg Atoms.* Cambridge University Press.

Gallagher, T. F. and Pillet, P. (2008). *Dipole-Dipole Interactions of Rydberg Atoms.* In: et al, A. (Ed.), *Advances in Atomic, Molecular, and Optical Physics*, Vol. 56 of *Advances In Atomic, Molecular, and Optical Physics*, , pp. 161 – 218. Academic Press.

Gallagher, T. F., Safinya, K. A., Gounand, F., Delpech, J. F., Sandner, W., and Kachru, R. (1982). *Resonant Rydberg-atom–Rydbert-atom collisions*. Phys. Rev. A, **25**, 1905.

Gärttner, M. and Evers, J. (2013). *Nonlinear absorption and density-dependent dephasing in Rydberg electromagnetically-induced-transparency media*. Phys. Rev. A, **88**, 033417.

Gärttner, M., Whitlock, S., Schönleber, D. W., and Evers, J. (2014a). *Collective Excitation of Rydberg-Atom Ensembles beyond the Superatom Model*. Phys. Rev. Lett., **113**, 233002.

Gärttner, M., Whitlock, S., Schönleber, D. W., and Evers, J. (2014b). *Semianalytical model for nonlinear absorption in strongly interacting Rydberg gases*. Phys. Rev. A, **89**, 063407.

Gaul, C., DeSalvo, B. J., Aman, J. A., Dunning, F. B., Killian, T. C., and Pohl, T. (2016). *Resonant Rydberg Dressing of Alkaline-Earth Atoms via Electromagnetically Induced Transparency*. Phys. Rev. Lett., **116**, 243001.

Gavryusev, V., Ferreira-Cao, M., Kekić, A., Zürn, G., and Signoles, A. (2016a). *Interaction-Enhanced Imaging of Rydberg P states*. arXiv:1602.04143.

Gavryusev, V., Signoles, A., Ferreira-Cao, M., Zürn, G., Hofmann, C. S., Günter, G., Schempp, H., de Saint-Vincent, M. R., Whitlock, S., and Weidemüller, M. (2016b). *Density matrix reconstruction of three-level atoms via Rydberg electromagnetically induced transparency*. Journal of Physics B: Atomic, Molecular and Optical Physics, **49**, 164002.

Gehr, R., Volz, J., Dubois, G., Steinmetz, T., Colombe, Y., Lev, B. L., Long, R., Estève, J., and Reichel, J. (2010). *Cavity-Based Single Atom Preparation and High-Fidelity Hyperfine State Readout*. Phys. Rev. Lett., **104**, 203602.

Gibble, K. E., Kasapi, S., and Chu, S. (1992). *Improved magneto-optic trapping in a vapor cell*. Opt. Lett., **17**, 526.

Glaetzle, A. W., Dalmonte, M., Nath, R., Gross, C., Bloch, I., and Zoller, P. (2015). *Designing Frustrated Quantum Magnets with Laser-Dressed Rydberg Atoms*. Phys. Rev. Lett., **114**, 173002.

Glauber, R. J. (1963). *Coherent and Incoherent States of the Radiation Field*. Phys. Rev., **131**, 2766.

Goldschmidt, E. A., Boulier, T., Brown, R. C., Koller, S. B., Young, J. T., Gorshkov, A. V., Rolston, S. L., and Porto, J. V. (2016). *Anomalous Broadening in Driven Dissipative Rydberg Systems*. Phys. Rev. Lett., **116**, 113001.

Gorniaczyk, H., Tresp, C., Bienias, P., Paris-Mandoki, A., Li, W., Mirgorodskiy, I., Büchler, H. P., Lesanovsky, I., and Hofferberth, S. (2016). *Enhancement of Rydberg-mediated single-photon nonlinearities by electrically tuned Förster resonances*. Nature Communications, **7**, 12480.

Gorniaczyk, H., Tresp, C., Schmidt, J., Fedder, H., and Hofferberth, S. (2014). *Single-Photon Transistor Mediated by Interstate Rydberg Interactions*. Phys. Rev. Lett., **113**, 053601.

Gorshkov, A. V., Nath, R., and Pohl, T. (2013). *Dissipative Many-Body Quantum Optics in Rydberg Media*. Phys. Rev. Lett., **110**, 153601.

Gorshkov, A. V., Otterbach, J., Fleischhauer, M., Pohl, T., and Lukin, M. D. (2011). *Photon-Photon Interactions via Rydberg Blockade*. Phys. Rev. Lett., **107**, 133602.

Govorov, A., Martínez, P., and Demir, H. (2016). *Understanding and Modeling Förster-type Resonance Energy Transfer (FRET): Introduction to FRET*. Number v. 1 in Springer Briefs in Applied Sciences and Technology. Springer Singapore.

Grangier, P., Levenson, J. A., and Poizat, J.-P. (1998). *Quantum non-demolition measurements in optics*. Nature, **396**, 537.

Gregory, P. D., Molony, P. K., Köppinger, M. P., Kumar, A., Ji, Z., Lu, B., Marchant, A. L., and Cornish, S. L. (2015). *A simple, versatile laser system for the creation of ultracold ground state molecules*. New Journal of Physics, **17**, 055006.

Greif, D., Parsons, M. F., Mazurenko, A., Chiu, C. S., Blatt, S., Huber, F., Ji, G., and Greiner, M. (2016). *Site-resolved imaging of a fermionic Mott insulator*. Science, **351**, 953.

Greiner, M., Mandel, O., Esslinger, T., Hänsch, T. W., and Bloch, I. (2002). *Quantum phase transition from a superfluid to a Mott insulator in a gas of ultracold atoms*. Nature, **415**, 39.

Grimm, R., Weidemüller, M., and Ovchinnikov, Y. B. (2000). *Optical Dipole Traps for Neutral Atoms.* In: Bederson, B. and Walther, H. (Eds.), *Advances in Atomic, Molecular, and Optical Physics*, Vol. 42 of *Advances In Atomic, Molecular, and Optical Physics*, , pp. 95 – 170. Academic Press.

Guerlin, C., Bernu, J., Deléglise, S., Sayrin, C., Gleyzes, S., Kuhr, S., Brune, M., Raimond, J.-M., and Haroche, S. (2007). *Progressive field-state collapse and quantum non-demolition photon counting.* Nature, **448**, 889.

Günter, G. (2014). *Interfacing Rydberg atoms with light and observing their interaction driven dynamics.* PhD thesis, Fakultat fur Physik, Ruprecht-Karls-Universität Heidelberg.

Günter, G., Robert-de Saint-Vincent, M., Schempp, H., Hofmann, C. S., Whitlock, S., and Weidemüller, M. (2012). *Interaction Enhanced Imaging of Individual Rydberg Atoms in Dense Gases.* Phys. Rev. Lett., **108**, 013002.

Günter, G., Schempp, H., Robert-de Saint-Vincent, M., Gavryusev, V., Helmrich, S., Hofmann, C. S., Whitlock, S., and Weidemüller, M. (2013). *Observing the Dynamics of Dipole-Mediated Energy Transport by Interaction-Enhanced Imaging.* Science, **342**, 954.

Gurian, J. H., Cheinet, P., Huillery, P., Fioretti, A., Zhao, J., Gould, P. L., Comparat, D., and Pillet, P. (2012). *Observation of a Resonant Four-Body Interaction in Cold Cesium Rydberg Atoms.* Phys. Rev. Lett., **108**, 023005.

Han, J., Jamil, Y., Norum, D. V., Tanner, P. J., and Gallagher, T. F. (2006). *Rb nf quantum defects from millimeter-wave spectroscopy of cold 85Rb Rydberg atoms.* Phys. Rev. A, **74**, 054502.

Han, J., Vogt, T., and Li, W. (2016). *Spectral shift and dephasing of electromagnetically induced transparency in an interacting Rydberg gas.* Phys. Rev. A, **94**, 043806.

Han, J., Vogt, T., Manjappa, M., Guo, R., Kiffner, M., and Li, W. (2015). *Lensing effect of electromagnetically induced transparency involving a Rydberg state.* Phys. Rev. A, **92**, 063824.

Harris, S. E. (1997). *Electromagnetically Induced Transparency.* Physics Today, **50**, 36.

Harty, T. P., Allcock, D. T. C., Ballance, C. J., Guidoni, L., Janacek, H. A., Linke, N. M., Stacey, D. N., and Lucas, D. M. (2014). *High-Fidelity Preparation, Gates, Memory, and Readout of a Trapped-Ion Quantum Bit.* Phys. Rev. Lett., **113**, 220501.

Hau, L. V., Harris, S. E., Dutton, Z., and Behroozi, C. H. (1999). *Light speed reduction to 17 metres per second in an ultracold atomic.* Nature, **397**, 594.

Hazzard, K. R. A., van den Worm, M., Foss-Feig, M., Manmana, S. R., Dalla Torre, E. G., Pfau, T., Kastner, M., and Rey, A. M. (2014). *Quantum correlations and entanglement in far-from-equilibrium spin systems.* Phys. Rev. A, **90**, 063622.

Heidemann, R., Raitzsch, U., Bendkowsky, V., Butscher, B., Löw, R., Santos, L., and Pfau, T. (2007). *Evidence for Coherent Collective Rydberg Excitation in the Strong Blockade Regime.* Phys. Rev. Lett., **99**, 163601.

Helmrich, S. (2013). *Improving optical resolution by noise correlation analysis.* Master's thesis, Fakultat fur Physik, Ruprecht-Karls-Universität Heidelberg.

Helmrich, S., Arias, A., Pehoviak, N., and Whitlock, S. (2016). *Two-body interactions and decay of three-level Rydberg-dressed atoms.* Journal of Physics B: Atomic, Molecular and Optical Physics, **49**, 03LT02.

Hirsch, M., Wareham, R. J., Martin-Fernandez, M. L., Hobson, M. P., and Rolfe, D. J. (2013). *A Stochastic Model for Electron Multiplication Charge-Coupled Devices – From Theory to Practice.* PLoS ONE, **8**, e53671.

Hofmann, C., Günter, G., Schempp, H., Müller, N., Faber, A., Busche, H., Robert-de Saint-Vincent, M., Whitlock, S., and Weidemüller, M. (2014). *An experimental approach for investigating many-body phenomena in Rydberg-interacting quantum systems.* Frontiers of Physics, **9**, 571.

Hofmann, C. S. (2013). *Emergence of correlations in strongly interacting ultracold Rydberg gases.* PhD thesis, Fakultat fur Physik, Ruprecht-Karls-Universität Heidelberg.

Hofmann, C. S., Günter, G., Schempp, H., Robert-de Saint-Vincent, M., Gärttner, M., Evers, J., Whitlock, S., and Weidemüller, M. (2013). *Sub-Poissonian Statistics of Rydberg-Interacting Dark-State Polaritons.* Phys. Rev. Lett., **110**, 203601.

Isenhower, L., Urban, E., Zhang, X. L., Gill, A. T., Henage, T., Johnson, T. A., Walker, T. G., and Saffman, M. (2010). *Demonstration of a Neutral Atom Controlled-NOT Quantum Gate.* Phys. Rev. Lett., **104**, 010503.

Jacob, D., Mimoun, E., Sarlo, L. D., Weitz, M., Dalibard, J., and Gerbier, F. (2011). *Production of sodium Bose-Einstein condensates in an optical dimple trap.* New Journal of Physics, **13**, 065022.

Jaksch, D., Cirac, J. I., Zoller, P., Rolston, S. L., Côté, R., and Lukin, M. D. (2000). *Fast Quantum Gates for Neutral Atoms.* Phys. Rev. Lett., **85**, 2208.

Janesick, J. (2001). *Scientific Charge-coupled Devices.* Press Monograph Series. Society of Photo Optical.

Janesick, J. (2007). *DN to [lambda]:.* SPIE Press Book. SPIE.

Janesick, J., Klaasen, K., and Elliott, T. (1985). *CCD Charge Collection Efficiency And The Photon Transfer Technique.* Vol. 0570, , pp. 7–19.

Jastrow, R. (1948). *On the Rydberg-Ritz Formula in Quantum Mechanics.* Phys. Rev., **73**, 60.

JCGM (2008). *JCGM 100: Evaluation of Measurement Data - Guide to the Expression of Uncertainty in Measurement.* Technical report, JCGM.

JCGM (2009). *JCGM 104:2009 Evaluation of measurement data – An introduction to the "Guide to the expression of uncertainty in measurement" and related documents.* Technical report, JCGM.

JCGM (2012). *JCGM 200:2012 International vocabulary of metrology − Basic and general concepts and associated terms (VIM).* Technical report, JCGM.

Ji, S., Ates, C., Garrahan, J. P., and Lesanovsky, I. (2013). *Equilibration of quantum hard rods in one dimension.* Journal of Statistical Mechanics: Theory and Experiment, **2013**, P02005.

Johnson, T. (2008). *Rabi Oscillations and Excitation Blockade between Ground and Rydberg states of single optically trapped Rubidium Atoms.* PhD thesis, University of Wisconsin-Madison.

Joseph, D. and Collins, S. (2002). *Modeling, calibration, and correction of nonlinear illumination-dependent fixed pattern noise in logarithmic CMOS image sensors.* IEEE Transactions on Instrumentation and Measurement, **51**, 996.

Karlewski, F., Mack, M., Grimmel, J., Sándor, N., and Fortágh, J. (2015). *State-selective all-optical detection of Rydberg atoms*. Phys. Rev. A, **91**, 043422.

Kerst, T. (2014). *Laser Frequency Stabilization on a high-finesse Fabry-Pérot cavity*. Master's thesis, Fakultat fur Physik, Ruprecht-Karls-Universität Heidelberg.

Ketterle, W., Durfee, D. S., and Stamper-Kurn, D. M. (1999). *Making, probing and understanding Bose-Einstein condensates*. In: M. Inguscio, S. S. and Wieman, C. (Eds.), *Bose-Einstein condensation in atomic gases*, Proceedings of the International School of Physics "Enrico Fermi", Course CXL, , pp. 67 – 176. IOS Press, Amsterdam.

Kherlopian, A. R., Song, T., Duan, Q., Neimark, M. A., Po, M. J., Gohagan, J. K., and Laine, A. F. (2008). *A review of imaging techniques for systems biology*. BMC Systems Biology, **2**, 74.

Killian, T. C., Pattard, T., Pohl, T., and Rost, J. M. (2007). *Ultracold Neutral Plasmas*. Physics Reports, **449**, 77.

Kostelecký, V. A., Nieto, M. M., and Truax, D. R. (1988). *Fine structure and analytical quantum-defect wave functions*. Phys. Rev. A, **38**, 4413.

Kuznetsova, E., Liu, G., and Malinovskaya, S. A. (2014). *Adiabatic rapid passage two-photon excitation of a Rydberg atom*. Physica Scripta, **2014**, 014024.

Labuhn, H. (2013). *Laser Frequency Stabilization on an Ultra-Stable Fabry-Pérot Cavity for Rydberg Atom Experiments*. Master's thesis, Fakultat fur Physik, Ruprecht-Karls-Universität Heidelberg.

Labuhn, H., Barredo, D., Ravets, S., de Léséleuc, S., Macrì, T., Lahaye, T., and Browaeys, A. (2016). *Tunable two-dimensional arrays of single Rydberg atoms for realizing quantum Ising models*. Nature, **534**, 667.

Leibfried, D., DeMarco, B., Meyer, V., Lucas, D., Barrett, M., Britton, J., Itano, W. M., Jelenkovic, B., Langer, C., Rosenband, T., and Wineland, D. J. (2003). *Experimental demonstration of a robust, high-fidelity geometric two ion-qubit phase gate*. Nature, **422**, 412.

Leibfried, D., Meekhof, D. M., King, B. E., Monroe, C., Itano, W. M., and Wineland, D. J. (1996). *Experimental Determination of the Motional Quantum State of a Trapped Atom*. Phys. Rev. Lett., **77**, 4281.

Leonhardt, U. (1995). *Quantum-State Tomography and Discrete Wigner Function.* Phys. Rev. Lett., **74**, 4101.

Leonhardt, U. and Paul, H. (1995). *Measuring the quantum state of light.* Progress in Quantum Electronics, **19**, 89 .

Levi, E., Minár, J., Garrahan, J. P., and Lesanovsky, I. (2015). *Crystalline structures and frustration in a two-component Rydberg gas.* New Journal of Physics, **17**, 123017.

Lewenstein, M., Sanpera, A., Ahufinger, V., Damski, B., Sen(De), A., and Sen, U. (2007). *Ultracold atomic gases in optical lattices: mimicking condensed matter physics and beyond.* Advances in Physics, **56**, 243.

Li, W., Mourachko, I., Noel, M. W., and Gallagher, T. F. (2003). *Millimeter-wave spectroscopy of cold Rb Rydberg atoms in a magneto-optical trap: Quantum defects of the ns, np, and nd series.* Phys. Rev. A, **67**, 052502.

Lindblad, G. (1976). *On the generators of quantum dynamical semigroups.* Communications in Mathematical Physics, **48**, 119.

Linskens, A. F., Holleman, I., Dam, N., and Reuss, J. (1996). *Two-photon Rabi oscillationsc.* Phys. Rev. A, **54**, 4854.

Lochead, G., Boddy, D., Sadler, D. P., Adams, C. S., and Jones, M. P. A. (2013). *Number-resolved imaging of excited-state atoms using a scanning autoionization microscope.* Phys. Rev. A, **87**, 053409.

Löw, R., Weimer, H., Nipper, J., Balewski, J. B., Butscher, B., Büchler, H. P., and Pfau, T. (2012). *An experimental and theoretical guide to strongly interacting Rydberg gases.* Journal of Physics B: Atomic, Molecular and Optical Physics, **45**, 113001.

Lu, J.-T., Goy, A. S., and Fleischer, J. W. (2015). *Nonlinear digital imaging.* arXiv:1507.08601.

Lukin, M. D., Fleischhauer, M., Côté, R., Duan, L. M., Jaksch, D., Cirac, J. I., and Zoller, P. (2001). *Dipole Blockade and Quantum Information Processing in Mesoscopic Atomic Ensembles.* Phys. Rev. Lett., **87**.

Mack, M., Grimmel, J., Karlewski, F., Sárkány, L. m. H., Hattermann, H., and Fortágh, J. (2015). *All-optical measurement of Rydberg-state lifetimes*. Phys. Rev. A, **92**, 012517.

Malossi, N., Valado, M. M., Scotto, S., Huillery, P., Pillet, P., Ciampini, D., Arimondo, E., and Morsch, O. (2014). *Full Counting Statistics and Phase Diagram of a Dissipative Rydberg Gas*. Phys. Rev. Lett., **113**, 023006.

Manthey, T., Niederprüm, T., Thomas, O., and Ott, H. (2015). *Dynamically probing ultracold lattice gases via Rydberg molecules*. New Journal of Physics, **17**, 103024.

Manthey, T., Weber, T. M., Niederprüm, T., Langer, P., Guarrera, V., Barontini, G., and Ott, H. (2014). *Scanning electron microscopy of Rydberg-excited Bose–Einstein condensates*. New Journal of Physics, **16**, 083034.

Marangos, J. P. (1998). *Electromagnetically induced transparency*. J. Mod. Opt., **45**, 471.

Maxwell, D., Szwer, D. J., Paredes-Barato, D., Busche, H., Pritchard, J. D., Gauguet, A., Weatherill, K. J., Jones, M. P. A., and Adams, C. S. (2013). *Storage and Control of Optical Photons Using Rydberg Polaritons*. Phys. Rev. Lett., **110**, 103001.

McCarron, D. J., King, S. A., and Cornish, S. L. (2008). *Modulation transfer spectroscopy in atomic rubidium*. Measurement Science and Technology, **19**, 105601.

McDonnell, M. J., Stacey, D. N., and Steane, A. M. (2004). *Laser linewidth effects in quantum state discrimination by electromagnetically induced transparency*. Phys. Rev. A, **70**, 053802.

McQuillen, P., Zhang, X., Strickler, T., Dunning, F. B., and Killian, T. C. (2013). *Imaging the evolution of an ultracold strontium Rydberg gas*. Phys. Rev. A, **87**, 013407.

Mhaskar, R. R., Olson, S. E., and Raithel, G. (2006). *Open-channel fluorescence imaging of atoms in high-gradient magnetic fields*. The European Physical Journal D, **41**, 221.

Mohapatra, A. K., Jackson, T. R., and Adams, C. S. (2007). *Coherent Optical Detection of Highly Excited Rydberg States Using Electromagnetically Induced Transparency.* Phys. Rev. Lett., **98**, 113003.

Mohr, P. J., Newell, D. B., and Taylor, B. N. (2016). *CODATA recommended values of the fundamental physical constants: 2014*.* Rev. Mod. Phys., **88**, 035009.

Mooney, J. M., Sheppard, F. D., Ewing, W. S., Ewing, J. E., and Silverman, J. (1989). *Responsivity nonuniformity limited performance of infrared staring cameras.* Optical Engineering, **28**, 281151.

Moos, M., Höning, M., Unanyan, R., and Fleischhauer, M. (2015). *Many-body physics of Rydberg dark-state polaritons in the strongly interacting regime.* Phys. Rev. A, **92**, 053846.

Mourachko, I., Comparat, D., de Tomasi, F., Fioretti, A., Nosbaum, P., Akulin, V., and Pillet, P. (1998). *Many-body effects in a frozen Rydberg gas.* Phys. Rev. Lett., **80**, 253.

Muessel, W., Strobel, H., Joos, M., Nicklas, E., Stroescu, I., Tomkovic, J., Hume, D., and Oberthaler, M. (2013). *Optimized absorption imaging of mesoscopic atomic clouds.* Applied Physics B, **113**, 69.

Müller, M., Diehl, S., Pupillo, G., and Zoller, P. (2012). *Engineered Open Systems and Quantum Simulations with Atoms and Ions.* In: Paul Berman, E. A. and Lin, C. (Eds.), *Advances in Atomic, Molecular, and Optical Physics*, Vol. Volume 61, , pp. 1–80. Academic Press.

Müller, N. L. M. (2010). *Excitation and detection of Rydberg atoms in an ultracold gas - Electric field design and electromagnetically induced transparency.* Master's thesis, Fakultat fur Physik, Ruprecht-Karls-Universität Heidelberg.

Murray, C. and Pohl, T. (2016). *Quantum and Nonlinear Optics in Strongly Interacting Atomic Ensembles.* Advances In Atomic, Molecular, and Optical Physics, , pp. –. Academic Press.

Myerson, A. H., Szwer, D. J., Webster, S. C., Allcock, D. T. C., Curtis, M. J., Imreh, G., Sherman, J. A., Stacey, D. N., Steane, A. M., and Lucas, D. M. (2008). *High-Fidelity Readout of Trapped-Ion Qubits.* Phys. Rev. Lett., **100**, 200502.

Naber, J. B., Vos, J., Rengelink, R. J., Nusselder, R. J., and Davtyan, D. (2015). *Optical techniques for Rydberg physics in lattice geometries.* arXiv:1512.06241.

Nipper, J., Balewski, J. B., Krupp, A. T., Butscher, B., Löw, R., and Pfau, T. (2012a). *Highly Resolved Measurements of Stark-Tuned Förster Resonances between Rydberg Atoms.* Phys. Rev. Lett., **108**, 113001.

Nipper, J., Balewski, J. B., Krupp, A. T., Hofferberth, S., Löw, R., and Pfau, T. (2012b). *Atomic Pair-State Interferometer: Controlling and Measuring an Interaction-Induced Phase Shift in Rydberg-Atom Pairs.* Phys. Rev. X, **2**, 031011.

Ockeloen, C. F., Tauschinsky, A. F., Spreeuw, R. J. C., and Whitlock, S. (2010). *Detection of small atom numbers through image processing.* Phys. Rev. A, **82**, 061606.

Olmos, B., Li, W., Hofferberth, S., and Lesanovsky, I. (2011). *Amplifying single impurities immersed in a gas of ultracold atoms.* Phys. Rev. A, **84**, 041607.

O'Sullivan, M. S. and Stoicheff, B. P. (1985). *Scalar polarizabilities and avoided crossings of high Rydberg states in Rb.* Phys. Rev. A, **31**, 2718.

Ott, H. (2016). *Single atom detection in ultracold quantum gases: a review of current progress.* Reports on Progress in Physics, **79**, 054401.

Ourjoumtsev, A., Tualle-Brouri, R., and Grangier, P. (2006). *Quantum Homodyne Tomography of a Two-Photon Fock State.* Phys. Rev. Lett., **96**, 213601.

Parigi, V., Bimbard, E., Stanojevic, J., Hilliard, A. J., Nogrette, F., Tualle-Brouri, R., Ourjoumtsev, A., and Grangier, P. (2012). *Observation and Measurement of Interaction-Induced Dispersive Optical Nonlinearities in an Ensemble of Cold Rydberg Atoms.* Phys. Rev. Lett., **109**.

Paris-Mandoki, A., Gorniaczyk, H., Tresp, C., Mirgorodskiy, I., and Hofferberth, S. (2016). *Tailoring Rydberg interactions via Förster resonances: state combinations, hopping and angular dependence.* Journal of Physics B: Atomic, Molecular and Optical Physics, **49**, 164001.

Park, H., Tanner, P. J., Claessens, B. J., Shuman, E. S., and Gallagher, T. F. (2011). *Dipole-dipole broadening of Rb ns-np microwave transitions.* Phys. Rev. A, **84**, 022704.

Petrosyan, D., Mølmer, K., and Fleischhauer, M. (2016). *On the adiabatic preparation of spatially-ordered Rydberg excitations of atoms in a one-dimensional optical lattice by laser frequency sweeps.* Journal of Physics B: Atomic, Molecular and Optical Physics, **49**, 084003.

Petrosyan, D., Otterbach, J., and Fleischhauer, M. (2011). *Electromagnetically Induced Transparency with Rydberg Atoms.* Phys. Rev. Lett., **107**, 213601.

Peyronel, T., Firstenberg, O., Liang, Q.-Y., Hofferberth, S., Gorshkov, A. V., Pohl, T., Lukin, M. D., and Vuletić, V. (2012). *Quantum nonlinear optics with single photons enabled by strongly interacting atoms.* Nature, **488**, 57.

Pillet, P. and Gallagher, T. F. (2016). *Rydberg atom interactions from 300 K to 300 K.* Journal of Physics B: Atomic, Molecular and Optical Physics, **49**, 174003.

Pohl, T., Adams, C. S., and Sadephpour, H. R. (2011). *Cold Rydberg gases and ultra-cold plasmas.* Journal of Physics B: Atomic, Molecular and Optical Physics, **44**, 180201.

Pohl, T., Demler, E., and Lukin, M. D. (2010). *Dynamical Crystallization in the Dipole Blockade of Ultracold Atoms.* Phys. Rev. Lett., **104**, 043002.

Pritchard, Jonathan, D. (2011). *Cooperative Optical Non-linearity in a blockaded Rydberg Ensemble.* PhD thesis, Durham University.

Pritchard, J. D., Gauguet, A., Weatherill, K. J., and Adams, C. S. (2011). *Optical non-linearity in a dynamical Rydberg gas.* Journal of Physics B: Atomic, Molecular and Optical Physics, **44**, 184019.

Pritchard, J. D., Maxwell, D., Gauguet, A., Weatherill, K. J., Jones, M. P. A., and Adams, C. S. (2010). *Cooperative Atom-Light Interaction in a Blockaded Rydberg Ensemble.* Phys. Rev. Lett., **105**, 193603.

Pritchard, J. D., Weatherill, K. J., and Adams, C. S. (2013). *Annual Review of Cold Atoms and Molecules*, Vol. 1, chapter 8 - Nonlinear optics using cold Rydberg atoms, , pp. 301–350. World Scientific.

Regal, C. and Jin, D. (2007). *Experimental Realization of the BCS-BEC Crossover with a Fermi Gas of Atoms.* Vol. 54 of *Advances In Atomic, Molecular, and Optical Physics*, , pp. 1 – 79. Academic Press.

Reinaudi, G., Lahaye, T., Wang, Z., and Guéry-Odelin, D. (2007). *Strong saturation absorption imaging of dense clouds of ultracold atoms.* Opt. Lett., **32**, 3143.

Reinhard, A., Liebisch, T. C., Knuffman, B., and Raithel, G. (2007). *Level shifts of rubidium Rydberg states due to binary interactions.* Phys. Rev. A, **75**, 032712.

Reiter, F. and Sørensen, A. S. (2012). *Effective operator formalism for open quantum systems.* Phys. Rev. A, **85**, 032111.

Robbins, M. and Hadwen, B. (2003). *The noise performance of electron multiplying charge-coupled devices.* Electron Devices, IEEE Transactions on, **50**, 1227.

Robert-de Saint-Vincent, M., Hofmann, C. S., Schempp, H., Günter, G., Whitlock, S., and Weidemüller, M. (2013). *Spontaneous Avalanche Ionization of a Strongly Blockaded Rydberg Gas.* Phys. Rev. Lett., **110**, 045004.

Robicheaux, F. and Gill, N. M. (2014). *Effect of random positions for coherent dipole transport.* Phys. Rev. A, **89**, 053429.

Roos, C. F., Lancaster, G. P. T., Riebe, M., Häffner, H., Hänsel, W., Gulde, S., Becher, C., Eschner, J., Schmidt-Kaler, F., and Blatt, R. (2004). *Bell States of Atoms with Ultralong Lifetimes and Their Tomographic State Analysis.* Phys. Rev. Lett., **92**, 220402.

Ryabtsev, I. I., Tretyakov, D. B., Beterov, I. I., and Entin, V. M. (2010). *Observation of the Stark-Tuned Förster Resonance between Two Rydberg Atoms.* Phys. Rev. Lett., **104**, 073003.

Saffman, M. (2016). *Quantum computing with atomic qubits and Rydberg interactions: progress and challenges.* Journal of Physics B: Atomic, Molecular and Optical Physics, **49**, 202001.

Saffman, M., Walker, T. G., and Mølmer, K. (2010). *Quantum information with Rydberg atoms.* Rev. Mod. Phys., **82**, 2313.

Saßmannshausen, H., Merkt, F., and Deiglmayr, J. (2013). *High-resolution spectroscopy of Rydberg states in an ultracold cesium gas.* Phys. Rev. A, **87**, 032519.

Schauß, P., Cheneau, M., Endres, M., Fukuhara, T., Hild, S., Omran, A., Pohl, T., Gross, C., Kuhr, S., and Bloch, I. (2012). *Observation of spatially ordered structures in a two-dimensional Rydberg gas.* Nature, **491**, 87.

Schauß, P., Zeiher, J., Fukuhara, T., Hild, S., Cheneau, M., Macrì, T., Pohl, T., Bloch, I., and Gross, C. (2015). *Crystallization in Ising quantum magnets.* Science, **347**, 1455.

Schempp, H. (2014). *Formation of Aggregates and Energy Transport in ultracold Rydberg gases.* PhD thesis, Fakultat fur Physik, Ruprecht-Karls-Universität Heidelberg.

Schempp, H., Günter, G., Hofmann, C. S., Giese, C., Saliba, S. D., DePaola, B. D., Amthor, T., Weidemüller, M., Sevinçli, S., and Pohl, T. (2010). *Coherent Population Trapping with Controlled Interparticle Interactions.* Phys. Rev. Lett., **104**, 173602.

Schempp, H., Günter, G., Robert-de Saint-Vincent, M., Hofmann, C. S., Breyel, D., Komnik, A., Schönleber, D. W., Gärttner, M., Evers, J., Whitlock, S., and Weidemüller, M. (2014). *Full Counting Statistics of Laser Excited Rydberg Aggregates in a One-Dimensional Geometry.* Phys. Rev. Lett., **112**, 013002.

Schempp, H., Günter, G., Wüster, S., Weidemüller, M., and Whitlock, S. (2015). *Correlated Exciton Transport in Rydberg-Dressed-Atom Spin Chains.* Phys. Rev. Lett., **115**, 093002.

Schlagmüller, M., Liebisch, T. C., Engel, F., Kleinbach, K. S., Böttcher, F., Hermann, U., Westphal, K. M., Gaj, A., Löw, R., Hofferberth, S., Pfau, T., Pérez-Ríos, J., and Greene, C. H. (2016). *Ultracold Chemical Reactions of a Single Rydberg Atom in a Dense Gas.* Phys. Rev. X, **6**, 031020.

Schnellbächer, N. D. (2010). *A compact setup for frequency stabilization of diode lasers.* Master's thesis, Fakultat fur Physik, Ruprecht-Karls-Universität Heidelberg.

Schönleber, D. W., Eisfeld, A., Genkin, M., Whitlock, S., and Wüster, S. (2015). *Quantum Simulation of Energy Transport with Embedded Rydberg Aggregates.* Phys. Rev. Lett., **114**, 123005.

Schoser, J., Batär, A., Löw, R., Schweikhard, V., Grabowski, A., Ovchinnikov, Y. B., and Pfau, T. (2002). *Intense source of cold Rb atoms from a pure two-dimensional magneto-optical trap.* Phys. Rev. A, **66**, 023410.

Schwarzkopf, A., Anderson, D. A., Thaicharoen, N., and Raithel, G. (2013). *Spatial correlations between Rydberg atoms in an optical dipole trap*. Phys. Rev. A, **88**, 061406.

Schwarzkopf, A., Sapiro, R. E., and Raithel, G. (2011). *Imaging Spatial Correlations of Rydberg Excitations in Cold Atom Clouds*. Phys. Rev. Lett., **107**, 103001.

Scully, M. O. and Zubairy, M. S. (1997). *Quantum optics*. Cambridge University Press.

Seaton, M. J. (1983). *Quantum defect theory*. Reports on Progress in Physics, **46**, 167.

Sevinçli, S., Ates, C., Pohl, T., Schempp, H., Hofmann, C. S., Günter, G., Amthor, T., Weidemüller, M., Pritchard, J. D., Maxwell, D., Gauguet, A., Weatherill, K. J., Jones, M. P. A., and Adams, C. S. (2011a). *Quantum interference in interacting three-level Rydberg gases: coherent population trapping and electromagnetically induced transparency*. Journal of Physics B: Atomic, Molecular and Optical Physics, **44**, 184018.

Sevinçli, S., Henkel, N., Ates, C., and Pohl, T. (2011b). *Nonlocal Nonlinear Optics in Cold Rydberg Gases*. Phys. Rev. Lett., **107**, 153001.

Sherson, J. F., Weitenberg, C., Endres, M., Cheneau, M., Bloch, I., and Kuhr, S. (2010). *Single-atom-resolved fluorescence imaging of an atomic Mott insulator*. Nature, **467**, 68.

Shirley, J. H. (1982). *Modulation transfer processes in optical heterodyne saturation spectroscopy*. Opt. Lett., **7**, 537.

Singer, K. (2004). *Interactions in an ultracold gas of Rydberg atoms*. PhD thesis, Fakultät für Mathematik und Physik, Albert-Ludwigs-Universität Freiburg.

Singer, K., Reetz-Lamour, M., Amthor, T., Fölling, S., Tscherneck, M., and Weidemüller, M. (2005). *Spectroscopy of an ultracold Rydberg gas and signatures of Rydberg–Rydberg interactions*. Journal of Physics B: Atomic, Molecular and Optical Physics, **38**, S321.

Singer, K., Reetz-Lamour, M., Amthor, T., Marcassa, L. G., and Weidemüller, M. (2004). *Suppression of Excitation and Spectral Broadening Induced by Interactions in a Cold Gas of Rydberg Atoms*. Phys. Rev. Lett., **93**, 163001.

Smithey, D. T., Beck, M., Raymer, M. G., and Faridani, A. (1993). *Measurement of the Wigner distribution and the density matrix of a light mode using optical homodyne tomography: Application to squeezed states and the vacuum.* Phys. Rev. Lett., **70**, 1244.

Stanojevic, J., Parigi, V., Bimbard, E., Ourjoumtsev, A., and Grangier, P. (2013). *Dispersive optical nonlinearities in a Rydberg electromagnetically-induced-transparency medium.* Phys. Rev. A, **88**, 053845.

Stebbings, R. F. and Dunning, F. B. (1983). *Rydberg States of Atoms and Molecules.* Cambridge University Press.

Steck, D. A. (2001). *Rubidium 87 D line data.* available online http://steck.us/alkalidata.

Steck, D. A. (2007). *Quantum and Atom Optics.* revision 0.11.3, 9 October 2016.

Sultana, S. and Zubairy, M. S. (1994). *Effect of finite bandwidth on refractive-index enhancement and lasing without inversion.* Phys. Rev. A, **49**, 438.

Tauschinsky, A., Thijssen, R. M. T., Whitlock, S., van Linden van den Heuvell, H. B., and Spreeuw, R. J. C. (2010). *Spatially resolved excitation of Rydberg atoms and surface effects on an atom chip.* Phys. Rev. A, **81**, 063411.

Teixeira, R. C., Hermann-Avigliano, C., Nguyen, T. L., Cantat-Moltrecht, T., Raimond, J. M., Haroche, S., Gleyzes, S., and Brune, M. (2015). *Microwaves Probe Dipole Blockade and van der Waals Forces in a Cold Rydberg Gas.* Phys. Rev. Lett., **115**, 013001.

Thaicharoen, N., Schwarzkopf, A., and Raithel, G. (2015). *Measurement of the van der Waals interaction by atom trajectory imaging.* Phys. Rev. A, **92**, 040701.

Thoumany, P., Hänsch, T., Stania, G., Urbonas, L., and Becker, T. (2009). *Optical spectroscopy of rubidium Rydberg atoms with a 297 nm frequency-doubled dye laser.* Opt. Lett., **34**, 1621.

Tiarks, D., Baur, S., Schneider, K., Dürr, S., and Rempe, G. (2014). *Single-Photon Transistor Using a Förster Resonance.* Phys. Rev. Lett., **113**, 053602.

Tong, D., Farooqi, S. M., Stanojevic, J., Krishnan, S., Zhang, Y. P., Côté, R., Eyler, E. E., and Gould, P. L. (2004). *Local Blockade of Rydberg Excitation in an Ultracold Gas.* Phys. Rev. Lett., **93**, 063001.

Tresp, C., Bienias, P., Weber, S., Gorniaczyk, H., Mirgorodskiy, I., Büchler, H. P., and Hofferberth, S. (2015). *Dipolar Dephasing of Rydberg D-State Polaritons.* Phys. Rev. Lett., **115**, 083602.

Urvoy, A., Ripka, F., Lesanovsky, I., Booth, D., Shaffer, J. P., Pfau, T., and Löw, R. (2015). *Strongly Correlated Growth of Rydberg Aggregates in a Vapor Cell.* Phys. Rev. Lett., **114**, 203002.

van Amerongen, H., Valkūnas, L., and van Grondelle, R. (2000). *Photosynthetic Excitons.* World Scientific.

van Bijnen, R. (2013). *Quantum Engineering with Ultracold Atoms.* PhD thesis, Eindhoven University of Technology.

van Bijnen, R. M. W. and Pohl, T. (2015). *Quantum Magnetism and Topological Ordering via Rydberg Dressing near Förster Resonances.* Phys. Rev. Lett., **114**, 243002.

van Bijnen, R. M. W., Smit, S., van Leeuwen, K. A. H., Vredenbregt, E. J. D., and Kokkelmans, S. (2011). *Adiabatic formation of Rydberg crystals with chirped laser pulses.* Journal of Physics B: Atomic, Molecular and Optical Physics, **44**, 184008.

van Ditzhuijzen, C. S. E., Koenderink, A. F., Hernàndez, J. V., Robicheaux, F., Noordam, L. D., and van Linden van den Heuvell, H. B. (2008). *Spatially Resolved Observation of Dipole-Dipole Interaction between Rydberg Atoms.* Phys. Rev. Lett., **100**, 243201.

van Frank, S., Bonneau, M., Schmiedmayer, J., Hild, S., Gross, C., Cheneau, M., Bloch, I., Pichler, T., Negretti, A., Calarco, T., and Montangero, S. (2016). *Optimal control of complex atomic quantum systems.* Scientific Reports, **6**, 34187.

Vanhaecke, N., Comparat, D., Tate, D. A., and Pillet, P. (2005). *Ionization of Rydberg atoms embedded in an ultracold plasma.* Phys. Rev. A, **71**, 013416.

Vermersch, B., Punk, M., Glaetzle, A. W., Gross, C., and Zoller, P. (2015). *Dynamical preparation of laser-excited anisotropic Rydberg crystals in 2D optical lattices.* New Journal of Physics, **17**, 013008.

Viteau, M., Huillery, P., Bason, M. G., Malossi, N., Ciampini, D., Morsch, O., Arimondo, E., Comparat, D., and Pillet, P. (2012). *Cooperative Excitation and Many-Body Interactions in a Cold Rydberg Gas.* Phys. Rev. Lett., **109**, 053002.

Vogel, K. and Risken, H. (1989). *Determination of quasiprobability distributions in terms of probability distributions for the rotated quadrature phase.* Phys. Rev. A, **40**, 2847.

Vogt, T., Viteau, M., Zhao, J., Chotia, A., Comparat, D., and Pillet, P. (2006). *Dipole Blockade at Förster Resonances in High Resolution Laser Excitation of Rydberg States of Cesium Atoms.* Phys. Rev. Lett., **97**, 083003.

Vrinceanu, D., Sadeghpour, H. R., and Pohl, T. (2009). *Rydberg atom formation in ultracold plasmas: Non-equilibrium dynamics of recombination.* Journal of Physics: Conference Series, **194**, 012067.

Walker, T. G. and Saffman, M. (2008). *Consequences of Zeeman degeneracy for the van der Waals blockade between Rydberg atoms.* Phys. Rev. A, **77**, 032723.

Wang, D., Neyenhuis, B., de Miranda, M. H. G., Ni, K.-K., Ospelkaus, S., Jin, D. S., and Ye, J. (2010). *Direct absorption imaging of ultracold polar molecules.* Phys. Rev. A, **81**, 061404.

Weber, T., Herbig, J., Mark, M., Nägerl, H. C., and Grimm, R. (2002). *Bose-Einstein Condensation of Cesium.* Science, **299**, 232.

Weber, T. M., Honing, M., Niederprum, T., Manthey, T., Thomas, O., Guarrera, V., Fleischhauer, M., Barontini, G., and Ott, H. (2015). *Mesoscopic Rydberg-blockaded ensembles in the superatom regime and beyond.* Nature Physics, **11**, 157.

Weimer, H., Löw, R., Pfau, T., and Büchler, H. P. (2008). *Quantum Critical Behavior in Strongly Interacting Rydberg Gases.* Phys. Rev. Lett., **101**, 250601.

Weimer, H., Müller, M., Lesanovsky, I., Zoller, P., and Büchler, H. P. (2010). *A Rydberg quantum simulator.* Nature Physics, **6**, 382.

Westermann, S., Amthor, T., de Oliveira, A. L., Deiglmayr, J., Reetz-Lamour, M., and Weidemüller, M. (2006). *Dynamics of resonant energy transfer in a cold Rydberg gas.* Eur. Phys. J. D, **40**, 37.

Whitlock, S., Glaetzle, A. W., and Hannaford, P. (2016). *Simulating Quantum Spin Models using Rydberg-Excited Atomic Ensembles in Magnetic Microtrap Arrays.* arXiv:1608.00251.

Williams, J. G. (2007). *Organic Light-Emitting Devices: Synthesis, Properties and Applications.* Platinum Metals Review, **51**, 85.

Wolf, S., Oliver, S. J., and Weiss, D. S. (2000). *Suppression of Recoil Heating by an Optical Lattice.* Phys. Rev. Lett., **85**, 4249.

Wolfram Research Inc. (2012). *Mathematica 9.0.*

Yu, H. and Robicheaux, F. (2016). *Coherent dipole transport in a small grid of Rydberg atoms.* Phys. Rev. A, **93**, 023618.

Zeiher, J., Schauß, P., Hild, S., Macrì, T., Bloch, I., and Gross, C. (2015). *Microscopic Characterization of Scalable Coherent Rydberg Superatoms.* Phys. Rev. X, **5**, 031015.

Zeiher, J., van Bijnen, R., Schausz, P., Hild, S., Choi, J.-y., Pohl, T., Bloch, I., and Gross, C. (2016). *Many-body interferometry of a Rydberg-dressed spin lattice.* Nat Phys, **advance online publication**, .

Zhang, H., Zhang, L., Wang, L., Bao, S., Zhao, J., Jia, S., and Raithel, G. (2014). *Autler-Townes spectroscopy with interaction-induced dephasing.* Phys. Rev. A, **90**, 043849.

Zhang, L. and Evers, J. (2016). *Nonlocal nonlinear response of thermal Rydberg atoms and modulational instability in an absorptive nonlinear medium.* Phys. Rev. A, **94**, 033402.

Zimmerman, M. L., Littman, M. G., Kash, M. M., and Kleppner, D. (1979). *Stark structure of the Rydberg states of alkali-metal atoms.* Phys. Rev. A, **20**, 2251.

List of Figures

161

List of Tables

Acknowledgments

This work would not have been possible without the support and contribution of many people that I would like to warmly thank here.

First of all I am very grateful to my supervisor **Prof. Dr. Matthias Weidemüller** for having given me the possibility to work in such great group and to contribute to a really "exciting" experiment. I learned a lot from the discussions together, from your deep insight and perspective on physics, and I will carry these precious gifts in my future path.

I would like to thank **Prof. Dr. Selim Jochim** for taking the duty to be my second referee, for all the insightful conversations and advice. Furthermore, I would like to thank for the opportunities for fruitful exchange with members of your team.

My greatest thanks go to **Adrien Signoles**. Working together on our publications, your scientific insight and the support you gave me along the path that brought me to this finishing line have been crucial.

I would like to sincerely thank **Gerhard Zürn** for all the small and big projects that we did together. Your vision and technical knowledge have taught me a lot. And I especially appreciate your German quick translation.

It has been a privilege to work with **Shannon Whitlock**. Your deep insight in all the questions that I could come up with and the support that you gave me during this time have allowed me to reach this point. For this I would like to express you my deep gratitude.

My first year in Heidelberg would have been totally different without the support and friendship with **Martin Robert-de-Saint-Vincent**. We shared a great time inside and outside the lab. Thank you very much!

My greatest thanks go to my friend and only then colleague **Miguel Ferreira-Cao**. We shared a great time working together on fascinating experiments, but most of all we have wonderful things to remember outside the lab. I wish you the greatest luck in your path towards the PhD and I'm confident that we will have many more memories together.

I would like to warmly thank **Renato Ferracini-Alves**, this year together has been great and we shared many nice moments together. I wish you good luck with the experiment!

The experiments that I did where enabled by the prior work and support of **Hanna Schempp**, **Georg Günter** and **Christoph Hoffmann**, who were great colleagues and taught me much. I warmly thank you and wish you all the best!

I would have missed much without the great time that we had together, planning for our alternative Rydberg project. Thank you very much **Maria Martinez Valado** and I wish you all the best!

During my four years in Heidelberg I had the great opportunity to work together with **Giulia Faraoni** and **Thomas Kerst**. I hold precious memories of this time and I wish that we will meet soon again. It has been a pleasure to work with **Armin Kekić**, **Titus Franz**, **Yu Lu** and **Fa Chao**. I hope I had been of help for you and I wish you good luck in your future path.

I would like to thank **Juris Ulmanis**, **Stephan Häfner**, **Henry López**, **Bastian Höltkemeier**, **Alda Arias Suarez** and **Stephan Helmrich** for the many kicker games, jokes and simply good time that we had together. I would also like to thank **Puneet Murthy** for the nice discussions and collaboration. And I cannot forget about **Valentin Ivannikov**, a friend from whom I learned a lot, thank you very much!

I would like to warmly thank **Rick van Bijnen**, **Jörg Evers**, **Martin Gärttner** and **David Schönleber** for the insightful discussions we had and that have allowed me to progress much further. It was a pleasure for me to meet you! All the best!

A big thank you goes to **Ralf Ziegler**, **Dominic Litsch**, **Dr. Venelin Angelov**, and all the personnel of the electronics and mechanics workshops. Without your work and contribution it wouldn't have been possible to achieve these results.

My sincere thanks go to **Claudia Krämer** and **Danica Subally-Haupt**, your help and support have made my years in Heidelberg a nice time to remember!

Thank you very much to **all my friends** who where close to me during these years, sharing the good and the bad times, your support has been very important. A deep thank you goes to **Veronika Chevyreva** who knows what reading obscure pages at night means, but also how to have a great time!

Finally I would like to thank my **family** and my wife **Elisa** for their love and continued support in everything that I do. This thesis is dedicated to them.

Сердечная благодарность моим родителям, **Владимиру** и **Елене**, за то что всегда были рядом и верили в меня. Искренне благодарю мою сестру **Екатерину** за поддержку и ценные советы. Крепко обнимаю и целую мою бабушку **Нину**.

Un ringraziamento sincero va a **Paola** e **Riccardo**, genitori di Elisa, per aver sempre creduto in me.

Un semplice ringraziamento non basta per esprimere la mia riconoscenza al mio amore, **Elisa**, per tutta la fiducia che hai riposto in me ed il sostegno che mi hai dato in questi lunghi anni. Nonostante la difficoltá della distanza abbiamo rafforzato noi e svelato quanto ci sappiamo arricchire l'un l'altro. Ti amo per questo e non solo.